BEHAVIOUR OF SOLIDS UNDER HIGH STRAIN-RATE DEFORMATION

By

SUNIL RAWAT

(PHYS01200704031)

Bhabha Atomic Research Centre, Trombay, Mumbai,

Maharashtra, INDIA

A thesis submitted to the

Board of Studies in Physical Sciences

In partial fulfillment of requirements

For the Degree of

DOCTOR OF PHILOSOPHY

of

HOMI BHABHA NATIONAL INSTITUTE

October 2012

Homi Bhabha National Institute

Recommendations of the Viva Voce Board

As members of Viva Voce Board, we certify that we have read the dissertation prepared by "**Sunil Rawat**" entitled "**Behaviour of Solids under High Strain Rate Deformation** " and recommend that it may be accepted as fulfilling the dissertation requirement for the Degree of Doctor of Philosophy.

_____ **Date:** 31/8/13

Chairman - Dr. N K Gupta, BARC, Mumbai

_____ **Date:** 31/8/13

Guide - Dr. Shashank Chaturvedi, BARC, Vizag

_____ **Date:**

Technical Advisor - Shri Vivek M. Chavan, BARC, Mumbai

_____ **Date:**

Member 1 - Dr. R. Ganesh, IPR, Gandhinagar

_____ **Date:** 31/08/13

Member 2 - Dr. Manoj Warrier, BARC, Vizag

_____ **Date:** 31/08/13

External Examiner - Dr. M. C. Valsakumar, SEST, Hyderabad

Final approval and acceptance of this dissertation is contingent upon the candidate's submission of the final copies of the dissertation to HBNI.

I hereby certify that I have read this dissertation prepared under my direction and recommend that it may be accepted as fulfilling the dissertation requirement.

Date: 31/8/13

Place: BARC, Mumbai

Guide: 31/8/13

(Dr. Shashank Chaturvedi)

STATEMENT BY AUTHOR

This dissertation has been submitted in partial fulfillment of requirements for an advanced degree at Homi Bhabha National Institute (HBNI) and is deposited in the Library to be made available to borrowers under rules of the HBNI.

Brief quotations from this dissertation are allowable without special permission, provided that accurate acknowledgement of source is made. Requests for permission for extended quotation from or reproduction of this manuscript in whole or in part may be granted by the Competent Authority of HBNI when in his or her judgment the proposed use of the material is in the interests of scholarship. In all other instances, however, permission must be obtained from the author.

Signature of the Candidate

Sunil Rawat

DECLARATION

I, Sunil Rawat, hereby declare that the investigation presented in the thesis has been carried out by me. The work is original and has not been submitted earlier as a whole or part for a degree/diploma at this or any other Institution/University.

Signature of the Candidate

Sunil Rawat

CERTIFICATION FROM GUIDE

This is to certify that the corrections suggested by the examiners of the thesis have been incorporated in the thesis submitted to HBNI.

Date: 31/8/13

Guide: A. Chaturvedi 31/8/13

(Dr. Shashank Chaturvedi)

I dedicate this work to my

mother Rambeti,
father D. S. Rawat,
brother M. K. Rawat, and
wife Pratiksha

for support, encouragement and love.

ACKNOWLEDGEMENTS

This work would not have been completed without the constant support and care of my thesis supervisor, Dr. Shashank Chaturvedi, Head, Computational Analysis Division (CAD), BARC-Vizag. I am greatly appreciate his way of teaching and guidance during these years. I remember those days at BARC-Vizag when he discussed the problems even during tea and lunch. I also remember the discussions at TSH, BARC-Mumbai after the dinner when he gave me brilliant ideas for the problems which I was facing since long times. I am very much thankful to him for sending emails to different divisions at BARC-Mumbai to get approvals for various experimental analysis which saved my lot of time. I thank him for arranging the accounts at supercomputer at BARC-Mumbai which helped me to perform simulations in parallel to experiments. I am also very much thankful to him for giving me freedom and support to interact with various people in BARC which have expertise in different areas. He gave me invaluable advices for the problems whether they were scientific or not that would be valuable assets for my entire life. I remember one proverb which very much suits for him to teach and guide his students "Give a man a fish, and you have fed him once. Teach him how to fish and you have fed him for a lifetime".

I would like to express my heartiest gratitude to Dr. Manoj Warrier from CAD, BARC-Vizag for his constant help, care, teaching and guidance throughout the years. I would like to thank him for providing me various post-processing softwares and giving me a lot of time whenever needed for discussions and comments throughout my PhD work. I am sincerely appreciate his help for sending me the suggestions/changes for the manuscripts even during his bad days. He has not only reviewed the work carried out by me, but also provided directions which have helped to get the nice results.

I am highly indebted and thankful to Shri Aaditya Majalee from CAD, BARC-Vizag for useful discussions on shock, gnu-plot, and providing me various e-books and latex documents for creating hyper reference pdf files. I am heartily appreciate

for his help, support, and care for my stay at his home at Vizag during my bad days. I remember those days at Vizag when we start long discussions on shock after dinner.

I express my sincere thanks for useful discussions to all CAD members, especially Dr. V. R. Ikkurthi, Shri Madhavan, Shri N. Sakthivel and Dr. Vishal Mehra. I thank Shri Krishna Kanth from BARC-Vizag for help in official matters and Shri Amit Saraswat and Shri Lalji from Engineering Services Division, BARC-Vizag for help during my Vizag stay.

I feel immensely grateful to my technical guide, Shri Vivek M. Chavan, Refueling Technology Division (RTD), BARC-Mumbai, for his encouragement and insightful comments on experiments performed under his guidance. He has taken care of me for everything in all regards during my stay at BARC, Mumbai.

I would like to thank Shri R. G. Agrawal (Ex-HOD, RTD) and Shri R. J. Patel (Head, RTD) for providing the necessary facilities and official formalities during the course of the work. I thank Shri Sudhansu Sharma from RTD for dynamic compression experiments, Shri Hajrat Ali from RTD for specimen preparation and Shri J. V. Mane from APD for useful discussions. I thank Shri Gopal, Smt. Mariya and Smt. Madhuri from RTD office for help in official matters.

I thank Dr. Rajiv Kapoor from MMD for useful discussions to get stress-strain curve from quasi-static compression data.

I thank Shri J. S. Dubey from PIED for quasi-static compression experiments.

I thank Dr. S. K. Gupta, HEAD, TPD, for giving me some single crystal copper.

I thank Shri Rajib Kar from L&PTD for doing surface morphology analysis and EDX analysis of deformed specimens. I also thank to Dr D. S. Patil from L&PTD for help and support.

I am highly indebted and thankful to Prof. Thamizhavel from Tata Institute of Fundamental Research (TIFR) for providing me single crystal copper specimen which helped to complete my experimental studies within the permitted time. I am thankful to Shri Ulhas Vaidya from TIFR for useful discussions and for introducing me to Prof. Thamizhavel.

I would like to express my sincere thanks and regards to Dr Mala N Rao from SSPD, BARC-Mumbai, for carrying out neutron diffraction experiments for crystalline perfection and orientation analysis and to estimate dislocation density before and after the deformation of the samples.

I thank my doctoral committee for very nice suggestions during my reviews.

I would like to have my sincere thanks and regards to Dr. R. B. Grover, Director, HBNI, for giving me an opportunity to work under Dr. Shashank Chaturvedi, Dr R. R. Puri from HRDD for helping me to provide BARC email account, Dr. D. M. Gaitonde from HRDD for help in official formalities, and Shri S. K. Singh from HRDD for providing me stay at TSH.

I owe my sincere thanks to Shri Kisley, Shri Vaibhav, Shri Vinod Kumar, Shri Venkat, Shri Malik, Miss Vibhuti and my friends, Shri Nirbhay and Miss Urvashi, from Compute Division for help and support during my simulations at BARC Clusters.

I would like to have my special thanks to my friends Debes Ray from BARC, Vikrant and Gurudutt from IPR, Kapil from IIT Madras, Ashiq from IIT Kanpur, Haider from JNU for providing me various references. I also thank to my senior, Dr. Bhaskar Chaudhary, for providing the references which were not accessible in India.

I am deeply indebted to my friends Pankaj, Naveen, Charu, Nishant, Krishna, Ram, Manish, Rajib, Rohan, Avdhesh Mishra, saroj and Sai Venkat for sharing good and bad times.

I would like to acknowledge my family for constant support and love during my PhD work. My special thanks to my brothers, Avdhesh Rawat and Umesh Rawat, and sisters, Asha, Baubi, Mamta, Anita and Poonam, for encouragement and support. I would also like to thank my father in law, Shri P. K. Upadhyay, for encouragement and support.

Lastly, I thank to all of those who supported me in any respect directly or indirectly during the completion of my thesis.

(Sunil Rawat)

List of Publications

Peer Reviewed Journals:

1. **"Temperature sensitivity of void nucleation and growth parameters for single crystal copper: a molecular dynamics study"**,
   S. Rawat, M. Warrier, S. Chaturvedi and V. M. Chavan, *Modelling and Simulation in Material Science and Engineering* **(19)** (2011) 025007 (20 pp).

2. **"Effect of material damage on the spallation threshold of single crystal copper: a molecular dynamics study"**,
   S. Rawat, M. Warrier, S. Chaturvedi and V. M. Chavan, *Modelling and Simulation in Material Science and Engineering* **(20)** (2012) 015012 (18 pp).

3. **"Computation of spall data for single crystals with pre-existing defects using atomistic simulations"**,
   S. Rawat, V. R. Ikkurthi, M. Warrier, S. Chaturvedi, V. M. Chavan and R. J. Patel, *Under review (Acta Mechanica Sinica).*

4. **"High strain rate deformation of single crystal copper: experiments and molecular dynamics simulations"**,
   S. Rawat et al, *Under preparation.*

Refereed Conferences:

1. **"Effect of temperature on the void nucleation and growth parameters for single crystal copper"**,
   S. Rawat, M. Warrier, S. Chaturvedi and V. M. Chavan, *AIP Conf. Proc.* **1349** (2011) 87-88.

2. **"Molecular dynamics simulations of crystal copper: Bulk modulus and shocks"**,
   M. Warrier, S. Rawat and S. Chaturvedi, *AIP Conf. Proc.* **1349** (2011) 95-96.

3. **"Fracture during high velocity impact of copper plates: a molecular dynamics study"**,

S. Rawat, M. Warrier, S. Chaturvedi and V. M. Chavan, *J. Phys.: Conf. Ser.* **377** (2012) 012104 (4pp).

4. **"Excitation of characteristic modes of a crystal during solid fracture at high tensile pressure"**,
   S. Rawat, M. Warrier, D. Raju, S. Chaturvedi and V. M. Chavan, *J. Phys. Conf. Ser.* **377** (2012) 012107 (4pp).

5. **"Reduction in spall threshold due to non-contact impact: a molecular dynamics study"**,
   S. Rawat, M. Warrier, S. Chaturvedi and V. M. Chavan, *AIP Conf. Proc.* **1447** (2012) 123-124.

6. **"Activation of slip systems and shape changes during deformation of single crystal copper: a molecular dynamics study"**,
   S. Rawat, V. M. Chavan, M. Warrier, S. Chaturvedi, S. Sharma and R. J. Patel, *AIP Conf. Proc.* **1512** (2013) 84-85.

7. **"Neutron diffraction measurements of dislocation density in copper crystals deformed at high strain rate"**,
   M. N. Rao, S. Rawat, S. Sharma, V. M. Chavan, R. J. Patel and S. L. Chaplot, *AIP Conf. Proc.* **1512** 2013 526-527.

8. **"Effect of strain rate on the void nucleation and growth characteristics in single crystal copper: a molecular dynamics study"**,
   S. Rawat, M. Warrier, S. Chaturvedi, V. M. Chavan and R. J. Patel, *Accepted in 4^{th} International Congress on Computational Mechanics and Simulation (ICCMS), IIT Hyderabad, India, December 9-12, 2012.*

9. **"Multi-scale model for single crystal spallation at high strain rates"**,
   V. R. Ikkurthi, S. Rawat, R. Sugandhi, M. Warrier and S. Chaturvedi, *Accepted in 4^{th} International Congress on Computational Mechanics and Simulation (ICCMS), IIT Hyderabad, India, December 9-12, 2012.*

Non-refereed Conferences:

1. **"Molecular dynamics simulation studies of material failure under extreme conditions"**,
   S. Rawat, M. Warrier, S. Chaturvedi and V. M. Chavan, *54^{th} DAE Solid State Physics Symposium (2009).*

2. **"Void nucleation and growth parameters for single crystal copper and their sensitivity to temperature"**,
   S. Rawat, M. Warrier, S. Chaturvedi and V. M. Chavan, *First International Conference on Advances in Interaction and Multiscale Mechanics (AIMM10)*, May 31 - June 2, 2010, pp. 119, Jeju, Korea.

3. **"Void nucleation threshold for single crystal copper and its validation by shock wave simulation"**,
   S. Rawat, M. Warrier, S. Chaturvedi and V. M. Chavan, *Second International Conference on Advances in Nuclear Materials (ANM 2011)*, Feb 9 - 11, 2011, Mumbai, India.

4. **"Multi-scale simulations of damage of perfect crystal copper at high strain rates"**,
   S. Rawat, M. Warrier, S. Chaturvedi and V. Ikkurthi, *The ISAMP Topical Conference (TC 2012) "Laser interaction with atoms, molecules and clusters", Jan 9 - 12, 2011, Hyderabad, India.*

5. **"Computation of spall data for single crystals with pre-existing defects using atomistic simulations"**,
   S. Rawat, M. Warrier, S. Chaturvedi, V. M. Chavan and R. J. Patel, *9^{th} International Conference on New Models and Hydrocodes for Shock Processes in Condensed Matter (NMH 2012)*, April 23 - 27, 2012, London, UK.

Work Presented:

1. **"Computer simulations for high strain rate processes"**,
   V. R. Ikkurthi, S. Madhavan, A. Majalee, V. Mehra, V. Mishra, P. Pahari, S. Pahari, **S. Rawat**, N. Sakthivel, N. Shiv, C. D. Sijoy, M. Warrier and S.

Chaturvedi, *National Workshop on High Strain Rate Behaviour of Materials, Feb 25 - 26, 2010, Terminal Ballistics Research Laboratory, Ministry of Defence, Chandigarh, India.*

2. **"High velocity impact for determining materials properties under extreme conditions: simulations and experiment**",
   S. Pahari, S. Madhavan, V. Mehra, C. D. Sijoy, **S. Rawat**, M. Warrier, I. V. V. Suryaprasad, N. Shiv and S. Chaturvedi, *25^{th} National Symposium on Plasma Science and Technology, Dec 8-11, 2010, Institute of Advanced Study in Science and Technology, Guwahati, India.*

Contents

Homi Bhabha National Institute

Ph.D. PROGRAMME

1. **Name of the Student:**	Sunil Rawat
2. **Name of the Constituent Institution:**	Bhabha Atomic Research Centre
3. **Enrolment No.:**	PHYS01200704031
4. **Title of the Thesis:**	Behaviour of solids under high strain rate deformation
5. **Board of Studies:**	Physical Sciences

SYNOPSIS

Introduction

Solid fracture under high strain rate deformation is of interest for high velocity impact and penetration problems. High velocity projectiles produce shock in a material which creates tensile pressures that can lead to nucleation, growth and coalescence of voids which cause material fracture [1]. To model the fracture of materials under extreme conditions of pressure and temperature, an understanding of the basic mechanism of fracture and behaviour of materials under these conditions is required.

In plate impact experiments, a flyer plate is accelerated by some means, such as gas, explosives, lasers, etc., depending on the strain rate requirement, on to a target plate. The impact of a flyer plate produces compressive stress waves at the point of impact which travel toward the free surfaces of the flyer and target plates. When they reach the respective free surfaces of the flyer and the target, they reflect as

release waves and interact at some location in the target plate, depending upon the thicknesses of the plates. The interaction of these waves leads to a state of tension in the material. If the tension created exceeds the tensile strength of the material, nucleation, growth and coalescence of voids take place, leading to fracture of the material. This process is called spallation and the fracture of the material is called spall fracture.

Various methods are used to study spall fracture at different level of strain rates. Plate impact experiments [2] can give strain rates in the range of (10^5 - 10^6)/s. Shock loading by nano-second laser pulses [3] can give strain-rates $>10^7$/s. Ultra-high strain rates exceeding 10^8/s can be obtained by femto-second laser pulses [4]. A maximum strain-rate of 10^{10}/s using high power laser pulses has been reported in the literature [5].

Many workers have studied the process of material failure by experiments [2–4,6], hydrodynamic simulations [7], multi-scale simulations [8] and atomistic simulations using molecular dynamics [9–13].

Hydrodynamic simulations are widely used to study material deformation and fracture. The main inputs to hydrodynamic simulations are:

1. Fracture model, such as void Nucleation and Growth (NAG) model [1], Void Growth (VG) model [14].
2. Material strength model, such as Johnson-Cook model [15].
3. Equation of state (EOS) model, such as Murnaghan EOS. [16]

This thesis studies the high strain rate deformation of single crystal copper, both by simulations and experiments, and covers two inputs to the hydrodynamic simulations:

1. Void NAG model [1] which is one of the fracture models. The parameters for this model are determined by molecular dynamic simulations.
2. Johnson-Cook model [15] which is one of the material strength models. The parameters are obtained by performing dynamic compression experiments on single crystal copper using Split Hopkinson Pressure bar.

The above models involve several parameters. For example, the NAG model involves parameters such as the void nucleation threshold, void growth threshold, pressure sensitivity of void nucleation rate, material viscosity and void nucleation rate at threshold. In the literature, the parameters for these models are available only for a few materials; even for these materials, the parameters are only available at a single temperature. Therefore, for predictive simulations, it is necessary to generate these parameters for different materials of interest to the Department of Atomic Energy (DAE), either by experiments or by first principle/atomistic simulations.

Spall fracture occurs when the release waves from the flyer and target free surfaces interact to produce tension in the target material. The interaction of these waves leads to the triaxial state of stress following uniaxial strain [10,12]. It is in this triaxial state of stress that voids nucleate, grow and coalesce if the tension developed during this phase exceeds the tensile strength of the material. In this thesis, this process has been simulated using classical molecular dynamics (MD) simulations to triaxially deform a solid at high strain rate till the nucleation, growth and coalescence of voids occur.

The following studies have been performed in this thesis:

- *Application of a macroscopic void nucleation and growth model for polycrystallites at the atomistic scales for perfect crystal copper:* It is found that the nucleation and growth (NAG) model [1], originally developed for polycrystalline materials, is also valid at high strain rates at the atomistic scale for single crystals. The void nucleation threshold obtained for perfect single crystal copper is validated by shock simulations.

- *Temperature sensitivity of void nucleation and growth parameters for single crystal copper- a molecular dynamics study:* A systematic study has been performed to determine the effect of temperature on NAG parameters for perfect single crystal copper triaxially deformed at high strain rates. The presence of a curious double-dip in the pressure-time profile, for temperatures close to melting, has been analyzed using radial distribution function, structure factor, centro-symmetry parameter and common neighbour analysis.

- *Effect of material damage on the spallation threshold of single crystal copper-a molecular dynamics study:* The effect of pre-existing defects on the spallation threshold of single crystal copper has been studied. In addition to this, studies have been performed to analyze:
  - The nucleation and growth of voids which arose at two locations in the target for an impact velocity of 1100 m/s, but spallation occurred only at one location.
  - The impact at 1100 m/s in contact case where flyer and target remains in contact before the impact. This leads to a high value of spall strength than that in the non-contact case, where the flyer is kept some distance away from the target before the impact.
  - Appearance of a spall-like signal in the free surface velocity of the target for an impact velocity of 1000 m/s along the <100> direction, but no spall occurs in the target.
  - Effect of crystal orientation and grain boundary on the spall-like signal in the free surface velocity of the target.
  - Stochastic effect on spallation process for the impact velocities close to spallation threshold of the material.
- *Multi-scale simulations of damage of single crystal copper at high strain rates:* A new multi-scale model has been developed, wherein NAG parameters for single crystal copper obtained from MD simulations are used in a hydrodynamic code to generate spall data for single crystal copper. A good agreement is found with the experimental spall data available in the literature [17]
- *High strain rate deformation of single crystal copper-experiments and MD simulations:* The Johnson-Cook material model (strength model) parameters for single crystal copper have been obtained by performing experiments on single crystal copper using Split Hopkinson Pressure Bar (SHPB) method. MD simulations have been performed to reproduce the slip directions activated and to validate the shape changes observed in the experiments on single crystal copper.

The important results of the thesis are summarized below.

IMPORTANT RESULTS

1. Application of a macroscopic void nucleation and growth model for polycrystallites at the atomistic scales for perfect crystal copper

1.1. Motivation

Belak [9] studied the nucleation and growth of voids during isotropic tension in polycrystalline copper using MD and showed that the void at grain junction yields at a lower strain than that at the grain centre. Rudd et al [10], studying polycrystalline copper under triaxial expansion, found that the voids nucleate at weaker junctions and this void nucleation does not take place at all available junctions. Wang et al [18] studied the instabilities in perfect lattice at finite deformation using MD simulations and found that the instabilities in the lattice leads to the nucleation of a small disordered region which grows as a void.

Following the method used by Belak [9] and Rudd et al [10], the triaxial expansion of single crystal copper has been performed at 5×10^9/s strain-rate at 300 K to study the nucleation and growth of voids in single crystal copper. The number of atoms in the simulation domain is chosen such that any further increase does not change the results. The embedded-atom method [19, 20] with parameters obtained by Foiles et al [21] has been used for the study.

1.2. Results from this study

- The NAG model, originally developed for polycrystalline materials at high strain rate, is also applicable for single crystals at high strain rates, even at atomistic scales. The best-fit NAG parameters have been obtained for perfect single crystal copper at 300 K temperature.

- The comparison of NAG parameters for perfect single crystal copper with that obtained experimentally for polycrystalline copper which are available in literature shows that

  - The threshold for void nucleation (160 kbar) is very high for single crystal copper as compared to that for polycrystalline copper (5 kbar). This is reasonable, since there are weak points in polycrystalline materials, e.g. grain junctions, which can lead to void nucleation at lower value of tensile pressure [9]. This difference in void nucleation thresholds may also be the result of differences between the strain rates used in experiments and

in MD simulations. The void nucleation threshold (160 kbar) obtained for perfect single crystal copper is very close to the spall strength (155 kbar) measured under laser-driven experiments on polycrystalline copper foils of few micron thickness [22]. Though the experiments were done on polycrystalline copper foils with a thickness of only a few micrometers, it is possible that in the axial direction, it could still be a single crystal. The spall strength obtained from experiments [17,23–26] for single crystal copper varies from 33 kbar to 150 kbar.

  - The low value of pressure sensitivity for void nucleation for single crystal copper, as compared to polycrystalline copper, indicates the rapid nucleation of voids for pressure above the void nucleation threshold.
  - The low value of material viscosity for single crystal copper indicates the rapid growth of voids once the void nucleation threshold is crossed.

- Perfect single crystals are not available for experiments. Real single crystals that are available for experiments contain defects. This could lead to a significant difference between experimental and MD values of nucleation threshold for single crystals. Hence, in order to validate the nucleation threshold obtained above, we have performed shock-wave simulations at the atomistic scales and determined the threshold tensile pressure at which nucleation starts. A good match has been found.

This work has been published in [27, 28].

2. Temperature sensitivity of void nucleation and growth parameters for single crystal copper- A molecular dynamics study

2.1. Motivation

Various workers [29–31] have performed spallation studies at different temperatures and found that the spall strength of the materials decreases with rise in temperature. Note that nucleation, growth and coalescence of voids lead to spall of the material [1]. By studying the temperature dependence on NAG parameters, the dependence of spall strength on the temperature can be understood.

To study the dependence of the NAG parameters on temperature, MD simulations of single crystal copper deformed triaxially at 5×10^9/s strain rate have been

carried out at temperatures of 300 K, 600 K, 800 K, 1000 K and 1250 K. The triaxial deformation of single crystal copper leads to the creation of tension in the material and if the tension created exceeds the tensile strength of the material, nucleation and growth of the voids take place. This results in the release of tensile pressure in the system leading to a dip in the pressure-time profile.

For temperature close to melting temperature of single crystal copper, the triaxial deformation of single crystal copper at 5×10^9/s strain rate leads to a curious double-dip in the pressure-time history. To study the double-dip in the pressure-time history for single crystal copper deformed at 5×10^9/s strain-rate with 1250 K temperature, following investigations have been performed:

- Radial distribution function (RDF) analysis which gives information about the long-and short-range crystalline order in the material.
- Structure factor analysis which gives information about the structural changes (BCC/FCC/HCP) during the deformation of the material.
- Centro-symmetry parameter (CSP) [32] analysis which gives information about the defects created during deformation of the material.
- Common neighbour analysis (CNA) [33] which gives information about the local structural changes surrounding an atom, i.e. whether the atom belongs to FCC/BCC/HCP/ICOSAHEDRAL/UNKNOWN structure.

2.2. Results from this study

- Best-fit NAG parameters have been obtained for single crystal deformed triaxially at 5×10^9/s strain rate with different temperatures. It has been found that there is a monotonic decrease in the values of void nucleation and void growth thresholds with rise in temperature.
- The detailed analysis of double-dip in pressure-time history by structure factor, RDF, CSP and CNA:
  - Structure factor analysis: The first dip in pressure-time history corresponds to the loss of FCC structure and the structure created does not belong to BCC and HCP structures.

- RDF analysis: The first dip in pressure-time profile corresponds to loss of long-range crystalline order.
- CSP analysis: The first dip in pressure-time profile occurs due to creation of stacking faults and voids create corresponding to second dip in the pressure-time profile.
- CNA analysis: The first dip in pressure-time profile corresponds to creation of an unknown structure.

It means that the first dip in pressure-time profile is due to the creation of stacking faults (CSP analysis) and an unknown structure (CNA analysis) and second dip in the pressure-time profile is due to the creation of voids.

This work has been published in [34–36].

3. Effect of material damage on the spallation threshold of single crystal copper-A molecular dynamics study

3.1. Motivation

Various workers have performed MD simulations to study the spall process in materials. Bringa et al [37] simulated planar shocks in single crystal copper using MD and found the Hugoniot for single crystal copper along various crystal directions. Srinivasan et al [38] in their MD simulation of spallation in single crystal nickel found that interaction of release waves from flyer and target free surfaces creates crystals with different orientation and their boundaries become nucleation sites for void nucleation. Luo et al [39] in their MD simulations of spallation in single crystal copper found that more anisotropy in spall strength occurs for weak shocks, while it is decreased for strong shocks. Dremov et al [40] in their MD simulations of spallation in single nano-crystal and poly-nanocrystals found that in poly-nanocrystals, the void nucleation occurs along the grain boundaries whereas in nanocrystals, nucleation of voids occur at the stacking fault intersections.

In the previous work [28], the void nucleation threshold for NAG model for perfect single crystal copper has been validated by performing shock simulation for an impact velocity of 1100 m/s. The impact at 1100 m/s impact velocity leads to the creation of voids at two locations in the target and spallation occurs only at one location. To study why spallation occurs only at one location, not on both locations

in the target, centro-symmetry parameter analysis has been performed. To study the effect of contact and non-contact impact of flyer-target system on the spallation strength, impact has been performed at 1100 m/s impact velocity. When impact is done at low impact velocity (1000 m/s), the nucleation and growth of voids occur at lower value of tensile pressure and spall like signal appears in the free surface velocity of the target.

3.2. Results from this study

- For the impact at 1100 m/s impact velocity, the nucleation of voids takes place at two locations (x_1 and x_2) in the target. The CSP analysis for defects created shows that the stacking faults created rapidly converts to partial dislocations at location x_1 compared to that at location x_2. It is known that the dislocations soften the material surrounding the void and lead to growth of the voids. The rapid growth of voids at location x_1 due to availability of many dislocations surrounding the voids leads to the spall of the material. Due to the spall at location x_1, a compressive wave is generated which heals the voids at location x_2.

- For the non-contact impact of flyer-target system, spallation occurs at lower value of tensile pressure (112 kbar). This is due to the presence of defects which are created during initial passage of the shock. When the reflected release waves from the free surface interact subsequently causing tension, due to the defects, the nucleation threshold of voids decreases. For the in-contact impact of flyer-target system, defects are created only during the tension resulting from the interaction of release waves and not during initial passage of the shock. This means that there are no defects in advance to the tension in the contact case. These then lead to the nucleation of voids at higher value of tensile pressure (160 kbar) and hence spallation occurs at higher value of tensile pressure.

- Impact at 1000 m/s along the <100> direction shows that the nucleation and growth of voids take place at lower value of tensile pressure (124 kbar) corresponding to the tension resulting due to second traversal of the shock. Note that for impact at 1100 m/s, nucleation and growth of voids take place at high tensile pressure (160 kbar) corresponding to the tension resulting due to first

traversal of the shock. The CSP analysis shows that partial dislocations and stacking faults are created during the tension created by first traversal of the shock and these defects become void nucleation sites for the tension resulting due to second traversal of the shock and thus lower the void nucleation threshold. This implies that high strain-rate history of the material affects the void nucleation threshold of the material.

- For impact at 1000 m/s along the <100> direction, a spall like signal which is a signature of spallation [2] appears in the free surface velocity of the target. This is due to the stress relaxation resulting from the nucleation and growth of voids (which occur corresponding to second traversal of the shock) and not due to spallation of the material. When impact at 1000 m/s is performed along different crystal orientations (<110> and <111>), and with a simple grain boundary (bi-crystal), the nucleation and growth of voids occurs during the tension resulting from the first traversal of the shock and material undergoes spallation at late times.

- For impact at 1000 m/s along the <100> direction with a small change in the initial atomic positions along impact direction, the nucleation and growth of voids take place during the tension resulting due to second traversal of the shock and spallation occurs. This is different from the impact at 1000 m/s along <100> direction without perturbing initial atomic positions where nucleation and growth of voids take place during the tension due to second traversal of the shock and no spall occurs. This shows that for impact velocities close to spall threshold, spallation process is stochastic.

This work has been published in [41–43].

4. Multi-scale simulations of damage in single crystal copper with pre-existing defects

4.1. Motivation

Shehadeh et al [8] performed multi-scale simulation to study the shock propagation and interaction of dislocations in single crystal copper at high strain rate using a multi-scale dislocation dynamics plasticity model which couples the discrete dislocation dynamics (DD) with finite element method (FEM) analysis. Rudd et al [44]

proposed the multi-scale simulation of voids by coupling the molecular dynamics to the FEM. Zhuang et al [45] performed multi-scale simulation to study the material failure at high strain rate. In their approach, FEM is combined with discrete dislocation dynamics. Plastic strain is calculated by DD code and material parameters are obtained by MD.

In the previous work [34], NAG parameters were obtained for perfect single crystal copper. The void nucleation threshold of 160 kbar, obtained from those simulations for single crystal copper at 300 K, is well above the experimental values [17, 23, 25]. This mismatch arises due to the absence of pre-existing defects that would be present in a real single crystal. To study the effect of defects (dislocations of different lengths and vacancies) on the NAG parameters, specifically on the nucleation threshold, MD simulations have been performed for single crystal copper triaxially deformed at 5×10^9/s strain rate.

To generate the spall data for single crystal copper, the NAG parameters obtained from MD simulations for single crystal copper with defects are used in a macroscopic hydrodynamic code to simulate shock in single crystal copper. In reality, voids nucleate near dislocations, stacking faults etc. Since dislocation mechanism is missing in hydro code, pre-existing voids have been introduced to account for it.

4.2. Results from this study

- Best-fit NAG parameters have been obtained for single crystal copper triaxially deformed at 5×10^9/s strain rate with different defects (dislocations of different lengths and vacancies). The void nucleation threshold obtained decreases with increase in the length of the dislocation.

- Hydrodynamic simulation results for shock in single crystal copper show that

  - For NAG parameters obtained for perfect single crystal copper, no spallation occurs. Experimental single crystal spalls due to presence of defects.

  - For NAG parameters obtained for a pre-existing edge-dislocation having length equal to half of the side length of the simulation domain and containing only four atomic rows, pre-existing voids grow but no complete spall occurs. In this case, tensile pressure in the system exceeds the growth threshold of the material leading to incipient spall of the material [2].

  - For NAG parameters obtained for a pre-existing edge-dislocation having length equal to half the side length of the simulation domain and containing all atomic rows, nucleation and growth of the voids leads to the spall of the material. The results obtained match with the published experimental results [17] with 20% error.

- A multi-scale model has been developed where NAG parameters obtained using MD simulations for crystal copper with defects are used in a macroscopic hydrodynamic code to simulate shock in single crystal.

This work has been published in [46, 47].

5. High strain rate deformation of single crystal copper-Experiments and MD simulations

5.1. Motivation

Kalidindi et al [48] performed quasi-static compression experiments on <110> single crystal copper and found that one dimension of the sample remains unchanged. Qizhen [49] performed quasi-static loading using Universal Testing Machine (UTM) and dynamic loading using Split Hopkinson Pressure Bar (SHPB) on magnesium single crystals and obtained the Johnson-Cook model parameters. Tschopp et al [50] performed MD simulations to study the effect of crystal orientation on homogeneous dislocation nucleation under uniaxial loading and found that for compressive loading, stress required for dislocation nucleation along <110> direction is more than that along <111> and <100> crystal directions.

To determine the strength parameters for single crystal copper, quasi-static compression experiments using UTM and dynamic compression experiments using SHPB have been performed on single crystal copper along <100> and <110> directions. For single crystal copper deformed along <100> direction at 10^3/s strain rate using SHPB, neutron diffraction experiments have been performed before and after the compression of the specimens. The compression loading along <100> and <110> directions leads to different shapes of the specimens. MD simulations have been performed at 5×10^9/s strain rate in the manner simulated by Tschopp et al [50] to study the activation of slip systems and shape changes observed in the experiments on single crystal copper under uniaxial stress loading.

5.2. Results from this study

- Johnson-Cook model parameters have been obtained for single crystal copper deformed at 10^3/s strain rate along <100> and <110> directions using SHPB. The value of yield strength and strain hardening parameter for single crystal copper deformed at 10^3/s strain rate along <110> direction is large compared to that deformed along <100> direction.

- Neutron diffraction studies before and after the impact show the broadening of the diffraction peaks which is the signature of increased density of defects. The change in the diffraction peaks have been correlated with the dislocations in the sample.

- Using MD simulations, the number of slip directions activated during deformation of single crystal copper has been reproduced by computing the burger vector for homogeneous nucleation of dislocations and shape changes observed in the experiments on single crystal copper has been validated by computing Poisson's ratio.

Some part of this work has been submitted in [51, 52].

Bibliography

[1] D. R. Curran, L. Seaman, and D. A. Shockey, *Phys. Rep.* **147** 253-388 (1987).

[2] R. W. Minich, J. U. Cazamias, M. Kumar, and A. J. Schwartz, *Mater. Trans. A* **35A** 2663-2673 (2004).

[3] E. Moshe, S. Eliezer, E. Dekel, A. Ludmirsky, Z. Henis, M. Werdiger, I. B. Goldberg, N. Eliaz and D. Eliezer, *J. Appl. Phys.* **83** 4004-4011 (1998).

[4] E. Dekel, S. Eliezer, Z. Henis, E. Moshe, A. Ludmirsky and I. B. Goldberg, *J. Appl. Phys.* **84** 4851-4858 (1998)

[5] W. J. Murphy, A. Higginbotham, G. Kimminau, B. Barbrel, E. M. Bringa, J. Hawreliak, R. Kodama, M. Koenig, W. McBarron, M. A. Meyers, B. Nagler, N. Ozaki, N. Park, B. Remington, S. Rothman, S. M. Vinko, T. Whitcher and J. S. Wark, *J. Phys.: Condens. Matter* **22** 065404 (5pp) (2010).

[6] M. Zhou and R. J. Clifton, *Int. J. Impact Eng.* **19**(3) 189-206 (1997).

[7] V. R. Ikkurthi and S. Chaturvedi, *Int. J. Impact Eng.* **30** 275-301 (2004).

[8] M. A. Shehadeh, H. M. Zbib and T. D. Rubia, *Int. J. Plast.* **21** 2369-2390 (2005).

[9] J. Belak J, *J. Comp. Aided Mater. Des.* **5** 193-206 (1998).

[10] R. E. Rudd and J. Belak, *Comp. Mater. Sci.* **24** 148-153 (2002).

[11] S. Traiviratana, E. M. Bringa, D. J. Benson and M. A. Meyers, *Acta Mater.* **56** 3874-3886 (2008).

[12] E. T. Seppala, J. Belak and R. E. Rudd, *Phys. Rev. B* **69** 134101 (1-19) (2004).

[13] E. T. Seppala, J. Belak and R. E. Rudd, *Phys. Rev. Lett.* **93** 245503 (1-4) (2004)

[14] J. N. Johnson, *J. App. Phys.* **52** (4) 2812-2825 (1981).

[15] G. R. Johnson and W. H. Cook, *Eng. Fract. Mech.* **21** (1) 31-48 (1985).

[16] F. D. Murnaghan, *Proc. Nat. Acad. Sci.* **30** 244-247 (1944).

[17] T. H. Antoun, L. Seaman and D. R. Curran, *Technical Report No. DSWA-TR-96-77-V2*(Defence Special Weapons Agency, Alexandria, VA) (1998)

[18] J. Wang, S. Yip, S. R. Phillpot and D. Wolf, *Phys. Rev. Lett.* **71** 4182-4185 (1993).

[19] M. S. Daw and M. I. Baskes, *Phys. Rev. Lett.* **50** 1285-1288 (1983).

[20] M. S. Daw and M. I. Baskes, *Phys. Rev. B* **29** 6443-6453 (1984).

[21] S. M. Foiles, M. I. Baskes and M. S. Daw, *Phys. Rev. B* **33** 7983-7991 (1986).

[22] E. Moshe, S. Eliezer, Z. Henis, M. Werdiger, E. Dekel, Y. Horovitz, S. Maman, I. B. Goldberg and D. Eliezer, *Appl. Phys. Lett.* **76 (12)** 1555-1557 (2000).

[23] D. L. Tonks, D. J. Alexander, S. A. Sheffield, D. L. Robbins, A. K. Zurek and W. R. Thissell, *J. Phys. IV France* **10** 787-792 (2000).

[24] G. I. Kanel, S. V. Razorenov and V. E. Fortov, In Meyers M A, Murr L E and Staudhammer K P (Eds.) *Shock-Wave and High-Strain-Rate Phenomena in Materials* (Marcel Dekker, New York, NY, 1991) p 775

[25] S. V. Razorenov and G. I. Kanel, *Phys. Met. Metallog.* **74(5)** 526-530 (1992).

[26] R. G. McQueen and S. P. Marsh, *J. Appl. Phys.* **33(2)** 654-665 (1962).

[27] S. Rawat, M. Warrier, S. Chaturvedi and V. M. Chavan, *Proceedings of the* 54^{th} *DAE Solid State Physics Symposium* **54** 185-186 (2009).

[28] S. Rawat, M. Warrier, S. Chaturvedi and V. M. Chavan *Second International Conference on "Advances in Nuclear Materials (ANM 2011)", Mumbai, India, Feb 9-11, (2011).*

[29] G. I. Kanel, S. V. Razorenov, A. Bogatch, A. V. Utkin, V. E. Fortov and D. E. Grady, *J. Appl. Phys.* **79** 8310-8317 (1996).

[30] S. V. Razorenov, G. I. Kanel, K. Baumung and H. J. Bluhm *AIP Conf. Proc.* **620** 503-506 (2002).

[31] E. B. Zaretsky, *J. App. Phys.* **108** 083525 (1-7) (2010).

[32] C. L. Kelchner, S. J. Plimpton and J. C. Hamilton, *Phys. Rev. B* **58** 11085 (8pp) (1998).

[33] H. Tsuzuki, P. S. Branicio and J. P. Rino, *Comput. Phys. Commun.* **177** 518-523 (2007).

[34] S. Rawat, M. Warrier, S. Chaturvedi and V. M. Chavan, *Modell. Simul. Mater. Sci. Eng.* **19** 025007 (20pp) (2011).

[35] S. Rawat, M. Warrier, S. Chaturvedi and V. M. Chavan, *First International Conference on "Advances in Interaction and Multiscale Mechanics (AIMM10)", Jeju, Korea, May 31 - June 2, (2010).*

[36] S. Rawat, M. Warrier, S. Chaturvedi and V. M. Chavan, *AIP Conf. Proc.* **1349** 87-88 (2011).

[37] E. M. Bringa, J. U. Cazamias, P. Erhart, J. Stolken, N. Tanushev, B. D. Wirth, R. E. Rudd and M. J. Caturla, *J. Appl. Phys.* **96** 3793-3799 (2004).

[38] S. G. Srinivasan, M. I. Baskes and G. J. Wagner, *J. Mater. Sci.* **41** 7838-7842 (2006).

[39] S. N. Luo, Q. An, T. C. Germann and Li-Bo Han, *J. Appl. Phys.* **106** 013502 (1-8) (2009)

[40] V. Dremov, A. Petrovtsev, P. Sapozhnikov, M. Smirnova, D. L. Preston and M. A. Zocher, *Phys. Rev. B* **74** 144110 (1-5) (2006).

[41] S. Rawat, M. Warrier, S. Chaturvedi and V. M. Chavan, *Modell. Simul. Mater. Sci. Eng.* **20** 015012 (18pp) (2012).

[42] S. Rawat, M. Warrier, S. Chaturvedi and V. M. Chavan, *J. Phys.: Conf. Ser.* **377** 012104 (4pp) (2012).

[43] S. Rawat, M. Warrier, S. Chaturvedi and V. M. Chavan, *AIP Conf. Proc.* **1447** 123-124 (2012).

[44] R. E. Rudd and J. Q. Broughton, *Phys. Rev. B* **58** (10) R5893-R5896 (1998).

[45] Z. Zhuang, Z. L. Liu, X. C. You, and Y. Guo, *Adv. Mater. Res.* **33-37** 875-880 (2008).

[46] S. Rawat, M. Warrier, S. Chaturvedi and V. Ikkurthi, *The ISAMP Topical Conference (TC 2012) "Laser Interaction with Atoms, Molecules and Clusters", Hyderabad, India, Jan 9-12, (2011)*

[47] S. Rawat, V. R. Ikkurthi, M. Warrier, S. Chaturvedi, V. M. Chavan and R. J. Patel, *9th International Conference on New Models and Hydrocodes for Shock Processes in Condensed Matter (NMH 2012), The Institute of Shock Physics, Imperial College, London, UK, Apr. 23-27 (2012)*

[48] S. R. Kalidindi and L. Anand, *Metall. Trans. A* **24A** 989-992 (1993).

[49] Qizhen Li, *J. App. Phys.* **109** 103514 (1-8) (2011).

[50] M. A. Tschopp and D. L. McDowell, *J. Mech. Phys. Solids* **56** 1806-1830 (2008).

[51] S. Rawat, V. M. Chavan, M. Warrier, S. Chaturvedi, S. Sharma and R. J Patel, *57th DAE-Solid State Physics Symposium.*

[52] M. N. Rao, S. Rawat, S. Sharma, V. M. Chavan, R. J. Patel and S. L. Chaplot, *57th DAE-Solid State Physics Symposium.*

Publications

1 . Published:

Peer Reviewed Journals

(i) **"Temperature sensitivity of void nucleation and growth parameters for single crystal copper: a molecular dynamics study**", S. Rawat, M. Warrier, S. Chaturvedi and V. M. Chavan, *Modelling and Simulation in Material Science and Engineering* **(19)** 025007 (20pp) (2011).

(ii) **"Effect of material damage on the spallation threshold of single crystal copper: a molecular dynamics study**" S. Rawat, M. Warrier, S. Chaturvedi and V. M. Chavan, *Modelling and Simulation in Material Science and Engineering* **(20)** 015012 (18pp) (2012).

Refereed Conferences

(i) **"Effect of temperature on the void nucleation and growth parameters for single crystal copper"**, S. Rawat, M. Warrier, S. Chaturvedi and V. M. Chavan, *AIP Conf. Proc.* **1349** 87-88 (2011).

(ii) **"Molecular dynamics simulations of crystal copper: Bulk modulus and shocks"**, M. Warrier, S. Rawat and S. Chaturvedi, *AIP Conf. Proc.* **1349** 95-96 (2011).

(iii) **"Fracture during high velocity impact of copper plates: a molecular dynamics study**", S. Rawat, M. Warrier, S. Chaturvedi and V. M. Chavan, *J. Phys.: Conf. Ser.* **377** 012104 (4pp) (2012)

(iv) **"Excitation of characteristic modes of a crystal during solid fracture at high tensile pressure**",

S. Rawat, M. Warrier, S. Chaturvedi and V. M. Chavan, *J. Phys. Conf. Ser.* **377** 012107 (4pp) (2012)

(v) **"Reduction in spall threshold due to non-contact impact: a molecular dynamics study"**,
S. Rawat, M. Warrier, S. Chaturvedi and V. M. Chavan, *AIP Conf. Proc.* **1447** 123-124 (2012).

Non-refereed Conferences

(i) **"Molecular dynamics simulation studies of material failure under extreme conditions"**,
S. Rawat, M. Warrier, S. Chaturvedi and V. M. Chavan, *Proceedings of the 54^{th} DAE Solid State Physics Symposium* **54** *185-186 (2009)*

(ii) **"Void nucleation and growth parameters for single crystal copper and their sensitivity to temperature"**,
S. Rawat, M. Warrier, S. Chaturvedi and V. M. Chavan, *First International Conference on "Advances in Interaction and Multiscale Mechanics (AIMM10)", Jeju, Korea, May 31 - June 2, 2010*

(iii) **"Void nucleation threshold for single crystal copper and its validation by shock wave simulation"**,
S. Rawat, M. Warrier, S. Chaturvedi and V. M. Chavan, *Second International Conference on "Advances in Nuclear Materials (ANM 2011)", Mumbai, India, Feb 9 - 11, 2011*

(iv) **"Multi-scale simulations of damage of perfect crystal copper at high strain rates"**,
S. Rawat, M. Warrier, S. Chaturvedi and V. Ikkurthi, *The ISAMP Topical Conference (TC 2012) "Laser interaction with atoms, molecules and clusters", Hyderabad, India, Jan 9 - 12, 2012*

(v) **"Computation of spall data for single crystals with pre-existing defects using atomistic simulations"**,
S. Rawat, V. R. Ikkurthi, M. Warrier, S. Chaturvedi, V. M. Chavan and R. J. Patel, *9^{th} International Conference on New Models and Hydrocodes for Shock Processes in Condensed Matter (NMH 2012)", London, UK, April 23 - 27, 2012*

Work Presented

(i) **"Computer simulations for high strain rate processes"**,
V. R. Ikkurthi, S. Madhavan, A. Majalee, V. Mehra, V. Mishra, P. Pahari, S. Pahari, **S. Rawat**, N. Sakthivel, N. Shiv, C. D. Sijoy, M. Warrier and S. Chaturvedi, *National Workshop on High Strain Rate Behaviour of Materials, Terminal Ballistics Research Laboratory, Ministry of Defence, Chandigarh, India, Feb 25 -26, 2010*

(ii) **"High velocity impact for determining materials properties under extreme conditions: simulations and experiment"**,
S. Pahari, S. Madhavan, V. Mehra, C. D. Sijoy, **S. Rawat**, M. Warrier, I. V. V. Suryaprasad, N. Shiv and S. Chaturvedi, *25^{th} National Symposium on Plasma Science and Technology, Institute of Advanced Study in Science and Technology, Guwahati, India, Dec 8 - 11, 2010*

2 . Accepted:

Refereed Conferences

(i) **"Effect of strain rate on the void nucleation and growth characteristics in single crystal copper: a molecular dynamics study"**,
S. Rawat, M. Warrier, S. Chaturvedi, V. M. Chavan and R. J. Patel, *4^{th} International Congress on Computational Mechanics and Simulation (ICCMS)", IIT Hyderabad, India, December 9 - 12, 2012.*

3 . Communicated:

Peer Reviewed Journals

(i) **"Computation of spall data for single crystals with pre-existing defects using atomistic simulations"**,
S. Rawat, V. R. Ikkurthi, M. Warrier, S. Chaturvedi, V. M. Chavan and R. J. Patel, *Submitted to Acta Mechanica Sinica*

(ii) **"High strain rate deformation of single crystal copper: experiments and molecular dynamics simulations"**,
S. Rawat et al, *Under preparation*

Refereed Conferences

(i) **"Activation of slip systems and shape changes during deformation of single crystal copper: a molecular dynamics study"**,
S. Rawat, V. M. Chavan, M. Warrier, S. Chaturvedi, S. Sharma and R. J. Patel, *Submitted to 57th DAE-Solid State Physics Symposium.*

(ii) **"Neutron diffraction measurements of dislocation density in copper crystals deformed at high strain rate"**,
M. N. Rao, S. Rawat, S. Sharma, V. M. Chavan, R. J. Patel and S. L. Chaplot, *Submitted to 57th DAE-Solid State Physics Symposium.*

Signature of Student:

Date:

Doctoral Committee

S. N.	Name	Designation	Signature	Date
1.	Dr. N. K. Gupta	Chairman		10/8/12
2.	Dr. Shashank Chaturvedi	Convener		10/8/12
3.	Shri Vivek M. Chavan	Member		
4.	Dr. Rajaraman Ganesh	Member		
5.	Dr. Manoj Warrier	Member		10/08/2012

List of Figures

List of Tables

Chapter 1

Introduction

Solid fracture under high strain-rate deformation is of interest for high-velocity impact and penetration problems. High velocity projectiles impacting on a target produce shock waves in both the target and the projectile. Under certain conditions, this creates tensile pressures that can lead to nucleation, growth and coalescence of voids which, in turn, cause material fracture [5].

In plate impact experiments, a flyer plate is accelerated by some means, such as gas, explosives, lasers, etc., depending on the strain rate requirement, on to a target plate. The impact of a flyer plate produces compressive stress waves at the point of impact which travel toward the free surfaces of the flyer and target plates. When they reach the respective free surfaces of the flyer and the target, they reflect as release waves and interact at some location within the target plate, depending upon the thicknesses of the plates. The interaction of these waves leads to a state of tension in the material. If the tension created exceeds the tensile strength of the material, nucleation, growth and coalescence of voids take place, leading to fracture of the material. This process is called spallation and the fracture of the material is called spall fracture. The nucleation, growth and coalescence of voids in 1145 aluminum resulting from such impact is illustrated in Figure 1.1.

In order to model the fracture of materials under extreme conditions of pressure and temperature, it is necessary to develop an understanding of the basic mechanism of fracture and behaviour of materials under these conditions. Spall fracture takes place when release waves from the free surfaces of the flyer and target interact to produce tension in the target material. The interaction of these waves leads to a triaxial state of stress following uniaxial strain [7, 8]. It is during the triaxial state

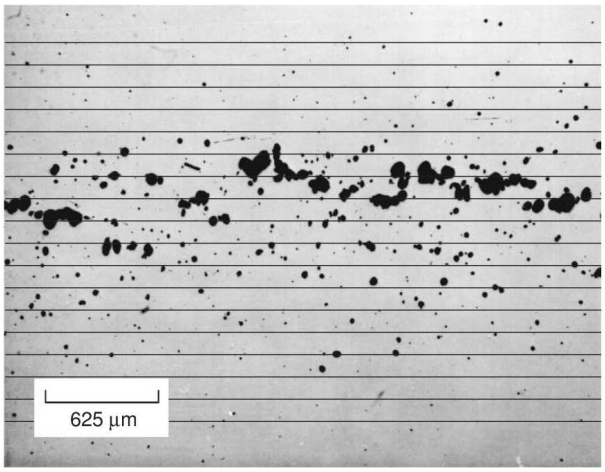

Figure 1.1: Nucleation, growth and coalescence of voids in impact-loaded specimens of 1145 aluminum. This figure is adapted from [1]

of stress that voids nucleate, grow and coalesce if the tension developed during this phase exceeds the tensile strength of the material.

Many researchers have studied the process of material failure through experiments [9–12], atomistic simulations using molecular dynamics [7, 8, 13–15], multi-scale simulations [16] and hydrodynamic simulations [17].

Spallation studies have been carried out at different levels of strain rates. Plate impact experiments result in strain rates of 10^5-10^6/s [12]. Strain rates exceeding 10^7/s can be achieved by shock loading produced by nanosecond laser pulses [10]. Ultra-high strain rates (exceeding 10^8/s) can be obtained by femto-second laser pulses [11]. An extremely high strain rate of 10^{10}/s using high power laser pulses has been reported in the literature [18].

Computer simulations of high strain-rate failure of materials have been performed at various length scales. At the atomistic scale, Molecular Dynamics (MD) simulations have been carried out to study various features of fracture at high strain rates. Belak's study [13] of nucleation and growth of voids in polycrystalline copper showed that voids at grain junctions yield at a lower strain than those at grain centres. Rudd et al [7], examining polycrystalline copper under triaxial expansion, found that voids nucleate at weaker junctions and this void nucleation does not take place at all available junctions. Traiviratana et al [14] simulated pre-existing voids in mono-crystalline and bi-crystalline copper at strain rates of 10^8/s and 5×10^9/s and estimated the void-size dependence of the stress threshold for dislocation emission

in mono-crystalline and bi-crystalline copper. Seppala et al [8] studied the effect of stress triaxiality on the growth of pre-existing voids in single crystal copper. Many workers have also studied the coalescence of voids. Seppala and others [15], in their coalescence study, estimated the inter-void ligament distance to be one void radius to coalesce the voids. Davila and others [19], in their study of void coalescence, found that shear loops nucleation based model is in good agreement with the observed molecular dynamics (MD) mechanism. These shear loops are also responsible for hardening the material near the void. Potirniche et al [20] simulated void growth and coalescence in single crystal nickel at high strain rate (10^8 - 10^{10}/s) and showed that the material length scale affects the stress-strain response of the material. It was also found that void growth dominates over void coalescence for the conditions examined in that study. Wang and co-workers [21] have studied instabilities in a perfect lattice at finite deformation using MD simulations. They showed that instabilities in the lattice lead to the nucleation of a small disordered region which grows as a void.

Molecular Dynamics simulations are generally confined to very small length scales (few hundreds nm) due to limitations of computing power. To bridge the atomistic (MD) and continuum length scales, multi-scale simulations have been done by several workers. In the multi-scale approach of Zhuang et al [22], the finite element method (FEM) is combined with discrete dislocation dynamics (DD). The plastic strain is calculated by the DD code and the material parameters are obtained by MD. The DD code works as a substitute for the constitutive form in the FEM code. Shehadeh et al [16] performed multi-scale simulation to study shock propagation and interaction of dislocations in single crystal copper at high strain rates ($>10^6$/s). He used the multi-scale dislocation dynamics plasticity (MDDP) model which couples discrete DD with FEM analysis. Rudd et al [23,24] have proposed the multi-scale simulation of voids by coupling MD to FEM. This technique is known as coarse grained molecular dynamics (CGMD).

1.1 Objective of this thesis

Hydrodynamic simulations of high velocity impact problems divide the domain of interest into computational cells. Such simulations require, as input, the following information for each of the materials involved in the problem:

1. An equation of state, which allows calculation of the pressure and specific internal energy in terms of the temperature and density of the material.

2. A model to predict the strength of the material during high strain-rate deformation, i.e., the variation of yield strength and shear modulus of the material with temperature, pressure, plastic strain, etc. [25, 26] and [27–31].

3. A dynamic fracture model, e.g., void nucleation and growth (NAG) model, where fracture properties depend upon the temperature and pressure values in the cell [17].

For a given cell in the hydrodynamic simulations, the temperature and pressure are taken to be constant during each hydrodynamic timestep. Hence it is sufficient to use a fracture model that describes the nucleation/growth of voids at a specified temperature and pressure.

This thesis studies the high strain rate deformation of single crystal copper, using both simulations and experiments, and involves generation of the following materials data:

- Void NAG model [5] which is one of the fracture models. The parameters for this model are determined by molecular dynamics simulations and checked using multi-scale simulations.

- Johnson-Cook model [27] which is one of the material strength models. The parameters are obtained by high stain rate compression experiments on single crystal copper using a Split Hopkinson Pressure bar (SHPB).

These models involve several parameters. For example, the NAG model involves parameters such as the void nucleation threshold, void growth threshold, pressure sensitivity of void nucleation, material viscosity and void nucleation rate at threshold. In the literature, the parameters for these models are available only for a few materials; even for these materials, the parameters are only available at a single temperature. Therefore, for predictive simulations, it is necessary to generate these parameters for different materials of interest to the Department of Atomic Energy (DAE), either by experiments or by atomistic simulations.

This thesis covers the following areas which have not been addressed by earlier workers:

- Validation of a macroscopic NAG model, which was originally developed for polycrystalline materials at macro scales, for single crystals at atomistic scales. Determination of best-fit NAG model parameters for single crystal copper deformed at high strain rates.

- Validation of void nucleation threshold obtained above for single crystal copper, using shock wave simulations at atomistic scales.

- Determination of the variation with temperature of NAG parameters for single crystal copper. It also includes a detailed analysis for unusual features observed at temperatures close to the melting point.

- Effect of pre-existing defects in the crystal on the spallation threshold of single crystal copper. In addition to this, studies have been performed to analyse:

  - Nucleation and growth mechanism under threshold conditions, when the impact velocity is close to the threshold for causing spallation.
  - Effect of crystal orientation and grain boundary on the fracture mechanism.
  - Stochastic effects on the spallation process for impact velocities close to the spallation threshold of the material.

- Multi-scale simulations of damage in single crystal copper: NAG parameters are generated using MD for single crystal copper with pre-existing defects. These parameters are then used in a hydrodynamic code to generate spall data, and the results compared with published experimental data.

1.2 Structure of the thesis

This thesis is organized as follows:

Chapter 2 describes the computational techniques used in this study. This covers a) Techniques used in molecular dynamics simulations, b) Details of the post-processor used for analysing the void distribution, c) An introduction to statistical methods used for analysing the crystal structure, such as centro-symmetry parameter, common neighbor analysis, structure factor, radial distribution function, d) An

outline of the singular value decomposition analysis used for determining characteristic modes of the crystal.

Chapter 3 covers MD simulations of uniform triaxial expansion of a perfect crystal, the resulting void nucleation and growth, and the use of MD data to determine best-fit values of NAG parameters. These NAG parameters, obtained using triaxial expansion, are then checked against shock-wave simulations. The location of the first nucleation site is also analyse in terms of characteristic modes of the crystal.

Chapter 4 discusses the temperature dependence of the NAG parameters for single crystal copper. Anomalous behaviour observed near the melting point is analyse in some detail.

Chapter 5 describes the effect of high strain rate history of the material on the spall threshold. Stochastic effects observed at impact velocities close to spall threshold are also presented.

Chapter 6 presents multi-scale simulations for the computation of spall data for single crystal copper. It describes the creation of various kinds of defects in the material and their effect on the NAG parameters.

Chapter 7 discusses the experiments on single crystal copper deformed at high strain rate using a Split Hopkinson Pressure Bar. It further explains the use of this data for obtaining material strength parameters for the Johnson-Cook strength model. The chapter also reports on different experimental measurements, such as neutron diffraction, for detailed characterisation of the specimens. Finally, it compares MD results for the activation of slip directions with experimental measurements.

Chapter 8 presents the conclusions and future scope of the present study.

Chapter 2

Simulation Technique

2.1 Molecular dynamics (MD) simulations

2.1.1 Why atomistic simulations?

In earlier days, in order to understand material failure, linear continuum mechanics theories were used to treat dislocations and cracks in the material by using phenomenological assumptions. Later, it was felt that if there is a need to understand material failure, the behavior of materials at the nano-scale should be understood [32,33]. For materials of sub-micron dimensions, the behaviour of materials by continuum approaches becomes questionable and full atomistic information is required to understand material phenomena [34].

Atomistic methods have been very successful in modern materials modeling. The reason is that these methods contain a very fundamental view point of materials phenomena and involve only one physical law (Newton's law) and an interaction potential to define how atoms interact with each other. Molecular dynamics simulations

- can be used to understand material failure at an atomistic level by investigating the complex behaviour of dislocations, cracks, voids and grain boundary processes at the fundamental level [34].
- do not require a-priori assumptions about defect dynamics, unlike many continuum mechanics approaches [34].

By choosing an accurate inter-atomic potential, which can be determined using

quantum mechanical methods such as density functional theory [35], we can simulate the complete behaviour of material failure [34].

2.1.2 Brief introduction

Molecular dynamics simulations are used to study the evolution of a system of N particles under conditions of interest. In these simulations, classical equations of motion are integrated to generate the trajectory of a system. The N-body force equation is given by

$$m_i \ddot{r}_i = -\sum_{i \neq j, j=1}^{N} \nabla_i E \tag{2.1}$$

where r_i is the position vector of the i^{th} particle, m_i is the mass of the i^{th} particle and E is the total potential energy of the system (described in section 2.1.4).

In spite of the advantages of this method, it also has some limitations:

- Limitation of time step: To simulate materials of interest, the timestep required to integrate Eqn. 2.1 is of the order of femto-seconds. This is dictated by the constraint that the change in potential due to change in position of a particle during a timestep must not be large. A thumb rule is that atoms should move at most $(1/20)^{th}$ of the nearest neighbour distance [36, 37].

  Due to this limitation on the timestep, typical impact problems, where the dynamics lasts for, say, 10 microseconds, would take 10^{10} steps to complete. Hence MD simulations are typically used for phenomena extending over picosecond to nanosecond time scales.

- Limitation of number of atoms used in the simulation: The number of atoms are limited to between 100 to 10^9 depending on the the type of potential used and speed of computers. The reason is that if all N atoms in a system under study interact with all atoms, then N^2 interactions are computed. It becomes very expensive if the system contains millions of atoms. Even if we limit the interactions to nearby atoms, this will also require the computation of N interactions. This limits the number of atoms in the system under study.

2.1.3 Ensembles used

The state of a system can be divided into two categories:

- Thermodynamic state of the system defined by temperature, pressure etc.
- Microscopic state of the system defined by atomic positions and momenta. A single point in phase space describes the state of the system.

A collection of all possible systems which have different microscopic states but have an identical macroscopic or thermodynamic state is called an ensemble.

Following are ensembles which are used in MD simulations:

1. Micro-canonical ensemble (NVE): The thermodynamic state of the system is characterized by fixed number of atoms (N), constant volume (V) and a fixed energy (E). This will be a totally isolated system.
2. Canonical ensemble (NVT): In this ensemble, the number of atoms (N), volume (V) and temperature (T) remain constant. The system is in contact with a heat bath.
3. Isobaric-Isothermal ensemble (NPT): It is characterized by a fixed number of atoms (N), constant pressure (P) and fixed temperature (T).
4. Grand canonical ensemble (μTV): It is characterized by a fixed chemical potential (μ), fixed volume (V) and constant temperature (T). The number of particles in the simulation can change and it is in contact with a heat bath.

MD simulations generate information at the microscopic level including atomic positions and velocities. The conversion of this microscopic information to macroscopic observables, such as pressure, temperature, energy etc, requires statistical mechanics. The mathematical expressions in statistical mechanics relate the macroscopic properties of the system to the distribution and motion of the atoms in the system of N particles. Therefore, statistical mechanics plays a great role in understanding and in predicting the macroscopic phenomenon from the properties of individual atoms in the system [38].

2.1.4 Potential used

Daw and Baskes [39,40] proposed a numerical method called embedded atom method (EAM) to calculate the atomic energetics. The basis of this potential is the quantum mechanical density functional theory. According to this theory, the ground state

energy and properties of a system are uniquely determined by the electron density. In this approach, the energy of a system is computed as the energy obtained by embedding an atom into local electron density due to remaining atoms of the system. In addition to this, there is an electrostatic interaction potential. Therefore, the total energy of a system is given by

$$E = \sum_i F^i \left(\sum_{j=1, j\neq i}^{n} \rho^j \left(r^{ij} \right) \right) + \frac{1}{2} \sum_{i \neq j} \phi^{ij}(r^{ij}) \tag{2.2}$$

where F^i is the embedding energy of atom i, r^{ij} is the distance between atoms i and j, ρ^i is the electron density, and ϕ^{ij} is the pair potential between atom i and its neighboring atom j. The electron density ρ^j is the sum of all the electron densities of all the atoms j with j$\neq i$.

In molecular dynamics, this energy is used to determine the force on each atom. The interaction force between atoms i and j along α direction is given by

$$f_\alpha^{ij} = \frac{\partial E}{\partial r^{ij}} \frac{r_\alpha^{ij}}{r^{ij}} \tag{2.3}$$

To calculate the stress in the system under study, the virial formula [41] to calculate the stress tensor is given by

$$\sigma_{\alpha\beta} = -\frac{1}{V} \left[\sum_i \frac{p_\alpha^i p_\beta^i}{m_i} + \sum_i \sum_{j>i} r_\alpha^{ij} f_\beta^{ij} \right] \tag{2.4}$$

where p_α^i is the momentum of the ith atom in the α direction, m_i is the mass of the ith atom, r_α^{ij} is the distance between the jth and ith atoms along the direction of α, f_β^{ij} is the force on the jth atom from ith atom in the β direction and V is the volume of the system.

The first term on the right hand side of Eqn. 2.4 is the kinetic contribution to the stress and the second term gives the virial potential stress. The stress for an atomistic system is defined as the volume average of per-atom tensor.

2.1.5 Boundary conditions

Any geometrical or thermodynamical constraint used in the system throughout the simulation is called boundary condition. There are two type of boundary conditions (BCs) used in MD simulations [42]:

1. Hard boundary conditions refer to a constraint on a given instantaneous value of the observable. This means that these boundary conditions are exactly satisfied at any time point of the simulation. Examples are

   (a) Spatial boundary conditions: To define the shape of the system and nature of its surrounding, these boundary conditions are used. Examples are free boundary conditions, fixed boundary conditions and periodic boundary conditions.

   (b) Thermodynamic boundary conditions: To define the macroscopic state of the system, these boundary conditions are used. Examples include extensive quantities such as number of atoms, energy, enthalpy etc.

   (c) Geometrical boundary conditions which include the bond-length constraints in the simulation.

2. Soft boundary conditions refer to a constraint on the average value of an observable. In these boundary conditions, a time scale during which average observable should match the desired value is also required. Examples are

   (a) Thermodynamic boundary conditions involving intensive quantities such as chemical potential, pressure, temperature etc.

   (b) Experimentally derived boundary conditions.

Periodic boundary conditions (PBC):

1. **Why PBC ?**
   The behaviour of finite systems (nanoclusters, molecules etc where there is large surface to volume ratio) is very different from the macroscopic systems. The typical number of atoms used in an classical MD simulation is of the order of 10^6–10^9. For such a system, the fraction of surface atoms will be more significant and the behaviour will be dominated by surface effects. Therefore, to overcome the problems of finite size effects and surface effects, periodic boundary conditions are used.

2. **Implementation of PBC**
   In the periodic boundary conditions, a primary box of particles is replicated in all three directions as image boxes (Figure 2.1) [43]. Note that the chosen

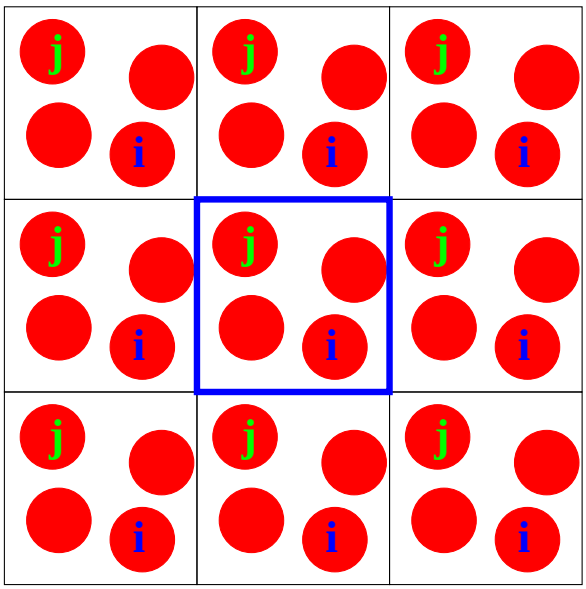

Figure 2.1: Replication of primary box in all three directions

primary box should be space filling and it should be replicated in all three directions. Replication is done by translational operations of the primary cell. In this, if one particle in the box is positioned at **r**, then this particle will represent a set of infinite particles located at **r** + l**a** + m**b** + n**c** (l, m, n = -∞, ∞), where l, m, n are the integers and **a**, **b**, **c** are the vectors corresponding to the edges of the box. At each timestep, atom coordinates are examined and if an atom crosses the boundary of the box, its coordinates are adjusted to bring it back inside the box as follows: if L_x is the side length of the box and r_{xi} is the x-coordinate of the i^{th} atom lying between -L_x/2 and L_x/2, then the coordinate adjustments done are:

- if $r_{xi} \geq L_x/2$, then replace r_{xi} by r_{xi} - L_x
- if $r_{xi} < -L_x/2$, then replace r_{xi} by r_{xi} + L_x

Similarly the periodic BCs are implemented along Y and Z directions.

2.1.6 Integration schemes:

Many algorithms have been developed to integrate Newton's equations of motion. In choosing an algorithm, the following criteria should be used [41]:

- It should be fast and require little memory
- It should permit the use of long time step
- It should reproduce the classical trajectory as closely as possible
- It should be time-reversible
- It should satisfy the conservation laws of energy and momentum
- It should be simple in form and easy to program

The discretization of the equations of motion can be obtained by Taylor expansion:

$$r_i(t+\Delta t) = r_i(t) + v_i(t)\Delta t + \frac{1}{2}a_i(t)\Delta t^2 + \frac{\Delta t^3}{6}\frac{d^3 r_i(t)}{dt^3} + O(\Delta t^4)..... \tag{2.5}$$

$$v_i(t+\Delta t) = v_i(t) + a_i(t)\Delta t + \frac{1}{2}\frac{d^2 v}{dt^2}\Delta t^2 + \frac{\Delta t^3}{6}\frac{d^3 v_i(t)}{dt^3} + O(\Delta t^4)..... \tag{2.6}$$

In the present simulations, we have used velocity Verlet algorithm [41] to integrate the equations of motion. The advantage of this algorithm is that the positions, velocities and accelerations of the atoms are computed at the same time t. The equations in this method are as follows:

$$r_i(t+\Delta t) = r_i(t) + v_i(t)\Delta t + \frac{1}{2}a_i(t)\Delta t^2 \tag{2.7}$$

and

$$v_i(t+\Delta t) = v_i(t) + \frac{1}{2}[a_i(t) + a_i(t+\Delta t)]\Delta t \tag{2.8}$$

2.1.7 Thermostat and Barostat

Standard molecular dynamics simulations are performed in the micro-canonical (NVE) ensemble. The simulations in micro-canonical ensemble does not correspond to the conditions under which most experiments are performed. To study the behaviour of a system under experimental conditions (at a specific temperature), simulations are performed in canonical (NVT) ensemble. Several methods have been proposed to control the temperature of the system: (a) Andersen thermostat (velocity scaling) (b) Berendsen thermostat (c) Langevin thermostat (d) Nose-Hoover thermostat etc. The concept is that the velocities are adjusted by minute amounts

so that the right spread of Maxwellian is obtained without affecting the general dynamics.

In our study, we use Nose-Hoover thermostat and therefore we give a brief introduction to Nose-Hoover thermostat [44, 45]. The equations of motion in this thermostat [46] are

$$\frac{d^2\mathbf{r_i}}{dt^2} = \frac{\mathbf{F_i}}{m_i} - \xi\frac{d\mathbf{r_i}}{dt}$$

$$\frac{d\xi}{dt} = \frac{1}{\tau^2}[\sum_{i=1,N}(\frac{m_i\mathbf{v_i^2}}{fk_BT}) - 1] \tag{2.9}$$

where ξ is the dynamic friction coefficient of the heat bath to which the system is coupled, f is the total number of degrees of freedom and τ is the relaxation time of the thermostat which controls the speed with which the thermostat damps down the fluctuations in the temperature. The value of ξ may be positive or negative, leading to deceleration or acceleration of the atoms respectively, if their total kinetic energy is greater, or smaller, than f k_BT. A small value of τ results in the large value of the derivative of ξ and hence leads to the large additional friction force in the motion of the particles. This means that small value of coupling parameter (τ) refers to the strong coupling.

To control the pressure in the system, we have used Nose-Hoover barostat [44,45]. The resulting equations of motion for the barostat are

$$\begin{aligned}
\frac{dr}{dt} &= v(t) + \eta(t)[r(t) - R_0],\\
\frac{dv}{dt} &= \frac{F}{m} - [\eta(t) + \xi(t)]v(t),\\
\frac{d\xi}{dt} &= \frac{1}{\tau^2}[\sum_{i=1,N}(\frac{m_iv_i^2}{fk_BT}) - 1],\\
\frac{d\eta}{dt} &= \frac{P - P_0}{\tau_p^2 N k_B T}V(t),
\end{aligned}$$

$$\frac{dV}{dt} = 3\eta(t)V(t) \tag{2.10}$$

where τ_p is the pressure relaxation time, P_0 is the target pressure, R_0 is the centre of mass coordinate and V is the system volume. In this case, Gibbs free energy is the conserved quantity.

2.2 Analysis Methods for MD output

For analysing MD output, we have two major post-processing tasks:

1. Structural changes
2. Time-dependent phonon frequencies

For determining structural changes, we have used tools such as void analysis, radial distribution function, structure factor, centro-symmetry parameter and common neighbor analysis. For determining phonon frequencies, we have used singular value decomposition (SVD) analysis.

2.2.1 Post-processor

We have developed a post-processor to compute the void volume and number of independent voids and void clusters at a desired time. The following steps are followed for computing the number of independent voids and void clusters:

- Step 1: Divide the simulation domain into small cubic cells of size 1.01 times the unit cell size. Due to atomic vibrations, the unit cell may transiently become empty. This is why we use a size of cubic cell which is slightly ($\sim$ 1%) greater than the unit cell size. In our study, we have considered one small cubic cell as a void nucleation size parameter.
- Step 2: Run a loop over atoms to count the filled cubic cells and empty cubic cells at any time of interest. Note that empty cubic cells are the indications of the voids.
- Step 3: Run a loop over all empty cubic cells to check whether they have adjacent empty cells or not. An empty cell which does not have any empty cell adjacent to it is called independent or stand alone or isolated void. Those empty cells which have empty cells adjacent to them are called void clusters.
- Step 4: Check whether any empty cell in the void cluster has itself any adjacent empty cell or not. If it has, then include those adjacent empty cells in the void cluster. This may make duplicate entries in the void cluster.
- Step 5: Check duplicate entries in the void cluster due to step 4 and remove them if they occur.

- Step 6: Check again whether any empty cell in the void cluster has adjacent empty cell or not. If yes, follow step 4 and step 5.
- Step 7: Check whether all the void clusters are finished. If yes, print independent voids and void clusters, otherwise go to step 4.

These steps are summarized in the flowchart shown in Figure 2.2. To get a better understanding of the post-processor, a graphical representation of void identification in the simulation domain is shown in Figure 2.3. The computation of independent voids and void clusters occurring in Figure 2.3 is depicted in Figure 2.4.

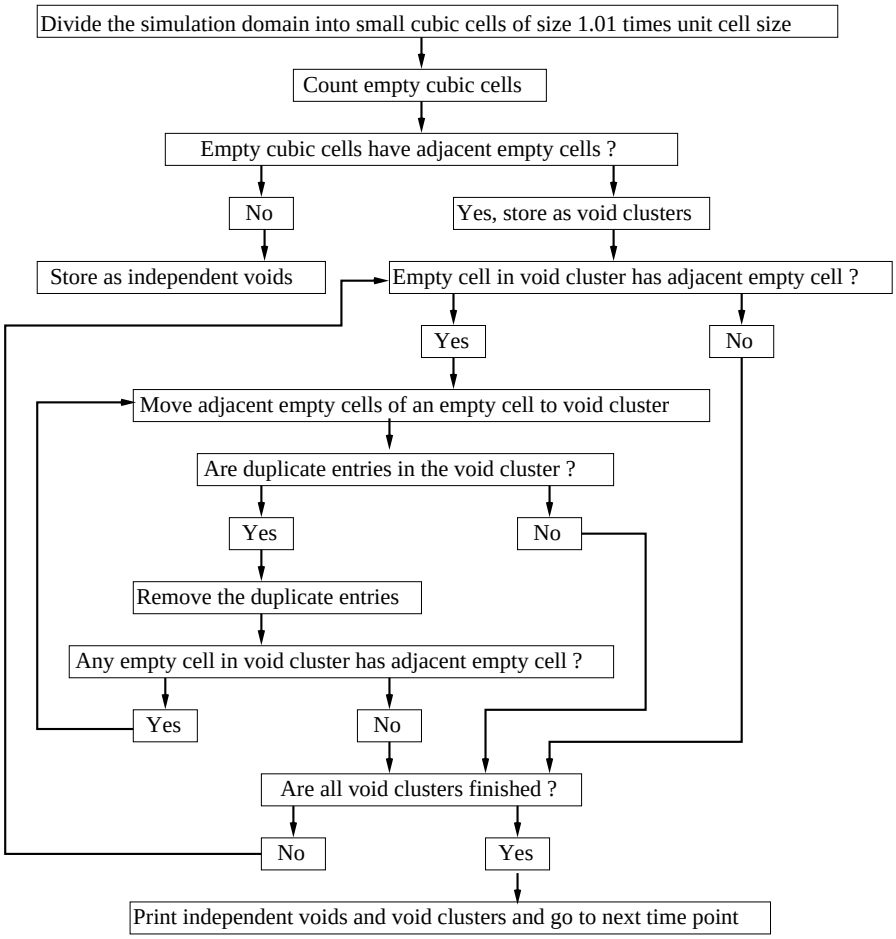

Figure 2.2: Flowchart for the post-processor used to compute independent voids and void clusters.

As the distension in the material increases, the void size also increases. This increase in void size includes the distension caused by the application of tension every few time steps and also the actual growth of the void. Therefore, we remove

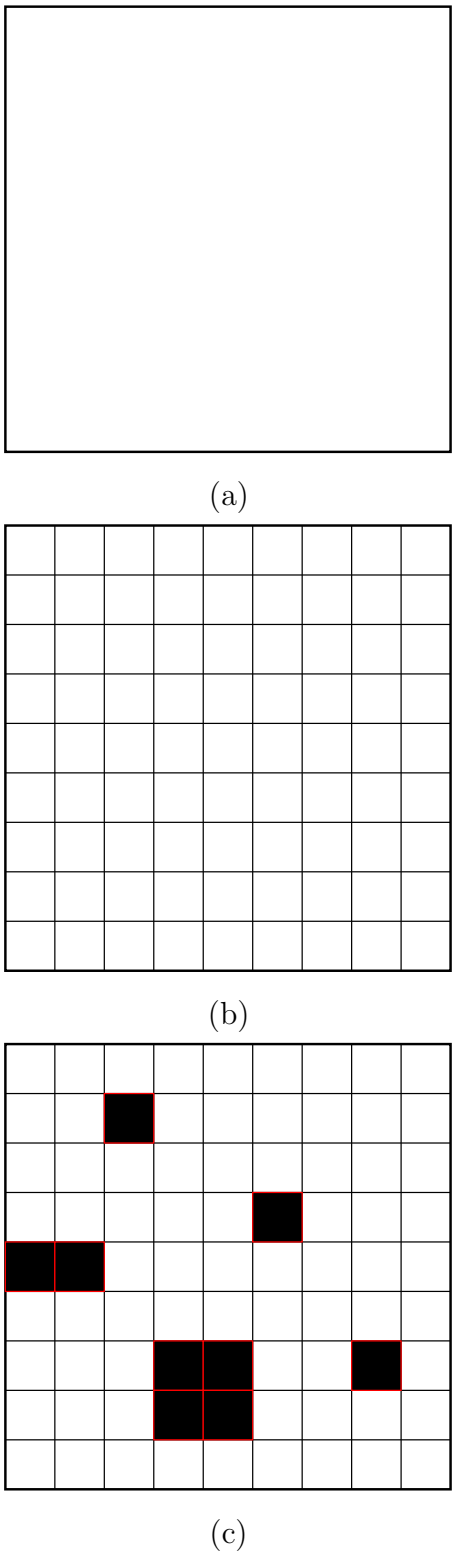

Figure 2.3: Graphical representation of void identification in the simulation domain. (a) Simulation domain at any time t (b) Creating small cubic cells in the domain at time t (c) Identifying the empty cells in the simulation domain at time t. Cells shown in black color denote empty cells in the simulation domain.

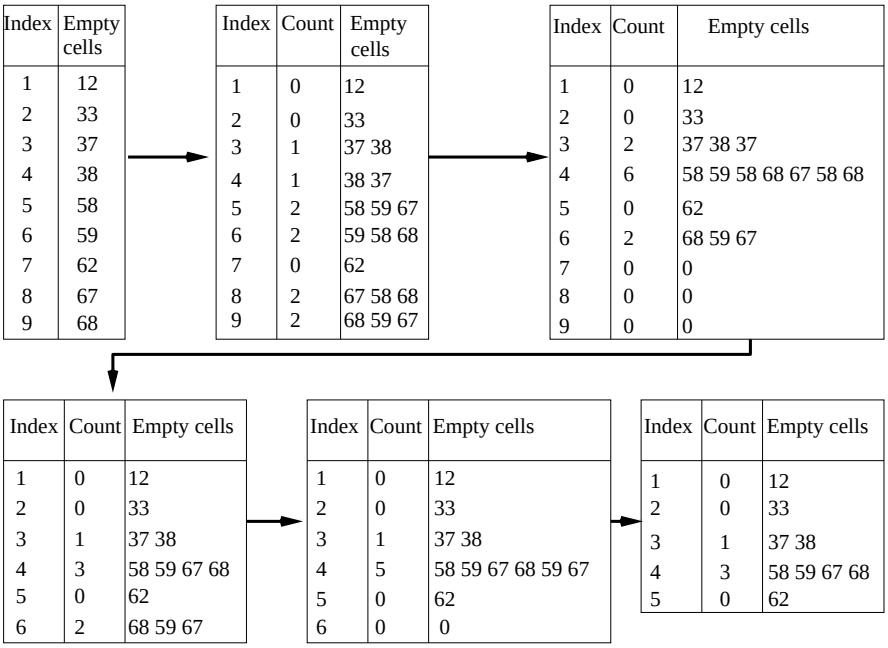

Figure 2.4: Computation of independent voids and void clusters in the simulations domain. There are three independent voids and two void clusters in the domain as shown in Figure 2.3.

this distension effect to obtain the void volume due to the actual growth of the void. At each time, the post-processor counts the empty cells in the simulation domain and by multiplying these empty cells with the initial size of the mesh, the total void volume is obtained. To get the void volume fraction at a particular time, the total void volume at that time is divided by the initial volume of the domain, not by the extended volume of the domain which is changing instantaneously due to expansion.

2.2.2 Radial distribution function (RDF)

RDF is the probability of finding a particle within a distance r from another particle. It is a very useful tool to describe how, on average, atoms in the system are radially packed around each other and gives information about whether or not the system has long-range crystalline order. If Δr is the thickness of the spherical shell (Figure 2.5) at a distance r from an atom under consideration, then the volume of the shell is given by

$$V = \frac{4\pi}{3}(r+\Delta r)^3 - \frac{4\pi}{3}r^3 \approx 4\pi r^2 \Delta r \tag{2.11}$$

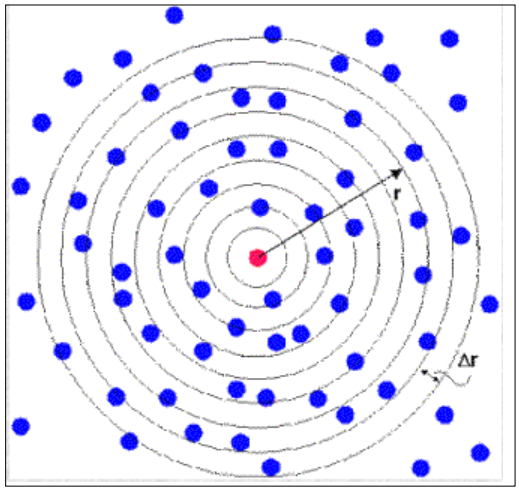

Figure 2.5: Computation of radial distribution function by making radial bins in the system.

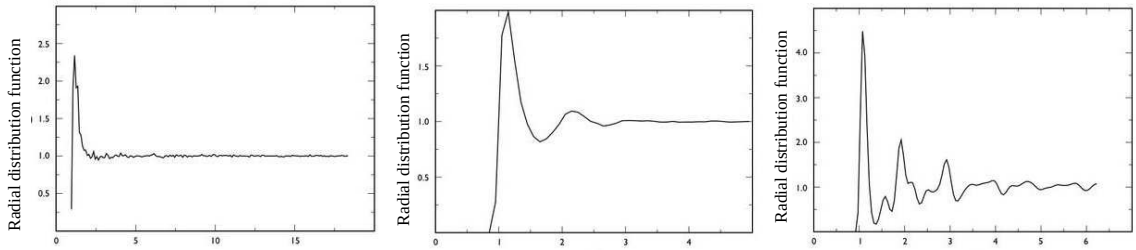

Figure 2.6: Typical radial distribution function as a function of inter-atomic separation for (*a*) gas (*b*) liquid and (*d*) solid.

To compute RDF for an atom, a series of concentric spheres are drawn around it at a fixed interval of distance Δ r, as shown in Figure 2.5. At desired time intervals, the number of atoms in each shell is counted and stored. At the end of the simulation, the average number of atoms in each shell is calculated and divided by the volume of each cell and the average density of atoms in the system, i.e.

$$g(r) \quad = \quad n(r)/\rho 4\pi r^2 \Delta r \tag{2.12}$$

where g(r) is the radial distribution function, n(r) is the average number of atoms in a shell of width Δr at a distance r and ρ is the average atom density.

A typical RDF as a function of inter-atomic separation for gas, liquid and solid [47] is shown in Figure 2.6.

- At small values of r, the RDF is zero. This is due to strong repulsive forces as atoms approach too close to each other.
- Occurrence of peaks at long range (large separations) indicates a high degree of ordering.
- At high temperatures, thermal motion results in broad peaks, while at low temperatures, the peaks are sharp.
- In crystalline materials where atoms are strongly confined in their positions, RDF shows sharp peaks.

2.2.3 Structure factor

Experimentally, one can get the structure factor by x-ray diffraction that can be used to identify the structure. For allowed reflections, the structure factor will be non-zero and for forbidden reflections, it will be zero. Using the reciprocal lattice vector corresponding to FCC, BCC and HCP, we can calculate the structure factor, S($\mathbf{k}$), for FCC, BCC and HCP as follows:

$$S(\mathbf{k}) = \frac{\sqrt{[\sum_i \cos(\mathbf{k}.\mathbf{r_i})]^2 + [\sum_i \sin(\mathbf{k}.\mathbf{r_i})]^2}}{N} \tag{2.13}$$

where $\mathbf{k}$ is the reciprocal lattice vector, $\mathbf{r}_i$ is the position vector of the ith atom and N is the total number of atoms in the system.

The reciprocal lattice vector ($\mathbf{k}$) is given by

$$\mathbf{k} = n_1\mathbf{k_1} + n_2\mathbf{k_2} + n_3\mathbf{k_3} \tag{2.14}$$

where n_1, n_2 and n_3 are integers and $\mathbf{k}_1$, $\mathbf{k}_2$ and $\mathbf{k}_3$ are the primitive translation vectors of the reciprocal lattice.

The primitive translation vectors for reciprocal lattice of FCC lattice are given by

$$\mathbf{k_1} = \frac{2\pi}{a}(\hat{\mathbf{i}} + \hat{\mathbf{j}} - \hat{\mathbf{k}}), \mathbf{k_2} = \frac{2\pi}{a}(-\hat{\mathbf{i}} + \hat{\mathbf{j}} + \hat{\mathbf{k}}), \mathbf{k_3} = \frac{2\pi}{a}(\hat{\mathbf{i}} - \hat{\mathbf{j}} + \hat{\mathbf{k}}) \tag{2.15}$$

The primitive translation vectors for reciprocal lattice of BCC lattice are given by

$$\mathbf{k_1} = \frac{2\pi}{a}(\hat{\mathbf{i}} + \hat{\mathbf{j}}), \mathbf{k_2} = \frac{2\pi}{a}(\hat{\mathbf{j}} + \hat{\mathbf{k}}), \mathbf{k_3} = \frac{2\pi}{a}(\hat{\mathbf{k}} + \hat{\mathbf{i}}) \tag{2.16}$$

The primitive translation vectors for reciprocal lattice of HCP lattice are given by

$$\mathbf{k_1} = \frac{2\pi}{a}(\frac{\hat{\mathbf{i}}}{\sqrt{3}} + \hat{\mathbf{j}}), \mathbf{k_2} = \frac{2\pi}{a}(-\frac{\hat{\mathbf{i}}}{\sqrt{3}} + \hat{\mathbf{j}}), \mathbf{k_3} = \frac{2\pi}{c}(\hat{\mathbf{k}}) \tag{2.17}$$

where $\hat{\mathbf{i}}$, $\hat{\mathbf{j}}$ and $\hat{\mathbf{k}}$ are unit vectors along the x-, y- and z- directions.

Position vector ($\mathbf{r}_i$) of the ith atom is given by

$$\mathbf{r_i} = x_i\mathbf{a_1} + y_i\mathbf{a_2} + z_i\mathbf{a_3} \tag{2.18}$$

where $\mathbf{a}_1$, $\mathbf{a}_2$ and $\mathbf{a}_3$ are the primitive translation vectors of the direct lattice. Using Eqn. 2.14 and Eqn. 2.18, Eqn. 2.13 becomes

$$S(\mathbf{k}) = \frac{\sqrt{[\sum_i \cos 2\pi(n_1x_i + n_2y_i + n_3z_i)]^2 + [\sum_i \sin 2\pi(n_1x_i + n_2y_i + n_3z_i)]^2}}{N} \tag{2.19}$$

For allowed reflections, the rules for FCC, BCC and HCP crystals are as follows:

- FCC: all odd or all even values of n_1, n_2 and n_3
- BCC: all even values of (n_1 + n_2 + n_3)
- HCP:
  - (n_1 + 2n_2) = 3m and n_3 = even
  - (n_1 + 2n_2) = 3m $\pm$ 1 and n_3 = odd
  - (n_1 + 2n_2) = 3m $\pm$ 1 and n_3 = even

Choice of n_1, n_2 and n_3 to perform structure factor calculations:

Ideally for all allowed sets of ($n_1n_2n_3$) for a given crystal structure, the structure factor should be equal. But due to thermal fluctuations, the structure factor will not be equal for all allowed sets of ($n_1n_2n_3$). To study the effect of temperature on the structure factor for different allowed sets of ($n_1n_2n_3$) for FCC crystal structure (single crystal copper), we have performed NPT MD for a system of 5×5×5 unit cells at different temperatures and 0 bar pressure. The thermal contribution to the structure factor for different allowed sets of ($n_1n_2n_3$) is shown in figure 2.7.

It is seen in figure 2.7 that the thermal contribution to the structure factor for single crystal copper increases with (n_1^2 + n_2^2 + n_3^2) at a constant temperature. It

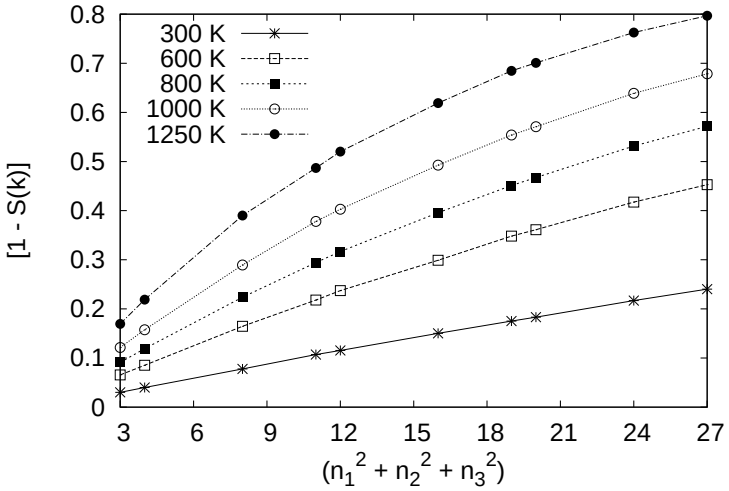

Figure 2.7: Thermal contribution to the structure factor for different allowed sets of $(n_1 n_2 n_3)$ for single crystal copper. The simulation domain contains 500 atoms corresponding to 5×5×5 unit cells.

is also seen in figure 2.7 that the thermal contribution to the structure factor at a constant temperature is minimum for the smallest allowed value of the $(\mathrm{n}_1^2 + \mathrm{n}_2^2 + \mathrm{n}_3^2)$.

Also an expression for the thermal contribution to the structure factor is given by

$$S_{th} = \sqrt{\exp(-2W)} \tag{2.20}$$

where W is called the thermal factor and is given by [48]

$$W = \frac{8\pi^2 \bar{u^2}}{3} \frac{\sin^2(\theta)}{\lambda^2} = \frac{8\pi^2 \bar{u^2}}{3} [\frac{n_1^2 + n_2^2 + n_3^2}{4a^2}] \tag{2.21}$$

where $\bar{u^2}$ is the mean square displacement of the atoms, λ is the wavelength of the X-rays/neutrons and θ is the angle. It is seen in Eqn. 2.21 that as temperature increases, the mean square displacement will increase leading to large thermal contribution to the structure factor with an increase in the value of $(\mathrm{n}_1^2 + \mathrm{n}_2^2 + \mathrm{n}_3^2)$. Therefore, to perform the structure factor calculations for FCC, BCC and HCP systems at a given temperature, the smallest allowed value of $(\mathrm{n}_1^2 + \mathrm{n}_2^2 + \mathrm{n}_3^2)$ should be used.

In this thesis, the structure factor calculations for FCC, BCC and HCP systems have been performed with $(1\bar{1}1)$ value of $(n_1 n_2 n_3)$ for FCC and (110) value of $(n_1 n_2 n_3)$ for BCC and HCP systems.

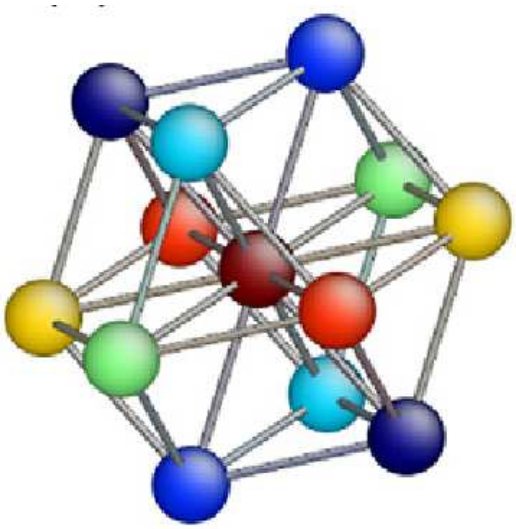

Figure 2.8: Opposite pairs (same color) in FCC structure for central (brown color) atom. There are six opposite pairs for central atom in FCC structure. Figure is adapted from [2].

2.2.4 Centro-Symmetry Parameter (CSP)

To distinguish between a perfect lattice and one having different types of defects due to triaxial deformation at high strain rates, the CSP calculation [49] can be used. It is known that centro-symmetric crystals (such as FCC and BCC) remain centro-symmetric under a uniform elastic deformation. This fact is used to compute centro-symmetric parameter for an atom. Each atom has pairs of equal and opposite bonds with its nearest neighbours. During deformation there will be change in the direction and/or length of the bonds, but they will remain equal and opposite within the same pair. When a defect is close to an atom under consideration, centro-symmetry will no longer hold and changes in the length and direction of the bonds will contribute to the CSP. The CSP for an atom in the material is calculated as follows [49]:

$$\text{CSP} \quad = \quad \sum_{i=1,N/2} |\mathbf{R}_i + \mathbf{R}_{i+N/2}|^2 \tag{2.22}$$

where $\mathbf{R}_i$ and $\mathbf{R}_{i+N/2}$ are the vectors which correspond to N/2 pairs (e.g. 6 pairs in Figure 2.8 for FCC crystal) of opposite neighbours in the material and N is the coordination number of the atom under consideration.

Zhao has defined limits on CSP [50] for single crystal copper, to distinguish between a perfect lattice and different kinds of defects:

- Perfect lattice: CSP < 0.5
- Partial dislocations: $0.5 <$ CSP < 3.0
- Stacking faults: $3.0 <$ CSP < 16.0
- Surface atoms: CSP > 16.0

This analysis allows detection of stacking faults in contrast to the energy method in which it becomes difficult to observe stacking faults in the system.

2.2.5 Common neighbor analysis

Common neighbor analysis [2,51] has been used by various workers [52] to determine the local crystal structure around an atom. In this method, the calculation of number of nearest neighbours is used to distinguish between different structural characteristics. The bonds between an atom and its nearest neighbours are examined to determine whether the crystal structure is BCC, FCC, HCP, icosahedral or other (i.e. atoms which do not belong to FCC, BCC, HCP and icosahedral environments).

In this method, three indices "lmn" are assigned to each pair of nearest neighbor where "l" refers to the number of common neighbours, "m" refers to the number of bonds between common neighbours and "n" refers to the longest chain formed by the bonds of the common neighbours. The local structure around an atom depends on the types of indices assigned for nearest neighbours. The local structure defined by CNA method for an FCC atom is shown in Figure 2.9.

It is seen in Figure 2.9 that there are 4 common neighbours (k) of a pair of atoms (i and j). There are two bonds between the common neighbours and the longest chain formed by bonds of the common neighbours is 1. Therefore, the indices assigned for each atom of the pair will be 421. All nearest neighbours of an atom belonging to FCC structure have 421 indices.

The type of indices for FCC, HCP, BCC and Icosahedral structures [2, 53] are shown in Table 2.1.

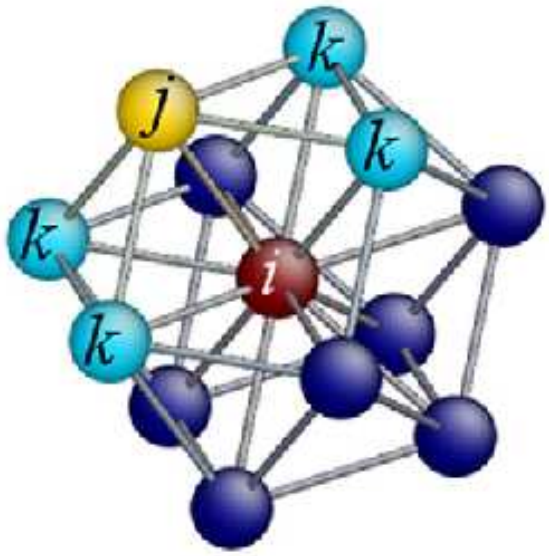

Figure 2.9: Local structure defined by CNA method for FCC structure. Here brown (i) and yellow (j) atoms are nearest neighbours which have 4 light-blue common neighbours (k). The common neighbours have two bonds and the longest chain of the bonds between the common neighbor is 1. Figure is adapted from [2].

Structure	Indices	Number of pairs
FCC	421	6
HCP	421	3
	422	3
BCC	444	3
	666	4
Icosahedral	555	6

Table 2.1: Indices used to determine local structure around an atom.

In the CNA calculation, the results can be sensitive to the specified cut-off value. Therefore, an appropriate cut-off distance should be chosen for a given crystal structure. To get an appropriate cut-off distance, the following formulas can be used for

CNA computation:

$$\begin{aligned} r_c^{fcc} &= \frac{1}{2}(\frac{\sqrt{2}}{2}+1)a \simeq 0.8536a \\ r_c^{bcc} &= \frac{1}{2}(\sqrt{2}+1)a \simeq 1.207a \\ r_c^{hcp} &= \frac{1}{2}(1+\frac{\sqrt{4+2x^2}}{3}+1)a \end{aligned}$$

For CNA analysis, values used to identify the crystal structure in LAMMPS code are shown in Table 2.2. Note that CNA analysis is appropriate only for mono-component

CNA value	Crystal structure
1	FCC
2	HCP
3	BCC
4	Icosahedral
5	Unknown

Table 2.2: CNA values to identify local crystal structure around an atom

systems.

2.2.6 Singular Value Decomposition (SVD) Analysis

Details of the singular value decomposition analysis are described in [54]. A brief description of the method is presented here. In this technique, a matrix $A_{m\times n}$ is decomposed into three new matrices:

$$A_{m\times n} = U_{m\times m}\, S_{m\times n}\, V^T_{n\times n} \tag{2.23}$$

where $UU^T = I$, $VV^T = I$ (i.e., U and V are orthogonal matrices); the columns of U are the orthogonal eigen vectors of AA^T, the columns of V are the orthogonal eigen vectors of A^TA and S is a diagonal matrix containing the square roots of eigen values from U or V in descending order.

Application to MD output

Matrix A_{MN} generated from MD output is given as follows:

$$A_{MN} = \begin{bmatrix} A_{11} & A_{12} & A_{13} & \cdots & A_{1N} \\ A_{21} & A_{22} & A_{23} & \cdots & A_{2N} \\ A_{31} & A_{32} & A_{33} & \cdots & A_{3N} \\ \cdots & \cdots & \cdots & \cdots & \cdots \\ \cdots & \cdots & \cdots & \cdots & \cdots \\ A_{M1} & A_{M2} & A_{M3} & \cdots & A_{MN} \end{bmatrix} \tag{2.24}$$

where M is the number of time steps for which atomic positions are output and N = d N_{atoms}, where N_{atoms} is the number of atoms used in the MD simulation and d is the dimension of the system. Therefore, we can write

$$A_{11} = x_{11}, A_{12} = y_{11}, A_{13} = z_{11}; A_{14} = x_{12}, A_{15} = y_{12}, A_{16} = z_{12}, ...$$

Rewriting the above matrix (Eqn. 2.24) as follows:

$$A_{MN} = \begin{bmatrix} x_{11}\ y_{11}\ z_{11} & x_{12}\ y_{12}\ z_{12} & \cdots & x_{1N}\ y_{1N}\ z_{1N} \\ x_{21}\ y_{21}\ z_{21} & x_{22}\ y_{22}\ z_{22} & \cdots & x_{2N}\ y_{2N}\ z_{2N} \\ x_{31}\ y_{31}\ z_{31} & x_{32}\ y_{32}\ z_{32} & \cdots & x_{3N}\ y_{3N}\ z_{3N} \\ \cdots & \cdots & \cdots & \cdots \\ \cdots & \cdots & \cdots & \cdots \\ x_{M1}\ y_{M1}\ z_{M1} & x_{M2}\ y_{M2}\ z_{M2} & \cdots & x_{MN}\ y_{MN}\ z_{MN} \end{bmatrix} \tag{2.25}$$

here x, y and z are the atomic positions.

Decomposition of this matrix using SVD gives information on temporal variations of atoms (U), information on spatial correlations amongst the atoms (V) and the amplitude (S) of the modes excited in the system. As discussed above, the singular values (S values) which are the representative of the amplitude of modes are arranged in descending order which means that even fairly weak modes excited in the system can be identified. For each mode, the V-vector gives information about spatial distortions produced by the mode, while U gives the time series. FFT of the U-vector gives the dominant frequencies associated with that mode.

2.3 Visualization Tools

For the visualization of MD results, various open source visualization tools are available which are very useful for understanding and interpreting the results. Some of the widely used visualization tools are Visual Molecular Dynamics (VMD) [3], Atomeye [4], Ovito [55] etc.

Chapter 3

Application of a macroscopic void nucleation and growth model at the atomistic scales for perfect crystal copper

3.1 Introduction

As mentioned in Chapter 1, hydrodynamic simulations divide the domain of interest into computational cells and require the following:

1. An equation of state.
2. A model to predict the strength of the material during high strain-rate deformation, i.e., the variation of yield strength and shear modulus of the material with temperature, pressure, plastic strain, etc. [25, 26] and [27–31].
3. A dynamic fracture model, e.g., void nucleation and growth model, where fracture properties depend upon the temperature and pressure values in the cell [17].

For a given cell in the hydrodynamic simulations, the temperature and pressure are taken to be constant during each hydrodynamic timestep.

This chapter focuses upon the third item, i.e., a dynamic fracture model.

Existing macroscopic fracture models at high strain rates, such as the Nucleation and Growth (NAG) [5] and Void Growth (VG) [56] models, involve several parameters, best-fit values of which are required for different materials. These best-fit parameters are available in the literature only for a few materials. If some of these parameters can be determined from first principles, the others can be determined by comparison with experiments, e.g., spall produced by plate impact [6]. One way of getting first principles data is to use "Classical Molecular Dynamics" using known potentials, e.g., the EAM potential for metals.

Due to limitations on computing power, Molecular Dynamics (MD) simulations are restricted in terms of small sample size, short time scales and high loading rates. Hence MD simulations cannot directly replace hydrodynamic simulations. What these simulations *can* do is to provide the best-fit values of parameters in the NAG model at high strain rates. These best-fit NAG parameters can be used in hydrodynamic simulations to simulate fracture at the macro-scale.

In this chapter, we report on MD simulations to check the validity of the NAG model at high strain rates for perfect crystal copper at atomistic scales. We also attempt to determine best-fit values of NAG parameters.

3.2 Nucleation and Growth (NAG) Model

The Nucleation and Growth model (also known as DFRACT model) developed at Stanford Research Institute [5] is a micro-physical, semi-empirical model which describes the fracture processes that occur as a nucleation and growth of voids in ductile materials. The model was developed to represent the nucleation and growth rate processes in polycrystalline materials at (10^4 - 10^6/s) strain rates and tensile durations of 10^{-6} to 10^{-8} s. The nucleation and growth rates of the voids in the model are found to be independent of loading sources and describe the damage resulting from impact, explosion and radiation deposition [1].

This model was proposed on the basis of the damage observations in the cross sections of the target materials impacted using the gas gun experiments. The number of voids was counted and void size distributions were obtained at different locations of the target material. The number of voids was found to be increased as a function of the stress intensity (which depends on the impact velocities) and stress duration (which depends on specimen thicknesses). This model can predict many aspects of

the spall fracture: modification of stress or free surface velocity (particle velocity histories) by the development of damage and location, number and size of voids throughout the material [1]. In this approach

- characteristic dimensions of the damage were from 1 μm to about 100 μm
- the damage was considered statistically, i.e. the voids are counted to get the void size distributions and the NAG model was proposed on the basis of these void size distributions, not on the basis of individual voids.

The nucleation rate of the voids is determined from the void densities obtained by performing a set of experiments at different stress intensities and stress durations. The growth rate of the voids is determined by comparing the void size distributions with the stress histories at the same x-locations in the target material at different stress durations. The void growth rate in the NAG model is consistent with the growth equation derived by Poritsky [57] for expansion of a void under tension in a viscous fluid.

The shortcoming of the NAG model is that it involves many parameters which lead to difficulties in getting the best-fit values.

3.2.1 Why SRI-NAG model?

Apart from the SRI NAG model, several other models are also available for high strain rate fracture in the literature [56, 58]. The SRI model describes not only the evolution of void volume fraction (damage) but also the void concentration as a function of distance (or time). All other NAG models, on the other hand, describe only the evolution of void volume fraction. Now, information regarding the size and number of voids allows for a closer comparison with experiment. That is why the SRI-NAG model was chosen for this study.

3.2.2 Nucleation

When the tensile pressure P_s in the solid material exceeds the nucleation threshold P_{n0} of the material, new voids are created. The rate of nucleation is given by

$$\dot{N} = \dot{N}_0 \exp\left[\frac{P_s - P_{n0}}{P_1}\right], \quad P_s > P_{n0} \tag{3.1}$$

$$\dot{N} = 0, \quad P_s \leq P_{n0} \tag{3.2}$$

where $\dot{N_0}$ is the threshold nucleation rate and P_1 is the pressure sensitivity for nucleation. Both $\dot{N_0}$ and P_1 are material constants. Note that P_s is the tensile pressure and not the average pressure in the system.

The volume of the voids nucleated in a time interval, Δt, is given by

$$\Delta V_n = 8\pi \dot{N} \Delta t R_n^3 \tag{3.3}$$

where R_n is a material parameter known as nucleation size parameter.

3.2.3 Growth

The existing voids grow if the tensile pressure in the material exceeds the threshold for void growth P_{g0}. The void volume at the end of a timestep is given by

$$V_g = V_{v0} \exp\left[\frac{3}{4} \frac{P_s - P_{g0}}{\eta} \Delta t\right] \tag{3.4}$$

where V_{v0} is the void volume at the beginning of the time interval and η is the material viscosity.

The total void volume at the end of the timestep, taking into account both nucleation and growth, is thus given by

$$V_v = V_{v0} \exp\left[\frac{3}{4} \frac{P_s - P_{g0}}{\eta} \Delta t\right] + \Delta V_n \tag{3.5}$$

3.3 Why Triaxial expansion for MD simulations?

In high velocity impact experiments, the interaction of release waves from projectile and target free surfaces leads to a triaxial state of stress following a uniaxial state of strain. This triaxial state of stress results in the nucleation, growth and coalescence of voids [7, 8].

To check whether there is a transition from uniaxial state of strain to triaxial state of stress during the interaction of release waves, we have performed an MD simulation of the impact of copper plates at an impact velocity of 1.5 km/s. We see in Figure 3.1 that the normal stress components (σ_{xx}, σ_{yy} and σ_{zz}) overlap each other after the interaction of release waves from the flyer and target free surfaces.

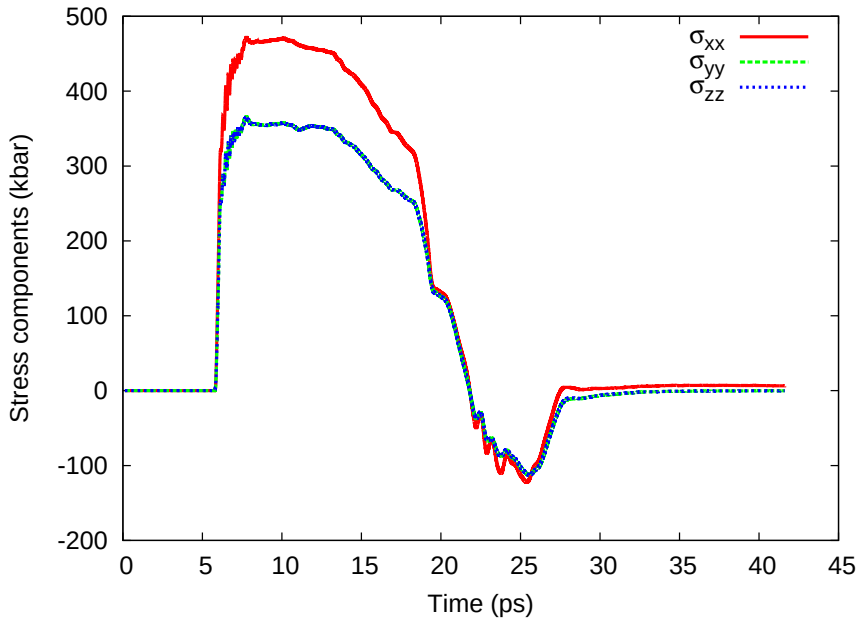

Figure 3.1: Transition from uniaxial state of strain to triaxial state of stress for the impact of copper plates at 1.5 km/s impact velocity. Results from MD simulations.

We can, therefore, say that it is hydrodynamic tensile pressure which results in the nucleation, growth and coalescence of voids.

Because of the connection of triaxial expansion with shock-induced dynamic fracture of materials, we have performed triaxial expansion of the material to study the nucleation, growth and coalescence of the voids in single crystal copper.

3.4 Why Copper?

We want to generate best-fit NAG parameters for materials of interest. In the present study, we have chosen copper as a test material, for the following reasons:

- Availability of experimental data: Data from a number of spall experiments on single crystal copper have been published by several workers. The results of these experiments vary with the presence of defect density and purity of the crystal along with other factors such as strain-rate, temperature, etc. Hence there is sufficient experimental data for comparison with MD results.

- Previous MD simulations on crystal copper: Many workers have performed molecular dynamics simulations on single crystal copper to study the fracture

at high strain-rate. Those studies have pointed out grey areas for further work.

3.5 Computational Technique for Triaxial Deformation

3.5.1 Initial Set up

We have triaxially expanded single crystal copper in the manner done by Belak et al [13]. The simulations have been done using the molecular dynamics code, LAMMPS (Large-scale Atomic/Molecular Massively Parallel Simulator) [59] for this study. A typical computation domain contains 4×10^6 atoms corresponding to $100\times100\times100$ unit cells. The number of atoms is chosen such that any further increase does not change the results, as explained in detail in Section 3.5.3.

The Embedded-Atom Method (EAM) [39, 40] potential parameters obtained by Foiles et al [60] have been used for this study. To integrate the equations of motion, we have used velocity Verlet algorithm with a timestep of 1 femto-second (fs). We have found that the results do not change for timesteps $\leq$ 1 fs, as shown in Section 3.5.4. The computational domain is replicated in all three directions using periodic boundary conditions. Atomic velocities are initialized using a Gaussian distribution with 300 K temperature. Before starting the actual simulation, NPT relaxation is performed at 0 bar and 300 K to relax the system. Nose-Hoover thermostat and barostat [44, 45] have been used to control the temperature and pressure of the system.

After the pressure and temperature thermalize, we have turned off the barostat and a strain rate of 5×10^9/s has been applied to expand the system triaxially at constant temperature. This is done by rescaling the atomic positions within the simulation domain, which is extended in all three directions as follows:

$$L(t) \;=\; L(0)(1+\dot{\epsilon}\times t) \tag{3.6}$$

where L(t) is the instantaneous length of one side of the system, L(0) is the original length of one side of the system, $\dot{\epsilon}$ is the engineering strain rate and t is the elapsed time. The rescaling is carried out every 0.1 ps (100 timesteps) because rescaling after every time step would hinder the dynamics of atoms. By deforming a box of length L(0) as explained in Eqn. 3.6, the inter-atomic distance changes by dL

(e.g., L(0) = 361.0 $\mathring{A}$ and dL = 0.0018 $\mathring{A}$) and would allow the atoms a couple of oscillations to equilibrate to the new pressure conditions.

3.5.2 Calculation of tensile pressure (P_s) from the average pressure (P)

The formula for computing the total pressure of the system (P) in LAMMPS is given by

$$P = \frac{Nk_BT}{V} + \frac{\sum_i^N r_i \cdot f_i}{d\,V} \tag{3.7}$$

where N is the number of atoms in the domain, k_B is the Boltzmann constant, T is the temperature, d is the dimensionality of the system, V is the system volume, r_i is the position vector of ith atom and f_i is the force on ith atom. The first term in this equation is the kinetic contribution to the pressure and the second term gives the virial contribution.

MD simulations yield the average pressure. Once voids appear in the system, the true (tensile) pressure in the solid can be calculated as follows [17]

$$P = P_s\,(1 - V_{vf}) \tag{3.8}$$

where V_{vf} is the void volume fraction in the domain. Details of this calculation have been given in Chapter 2.2.1.

We are simulating a perfect single crystal in which no defect is present. This means that there are no pre-existing voids, unlike polycrystalline materials which have some empty space between grain boundaries. Therefore, until void nucleation occurs, the average pressure in the system is the same as the tensile. Once nucleation and growth start, the tensile pressure is higher than the average pressure. For a typical problem, the average and tensile pressures as functions of time are shown in Figure 3.2.

3.5.3 Domain size effect

In order to study the domain size effect, we have performed a series of simulations by varying the number of atoms from 10^5 to 10^7. Figure 3.3 shows the temporal evolution of void volume fraction at a strain rate of 5×10^9/s. It can be seen in Figure 3.3 that for simulation domains containing N = 2,916,000 atoms (90×90×90

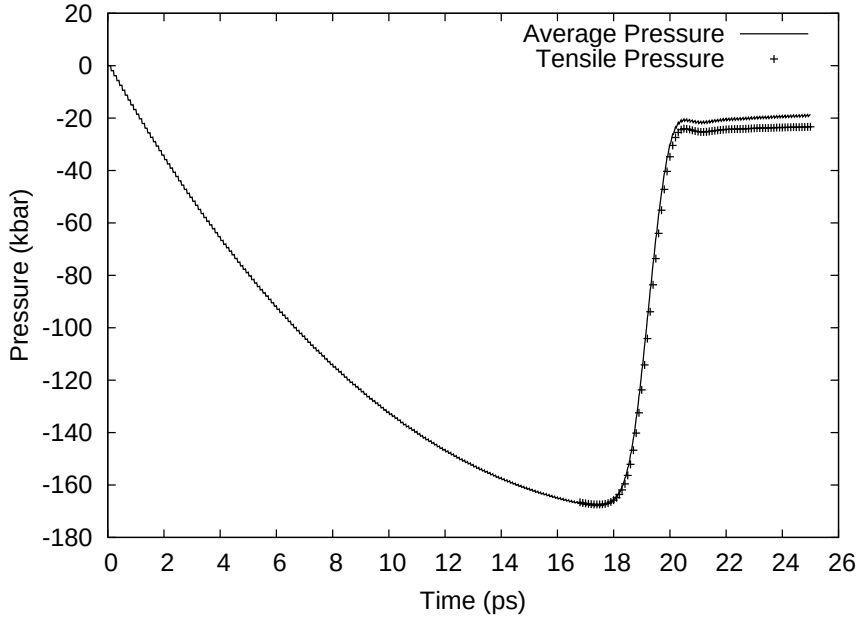

Figure 3.2: Comparison of average pressure (P) and tensile pressure (P_s) for single crystal copper expanded triaxially at high strain rate (5×10^9/s) at T=300 K. The simulation is done using N = 4×10^6 atoms.

unit cells), N = 4,000,000 atoms (100×100×100 unit cells), and N = 10,976,000 atoms (140×140×140 unit cells), the void volume fraction seems to be converged. This signifies that our results will not change for simulation domains with N > 2,916,000. Therefore, we have simulated isotropic triaxial tension in single crystal copper using N = 4,000,000 atoms to determine optimized NAG parameters.

3.5.4 Timestep optimization

We have performed several exercises to study the choice of timestep which has to be used in the simulation. The simulation domain for this study is taken as N = 4×10^6. Single crystal copper is triaxially deformed at 5×10^9/s strain rate with timesteps: 0.25 fs, 0.5 fs, 1.0 fs, 3.5 fs, and 9.5 fs. The resulting data is post-processed. A comparison of void volume fraction as a function of time for various timesteps (0.25 fs, 0.5 fs, 1.0 fs, 3.5 fs and 9.5 fs) is shown in Figure 3.4. It is seen that for timesteps 0.25 fs, 0.5 fs, and 1.0 fs, the void volume curves are almost identical. Therefore, 1.0 fs is chosen as the optimal timestep for subsequent simulations.

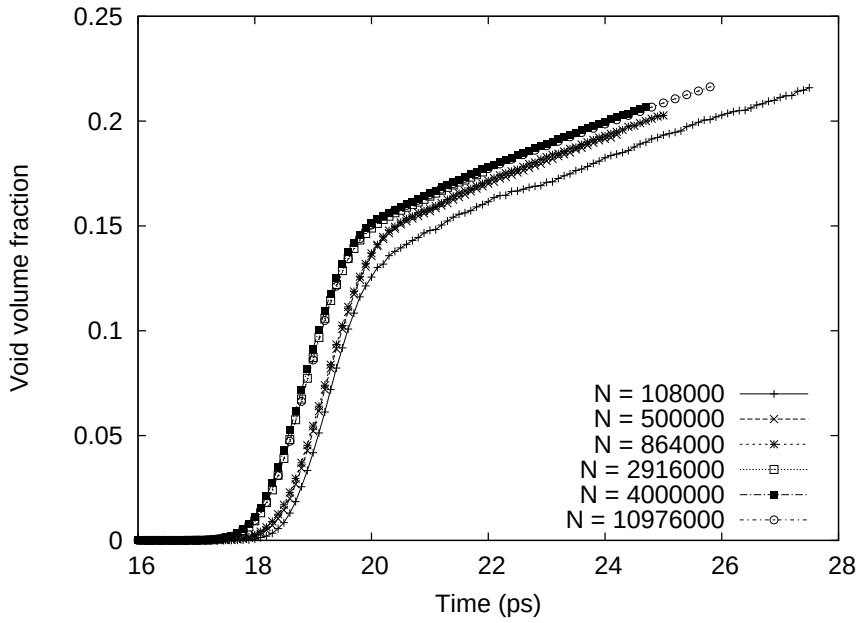

Figure 3.3: Void volume fraction as a function of time for domains of different sizes. Note that for N > 2916000, the void volume fraction does not change.

3.5.5 Effect of EAM parameters on results

Belak [13] performed molecular dynamics simulations for a domain of 32×32×32 unit cells corresponding to 131,072 atoms. That study used the EAM potential parameters obtained by Oh and Johnson [61] and simulated isotropic tension in single crystal copper with a 5.0 fs timestep. Therefore, to see the effect of various EAM potential parameters on the results, we have performed an exercise with the same domain (32×32×32 unit cells) and timestep (5.0 fs) as taken by Belak. We have used potential parameters obtained by Foiles et al [60], Adams et al [62], Zhou et al [63], and Mishin et al [64].

The pressure-time history for all four EAM parameters is shown in Figure 3.5. The pressure-time curves are almost the same in all cases upto the turn-around point, except with Zhou's parameters. We have not explored why Zhou's potential parameters yield such different results. Broadly speaking, it appears that changes in the EAM potential affect the results only to a limited extent.

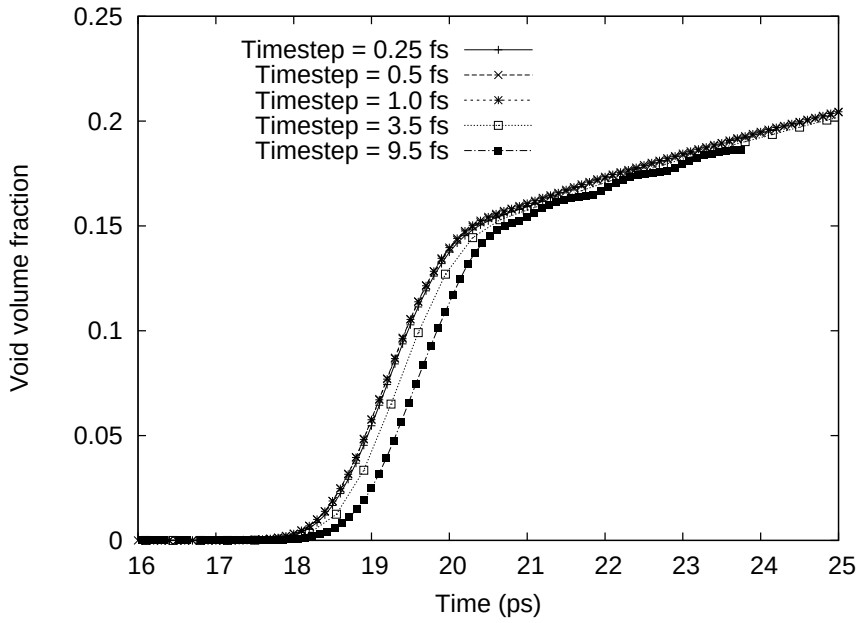

Figure 3.4: Void volume fraction as a function of time for a single crystal copper deformed triaxially at 5×10^9/s strain rate with timesteps: 0.25 fs, 0.5 fs, 1.0 fs, 3.5 fs, and 9.5 fs. N = 4×10^6.

3.6 Results and Discussion for Triaxial Deformation

3.6.1 Pressure-time profile

The resulting internal pressure (P = -1/3(σ_{xx}+σ_{yy}+σ_{zz})) as a function of time during triaxial deformation of single crystal copper at 300 K, with N = 4×10^6, for a strain rate of 5×10^9/s, is shown in Figure 3.6. As we can see in Figure 3.6, the magnitude of pressure increases continuously upto 168 kbar, after which it turns around and decreases with further expansion. The turn-around of pressure is the result of stress relaxation due to nucleation and growth of voids. Note that nucleation of more than one void takes place in our simulated volume (Figure 3.7).

It is noteworthy that the turn-around of pressure in Figure 3.6 is taking place at 168 kbar, close to the value determined by Seppala et al [8] in their study of triaxial expansion of single crystal copper at 10^9/s strain rate.

The pressure-time profile (Figure 3.6) can be divided into three regions:

1. Void nucleation region (region AB in Figure 3.6): This region corresponds

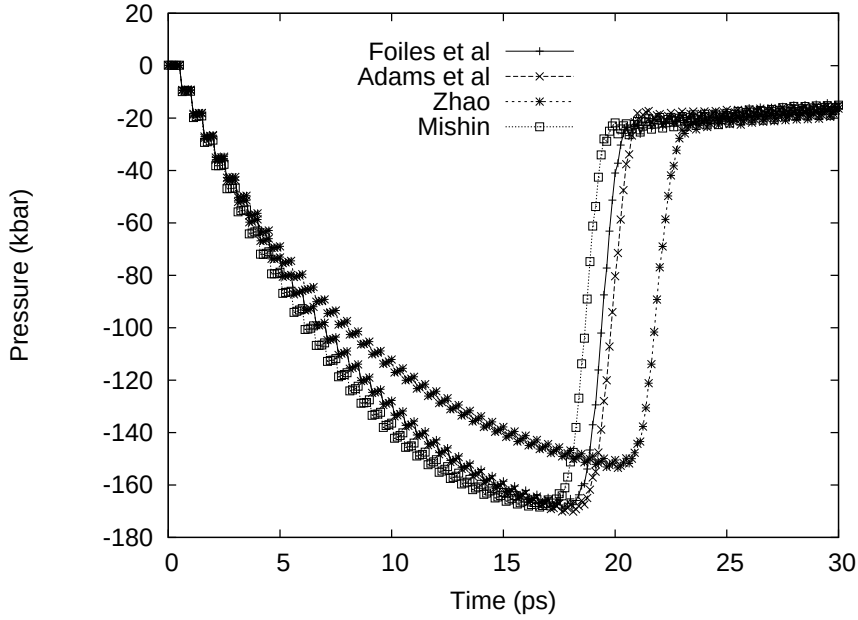

Figure 3.5: Pressure-time history for single crystal copper deformed triaxially at 5×10^9/s strain rate with various EAM potential parameters.

to the nucleation of voids. In this region, void volume generation due to the nucleation of voids dominates that due to growth of voids. The tensile pressure in this region is always higher than the threshold pressure for void nucleation.

2. Growth region (region BC in Figure 3.6): This region corresponds to growth of voids. Void volume generation due to growth of voids dominates that due to nucleation. The tensile pressure in this region is higher than the nucleation threshold for a few ps, following which void nucleation stops and only growth takes place. The threshold for void growth in this region is always lower than the tensile pressure in the system, leading to continuous growth of the voids.

3. Coalescence region (region beyond C in Figure 3.6): This region corresponds to coalescence of voids. In this region, the void volume due to coalescence of the voids dominates over growth of voids.

Some snapshots of void distribution in the domain created using [3], showing nucleation, growth and coalescence at different times, are given in Figure 3.7.

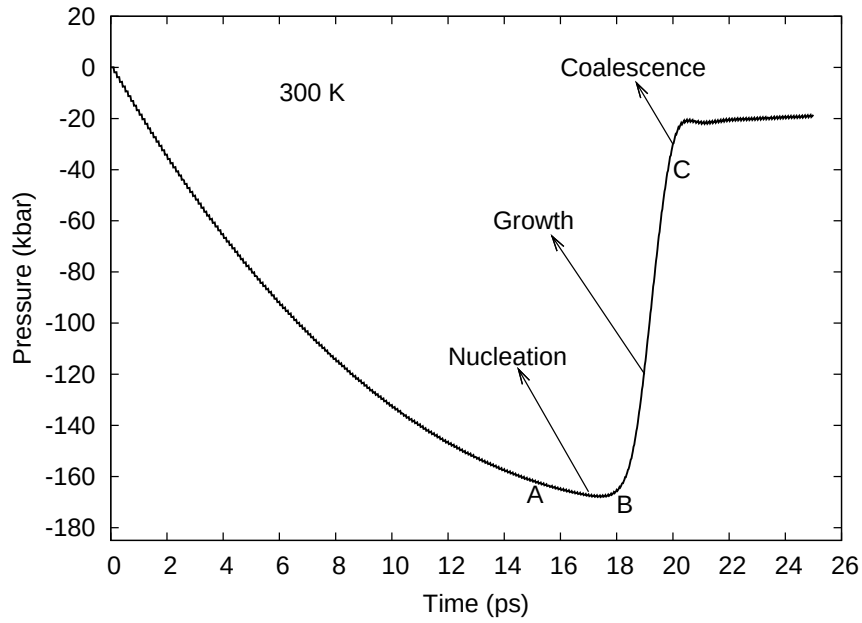

Figure 3.6: Internal pressure as a function of time for single crystal copper deformed triaxially at 5×10^9/s strain rate; N = 4×10^6. The region AB is the nucleation region, region BC is the growth region and the region beyond C is the coalescence region

3.6.2 Independent voids and void clusters

By independent voids, we refer to stand-alone voids which do not have any adjacent voids. Void clusters consist of more than one adjoining voids, as illustrated in Figure 3.8(a). Many independent voids and void clusters are created under the triaxial deformation of single crystal copper at 5×10^9/s strain rate. Uniform triaxial expansion of the crystal leads first to the nucleation of independent voids. These voids grow in time and eventually coalesce. Hence we expect the number of individual voids to initially grow, reach a maximum, and then start decreasing. The same holds for the number of void clusters. These trends can indeed be seen from Figure 3.8(b).

3.6.3 Nucleation and Growth (NAG) parameters

For a given (assumed) set of NAG parameters, the pressure-time profile yielded by MD simulations, and corrected to get the tensile pressure, can be used to determine the number of nuclei and the total void volume due to nucleation and growth as a function of time. It should be noted that in a pure single crystal, there is no pre-

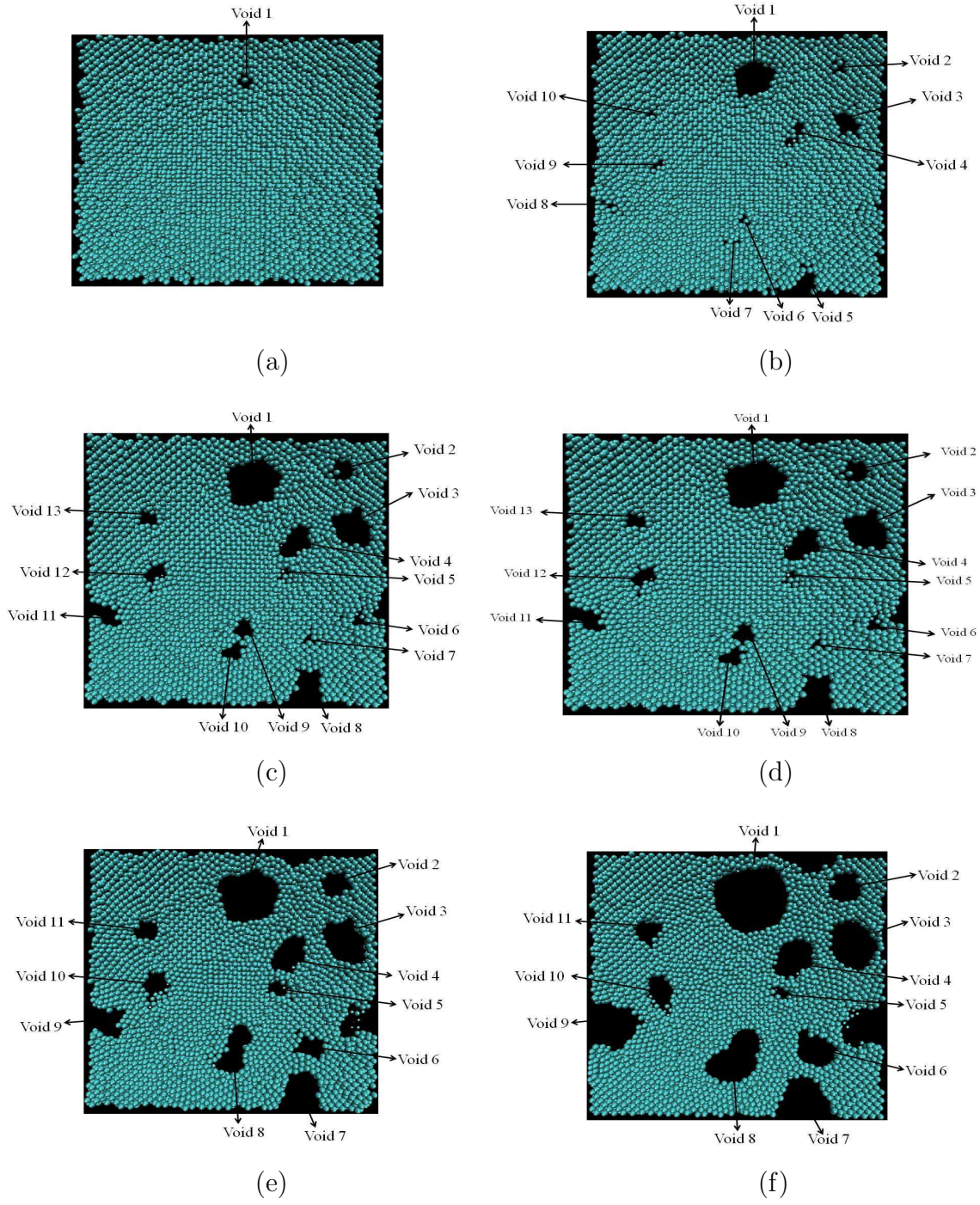

Figure 3.7: Snapshots (created using VMD [3]) of void distribution for single crystal copper triaxially deformed at 5×10^9/s strain rate with 300 K. (*a*) 17.7 ps, (*b*) 18.5 ps (*c*) 18.7 ps (*d*) 18.9 ps (*e*) 19.3 ps (*f*) 21.9 ps. This image is shown at one x-y cross-section through the domain.

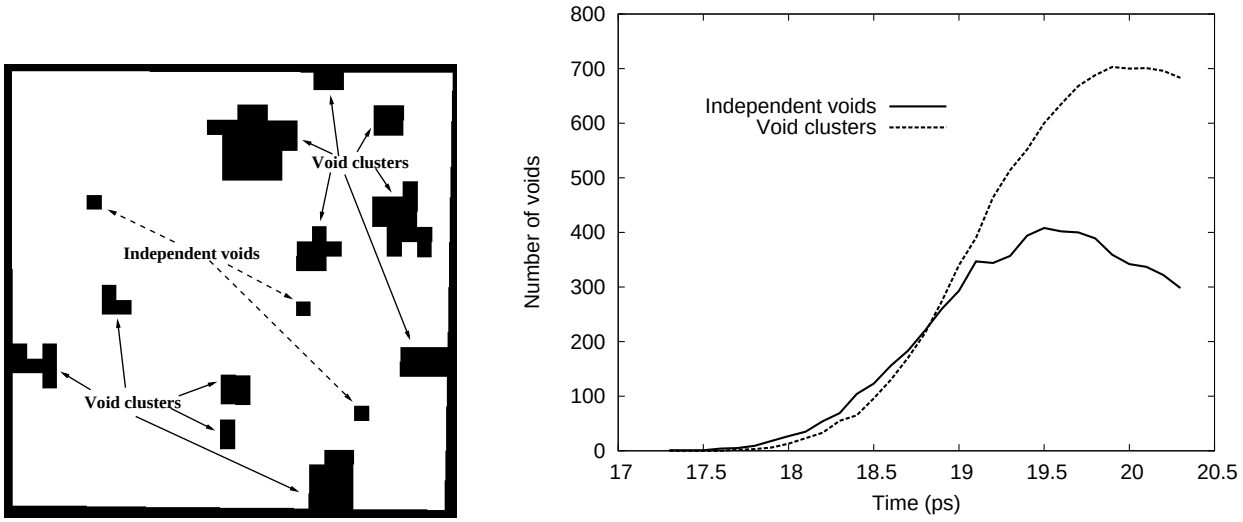

(a) (b)

Figure 3.8: (*a*) Illustration of independent voids and void clusters. (*b*) Temporal evolution of the number of independent voids and void clusters for single crystal copper uniformly expanded at 5×10^9/s strain rate at 300 K.

existing void. The total void volume obtained from NAG model (Eqn. 3.5) is then compared with the post-processed MD output. An overall minimization procedure is then used to determine best-fit NAG parameters (P_{n0}, P_1, $\dot{N}_0$, P_{g0}, and η). Note that we have not used Eqn. 3.3 for the void volume (ΔV_n) nucleated in Δt time interval. In our results, we have used $\dot{N}\Delta t R_n^3$ for the void volume (ΔV_n) nucleated in Δt time interval.

The relative error (ϕ) at any time point is defined as

$$\phi \;=\; 1 - \frac{V_{\rm pp}}{V_{\rm NAG}} \tag{3.9}$$

where $V_{\rm pp}$ is the total void volume obtained by the post-processor (Chapter 2.2.1) and $V_{\rm NAG}$ is the total void volume obtained by NAG model.

The square root of average squared relative error (Σ) is defined as

$$\Sigma \;=\; \sqrt{\frac{\sum_{i=1}^{M}\phi^2}{M}} \tag{3.10}$$

where M is the total number of data points.

The best-fit NAG parameters for single crystal copper deformed at 5×10^9/s strain rate with 300 K are shown in Table 3.1. Also shown for comparison are the values for polycrystalline OFHC copper.

NAG parameters	Single crystal copper	OFHC copper [5]
P_{n0} (kbar)	-160.4	-5.0
P_1 (kbar)	-0.167	-2.0
$\dot{N}_0$ (m^{-3}/s)	7.1×10^{18}	2.8×10^{18}
P_{g0} (kbar)	-21.2	-5.0
η (bar-sec)	-3.4×10^{-8}	-7.5×10^{-5}

Table 3.1: Comparison of best-fit NAG parameters obtained for single crystal copper with the experimental values for polycrystalline copper [5]. $\Sigma = 0.19$; $N = 4\times10^6$.

From Table 3.1, it can be seen that

- The threshold for void nucleation (P_{n0}) is much higher for single crystal copper than that for polycrystalline copper. This is reasonable, because in polycrystalline copper, there are weak points, e.g., grain junctions, which can lead to void nucleation at lower tensile pressures [13]. This difference in nucleation thresholds may also be the result of differences in the strain rates used in experiments and MD simulations. Our void nucleation threshold (160 kbar at 300 K) is very close to the spall strength (156 kbar) measured by Moshe et al [65] under laser shock experiments on copper foils with thickness in the range (1 - 10) μm and strain rate in the range (1.5 - 4.5)$\times10^8$/s. Moshe et al used polycrystalline copper for their study. However, with a thickness of only a few microns, it is possible that in the axial direction, it could still be a single crystal, although that is not certain.

  Many workers [6, 66–70] have performed experiments on single crystal copper. The spall strength measured by Tonks et al [66] for <100> single crystal copper is 73.0 kbar at 9.8×10^6/s strain rate. The spall strength measured by Kanel et al [6, 67, 68] for single crystal copper is in the range of (33 - 45) kbar for an impact velocity of (660±20) m/s. McQueen et al [70] performed experiments on single crystal copper for the shock pressure in the range of (300 - 600) kbar and found that the spall strength of single crystal copper is in the range of (50 - 150) kbar. Razorenov et al [69] in their spall experiments on single crystal copper in the range of impact velocities (600 - 700) m/s found that the spall strength of single crystal copper is 53 kbar at 300 K temperature. The experimentally measured spall strength of single crystal copper is summarized

in Table 3.2.

Spall strength (kbar)	References
33.0-45.0	[6, 67, 68]
54.0	[69]
73.0	[66]
50.0-150.0	[70]

Table 3.2: Experimentally measured spall strength of single crystal copper

The difference between these experiments and simulations could be due to two reasons:

- Single crystals used in experiments have defects and impurities
- Strain rates in the experiments are different as compared to the simulations.

The important effect of pre-existing defects on fracture thresholds is examined later in this thesis.

- The value of the pressure sensitivity parameter for nucleation (P_1) is lower for single crystals, which means that the nucleation rate in single crystals is much more sensitive to pressure than that for polycrystalline material, i.e. void nucleation in single crystal copper takes place very rapidly once the tensile pressure exceeds the nucleation threshold. Now, there are no preferred sites for nucleation in a perfect crystal. Hence, if inter-atomic 'bonds' are stretched far enough to cause one bond to fail, the other bonds would also be on the verge of failure. Hence the low value of P_1 is intuitively correct.

- The material viscosity of single crystal is very low compared to polycrystalline material. This signifies that growth of the nucleated voids takes place very rapidly once the nucleation threshold is crossed.

- The nucleation threshold (P_{n0}) is very high compared to the growth threshold (P_{g0}) for single crystal copper, while thresholds for nucleation and growth for polycrystalline copper [5] are the same. For aluminum [5], the nucleation

threshold is lower than the growth threshold, while in case of mild steel [17] the nucleation threshold is 5 times higher than the growth threshold. Therefore, it is not necessary that the nucleation threshold should be equal to the growth threshold.

As far as P_1 and $\dot{N}_0$ are concerned, multiple combinations of these parameters could yield a similar level of match between NAG and MD results. Hence it will not be appropriate to read physical meaning into the variations in $\dot{N}_0$ and P_1.

A comparison of void volume fraction, V_{NAG}, obtained by NAG model using the above best-fit parameters (Table 3.1) and that by post-processor (Chapter 2.2.1), V_{PP}, is shown in Figure 3.9. It can be seen in Figure 3.9 that there is qualitative

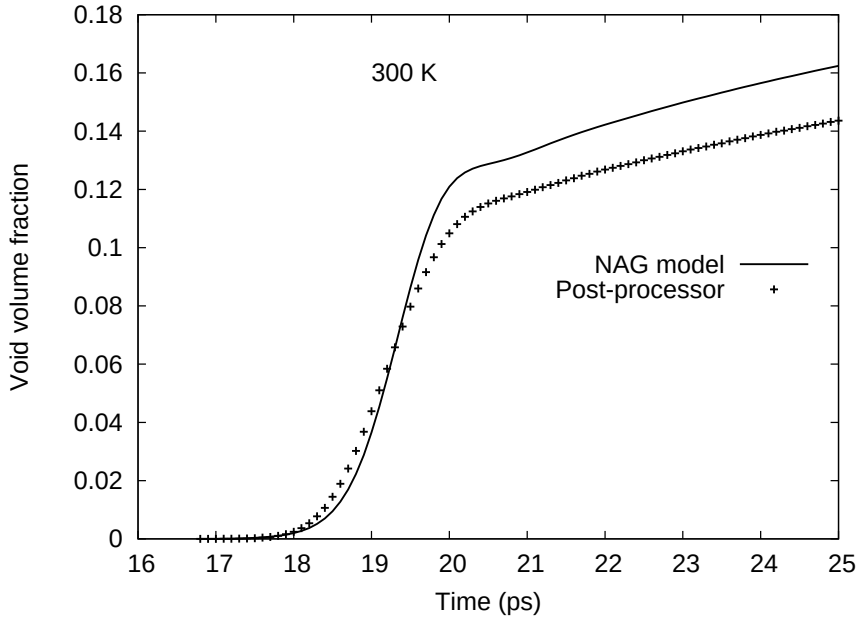

Figure 3.9: Comparison of void volume fraction obtained by NAG model and that obtained using the post-processor (Chapter 2.2.1) for single crystal copper expanded triaxially at 5×10^9/s strain rate with 300 K.

match of nucleating, exponentially growing and leveling off. This signifies that the NAG model is valid at atomistic scale for crystals at high strain rates. The relative error at each data point is shown in Figure 3.10. The root mean square value of relative error (Eqn. 3.10) is 19%.

To determine the uncertainties in the best-fit NAG parameters, we have performed some exercises by varying one parameter at a time, keeping the others the same at their optimal values. For example, the value of void nucleation threshold

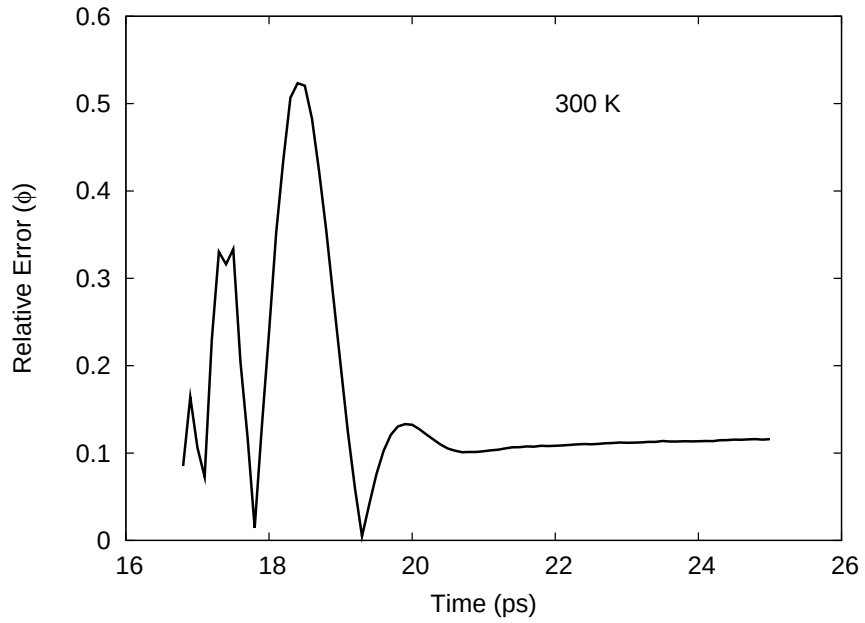

Figure 3.10: Relative error at each data point for single crystal copper triaxially deformed at 5×10^9/s strain rate.

(P_{n0}) is varied over a small range, keeping the other parameters (P_{g0}, P_1, η, $\dot{N}_0$) at their optimal values. This will lead to a sensitivity of each parameter for a given tolerance in the RMS error. The change in each parameter for 10 %, 20% and 50% increase in the RMS value of 0.19 is shown in Table 3.3.

It is seen in Table 3.3 that for each tolerance in the RMS value of 0.19, the change in the value of pressure sensitivity parameter (P_1) is very small compared to other parameters indicating that the NAG model for single crystal copper is very much sensitive to P_1. It is also seen that the change in the value of void growth threshold (P_{g0}) is quite large compared to others. This means that the NAG model for single crystal copper is not very much sensitive to void growth threshold.

3.7 Shock Wave Simulation

We have seen that the best-fit void nucleation threshold pressure for perfect single crystal copper is 160 kbar (Table 3.1), much higher than experimental data (Table 3.2). This is understandable, since "real" single crystals have many defects and impurities which tend to lower the threshold. It is necessary to check if, at least for perfect single crystals, the best-fit threshold applies under more complex strain

Change in NAG parameters	Increase in RMS value of 0.19		
	10 %	20%	50%
ΔP_{n0} (kbar)	0.016	0.024	0.042
ΔP_1 (kbar)	0.00038	0.00057	0.00102
ΔP_{g0}(kbar)	0.60	1.0	2.2
$\Delta\eta$ (bar-s)$\times 10^{-8}$	0.04	0.066	0.127
$\Delta\dot{N}_0$ (/(m^3-s))$\times 10^{18}$	0.56	0.82	1.28

Table 3.3: Change in NAG parameters for single crystal copper with increase in the RMS value of 0.19.

conditions, such as those that arise during impact-driven spall.

To validate the best-fit nucleation threshold, we have performed an MD simulation of high-velocity symmetric impact of copper using LAMMPS. Before starting the impact simulation, the simulations have been validated by reproducing the Shock Hugoniot for crystal copper [71].

3.7.1 Initial Set up

A cubic cell containing N = 1.08×10^6 atoms is created by replicating the $300\times30\times30$ FCC unit cells along the X, Y, and Z- axes. The embedded-atom method [39,40] with parameters obtained by Foiles et al [60] is used for our simulation. The equations of motion are integrated with a timestep of 0.5 fs using the velocity-Verlet algorithm. The periodic boundary conditions are used along Y- and Z- directions and free boundary conditions are used along X-direction. Thickness of the copper flyer is 361.5 Å (100 unit cells) and that of the target is 723 Å (200 unit cells). Impact is done along the X-direction with impact velocities of 950 m/s and 1100 m/s. The impact velocity of 1100 m/s is the minimum velocity at which spall of the material takes place. In this set up, the target is kept at rest and a velocity is given to the flyer so that it can transfer momentum to the target.

To analyse the shock-wave propagation, the system is divided into bins along the X-axis. The width of the bin used to analyse the shock wave is taken as 10.83 Å (3 unit cells).

3.7.2 Comparison of spall and no-spall cases

A comparison of spall and no-spall cases at two different impact velocities (950 m/s and 1100 m/s) is shown in Figure 3.11. It is seen in Figure 3.11 that for an impact

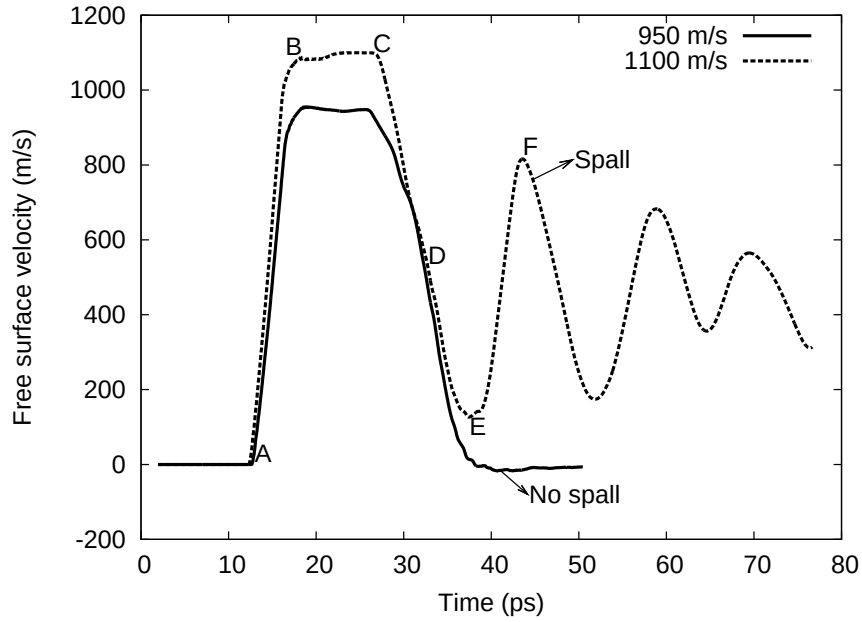

Figure 3.11: Free surface velocity of the target as a function time for a symmetric impact of copper at 1100 m/s.

velocity of 950 m/s, there is no pull-back in the free surface velocity of the target. Since pullback is considered the signature of spall [12], it is clear that no spallation occurs at 950 m/s. Spall occurs at an impact velocity of 1100 m/s, which can be seen by the pull back in the free surface velocity of the target.

3.7.3 Free surface velocity

The impact produces shocks traveling in opposite directions in the flyer and target. When the shocks reach the respective free boundaries, they reflect as rarefactions. Coalescence of the rarefactions within the target leads to a tensile pressure, causing spall [5]. The free surface velocity of the target as a function of time is shown in Figure 3.11. The point A in Figure 3.11 refers to the arrival of the shock wave at the free surface. It gets reflected from the free surface and propagates as a release wave into the target material. The reflection of the shock wave accelerates the free surface of the target to approximately twice of the particle velocity behind the shock

front [72] (point B in Figure 3.11). The CE region corresponds to the pull back in the free surface velocity. Point D refers to void nucleation due to the tension created by the coalescence of the release waves from flyer plate and target. In the ideal rear surface velocity [11], the point D corresponds to point where spall of the material takes place. The compressive wave is created as a result of the spall of the material which travels towards the free surface and accelerate it. This wave is also known as spall pulse (region EF in Figure 3.11). After that the shock and release waves are trapped between the spall plane and the free surface giving reverberations in the free surface. The period of oscillations in the free surface velocity can be used to calculate the thickness of the scab ejected from the target.

In the acoustic approximation, it is considered that the shock and rarefaction waves are weak and their velocities are considered to be equal to the sound velocity [11]. Within the acoustic approximation [11], the spall strength is given by

$$P_{sp} = -\frac{1}{2}\rho_0 c \Delta u_{fs} \tag{3.11}$$

where $\Delta u_{fs} = (u_C - u_E)$ is the pullback velocity, ρ is the initial density of the system, c is the sound velocity, u_C is the peak free surface velocity and u_E is the free surface velocity corresponding to first minimum of the velocity-time profile (Figure 3.11).

The strain rate using the same approximation [11] is given by

$$\dot{\epsilon} = \frac{1}{2c}\frac{\Delta u_{fs}}{\Delta t} \tag{3.12}$$

where Δt is the time interval corresponding to the region CE in the velocity-time profile (Figure 3.11).

The typical strain rate (Eqn. 3.12) in this simulation is $\sim O(10^9/s)$, comparable with the triaxial strain simulation (Section 3.5) and the spall strength (Eqn. 3.11) is found to be 170 kbar. This validates the best-fit NAG value obtained during uniform triaxial expansion.

3.7.4 Pressure-time profile

The pressure-time profile in the region where spall occurs is shown in Figure 3.12. It is seen that spall occurs as soon as the tensile pressure exceeds the material threshold (160 kbar). There is no significant nucleation of voids in the neighboring regions where the magnitude of the pressure stays below 160 kbar. Void nucleation was

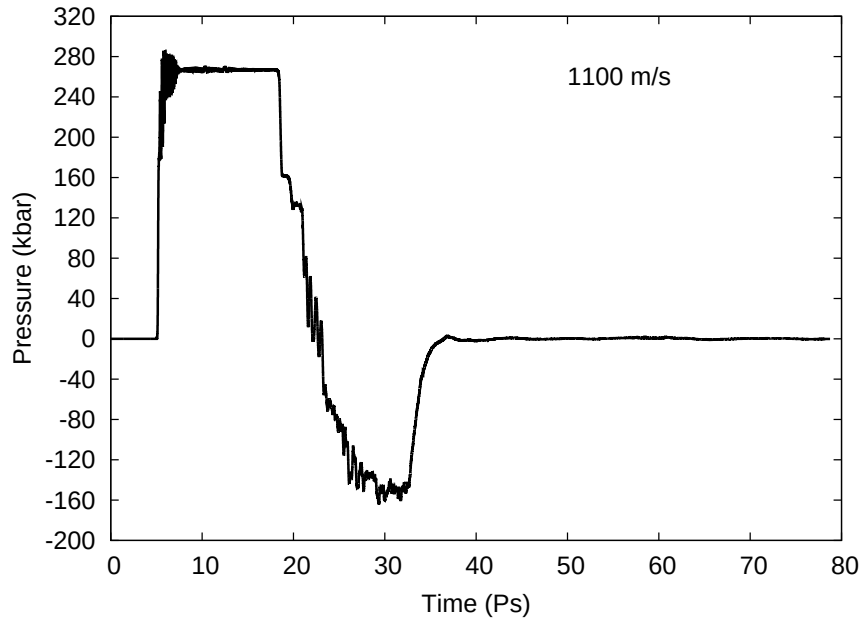

Figure 3.12: Pressure as a function of time in the region where spall occurs for the symmetric impact of copper at 1100 m/s impact velocity.

not observed at lower impact velocities, where the peak tensile pressure stays below 160 kbar. Thus the impact simulations validate the nucleation threshold obtained for single crystal copper under the triaxial deformation at 5×10^9/s strain rate (Section 3.5). Luo et al [73] performed MD simulation to investigate the spallation in single crystal copper at (10^{10} - 10^{11})/s strain rates and estimated the spall strength at 300 K as 159 kbar, which is closer to our results.

In Figure 3.12, it can be seen that the pressure flattens off around zero after 37 ps which is the indication of the spall of the material.

3.7.5 Centro-symmetry parameter (CSP)

To distinguish between the perfect lattice and different kinds of defects created, we have used centro-symmetry parameter (described in Chapter 2.2.4) filter described by Zhao et al [50]. The temporal evolution of fraction of atoms belonging to perfect lattice, dislocations, stacking faults and surface atoms in the region where spall occurs is shown in Figure 3.13. The tensile pressure created as a result of the coalescence of the release waves generates many defects in the system. When the tensile pressure exceeds the tensile strength of the material, the spall of the material

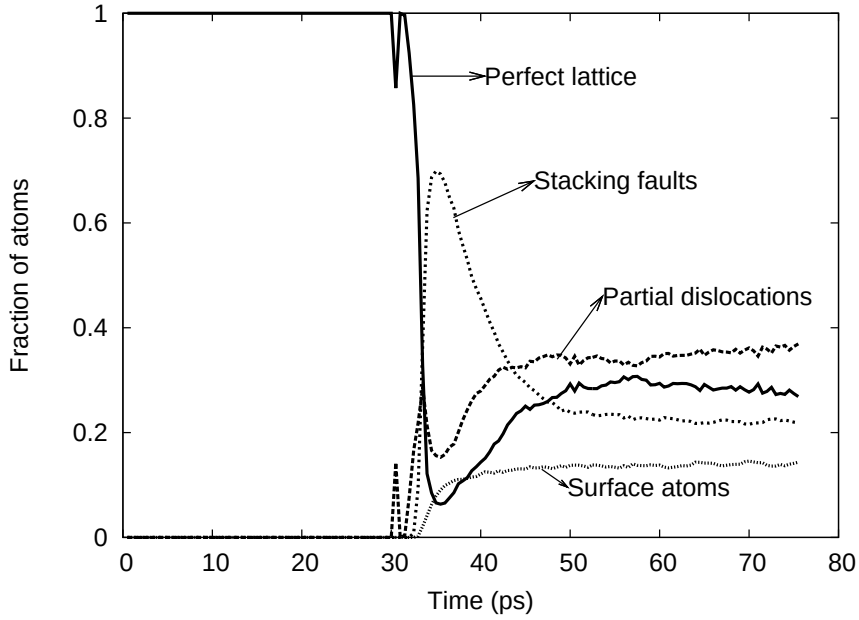

Figure 3.13: Fraction of atoms belonging to perfect lattice, partial dislocations, stacking faults and surface atoms as a function of time for the symmetric impact of copper at an impact velocity of 1100 m/s. Perfect lattice: CSP<0.5, Partial dislocations: 0.5<CSP<3.0, Stacking faults: 3.0<CSP<16.0, Surface atoms: CSP>16.0

takes place. It is seen in Figure 3.13 that the surface atoms appear when the tensile pressure in the system exceeds the threshold for void nucleation (160 kbar).

3.8 Analysis of characteristic modes

In real materials, there are various pre-existing void nucleation sites (impurities, dislocations etc). In perfect single crystals, there are no pre-existing void nucleation sites and when a perfect single crystal is expanded uniformly, one nucleation site should be as good as any other. Hence it is of interest to examine why nucleation first occurs at certain sites. As triaxial expansion takes places, the characteristic modes of the crystal are likely to be excited. *We speculate that the constructive interference of these modes at certain points leads to slightly higher inter-atomic gaps, leading to local bond breaking.*

A complete analysis of this process lies beyond the scope of this thesis. As a first step in this direction, however, we attempt to determine the characteristic modes of the crystal before and after nucleation.

We have performed singular value decomposition analysis (SVD) to determine the characteristic modes excited in the system, including their frequencies and associated distortions. A brief introduction to the singular value decomposition technique is given in Chapter 2.2.6.

Atomic position data for the SVD analysis is generated using a LAMMPS simulation of uniform triaxial expansion of a perfect crystal. Periodic boundary conditions are applied along all three directions. Since the attempt is only to get a 'feel' for the modes, rather than accurate quantitative analysis, we have chosen a very small domain, consisting of 360 atoms, corresponding to 10×3×3 unit cells. The system is first relaxed to 300 K and 0 bar pressure using an NPT simulation. A time step of 1 femto-second is used.

3.8.1 Excited characteristic modes before and after the void nucleation

Using the atomic coordinates output every 5 femto-seconds, we have performed the SVD analysis [74] to determine the characteristic modes excited in the system during deformation. For 360 atoms in the system, all 1080 modes are obtained using SVD. The variation of amplitude of modes excited in the system uniformly deformed at 5×10^9/s strain-rate before the void nucleation and after the first void nucleation is shown in Figure 3.14 (a) and Figure 3.14 (b), respectively.

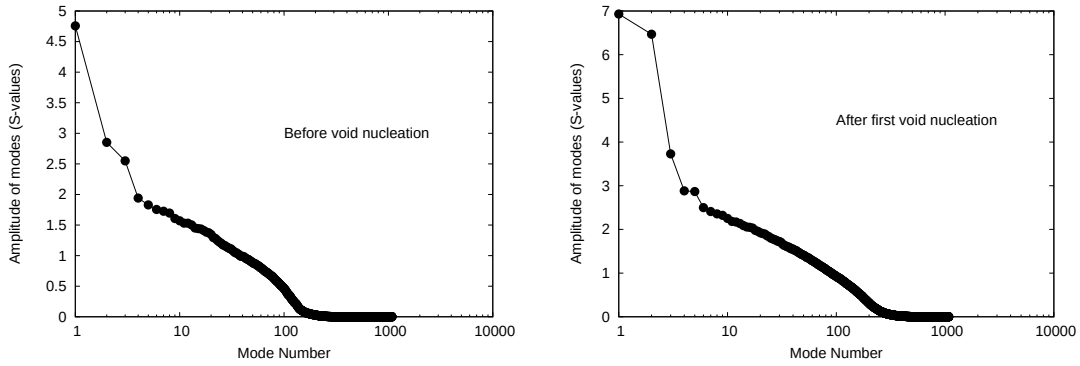

(a) (b)

Figure 3.14: Amplitude of modes (singular values 'S') as a function of mode number (a) before the nucleation of a void (b) after the nucleation of a first void.

3.8.2 Frequency Spectrum before and after the void nucleation

The comparison of frequency spectrum for first and fourth modes before and after the nucleation of first void is shown in Figure 3.15 (a) and Figure 3.15 (b), respectively. It is seen in Figure 3.15 (b) that a shift in the frequency occurs after the nucleation of a void. In addition to this, some new frequencies also appear after the first void nucleation. The creation of new frequencies and a shift in frequencies are the signature of the nucleation of a void.

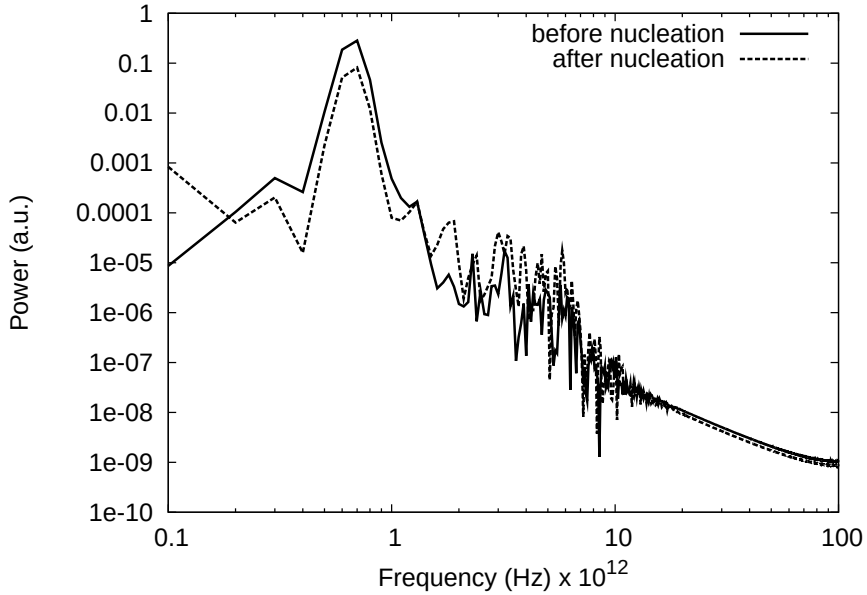

(a)

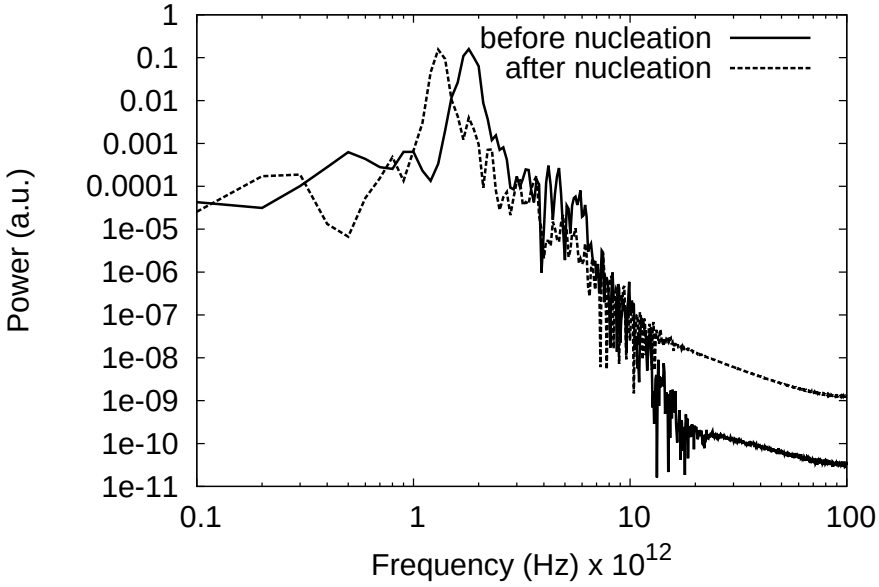

(b)

Figure 3.15: Frequency spectrum of (a) mode 1 (b) mode 4.

3.8.3 Temporal variation after the void nucleation

The temporal variation of the first strong mode after the first void nucleation is shown in Figure 3.16. A sudden growth in the amplitude of the mode (Figure 3.16) refers to the nucleation of a void in the system.

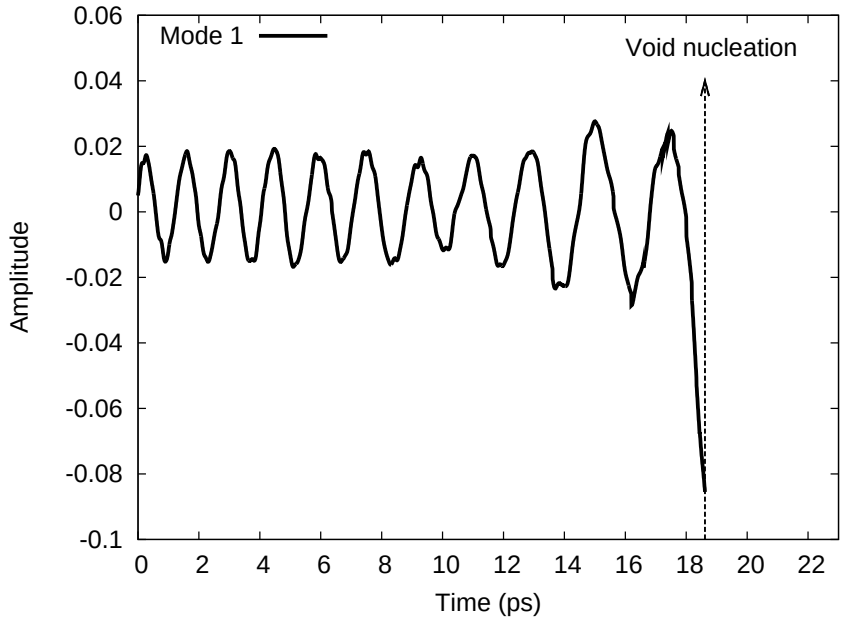

Figure 3.16: Temporal variation of the first mode after the first void nucleation.

3.8.4 Spatial variation before and after the void nucleation

The spatial variation of first four modes excited in the system before and after the first void nucleation is shown in Figure 3.17 (a) and Figure 3.17 (b), respectively.

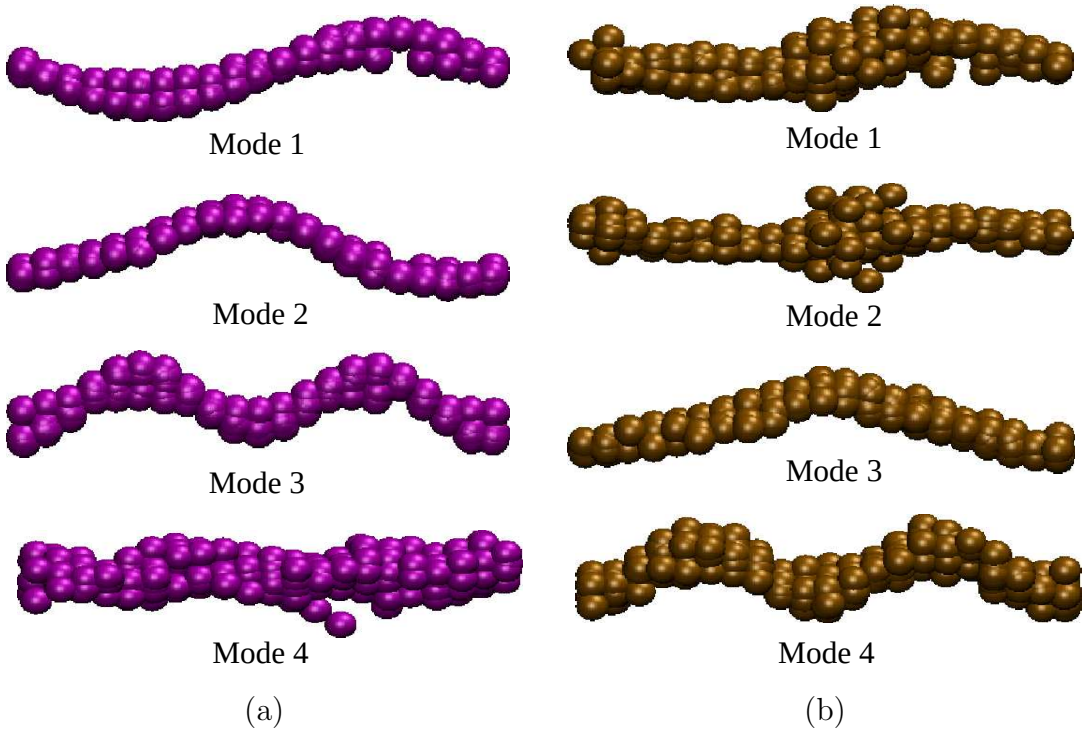

Figure 3.17: Spatial variation of modes (a) before the void nucleation (b) after the void nucleation.These snapshots are created using [3].

The first strong mode before and after the void nucleation corresponds to the wavelength of λ. Other weak modes correspond to the wavelengths of $3\lambda/2$ and $5\lambda/2$. Note that hierarchy of the modes has changed after the nucleation of the first void.

3.9 Limitations of this work

1. DFRACT model used for present study does not include the coalescence of the voids.

2. The best-fit NAG parameters presented here are for perfect crystal copper, while experimental single crystals contain various kinds of defects. Therefore, before comparing these results with the experimental data, a systematic study of effect of impurities and defects on the void nucleation threshold should be performed. *The effect of pre-existing defects is studied later in this thesis.*

3.10 Conclusions

Molecular dynamics simulations have been performed to study the nucleation and growth processes in perfect single crystal copper under high strain-rate deformation. From our simulations, we conclude the following:

1. The Nucleation and Growth (NAG) model, which was originally developed for polycrystalline materials at (10^4-10^6)/s strain rates, is also applicable at high strain rates (5×10^9/s) at atomistic scales for perfect single crystals.

2. The void nucleation threshold for perfect single crystal copper is much higher than that for polycrystalline copper, which is due to the absence of various kinds of defects in our simulated volume compared to real polycrystalline materials. The lower value of the viscosity parameter indicates that as soon as the nucleation threshold is crossed, the growth of the voids takes place very rapidly. The lower value of pressure sensitive parameter indicates that the void nucleation processes are very sensitive for perfect single crystal copper for pressures above the void nucleation threshold than that for polycrystalline copper.

3. The symmetric impact of copper plates at 1100 m/s validate the best-fit void nucleation threshold (160 kbar) obtained for perfect crystal copper deformed triaxially at 5×10^9/s strain rate.

4. A Singular Value Decomposition analysis for single crystal copper triaxially deformed at 5×10^9/s shows that after the nucleation of first void

   (a) there is a shift in the frequencies of modes

   (b) new frequencies are created

   (c) strong modes correspond to the wavelength of λ, $3\lambda/2$ and $5\lambda/2$.

   (d) the hierarchy of modes changes after the void nucleation

Chapter 4

Temperature sensitivity of void nucleation and growth parameters for single crystal copper: A molecular dynamics study

4.1 Introduction

In the previous chapter, we obtained NAG parameters at a temperature of 300 K. In real life, the material undergoing spall could be at any temperature. For example, during the passage of the shock in the material, there can be a significant rise in local temperature. Now, the nucleation, growth and coalescence of voids leads to spall of materials [5]. Therefore, by studying the temperature dependence of NAG parameters, the dependence of spall strength on temperature can be determined. The parameters of interest are:

- P_{n0}: The ambient pressure threshold for void nucleation.
- P_1: pressure sensitivity for nucleation.
- $\dot{N}_0$: nucleation rate at threshold.
- P_{g0}: threshold for void growth.
- η: material viscosity.

Spall experiments have been performed by many workers [69, 75–77] to investigate the effect of temperature on spall strength. Kanel et al [75], in their spall experiments on aluminum AD1 at different temperatures, showed that the spall strength decreases with increase in temperature. Zaretsky [77], in his planar impact experiments on cobalt with temperatures in the range of 300 K - 1400 K, found that the spall strength of cobalt decreases monotonically from 3.2 GPa at 300 K to 0.8 GPa at 1400 K. In experiments on aluminium single crystals with temperature varying from 20^0C to 648^0C, Kanel et al [76] reported that the spall strength was independent of temperature upto $\sim 630^o$C. They noticed a slight decrease in the spall strength as the temperature was further increased upto 648^0C. Razorenov et al [69], in their experiments with aluminum and copper single crystals, found that the spall strength of copper single crystals decreased from 5.4 GPa at room temperature to 4.8 GPa at 485^0C. These studies [75–77] show that the spall strength of polycrystalline materials decreases rapidly as the temperature of the samples approaches the melting temperature. On the other hand, the spall strength of single crystals remains high even fairly close to the melting point.

At atomistic scales, various workers [78–82] have performed MD simulations to study the effect of temperature on the failure of perfect crystalline materials.

In this chapter, we attempt to determine the dependence of NAG parameters on temperature, using MD simulations.

4.2 Nucleation and Growth parameters at different temperatures

4.2.1 Pressure-time profile at different temperatures

MD simulations are carried out for single crystal copper deformed triaxially at 5×10^9/s strain rate, and at temperatures of 300 K, 600 K, 800 K, 1000K and 1250 K. The highest temperature is close to the melting point of copper, i.e, 1358 K [83]. The internal pressure at different temperatures is shown in Figure 4.1. We see that as the temperature is increased, the turn-around value of pressure decreases. In all cases except 1250 K, we observe a single minimum (turn around) in the pressure-time profile. However, in the 1250 K case, we observe two minima in the pressure-time profile. It is seen that the mean stress in the system increases continuously upto a

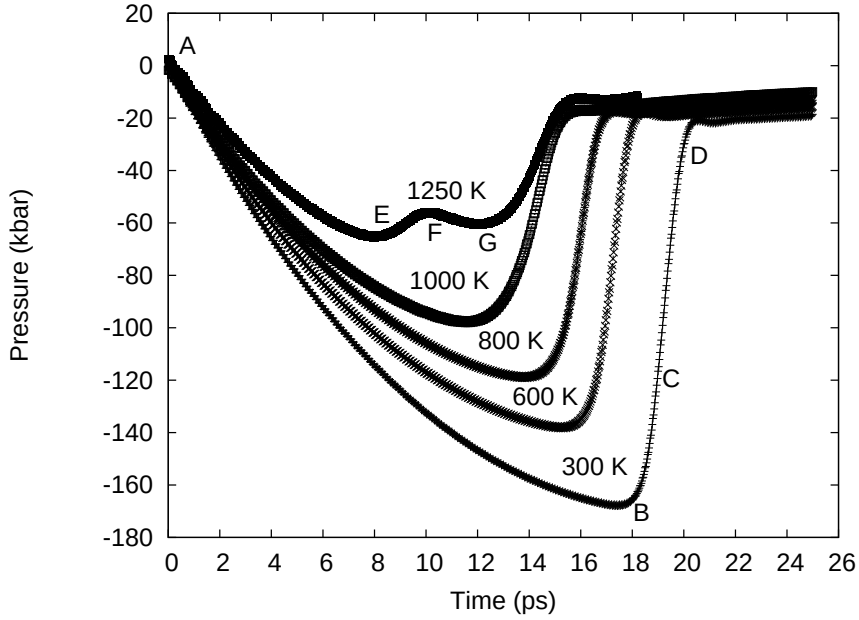

Figure 4.1: Temporal evolution of internal pressure for single crystal copper triaxially deformed at (5×10^9/s) strain rate, at different temperatures. The points A, B, C and D in the pressure-time profile for 300 K corresponds to the time points for which radial distribution function (RDF) is calculated, while for 1250 K the RDF calculations are performed at A, E, F and G time points.

time point. Triaxial expansion pulls the atoms away from their equilibrium positions, leading to an increase in the pressure of the system. The increased volume implies a drop in the density of the system. Further expansion leads to bond breaking and the nucleation of voids which are nothing but small disordered regions [13] nucleated due to the lattice instability, as discussed by Wang et al [21]. We note that more than a single void nucleates within the volume being simulated (Figure 4.2). This nucleation of voids causes a reduction of pressure due to relaxation of the built up stress. This turn-around in pressure is followed by a rapid reduction of pressure due to the exponential growth of voids. Finally, the rapid reduction in pressure stops and it begins to fluctuate around a small negative value corresponding to the pressure threshold for void growth (P_{g0}).

As the system is triaxially deformed with increasing temperatures, the turn-around of pressure takes place not only at a lower value of pressure, but also at earlier times. Therefore, the increase in temperature lowers the magnitude of the pressure threshold for void nucleation. It can also be seen that there is a single dip in the pressure-time profile for all temperatures except 1250 K, which has two

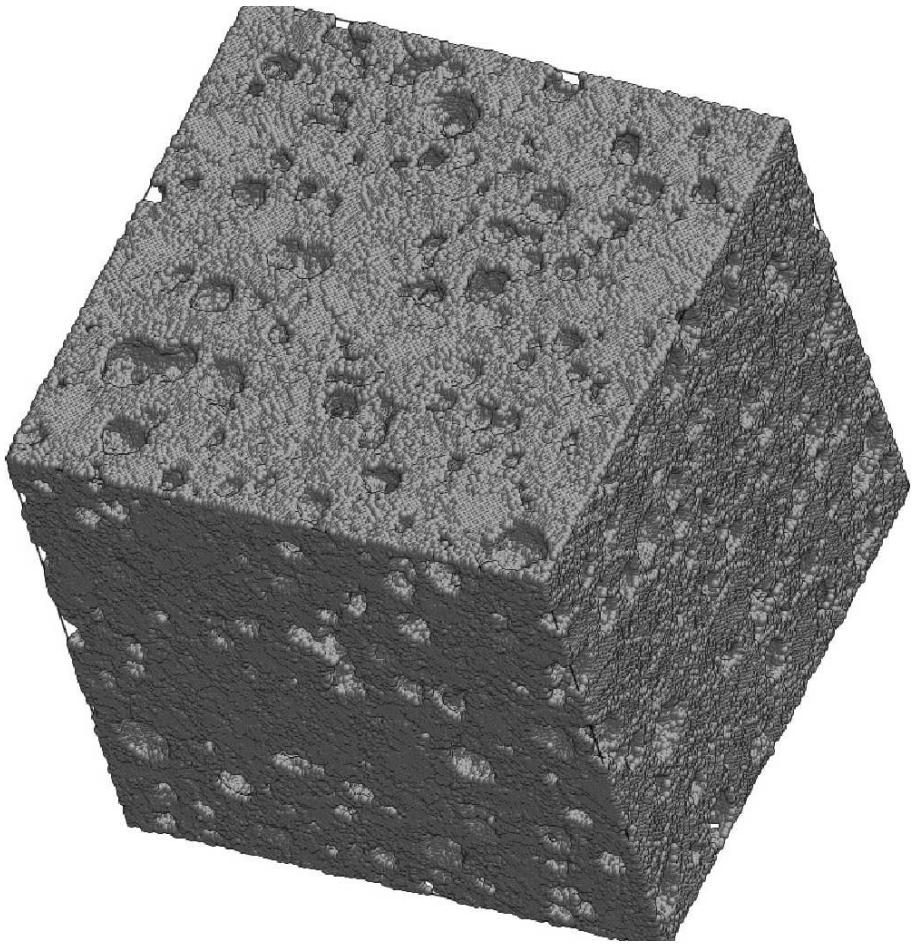

Figure 4.2: Nucleation of many voids in single crystal copper deformed triaxially at high strain rate (5×10^9/s) with 300 K. This snapshot is created using [4].

minima.

The void volume fraction at the above temperatures is plotted in Figure 4.3. Note that the void volume fraction becomes significant only after the time at which pressure turns around (Figure 4.1). The void volume fraction increases exponentially due to the growth of voids upto a time point and after then increases linearly. The onset of the linear region corresponds to the pressure threshold for void growth (P_{g0}). For the case of 1250 K, which has two minima in the pressure-time profile, the significant contribution to void volume fraction comes only after the second minimum in the pressure-time profile. The void volume fraction vs time graph can be divided into the following regions:

- The initial part of the curve is the region where the void volume generated by nucleation dominates over that generated by growth.

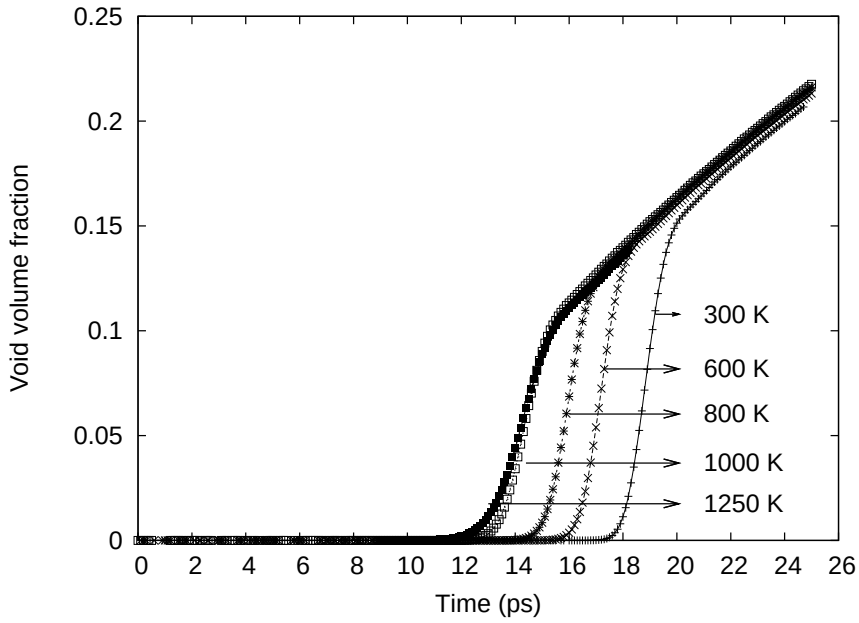

Figure 4.3: Void volume fraction for single crystal copper deformed triaxially at high strain rate (5×10^9/s) at different temperatures.

- The region where void volume grows exponentially with time. Here void volume generated by growth dominates over that by nucleation.
- Linear region, where the magnitude of tensile pressure in the system is no longer greater than that of the pressure threshold for void growth. The increase in void volume fraction is due to coalescence.

4.2.2 NAG parameters

The detailed procedure for getting best-fit NAG parameters is described in Chapter 3.6.3. The best-fit NAG parameters obtained for single crystal copper at different temperatures are presented in Table 4.1.

NAG parameters	Temperature (K)				
	300	600	800	1000	1250
P_{n0} (kbar)	-160.4	-124.0	-113.7	-80.0	-58.8
P_1 (kbar)	-0.167	-0.366	-0.119	-0.398	-0.156
$\dot{N}_0$ (m^{-3}/s)	7.1×10^{18}	3.1×10^{20}	3.1×10^{18}	1.0×10^{17}	4.6×10^{16}
P_{g0} (kbar)	-21.2	-18.5	-16.0	-12.2	-10.0
η (bar-s)	-3.4×10^{-8}	-2.8×10^{-8}	-2.5×10^{-8}	-2.2×10^{-8}	-2.3×10^{-8}
Average squared relative error (Σ)	0.19	0.14	0.16	0.24	0.11

Table 4.1: Comparison of best-fit NAG parameters obtained for single crystal copper (N = 4×10^6 atoms) with the experimental values for polycrystalline copper (P_{n0} = -5.0 kbar, P_1 = -2.0 kbar, $\dot{N}_0$ = 2.8×10^{18} m^{-3}/s, P_{g0} = -5.0 kbar, η = -7.5×10^{-5} bar-s and R_n = 1.0×10^{-6} m) [5]. The value of nucleation size parameter (R_n) in our simulation is 3.64 Å, which is the length dimension of the small cubic cell.

From Table 4.1, it can be seen that there is a monotonic decrease in the values of the void nucleation threshold (P_{n0}) and void growth threshold (P_{g0}) with increase in temperature. The enhanced atomic motions and increased average inter-atomic separation at higher temperature are responsible for decrease in these thresholds.

Figure 4.4 compares the void volume fraction obtained by two methods. The first, V_{NAG}, is computed using the above NAG parameters along with the pressure-time history yielded by MD simulations. The second, V_{PP}, is generated using post-processing of atomic coordinates yielded by the MD simulation, as described in Chapter 2.2.1. Results are shown for temperatures of 600, 800, 1000 and 1250 K.

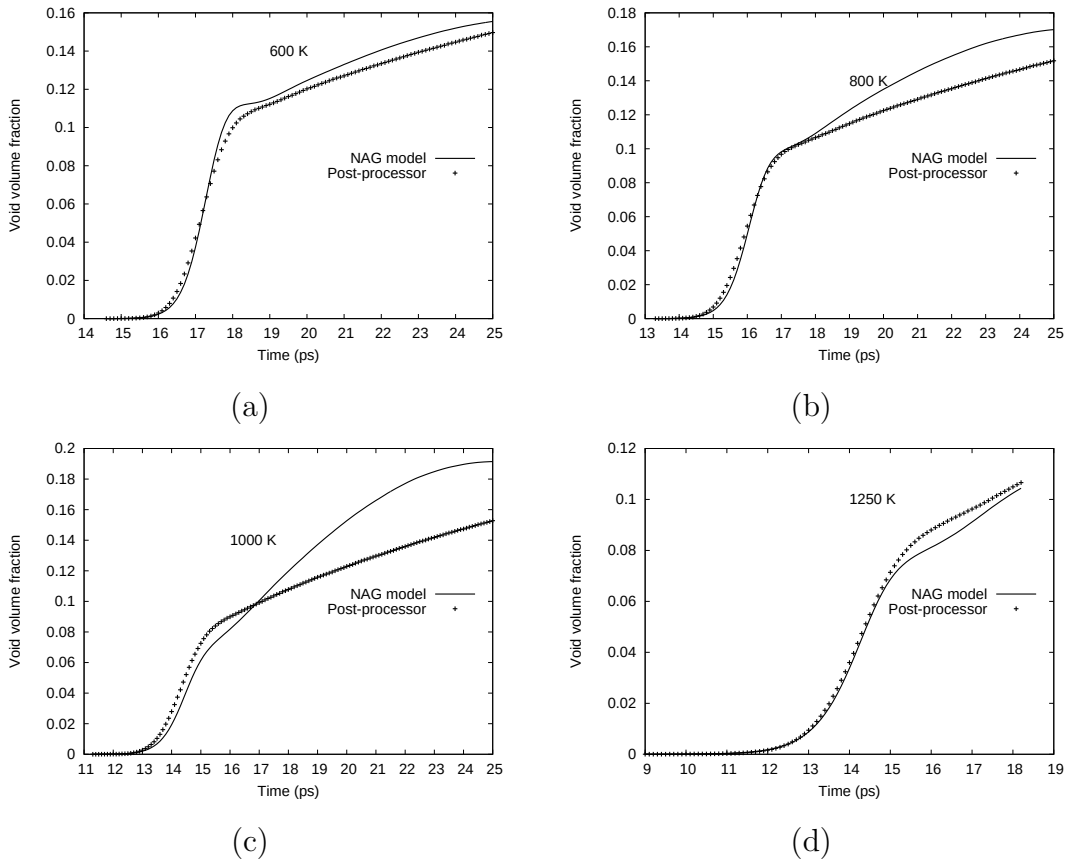

Figure 4.4: Comparison of void volume fraction obtained by NAG model and that obtained by post-processor for a single crystal copper deformed triaxially at high (5×10^9/s) strain rate, at temperatures of (*a*) 600 K, (*b*) 800 K, (*c*) 1000 K (*d*) 1250 K.

A comparison of the relative error between V_{NAG} and V_{PP} at different temperatures is shown in Figure 4.5.

4.3 Analysis of double dip in pressure-time profile at 1250 K

The internal pressure as a function of time for 300 K and 1250 K is shown in Figure 4.1. This behaviour, which seems to appear only near the melting point, is analyzed below using several techniques, viz., by calculating the Radial Distribution Function (RDF), Structure Factor, Centro-Symmetry Parameter (CSP) and Common Neighbor Analysis (CNA). For comparison, the same calculations have been done for 300 K.

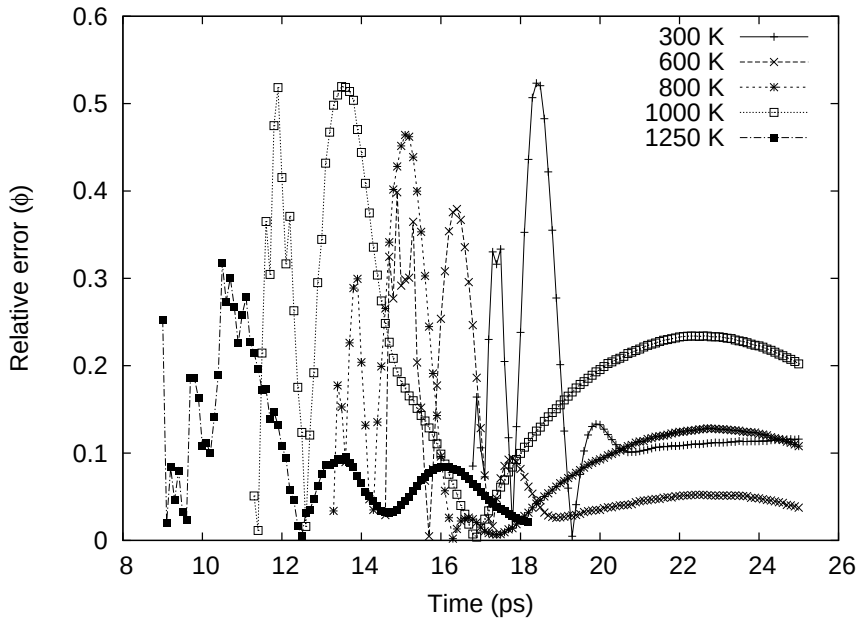

Figure 4.5: Comparison of relative error between V_{NAG} and V_{PP} for single crystal copper deformed at 5×10^9/s, at different temperatures.

4.3.1 Radial distribution function (RDF)

We have taken a small volume ($\sim$ 76 Å^3) from the centre of the simulation domain to compute the radial distribution function. This is because computation for all atoms in the domain becomes computationally demanding. At 300 K, the RDF has been calculated for A (0 ps), B (18 ps), C (19 ps) and D (20 ps) time points in the pressure-time profile (Figure 4.1) and shown in Figure 4.6. The RDF at 0 ps shows long-range order. After 18 ps, the RDF shows only short-range order. This short-range order is the result of stacking faults and the creation and growth of the voids due to which the system becomes disordered.

At 1250 K, the RDF is calculated for A (0 ps), E (8 ps), F (10 ps) and G (12 ps) time points in the pressure-time profile (Figure 4.1) and is shown in Figure 4.7. Note that 8 ps, 10 ps and 12 ps are the time points which cover the double-dip in the pressure-time profile (Figure 4.1).

At 0 ps, the RDF shows long-range order. However, this long-range order disappears after 8 ps, which also corresponds to the first minimum in the pressure-time profile (Figure 4.1). If we see the void volume fraction in Figure 4.3, it becomes significant only from 12 ps onwards. This means that the first minimum in the

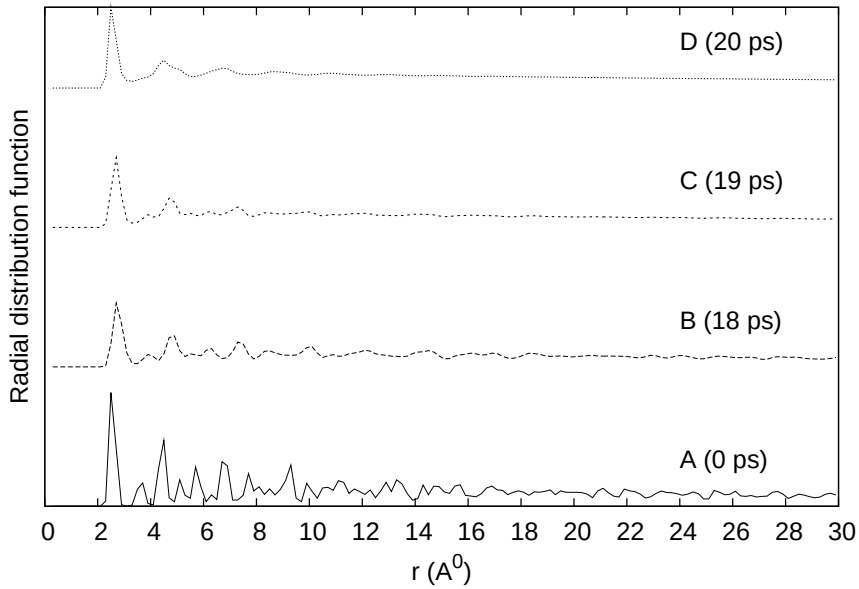

Figure 4.6: Radial distribution function as a function of distance at different time points. The plots for 18 ps, 19 ps, and 20 ps are shifted along the ordinate for easy comparison. Points A, B, C and D correspond to the time points in Figure 4.1. T = 300 K

pressure-time profile (Figure 4.1) corresponds to the loss of long range order, while the second minimum results from the nucleation and incipient growth of voids.

4.3.2 Structure factor

The calculation of structure factor will provide not only another check for the existence of crystalline order, but also indicates the kind of crystal structure, e.g. FCC/BCC/HCP. The structure factor for FCC, BCC and HCP is calculated for 300 and 1250 K and is shown in Figure 4.8.

At 300 K, the structure factor for FCC rapidly drops after 18 ps, as shown in Figure 4.8(a). This indicates that upto 18 ps, the system maintains FCC structure and after that it becomes disordered. This is due to the nucleation and incipient growth of voids. At 1250 K, the structure factor for FCC starts decreasing after 8 ps and vanishes after 11 ps (Figure 4.8 (d)). This means that the first minimum in the pressure-time profile corresponds to the order-to-disorder transition. However, this does not correspond to the nucleation and incipient growth of voids as we have mentioned in RDF analysis in Section 4.3.1 and as observed in Figure 4.3. In Figures 4.8 (b), 4.8 (c), 4.8 (e), and 4.8 (f), very small values of the structure

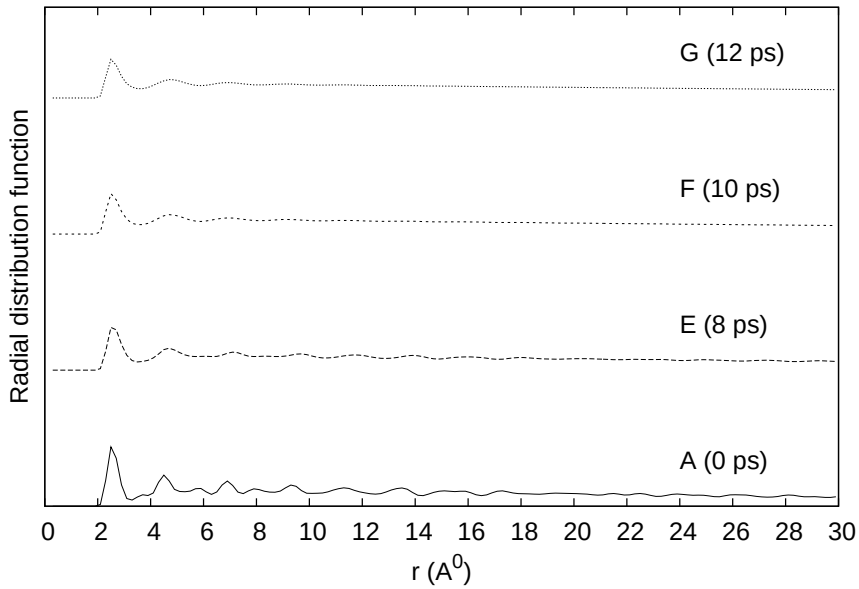

Figure 4.7: RDF as a function of distance at different time points. The plots for 8 ps, 10 ps, and 12 ps are shifted along the ordinate for easy comparison. Points A, E, F and G correspond to the time points in Figure 4.1. T = 1250 K.

factor signify that the loss of FCC structure in both cases does not correspond to the creation of BCC and HCP structures.

4.3.3 Centro-symmetry parameter (CSP)

To study the defects created in our system due to triaxial deformation at 5×10^9/s strain rate, we have calculated the centro-symmetry parameter for the cases of 300 and 1250 K. A brief introduction of centro-symmetry parameter is given in Chapter 2.2.4.

Zhao [50] has specified limits on CSP to distinguish between different kinds of defects:

- Perfect lattice: CSP < 0.5
- Partial dislocations: $0.5 <$ CSP < 3.0
- Stacking faults: $3.0 <$ CSP < 16.0
- Surface atoms: CSP > 16.0

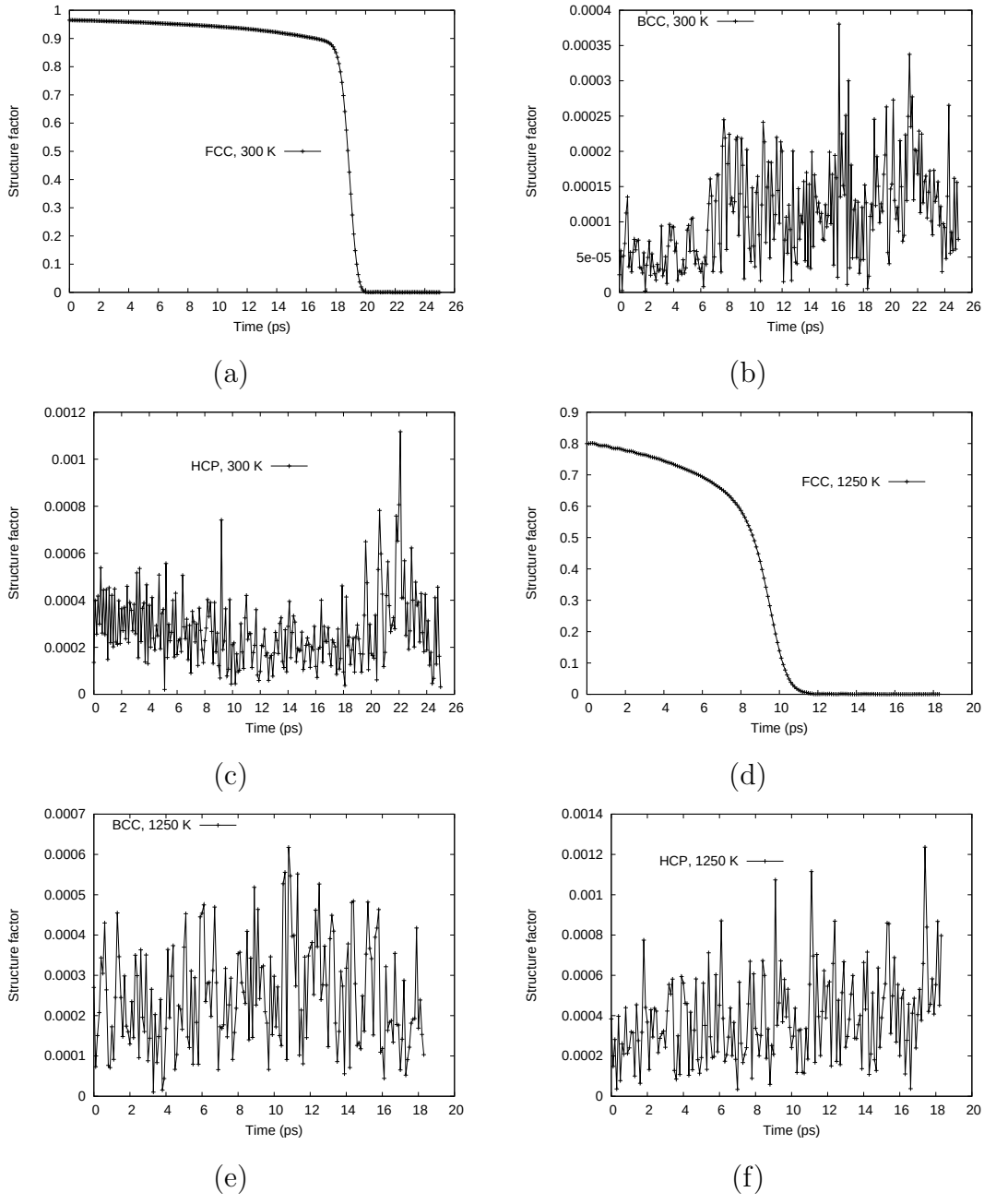

Figure 4.8: Structure factor as a function of time for single crystal copper. For 300 K: (*a*) FCC, (*b*) BCC, (*c*) HCP and for 1250 K: (*d*) FCC, (*e*) BCC, (*f*) HCP.

The CSP filter for single crystal copper given by Zhao et al [50] is for 0 K temperature. This does not take into account the effect of temperature. Therefore, for non-zero temperatures, it is necessary to determine corrected values, since particle displacements from their mean positions change with temperature. Firstly, we have verified using common neighbor analysis (Section 4.3.4) and structure factor (Section 4.3.2) calculations at 300 K that the domain is a perfect crystal with an FCC structure. For this case, we have determined the threshold value of CSP for the perfect lattice at 300 K, after performing NPT MD for single-crystal Cu at 1 atm pressure. This is found to be 3.4 $Å^2$. With this new threshold value for defining a perfect lattice, and using CSP limits 3.4 < CSP <16.0 for partial dislocations and stacking faults and CSP > 16.0 for surface atoms, the centro-symmetry parameter is computed for 300 and 1250 K and is shown in Figure 4.9 and Figure 4.10.

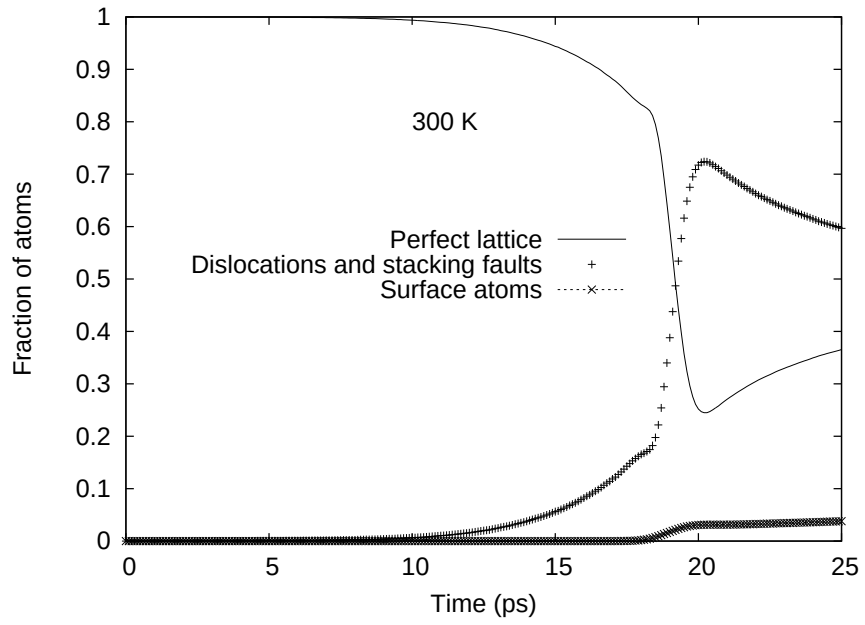

Figure 4.9: Centro-symmetry parameter as a function of time for a single crystal copper triaxially deformed at high strain rate (5×10^9/s) with 300 K. Perfect lattice: CSP < 3.4, partial dislocations and stacking faults: 3.4 < CSP < 16.0, surface atoms: CSP > 16.0

If we compare the centro-symmetry parameter for both cases, it can be seen that

- At t = 0 ps, the lattice for 300 K is free from any defect, while at 1250 K, partial dislocations and stacking faults are present at t = 0 ps. The reason for the computed presence of defects is that CSP has limitations due to thermal vibrations.

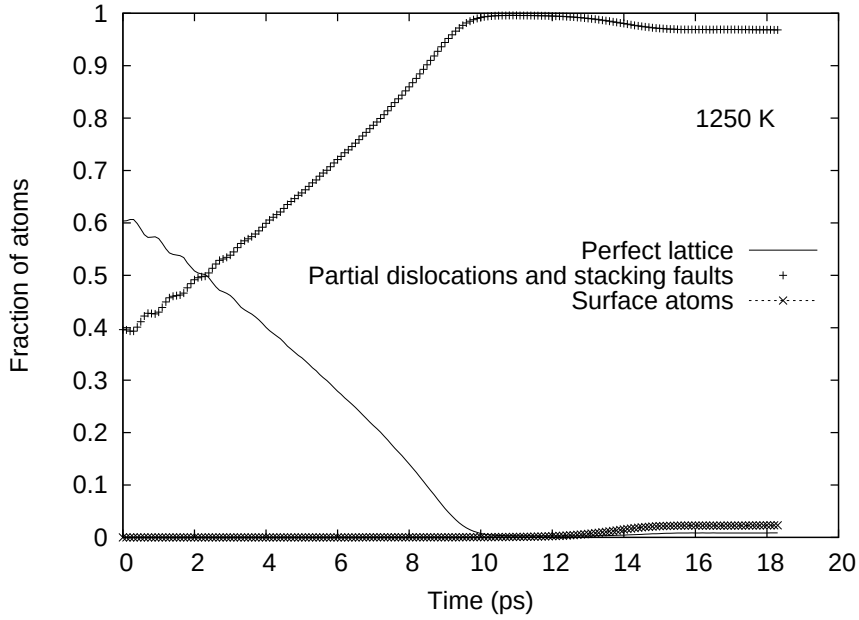

Figure 4.10: Centro-symmetry parameter as a function of time for a single crystal copper triaxially deformed at high strain rate (5×10^9/s) with 1250 K. Perfect lattice: CSP < 3.4, partial dislocations and stacking faults: $3.4 <$ CSP < 16.0, surface atoms: CSP > 16.0

- Stacking faults and dislocations for the 300 K case come into the picture significantly after some time point ($\sim$10 ps) and suddenly increase after 18 ps, which is the time at which pressure turns around (Figure 4.1). Note that there are no defects at the start of the simulation for this case. For the 1250 K case, stacking faults and dislocations are already present in the system at this temperature; hence, as triaxial expansion is applied, the defect density increases linearly and flattens off after 10 ps, which corresponds to the time at which maximum occurs between two minima in the pressure-time profile (Figure 4.1).

- Surface atoms for 300 K are observed after 18 ps. This is the time at which pressure turns around in the pressure-time profile (Figure 4.1). Our post-processor (Chapter 2.2.1) also indicates that the void volume fraction becomes significant after this time point (Figure 4.3). For 1250 K, surface atoms appear after 12 ps. This indicates that the second minimum in Figure 4.1 corresponds to the nucleation and incipient growth of voids.

After this analysis, we can conclude that the number and type of different defects

created are affected by temperature. The presence of surface atoms for 1250 K after 12 ps (second minimum in Figure 4.1) indicates that nucleation and incipient growth of voids take place around this time but not corresponding to the first minimum in the pressure-time profile (Figure 4.1).

Note that the deviations of atom positions from the mean (Eqn. 2.22) can change the CSP limits. At high temperatures, these deviations increase and the ranges change. For example, the maximum CSP for perfect crystal at 1250 K is 14.9 $Å^2$ from our simulations, which makes it within the range of partial dislocations. However, structure factor calculations show that lattice is FCC at t = 0 at 1250 K. Therefore, we conclude that CSP is not a good indicator for differentiating perfect lattice and partial dislocations at high temperatures.

4.3.4 Common Neighbor Analysis (CNA)

During the triaxial deformation of single crystal copper at high strain rate, numerous particle configurations are created that have different structural characteristics. In order to identify these structures, Common Neighbor Analysis (CNA) [2,51] is very useful. A brief introduction to the CNA method is given in Chapter 2.2.5.

We have computed the CNA pattern for each atom in the system for both 300 and 1250 K. The time evolution of fraction of atoms belonging to each crystal structure is shown in Figure 4.11 and Figure 4.12.

The CNA method shows that

- Loss of FCC structure at 1250 K does not result in the formation of BCC, HCP and Icosahedral structures, but results into an unknown structure (possibly amorphous). This method also supports the idea that FCC structure is lost at a time corresponding to the first minimum in the pressure-time profile (Figure 4.1).

- For 300 K, the system is a perfect FCC crystal corresponding to t = 0 ps, while for 1250 K only about 24% atoms belong to FCC crystal structure. It must be remembered that CNA analysis has limitations due to thermal vibrations, which become large at higher temperatures.

- For 300 K, most of the atoms belong to an unknown structure corresponding to t = 19 ps, while for 1250 K, all the atoms are part of unknown structure after t = 10 ps.

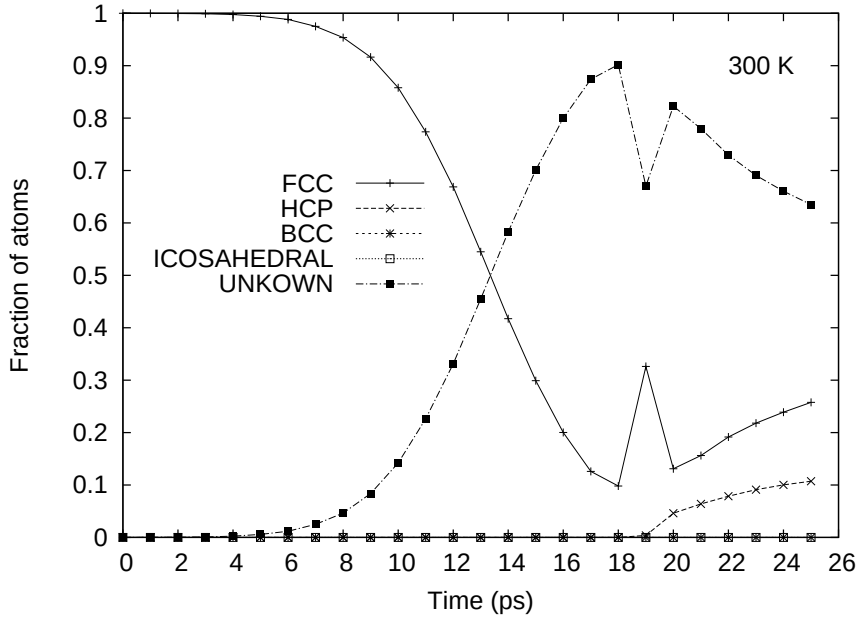

Figure 4.11: Fraction of atoms as a function of time. Common Neighbor Analysis has been done to identify the local crystal structure around an atom during triaxial deformation of single crystal copper at 5×10^9/s strain rate with 300 K. FCC (CNA = 1), HCP (CNA = 2), BCC (CNA = 3), Icosahedral (CNA = 4), Unknown (CNA = 5)

Thus, the analysis by CNA and CSP methods shows that for 1250 K, 100 % atoms belong to stacking faults at t = 10 ps, based on CSP analysis. Furthermore, CNA analysis reveals that they correspond to an unknown structure.

We have calculated structure factor, radial distribution function, centro-symmetry parameter and common neighbor analysis for single crystal copper at 300 K and 1250 K. All of these calculations show that, as expected, the system under study is a perfect FCC crystal at 300 K at t = 0 ps. For 1250 K, the structure factor calculation shows that it is FCC at t = 0 but CNA analysis does not show perfect FCC at this time and CSP analysis shows the presence of defects. The reason for this is that both CSP and CNA analysis have limitations due to atomic vibrations, and hence indicate defects at t = 0 for 1250 K.

4.3.5 Potential Energy of the system

The potential energy of the system as a function of time for 300 and 1250 K is shown in Figure 4.13 and Figure 4.14, respectively.

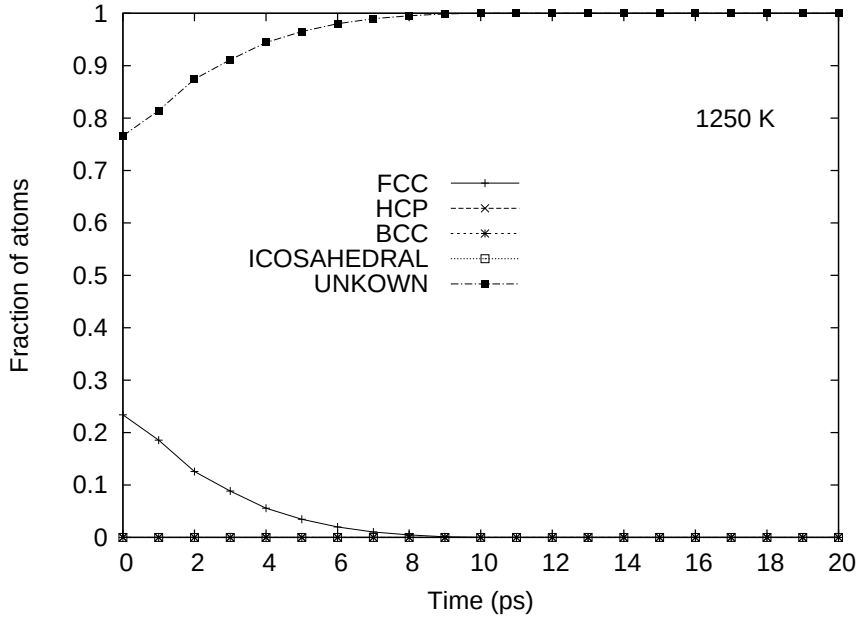

Figure 4.12: Fraction of atoms as a function of time. Common Neighbor Analysis has been done to identify the local crystal structure around an atom during triaxial deformation of single crystal cooper at 5×10^9/s strain rate with 1250 K. FCC (CNA = 1), HCP (CNA = 2), BCC (CNA = 3), Icosahedral (CNA = 4), Unknown (CNA = 5)

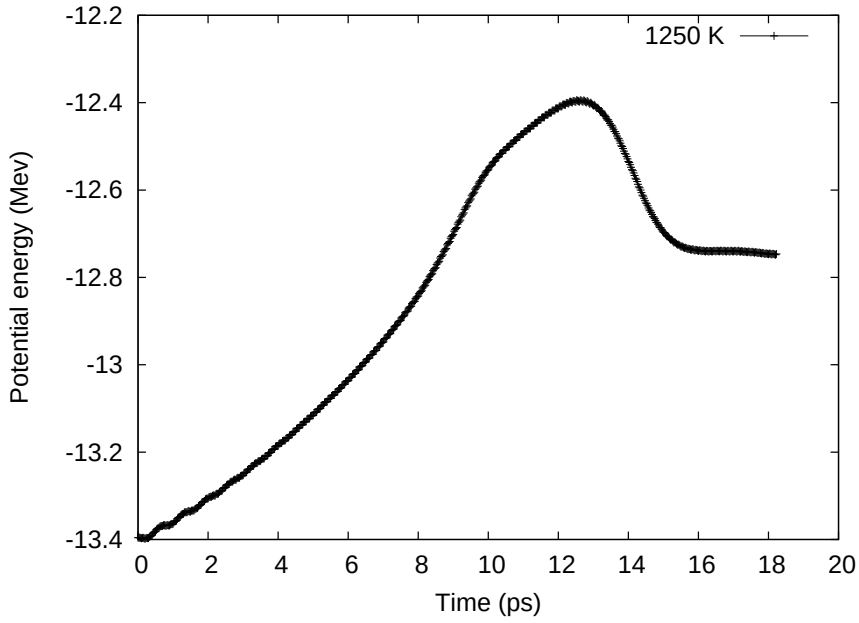

Figure 4.14: Potential energy of the system as a function of time for T = 1250 K. N = 4×10^6 atoms.

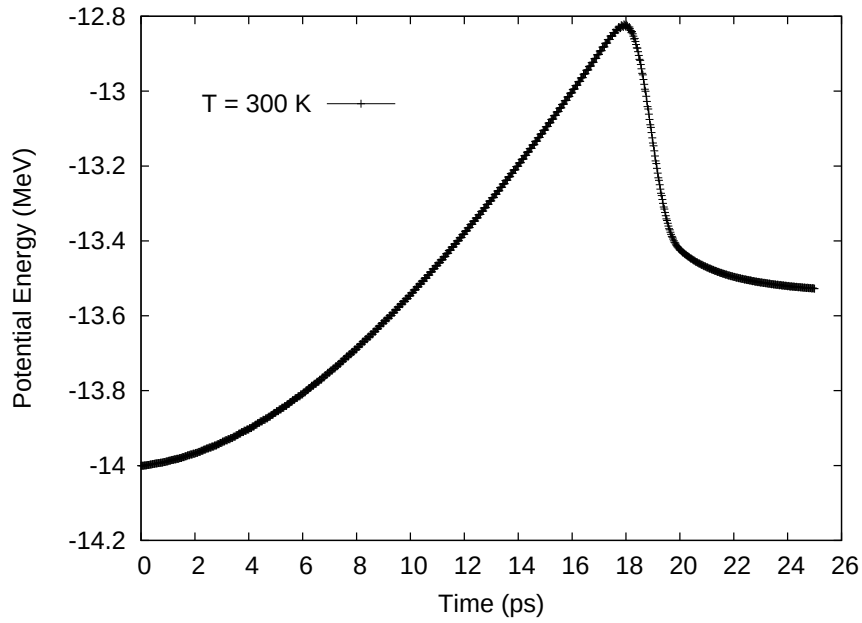

Figure 4.13: Potential energy of the system as a function of time for T = 300 K. N = 4×10^6 atoms.

At 300 K, it can be seen that the potential energy of the system increases (negative value decreases) as the density decreases due to expansion of the system. The potential energy peaks at 18 ps and after that drops suddenly, which is indicative of the creation and enhancement of voids. The effective two-atom interaction becomes stronger and the bond length shortens once the voids are nucleated, which results in rapid drop in potential energy. At 1250 K, the potential energy of the system also increases with time as mentioned above, but peaks only after 12 ps, not corresponding to the first minimum in Figure 4.1. This also indicates that nucleation of voids does not take place corresponding to the first minimum in the pressure-time profile.

4.4 Conclusions

We have studied the effect of temperature on the nucleation and growth parameters for single crystal copper deformed at 5×10^9/s. Best-fit NAG parameters have been obtained at different temperatures. We find a systematic reduction in the magnitude of nucleation and growth thresholds with rise in temperature.

As the melting point is approached, we observe a curious double-dip in the

pressure-time profile. Analysis of this double-dip by structure factor, RDF, CSP and CNA shows that the first minimum corresponds to the loss of the long-range order due to the creation of stacking faults and an unknown structure and the system no longer has a FCC structure. There is no nucleation of voids at this juncture. The second minimum corresponds to the nucleation and incipient growth of voids.

In this chapter, we have shown:

1. The effect of temperature on the nucleation and growth parameters of the DFRACT model for crystal copper.

2. Analysis of the structural changes of the crystal subjected to triaxial deformation at high strain rate at different temperatures.

Chapter 5

Effect of material damage on the spallation threshold of single crystal copper: A molecular dynamics study

5.1 Introduction

The phenomenon of spallation takes place through the nucleation, growth and coalescence of voids [5]. The high velocity impact of a flyer with a static target produces compressive stress waves at the point of impact which travel toward the free ends of the flyer and target. Upon reaching the free surfaces, these waves reflect as release waves and interact at some location inside the target. The interaction of release waves creates a state of extreme tension. If the tension created exceeds the spall strength of the material, nucleation, growth and coalescence of the voids take place leading to spall of the material.

Various workers have studied the phenomenon of spallation both experimentally and theoretically. The most widely used experimental methods for spallation in materials are plate impact [12, 84–86] and high power laser pulses [10, 11, 87–90]. Plate impact experiments [12,84–86] can give strain rates of (10^5-10^6)/s. Strain rates exceeding 10^7/s can be achieved by shock loading of nanosecond laser pulses [10, 87, 88]. Shock loading by femto-second laser pulses can give ultra-high strain rates (exceeding 10^8/s) [11, 89, 90]. A maximum strain rate of 10^{10}/s using high power

laser pulses has been reported in the literature [18].

Many theoretical models have been developed to describe spall fracture [5, 58, 91, 92]. These models deal with the nucleation and growth of voids and calculate the void volume in the spall region to quantify the damage level.

Many workers have performed molecular dynamics (MD) simulations to study spallation in metals. Bringa et al [71] simulated planar shocks in single crystal copper using molecular dynamics and found the Hugoniot for single crystal copper along various crystal directions. Srinivasan et al [93] performed MD simulation of spallation in single crystal nickel and found that interaction of release waves reflected from flyer and target creates crystals with different orientation and their boundaries become nucleation sites for void nucleation. Dremov et al [94] performed MD simulations to study spallation in single nanocrystals and polynanocrystals. In their study of single nanocrystals, they found that there is a strong dependence of micro-structures of the spall plane on the direction of shock loading relative to the lattice orientation. They also found that in poly-nanocrystals, void nucleation occurs along the grain boundaries, whereas in nanocrystals nucleation of voids occur at the stacking fault intersections. In the study of spallation in single crystal copper by Luo et al [73], the anisotropy in spall strength is found to be more for weak shocks and is decreased for strong shocks.

In this chapter, we report on simulations of high velocity impact of copper plates at impact velocities of 1100 m/s and 1000 m/s.

5.2 Computational Method

High velocity impact of copper plates has been simulated using the molecular dynamics code LAMMPS (Large-Scale Atomic/Molecular Massively Parallel Simulator) [59]. A simulation domain containing 1.08×10^6 atoms has been created by replicating $300 \times 30 \times 30$ unit cells along the x-, y- and z- directions, respectively. The cross-sectional area and the crystallographic orientation are the same for the flyer as well as target plates. The thickness of the target plate (361.5 Å$\sim$100 unit cells) is taken as two times that of the flyer plate (723 Å$\sim$200 unit cells). The direction (x-direction) of shock loading corresponds to the <100> crystal direction, and the transverse directions (y and z), are along <010> and <001>, respectively. In this set up, the target plate is kept at rest and an initial velocity is given to the

flyer plate. In the first setup, the flyer plate starts out in contact with the target plate.

We have used embedded atom method (EAM) [39, 40] potential parameters generated by Foiles et al [60]. Periodic boundary conditions are applied along the y- and z- directions and free boundary conditions are applied along the direction of impact (x-direction). Energy minimization followed by NVE simulations have been performed for 100 pico-second (ps) for the impact at 1100 m/s and 300 ps for impact at 1000 m/s. A shorter run (100 ps) is performed for impact at 1100 m/s since spall occurs at around 50 ps, whereas no spall occurs in the 1000 m/s case. In the 1000 m/s case, the shock reverberates through the system, creating defects; hence a longer run is required to study nucleation and growth of voids. The equations of motion are integrated with a time step of 0.5 femto-second using the velocity-Verlet algorithm.

In order to quantitatively analyse shock wave propagation through the system, the whole simulation domain at a given time is divided into bins along the direction of impact (x-direction) and pressure and centro-symmetry parameter are computed in each bin. The velocities of atoms in the last bin of the target is output as the free-surface velocity. The initial width of each bin is 10.83 Å (3 unit cells).

5.3 Impact at 1100 m/s

5.3.1 Free surface velocity

To understand the physical process of spallation, the wave propagation in the target is shown in Figure 5.1 and the corresponding free surface velocity of the copper target as a function of time is shown in Figure 5.2. The impact produces compressive stress waves that move toward the respective free surfaces of the target and flyer. When they reach the free surface of the target, they reflect as release waves. This process accelerates the free surface of the target by twice of the particle velocity [1]. The arrival of the shock at the free surface of the target is shown in Figure 5.1 (a). In Figure 5.1 (a), the shock reaches the free surface of the target at time 14 ps. This time point corresponds to point A in Figure 5.2. The interaction of the release waves reflected from the free surfaces of the flyer and target is shown in Figure 5.1 (b). It is seen that at time 20.5 ps, the interaction of the release waves takes place.

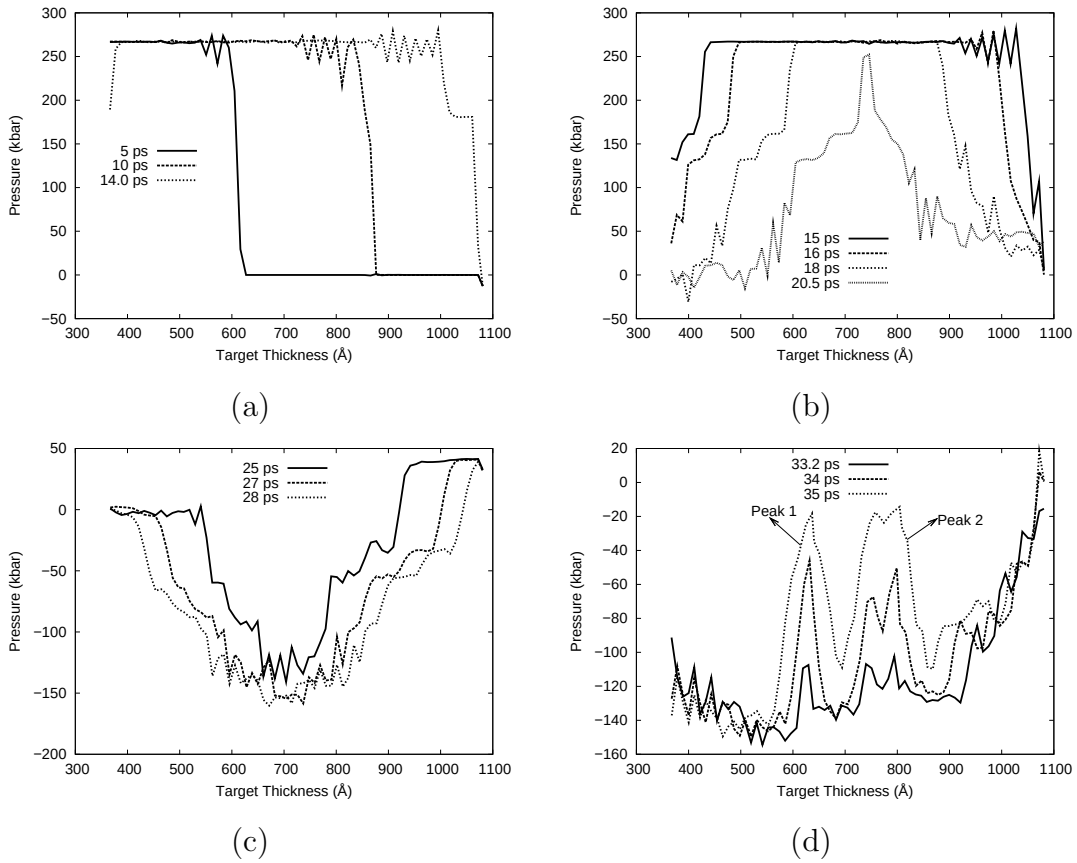

Figure 5.1: Propagation of waves in the target for an impact velocity of 1100 m/s. (*a*) Compressive waves move toward the free surface of the target and reflect back as release waves (*b*) Interaction of release waves reflected from the respective free surfaces of the target and flyer (*c*) Propagation of tension towards the free surface of the target (*d*) Propagation of the compressive waves resulting from the nucleation and growth of the voids toward the free ends of flyer and target

This time point corresponds to point B in the velocity-time profile (Figure 5.2). The interaction of the release waves leads to tension in the target. The tension created propagates towards the free surface of the target (Figure 5.1(c)) and when this reaches the free surface at 28 ps, the free surface velocity starts to decrease. This time point corresponds to point C in Figure 5.2. If the tensile strength of the material is exceeded by the tension created, it leads to nucleation, growth and coalescence of voids which, in turn, leads to spall of the material. In Figure 5.1 (d), it is seen that there are two peaks (peak 1 and peak 2) resulting from the stress relaxation due to creation of voids. This time point (35 ps) is shown by point D in Figure 5.2. The snapshot corresponding to point D is also shown in the side panel of

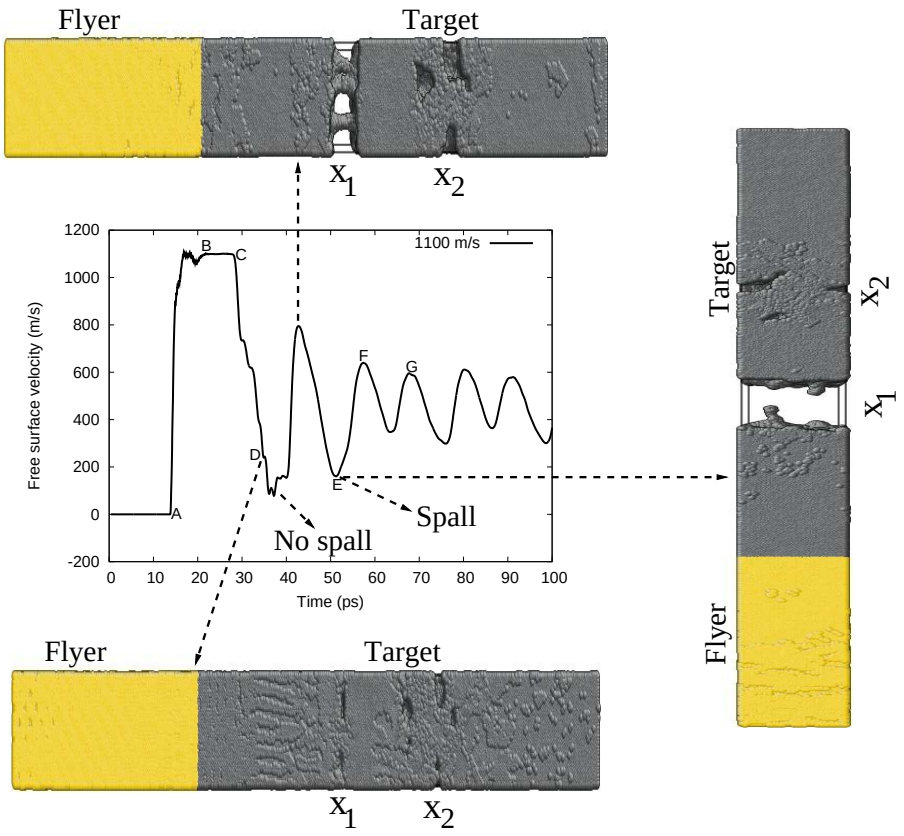

Figure 5.2: Free surface velocity of the target as a function of time for an impact velocity of 1100 m/s. Points A, B, C and D correspond to shock wave propagation in figure 5.1 (a), (b), (c) and (d), respectively. Point E corresponds to the spall of the material. The snapshots in the side panel of the Figure are created using [4].

Figure 5.2. It is seen in Figure 5.2 that the nucleation of multiple voids takes place at different locations (x_1 and x_2) in the target. The growth of voids at x_1 dominates that at x_2 and leads to spall of the material. The point E in Figure 5.2 corresponds to the spall of the material. The two waves (peak '1' and peak '2' in Figure 5.1 (d)) created due to nucleation and growth of the voids interact constructively and destructively and therefore result in generation of waves of different amplitudes (points F and G in Figure 5.2).

5.3.2 Pressure-time profile

Figure 5.3 shows the pressure-time in the region where spall occurs. At time point K, the shock arrives in the region where spall occurs. The flat region LM is the time duration during which the spall region remains in the compressed state. At time

point M, the release wave reaches the spall region and decompresses the material. The interaction of release waves around the center of the target creates tension in the system. Point N corresponds to the onset of tension in the spall region and region NP corresponds to the time upto which the spall region remains in tension. During this time duration, the tension exceeds the void nucleation threshold (160 kbar) [95] leading to nucleation and growth of the voids. The rapid growth of voids results in a sudden drop in pressure to zero. After that there is a flat region (beyond Q) indicating spall of the material.

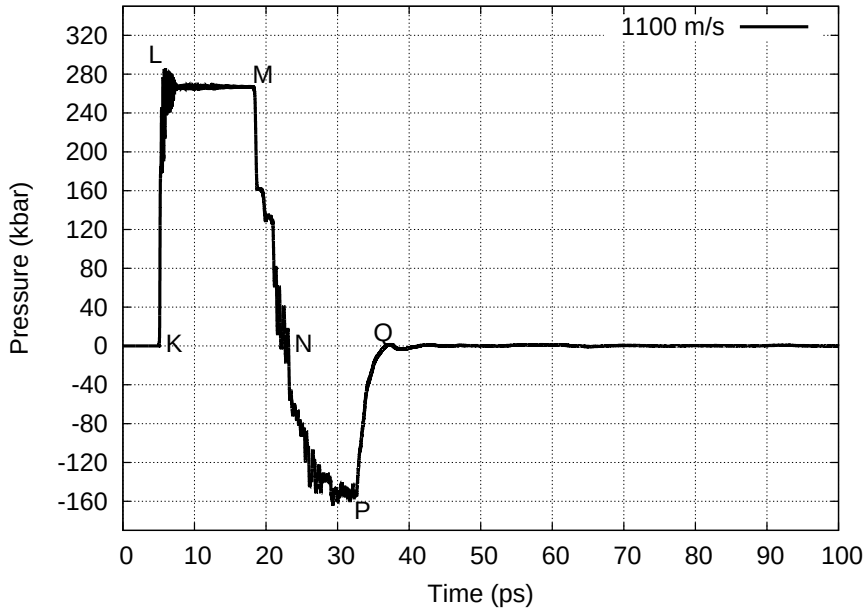

Figure 5.3: Pressure as a function of time in the spall region for an impact velocity of 1100 m/s.

5.3.3 Defects created at 1100 m/s

To study the various kinds of defects created due to shock, we have calculated the centro-symmetry parameter (CSP) as defined in Chapter 2.2.4. We have used Zhao's CSP limits [50] for single crystal copper to distinguish between different kinds of defects: Perfect lattice: CSP < 0.5, Partial dislocations: $0.5 <$ CSP < 3.0, Stacking faults: $3.0 <$ CSP < 16.0, Surface atoms: CSP > 16.0.

Surface atoms indicate either an external surface or the presence of voids. We have ignored the last bin (free surface) in the target to exclude the contribution to

the CSP by atoms at the free surface. The time evolution of the fraction of perfect lattice atoms and fraction of atoms which are part of various defects in the target is shown in Figure 5.4. In Figure 5.4 (d), the fraction of surface atoms peaks at 37.5

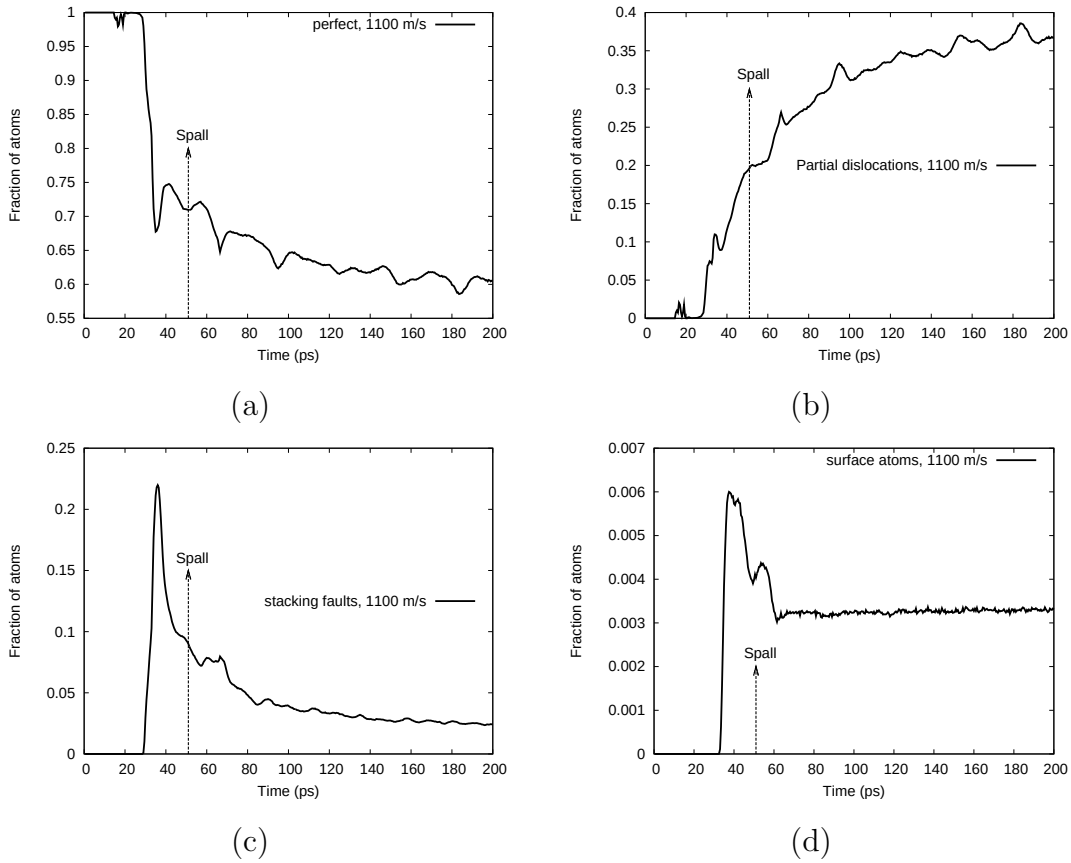

Figure 5.4: Time evolution of fraction of perfect lattice atoms and fraction of atoms which are part of defects in the target. High velocity impact of copper flyer on a copper target has been done with an impact velocity of 1100 m/s. (*a*) Perfect lattice (*b*) Partial dislocations (*c*) Stacking faults (*d*) Surface atoms.

ps due to nucleation, growth and coalescence of multiple voids. The flat portion after 60 ps in Figure 5.4 (d) corresponds to the fraction of atoms of the two free surfaces created after spall. The intermediate region between 37.5 ps to 60 ps can be understood by the following discussion:

The time evolution of defects at locations x_1 (spall region) and x_2 in Figure 5.2 are shown in Figure 5.5 and Figure 5.6, respectively. With the onset of tension at around 22.6 ps, the fraction of perfect lattice atoms drops rapidly over a few ps and rapid creation of stacking faults and partial dislocations is seen. The drop in partial dislocations at x_1 corresponds to the creation of voids around 34 ps. The partial

dislocations first drop rapidly between 30 and 33 ps, followed by a slower drop beyond 33 ps. The slower drop corresponds to the formation of voids. In region x_1, this is followed by quick conversion of stacking faults to partial dislocations, whereas at x_2 the voids heal to form partial dislocations and stacking faults convert to partial dislocations on a slower timescale. Spallation occurs at x_1. The surface atoms at location x_1 become constant after the spall of the material (Figure 5.5 d). The constant value of void fraction corresponds to the fraction of atoms of the two free surfaces created after spall. At location x_2, the fraction of surface atoms becomes zero after 60 ps (Figure 5.6 d) indicating 'healing' of the voids after the spall at location x_1 in the target material.

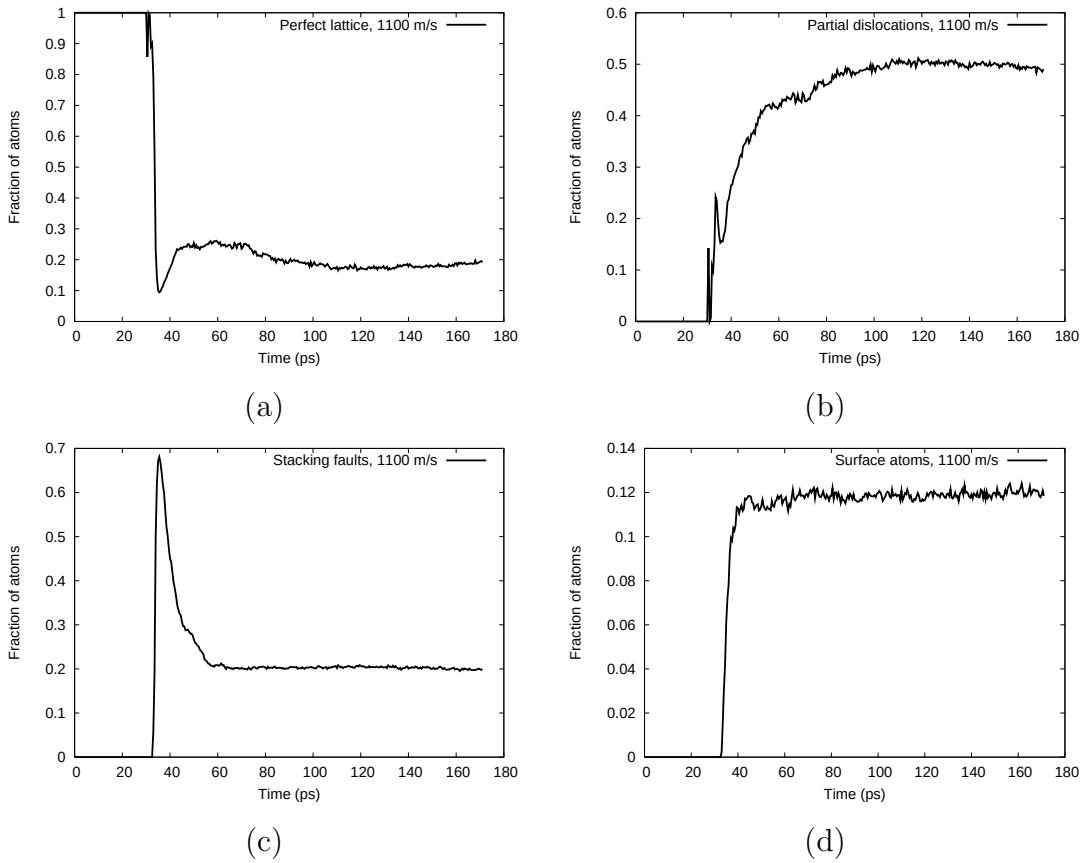

Figure 5.5: Time evolution of defects at location x_1 (spall region in Figure 5.2) for the impact of copper plates at 1100 m/s. (a) Perfect lattice (b) Partial dislocations (c) Stacking faults (d) Surface atoms.

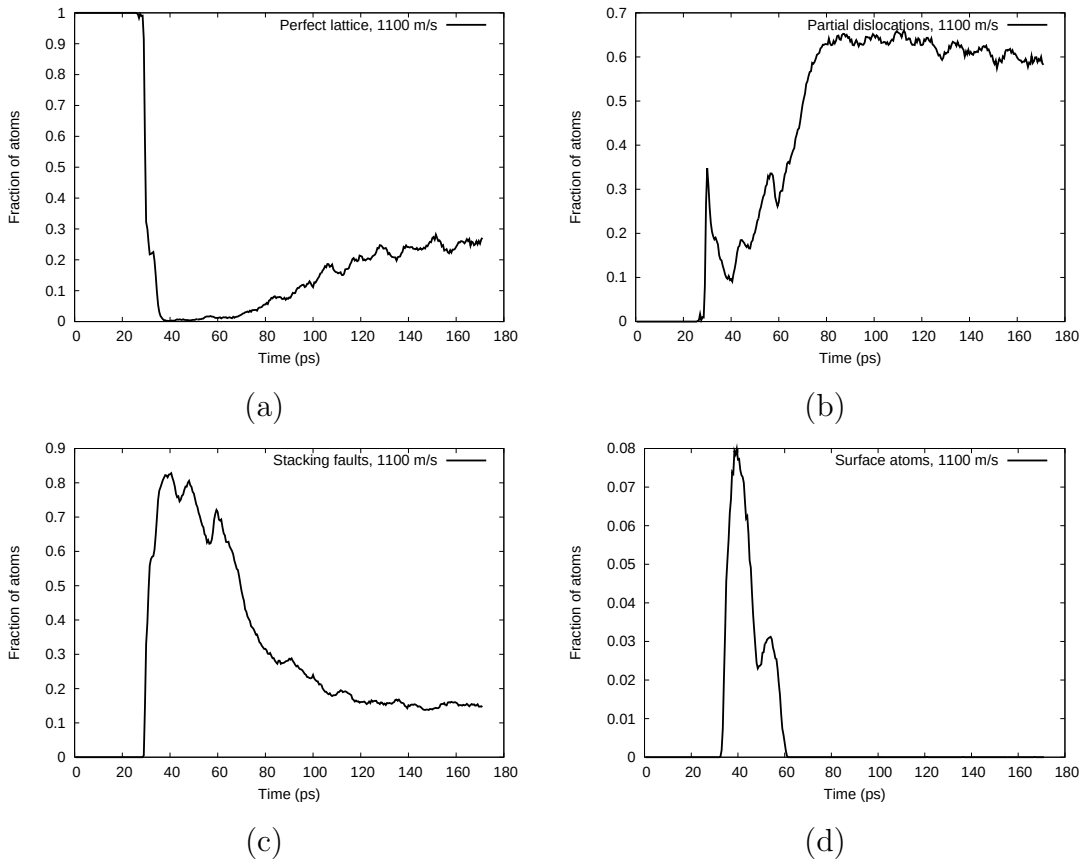

Figure 5.6: Time evolution of defects at location x_2 (Figure 5.2) for the impact of copper plates at 1100 m/s. (*a*) Perfect lattice (*b*) Partial dislocations (*c*) Stacking faults (*d*) Surface atoms.

5.3.4 Effect of domain size on the results

Bringa et al [71] performed MD simulations with a cross-section of 25×25 unit cells and compared the results with larger domain sizes. They found that the results do not change with system size. To study the effect of domain size on the evolution of defects, we have repeated our simulations with different domain sizes (300×30×30, 300×40×40, 300×50×50, and 300×100×100 unit cells). The time evolution of perfect lattice and defects in the full target (excluding the last bin, i.e., the free surface of the target) is shown in Figure 5.7. It is seen in Figure 5.7 that we see significant quantitative change in the fraction of stacking faults and surface atoms (Figure 5.7 (c) and Figure 5.7 (d)) for domain of 300×100×100 unit cells, except in the fraction of atoms corresponding to partial dislocations (Figure 5.7 (b)). However, there is no qualitative change. To see if there is any change in the spall threshold for the do-

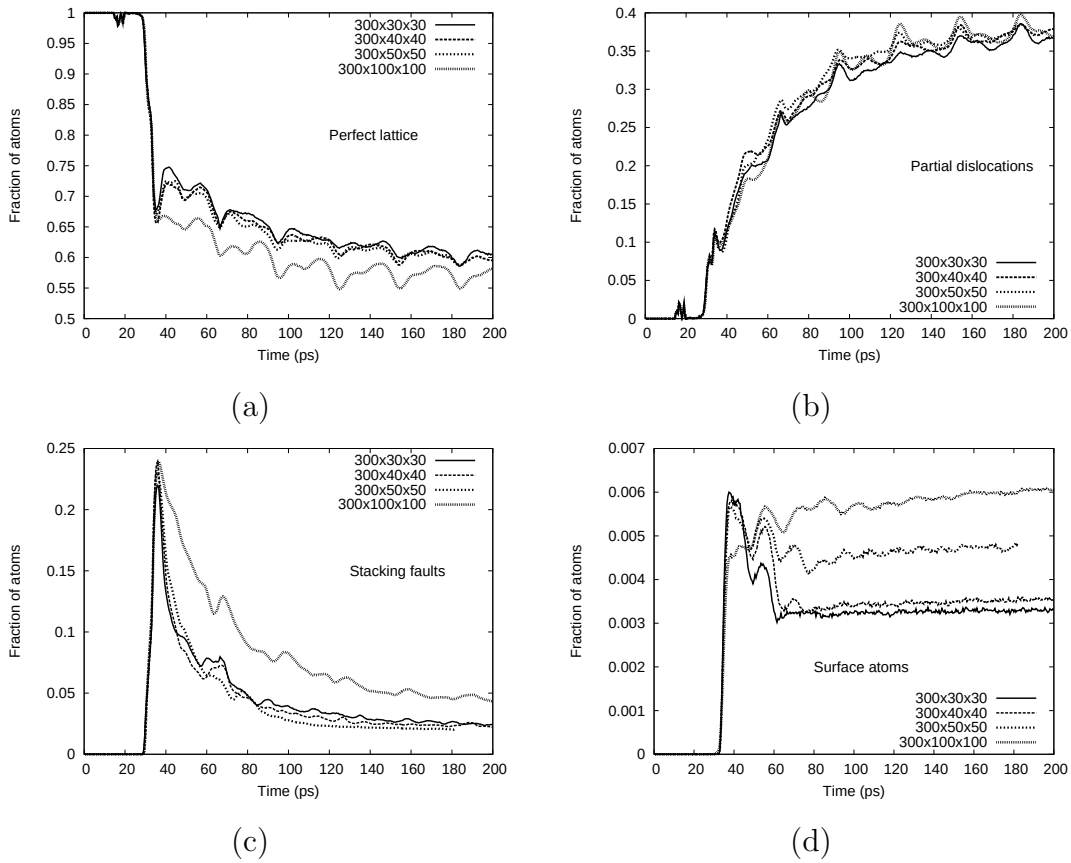

Figure 5.7: Comparison of temporal evolution of defects in full target (excluding last bin, i.e., the free surface) for the impact of copper plates at 1100 m/s. (*a*) Perfect lattice (*b*) Partial dislocations (*c*) Stacking faults (*d*) Surface atoms.

main of 300×100×100 unit cells, we have computed pressure in different bins of the target. A comparison of pressure-time histories in the spall regions for the domains of 300×30×30 and 300×100× 100 unit cells is shown in Figure 5.8. It is seen in Figure 5.8 that there is no change in the spall threshold of the material. This means that results do not change with the increase in domain size. This is in agreement with Bringa's results.

5.3.5 Effect of non-contact of flyer-target system on results

In the simulations so far, the flyer starts in contact with the target. In an actual spall experiment, there would be an initial gap. Hence we have also studied the non-contact case, i.e., when the flyer and target are not initially in contact with each other. As the flyer approaches the target, the impacting atoms will not be in

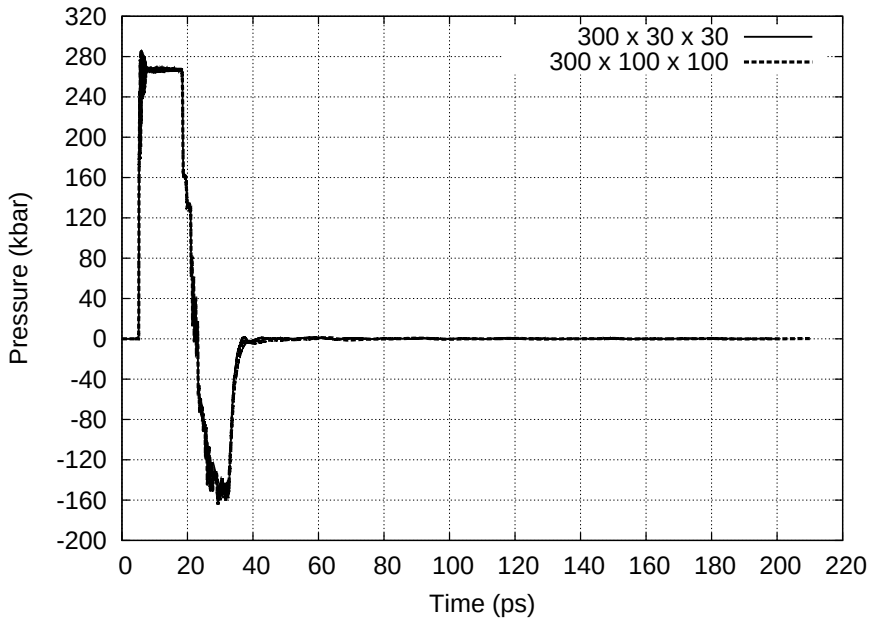

Figure 5.8: Comparison of pressure-time histories in the spall regions for the domains of 300×30×30 and 300×100×100 unit cells. Impact velocity is 1100 m/s.

corresponding FCC atom sites of the target atoms. This will lead to lack of perfect alignment between the two lattices and possible creation of defects at the impact locations. Any imperfections in the crystal are likely to reduce the threshold for nucleation. Hence we expect that the threshold for nucleation would be lower in the non-contact case. The flyer is started three unit cells away from the target, just beyond the cut-off distance of the EAM potential.

The free surface velocity of the target and pressure-time profile in the spall region, for the no-contact case, are shown in Figure 5.9 (a) and Figure 5.9 (b), respectively. The impact velocity is taken as 1100 m/s. As shown in Figure 5.9 (b), spall occurs at a lower value of tensile pressure (112 kbar) compared to the 160 kbar observed in the flyer-target contact case (Figure 5.3).

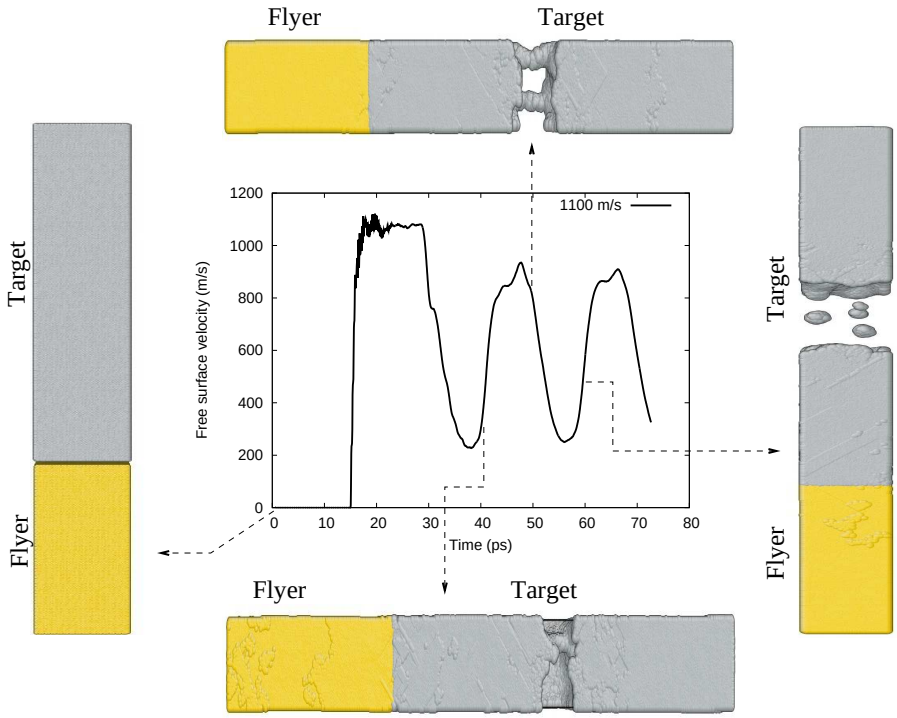

(a)

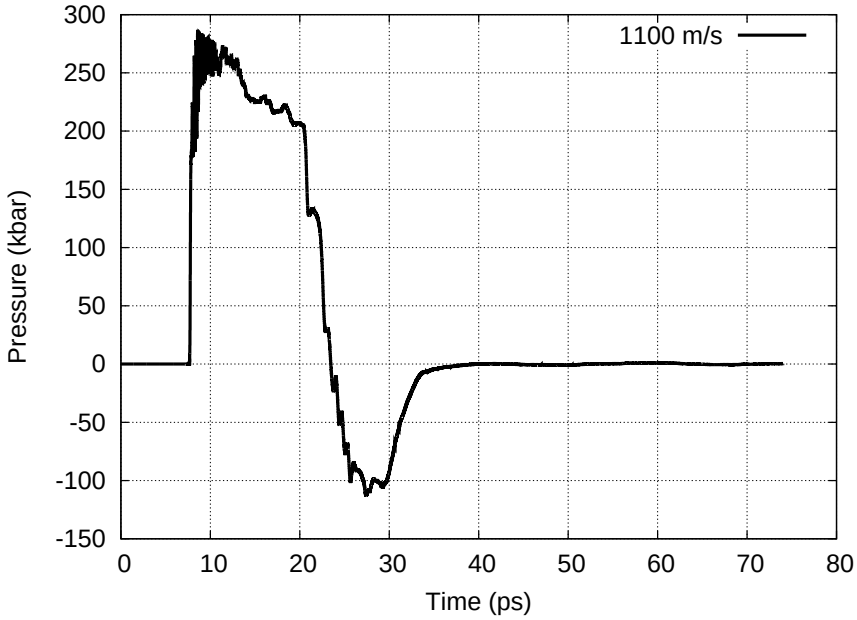

(b)

Figure 5.9: (*a*) Free surface velocity. The snapshots in the side panel of the figure are created using [4]. (*b*) pressure-time history in the spall region for an impact velocity of 1100 m/s. The flyer is kept three unit cells away from the target before impact.

To understand the difference between the two cases, we have estimated the motion of the shock front and the creation of defects during the passage of the shock. The motion of the shock front and the centro-symmetry parameter are computed using the binning analysis at the middle of the target, as shown in Figure 5.10 (a). The shock front motion and the creation of defects for the cases of no gap between

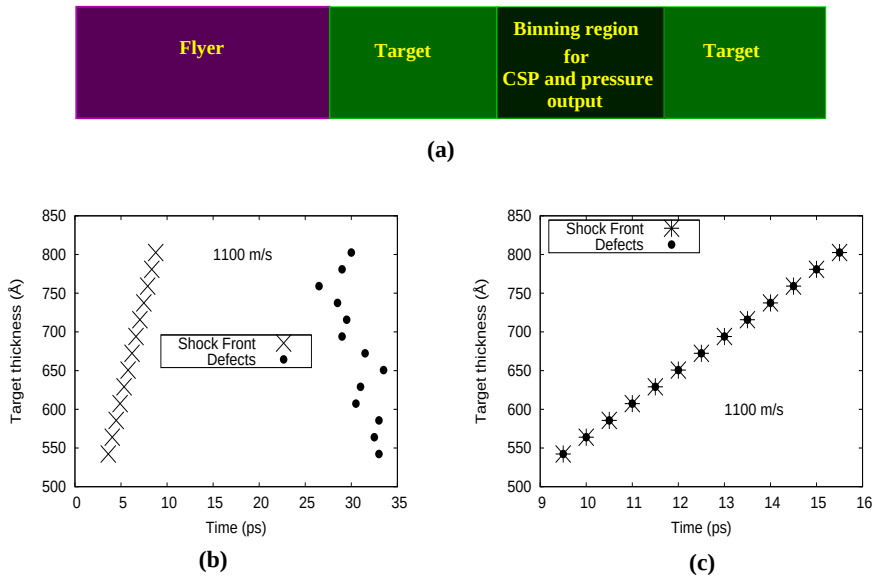

Figure 5.10: (*a*) Binning region for shock front and defects estimation (*b*) motion of shock front and defects creation for the contact case (no gap between the flyer and target before the impact) (c) shock front and defects creation for no-contact case (flyer is kept 3 unit cells away from the target before impact). Impact velocity is 1100 m/s.

the flyer and target and a gap of 3 unit cells between the flyer and target are shown in Figure 5.10 (b) and Figure 5.10 (c), respectively. It is seen in Figure 5.10 (b) (no gap between the flyer and target), the defects are created corresponding to the tension resulting from the interaction of release waves. No defect is created during the shock propagation. In the non-contact case, on the other hand, (Figure 5.10 (c)), defects are created during the shock propagation itself. These defects become preferred void nucleation sites at the time of interaction of release waves, leading to spall of the material at lower tensile pressure (Figure 5.9 (b)). This is in line with what we expected on physical grounds.

5.4 Impact at 1000 m/s

5.4.1 Pressure-time profile

The pressure-time profile in the region where voids nucleate is shown in Figure 5.11.

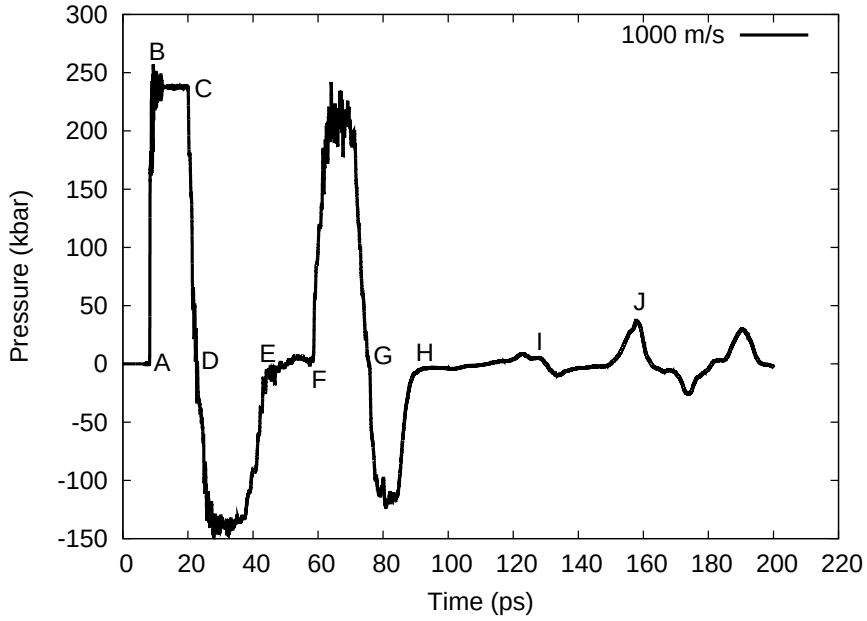

Figure 5.11: Pressure as a function of time in the region where voids nucleate for an impact velocity of 1000 m/s

The shock arrives at a time denoted by point A. Region BC is the time interval during which this region remains in a state of compression. Region CD corresponds to the release wave which decompresses the material in this region. After that the material goes into tension (region DE). In Chapter 3, we have shown that the void nucleation threshold for perfect crystal copper at 300 K is 160 kbar [95]. In Figure 5.11, it can be seen that tension corresponding to first traversal of shock stays below 160 kbar and, therefore, there is no void nucleation (region DE). Note that in the case of impact velocity of 1100 m/s (Section 5.3.2), the tensile pressure exceeds the threshold pressure (160 kbar) (Figure 5.3) and therefore results in the nucleation, growth and coalescence of voids, leading to spall of the material. In the 1000 m/s case (Figure 5.11), the flat region EF around zero indicates that material is not under any state of compression.

Region FG corresponds to the second traversal of the shock. Time point F

indicates the arrival of the compressive wave in this region and hence the material again goes into a compressed state. Interaction of release waves again leads to a state of tension in the material. Void nucleation and growth occur, corresponding to this tension created by second reverberation of the shock, at a lower value of tensile pressure (region GH). The reason for this is that various kinds of defects (dislocations, stacking faults, etc) are created during the first traversal of the shock (region DE) in the material. The time evolution of the defects created is shown in Figure 5.12. It is seen that partial dislocations and stacking faults are created

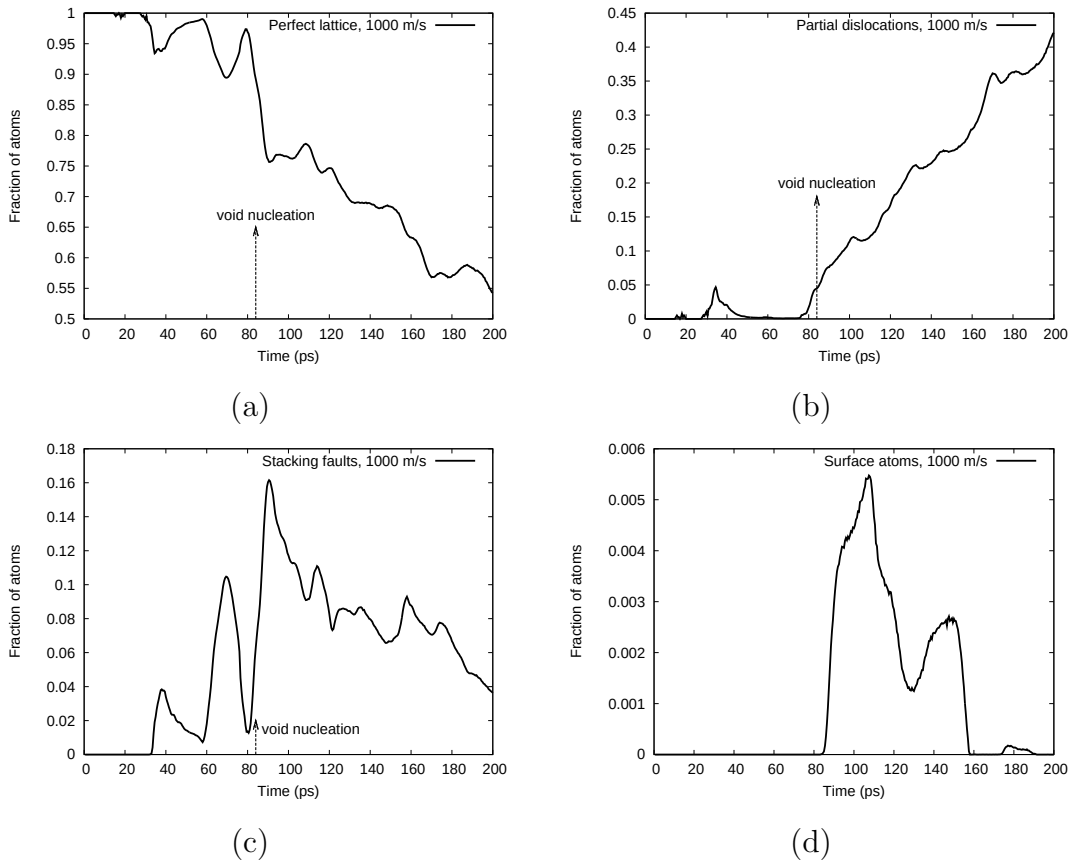

Figure 5.12: Time evolution of fraction of perfect lattice atoms, and fraction of atoms that are a part of defects, in the target. Impact velocity is 1000 m/s. Perfect lattice: CSP<0.5, Partial dislocations: 0.5 < CSP <3.0, Stacking faults: 3.0 < CSP <16.0, Surface atoms: CSP >16.0

corresponding to the tension developed during the first traversal of the shock. Note also that no surface atoms are created during this time, which means that no voids are created. These defects accumulate and become void nucleation sites in the target, leading to void nucleation at a lower value of tensile pressure during the

second traversal of the shock. As soon as the nucleation and growth of the voids take place, the pressure in the region drops rapidly to zero.

The creation of voids generates compressive waves resulting from stress relaxation. These waves move toward the free surfaces of the flyer and target. In Figure 5.13 (a), peak 1 corresponds to the compressive wave resulting from the nucleation and growth of the voids. Note that in Figure 5.1 (d), there are two peaks resulting from the creation of voids at two locations in the target. In Figure 5.13 (a), peak 1 resulting from the stress relaxation is not sharp. This means that there is more than one void which nucleates and grows. A snapshot of the voids at 87.5 ps is shown in Figure 5.13 (b).

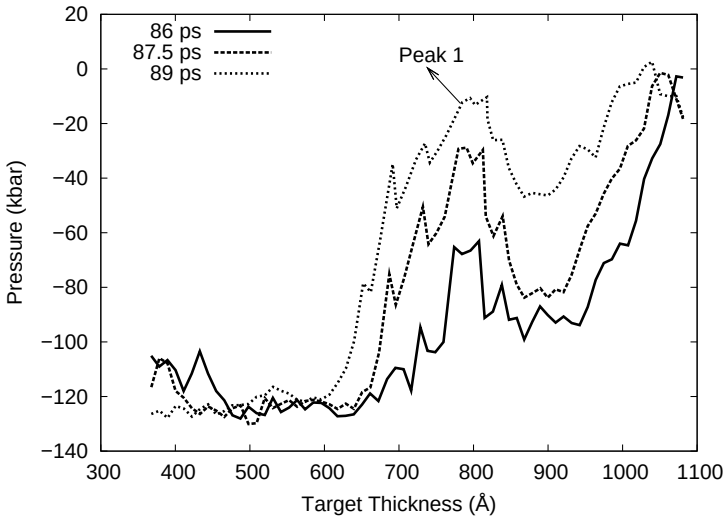

(a)

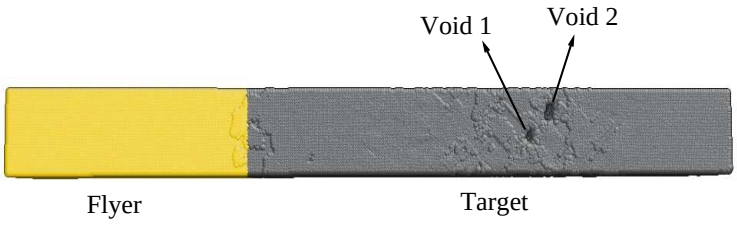

(b)

Figure 5.13: (*a*) Propagation of compressive wave resulting from the nucleation and growth of the voids (*b*) Snapshot of voids at 87.5 ps created for an impact velocity of 1000 m/s. The snapshot is created using [4].

In Figure 5.11, the flat region HI around zero is the signature of the presence of voids. Pressure peak J indicates the healing of the voids.

5.4.2 Physical interpretation of free surface velocity variation

There is a somewhat complex behaviour of the free-surface velocity in the 1000 m/s impact case. This can be physically understood in terms of the distance-time graph shown in Figure 5.14, which illustrates the motion of the shock front and the release wave. The free surface velocity of the target as a function of time is shown in Figure 5.15.

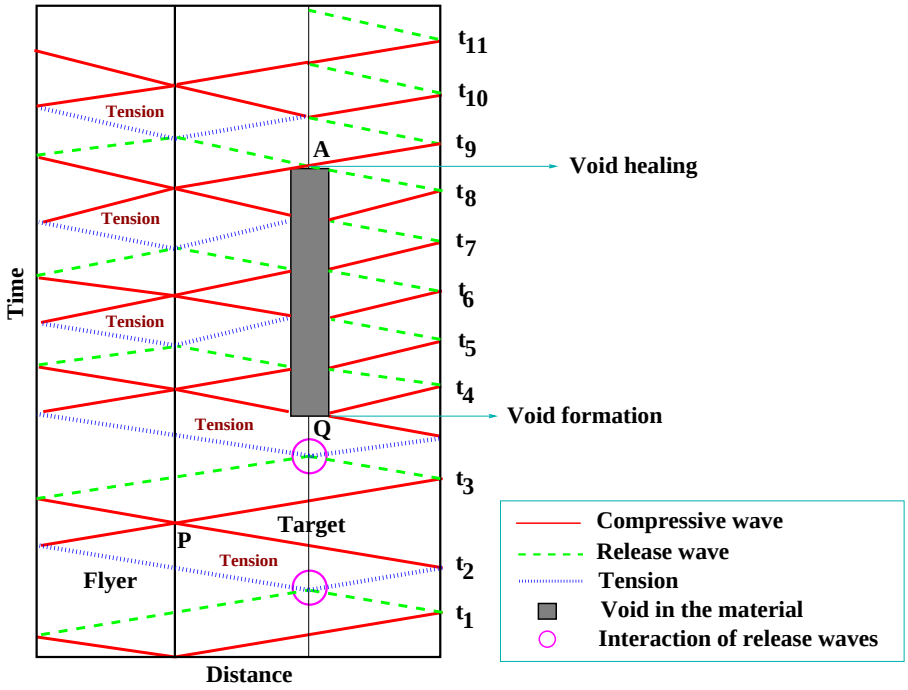

Figure 5.14: x-t graph for an impact velocity of 1000 m/s.

Impact at 1000 m/s produces compressive waves which travel toward the respective free surfaces of the flyer and target. In Figure 5.14, the compressive wave arrives at the free surface of the target at time t_1. This time point corresponds to the time T_1 in the free surface velocity of the target (Figure 5.15). The arrival of the shock at the free surface accelerates it by twice the particle velocity as shown in Figure 5.15 [1]. When the compressive waves reach the free surfaces of the flyer and target, they reflect back as release waves. These release waves decompress the material which is compressed by the passage of the shock and interact around the centre of the target. The interaction of the release waves creates tension in the

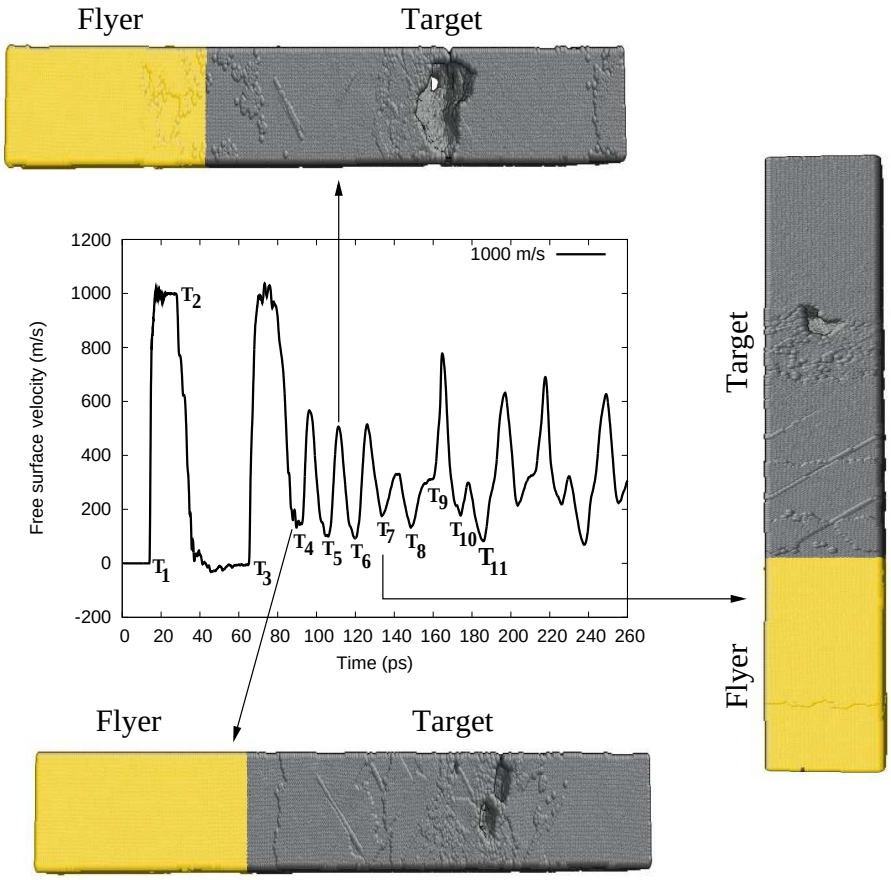

Figure 5.15: Velocity-time profile at the free surface of the copper target impacted by copper flyer with an impact velocity of 1000 m/s. The snapshots in the side panel of the Figure are created using [4].

target. If the tension created exceeds the dynamic strength of the material, spall of the material takes place. In Figure 5.14, the tension reaches the free surface of the target at time t_2. As the tension reaches the free surface of the target, the free surface velocity starts to decrease. This time point corresponds to point T_2 in Figure 5.15. When the release waves reach the free surfaces of the flyer and target, they get reflected and return back as compressive waves. Note that in Figure 5.15, there is no pullback in the free surface velocity of the target which is the signature of the spall [12]. This means that there is no spall during the first traversal of the shock, as discussed in the previous section.

The compressive waves resulting from the reflection of release waves from respective free surfaces of the flyer and target interact around the interface of the flyer and target (point P in Figure 5.14) and result in high-intensity compressive waves which

travel toward the free surfaces of the flyer and target. This high intensity compressive wave reach the free surface of the target at time t_3 and accelerates it. This time point corresponds to point T_3 in Figure 5.15. These compressive waves again get reflected from the free surfaces of the flyer and target and return as release waves. The interaction of release waves leads to tension in the material, which results in nucleation and growth of voids. The compressive waves resulting from stress relaxation due to nucleation and growth of voids move toward the free surfaces of the flyer and target. The compressive wave reaches the free surface of the target at time t_4 in Figure 5.14 and accelerates it. This time point corresponds to time T_4 in the free surface velocity (Figure 5.15). Note that there is a pullback in the free surface velocity at T_4. This is due to the creation of voids (point Q, Figure 5.14), not due to spall of the material. In this case the voids grow and coalesce leading to incipient spall-like conditions [12]. However, spallation does not take place. The nucleation, growth and coalescence of voids are shown in the side panels of Figure 5.15. Note that the growth and coalescence of voids between time points T_5 to T_7 lead to the formation of almost two parts, but there is no complete spallation of the material. Time points t_5, t_6, t_7 and t_8 in Figure 5.14 correspond to the points T_5, T_6, T_7 and T_8 in Figure 5.15. The compressive wave resulting from stress relaxation due to creation of voids reverberates between the void surface and the free surface of the target. The time period between two consecutive peaks (region between points T_4 to T_7) in the free surface velocity of the target shows that the velocity of the wave corresponds to the speed of sound in copper.

As seen in Figure 5.15, the growth and coalescence of voids between 90 ps to 130 ps lead to the formation of a big void. This results in the trapping of the shock between the void surface and the free surface of the flyer. Shock propagation between the surface of the void and the free surface of the flyer are shown in Figure 5.16. Sound reverberations on the other side of the void can also be seen in Figure 5.16. The void heals at 157 ps and the shock couples with the reverberation on the other side of the void (Figure 5.16). This is the reason for the big peak seen in Figure 5.15 at 165 ps and also the subsequent pattern of the peaks in the free surface velocity of the target. Point A in Figure 5.14 corresponds to the healing of the void. This time point corresponds to the point T_9 in the free surface velocity of the target (Figure 5.15).

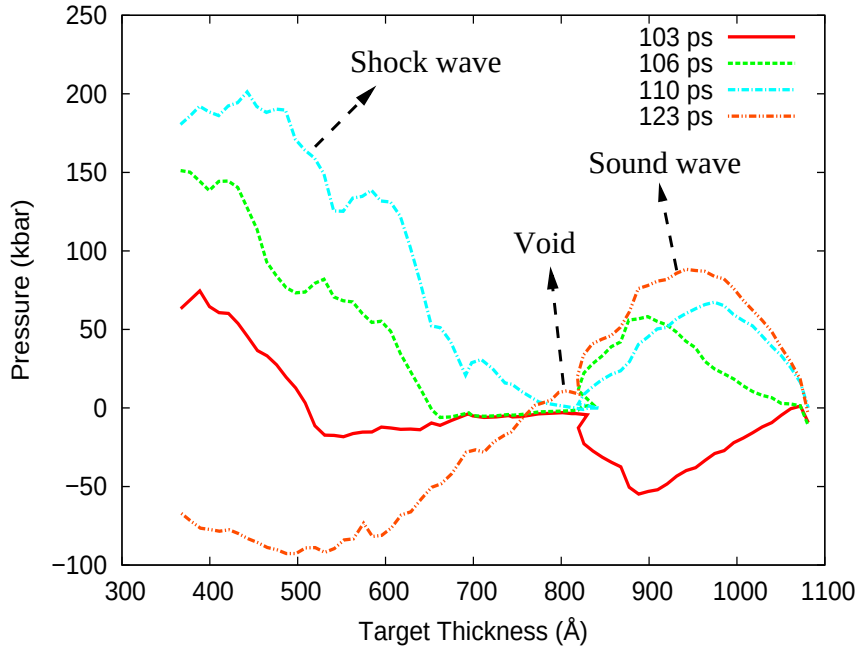

Figure 5.16: Shock wave and sound wave propagation on the two sides of the void at 110 ps.

5.4.3 Effect of crystal orientation and grain boundary

It is important to study the effect of crystal orientation and grain boundary on fracture properties. Simulations have been performed for the impact of copper plates at 1000 m/s for two sets of crystal orientations:

- <110> is the direction of impact (x-direction), while y- and z- directions (transverse directions) are along <$\bar{1}$10> and <001>, respectively.
- <111> is the direction of impact (x-direction), while y- and z- directions (transverse directions) are along <1$\bar{1}$0> and <11$\bar{2}$>, respectively.

The simulation domain in both of cases involves 300×30×30 unit cells. The free surface velocities for both cases are shown in Figure 5.17.

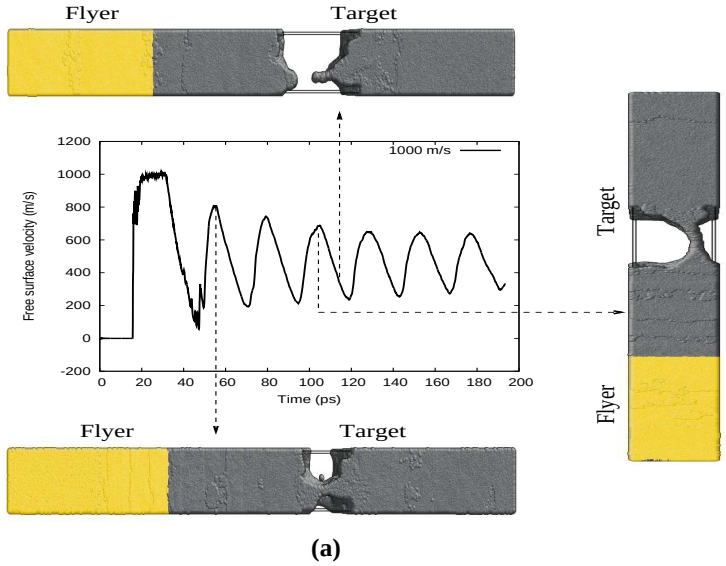

(a)

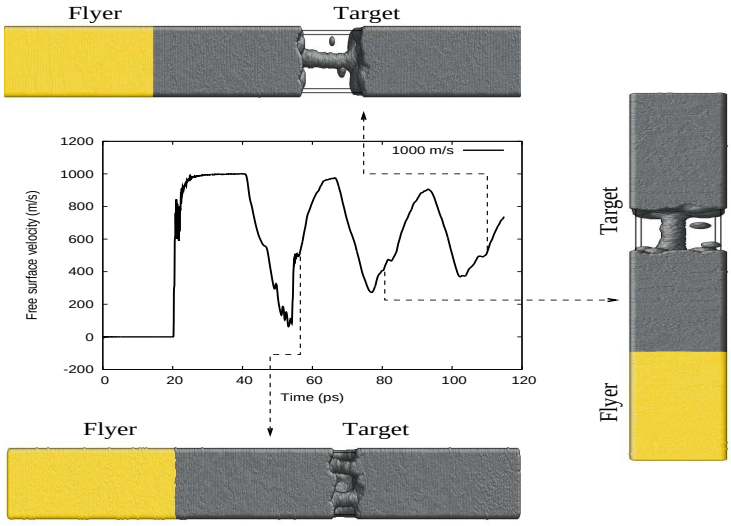

(b)

Figure 5.17: Free surface velocity as a function of time for the impact of copper plates at 1000 m/s along (*a*) <110> direction (*b*) <111> direction. The snapshots in the side panel of the figure are created using [4].

In both cases (Figure 5.17 (a) and Figure 5.17 (b)), nucleation and growth of the voids take place corresponding to first traversal of the shock and spall occurs only at late times. In the case of impact along <100> direction (Figure 5.15), nucleation and growth of voids correspond to the second traversal of the shock and no spall occurs.

To study the effect of grain boundary on the free surface velocity of the target, we have simulated the impact of bicrystal copper plates at 1000 m/s. The direction of impact (x-direction) is taken along the <100> direction, which is the tilt axis. The grain boundary normals are <021> and <02$\bar{1}$> which correspond to the y-axes. The z-axes are along the <0$\bar{1}$2> direction for grain 1 and <012> direction for grain 2. The angle of misorientation (θ) about the tilt axis (<100>) is 36.87°, which is calculated as follows:

$$\cos\theta = \frac{h_1h_2 + k_1k_2 + l_1l_2}{(\sqrt{h_1^2 + k_1^2 + l_1^2})(\sqrt{h_2^2 + k_2^2 + l_2^2})} \tag{5.1}$$

where <$h_1k_1l_1$> and <$h_2k_2l_2$> correspond to <021> and <02$\bar{1}$> directions, respectively. The simulation domain contains 3×10^6 atoms corresponding to 300×50×50 unit cells. The resulting free surface velocity as a function of time is shown in Figure 5.18.

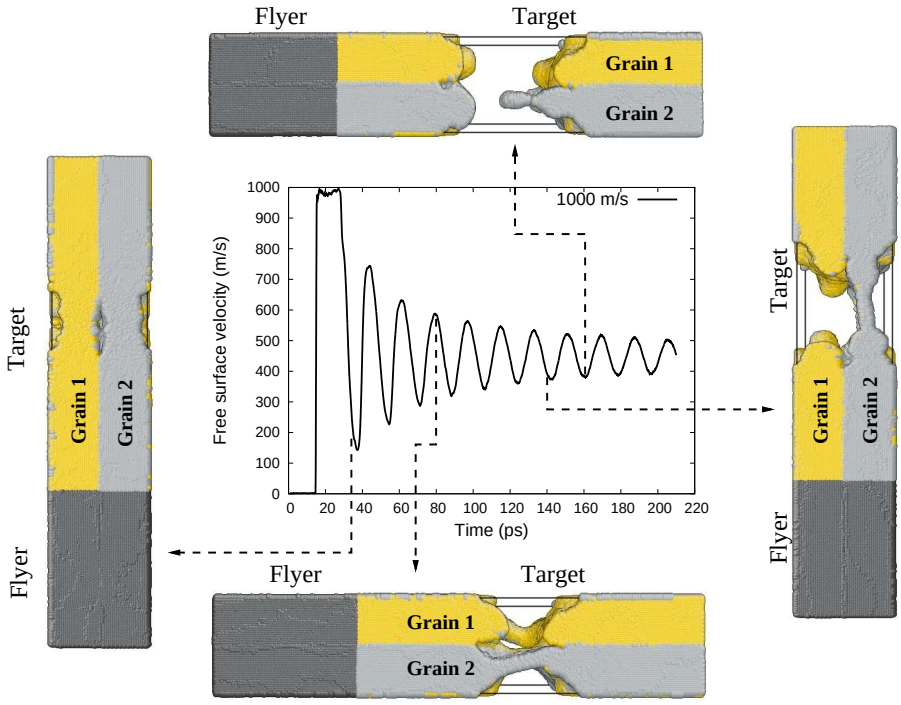

Figure 5.18: Free surface velocity as a function of time for the impact of bicrystal copper plates at 1000 m/s. The snapshots in the side panel of the figure are created using [4].

Snapshots are also shown in the side panel of the Figure 5.18. It is seen in Figure 5.18 that nucleation and growth of voids take place along the grain boundary, which is due to the presence of nucleation sites (defects) at the grain boundary. This

nucleation and growth correspond to the first traversal of the shock, as in case of impact involving crystals oriented along <110> and <111> directions (Figure 5.17) and spall occurs at late times. This is different from the impact along <100> direction (Figure 5.15), in which nucleation and growth of the voids take place corresponding to second traversal of the shock and no spall occurs. It is also seen in Figure 5.18 that there is a rapid damping in free surface velocity as compared to the impact involving single crystal copper plates. This is due to the presence of a large number of defects which lead to rapid dissipation of energy.

5.4.4 Study of stochastic effect

In a real system, thermal motion will lead to stochastic effects. This has been simulated at 1000 m/s by perturbing initial atomic coordinates. The initial x-coordinates of the atoms are randomly perturbed between ± 0.001 $\mathring{A}$. No perturbation is applied to the y and z coordinates. The results are discussed below.

Free surface velocity

The free surface velocity of the target is shown in Figure 5.19 (a). There is no pullback in the free surface velocity of the target corresponding to first traversal of the shock. Pullback occurs after 80 ps due to nucleation and growth of voids. In this case, growth and coalescence of the voids lead to the spall. Note that no spall had occurred in the case of impact at the same velocity, but without perturbing the initial coordinates (Section 5.4.1 – Figure 5.11). The compressive wave resulting from stress relaxation due to spall of the material reverberates between the free surface and spall surface of the scab. The ringing in the free surface velocity after 90 ps (Figure 5.19 (a)) corresponds to reverberations of the trapped compressive wave. The snapshots at different time points in the free surface velocity are shown in the side panel of the Figure 5.19 (a).

Pressure-time history

The pressure as a function of time in the spall region is shown in Figure 5.19 (b). No void nucleation occurs during the tension created by first traversal of the shock. However, various defects (partial dislocations, stacking faults, etc) are created. These defects become void nucleation sites for the tension corresponding to

second traversal of the wave and hence lead to the nucleation and growth of voids at very low tensile pressure. This, in turn, results in spall. Therefore we see that, close to the spall threshold of the material, a small change in the atomic coordinates affects the spallation process of the material.

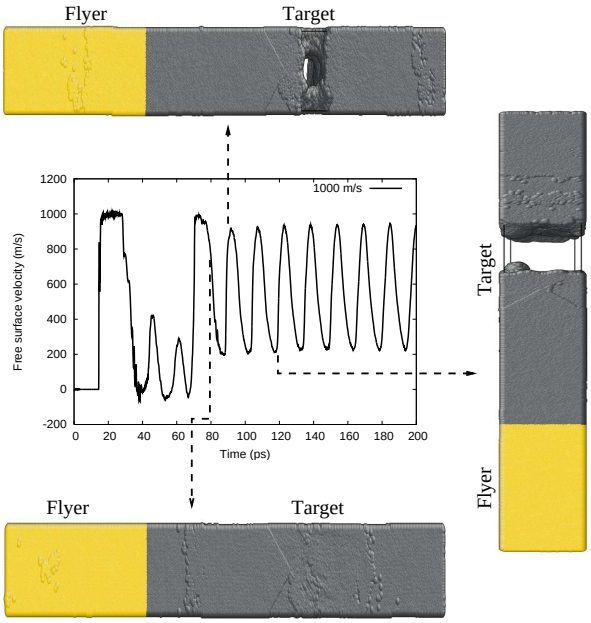

(a)

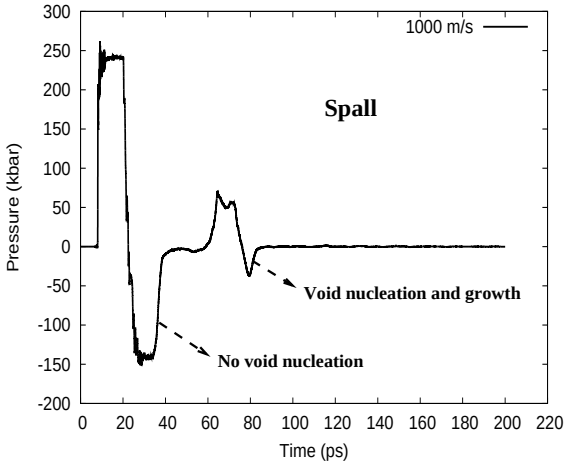

(b)

Figure 5.19: (*a*) Free surface velocity of the target for an impact velocity of 1000 m/s. The snapshots in the side panel of the figure are created using [4] (*b*) Pressure as a function of time in the spall region

5.5 Conclusions

We have simulated high velocity impact of one copper plate on another with impact velocities of 1100 m/s and 1000 m/s. For impact at 1100 m/s, voids are nucleated at two locations in the target. The growth of voids at the spall location (x_1 in Figure 5.2) is faster than that at other locations (x_2 in Figure 5.2) in the target material and hence leads to spall of the material. A comparison of contact configuration of flyer-target system and non-contact configuration of flyer-target system is addressed. It is found that the non-contact configuration leads to spall at lower value of tensile pressure, which is due to the presence of defects (nucleation sites) in advance for the tension resulting from the interaction of release waves. However, this does not happen for the contact configuration of flyer and target system in which defects are created during the tension developed by the interaction of release waves.

For impact at 1000 m/s along <100> direction, the nucleation and growth of voids take place corresponding to the second traversal of the shock. An analysis based on the centro-symmetry parameter shows that partial dislocations and stacking faults are generated due to the tension created by the first traversal of the shock. These defects become void nucleation sites for the tension due to second traversal of the shock and thus lower the void nucleation threshold. This indicates that the high strain-rate history of the material affects the void nucleation threshold of the material.

The effect of crystal orientation and grain boundary on the free surface velocity of the target at 1000 m/s has been studied. It has been found that nucleation and growth of the voids correspond to the first traversal of the shock and material spalls at late times. For impact at 1000 m/s along the <100> direction, we find that a spall like signal is generated which corresponds to the stress relaxation resulting from the nucleation and growth of the voids and not due to spall of the material. Damage creation for a given impact velocity depends on the crystal orientation and in a macroscopic metal with polycrystallites, all these effects come into play.

Stochastic effects on the spallation process have been studied by simulating impact at 1000 m/s. We find that a small change in the initial atomic coordinates affects the spallation process. This means that for impact velocities close to the spall threshold, the spallation process is stochastic. This effect must be taken into account during numerical determination of the threshold velocity for spall.

Chapter 6

Multi-scale simulations of damage of single crystal copper at high strain rates

Laser induced shock waves in materials can create high strain rates in solids, of the order of (10^7 - 10^{10})/s [11, 18, 87, 89]. Dynamics of atoms/molecules subjected to such high strain-rates can be computationally investigated by molecular dynamics which is well suited to study the evolution of systems containing several millions of atoms for several nanoseconds. The information gleaned at the atomistic scales can be used to generate parameters that serve as inputs to simulations at macro-scales, within a multi-scale modeling paradigm.

In Chapter 3, NAG parameters have been determined for single crystal copper deformed triaxially at 5×10^9/s strain-rate. We have also studied the dependence of these parameters on temperature in Chapter 4. Those studies were performed on perfect single crystal copper. However, the nucleation threshold of $\sim$ 160 kbar, obtained from those simulations for single crystal copper at 300 K, is well above the experimental values [6, 66, 68]. This mismatch arises due to the absence of pre-existing defects that would be present in a real single crystal. The effect of different kinds of defects on the NAG parameters, specifically on the nucleation threshold, is the subject of this chapter.

In this chapter, we study the role of pre-existing defects on fracture properties of single crystals. The results are used for hydrodynamic simulations at macro-scales.

6.1 Molecular dynamics simulation

Isotropic tension in single crystal copper, with various kinds of pre-existing defects, is simulated at 5×10^9/s strain rate with 300 K temperature. The method used has been explained in Chapter 3.5.1.

To study the effect of pre-existing defects on the NAG parameters, we have created the following kinds of defects in single crystal copper:

- *Vacancies:* Vacancies are created by deleting atoms from different locations in the simulation domain, as shown in Figure 6.1 (a).
- *Edge dislocations:* We have created dislocations of different lengths. On the basis of their lengths, we have categorized dislocations as follows:
  - Edge dislocation-1: This dislocation is created by removing 3 atomic rows in the YZ plane and has a height of one tenth of the side length of the simulation domain (361 Å) along the Z-axis, as shown in Figure 6.1 (b).
  - Edge dislocation-2: This dislocation is created by removing 4 atomic rows in the YZ plane and has a height of half the side length of the simulation domain along the Z-axis as shown in Figure 6.1 (d).
  - Edge dislocation-3: This dislocation is created by removing all atomic rows in the YZ plane and has a height of half the side length of the simulation domain along the Z-axis as shown in Figure 6.1 (e).
- *Edge dislocation-1 with few vacancies:* Edge dislocation-1 is created in the domain along with a few vacancies to see the combined effect of edge dislocations and vacancies on the results. The initial setup of this defect is shown in Figure 6.1 (c).

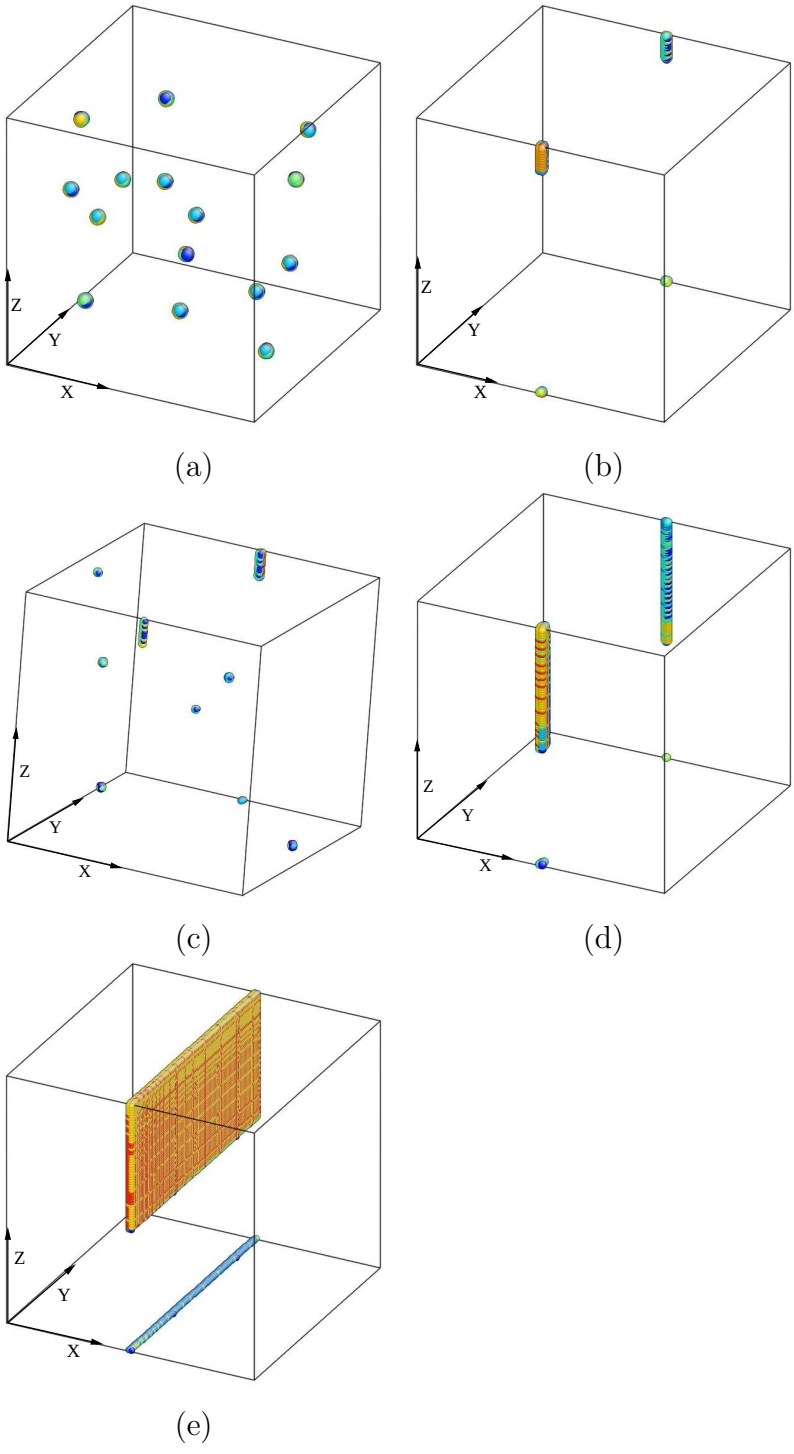

Figure 6.1: Single crystal copper is deformed triaxially at 5×10^9/s strain rate with (*a*) vacancies (*b*) edge dislocation-1 of length equal to one tenth of the side length of the simulation domain (*c*) edge dislocation-1 and few vacancies (*d*) edge dislocation-2 of length equal to half of the side length of the simulation domain (only 4 atomic planes are taken) (*e*) edge dislocation-3 of length equal to half of the side length of the simulation domain. These snapshots are created using [4].

Following the introduction of these defects, the system is thermalized using NPT at 300 K and 0 bar pressure. This leads to some change in the defect structure. Figure 6.2 shows the configuration of defects both before and after relaxation, for edge dislocation-3 for a domain of 20×20×20 unit cells. These defects behave as void nucleation sites and thus lead to nucleation of voids at lower values of tensile pressure than in perfect crystals.

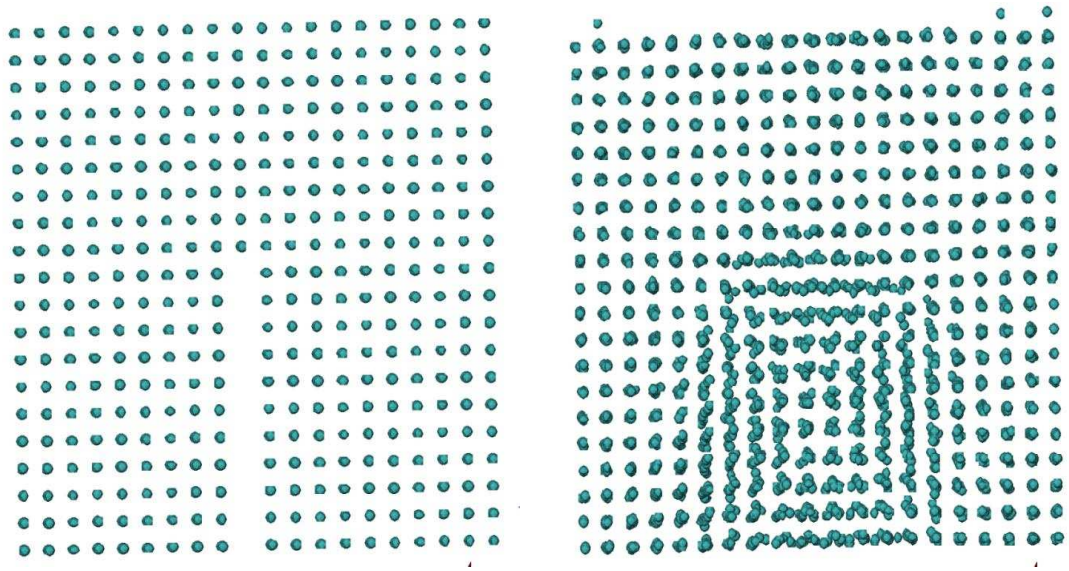

(a) (b)

Figure 6.2: (*a*) Snapshot of system after removing half plane from the simulation domain (20×20×20 unit cells) creating edge dislocation-3. This snapshot is taken before performing NPT relaxation (*b*) Snapshot after performing NPT at 300 K and 0 bar.

6.1.1 Pressure-time profile

The pressure-time profile for single crystal copper triaxially deformed at 5×10^9/s strain rate with pre-existing defects is shown in Figure 6.3 (a). The void volume fraction as a function of time is also shown in Figure 6.3 (b).

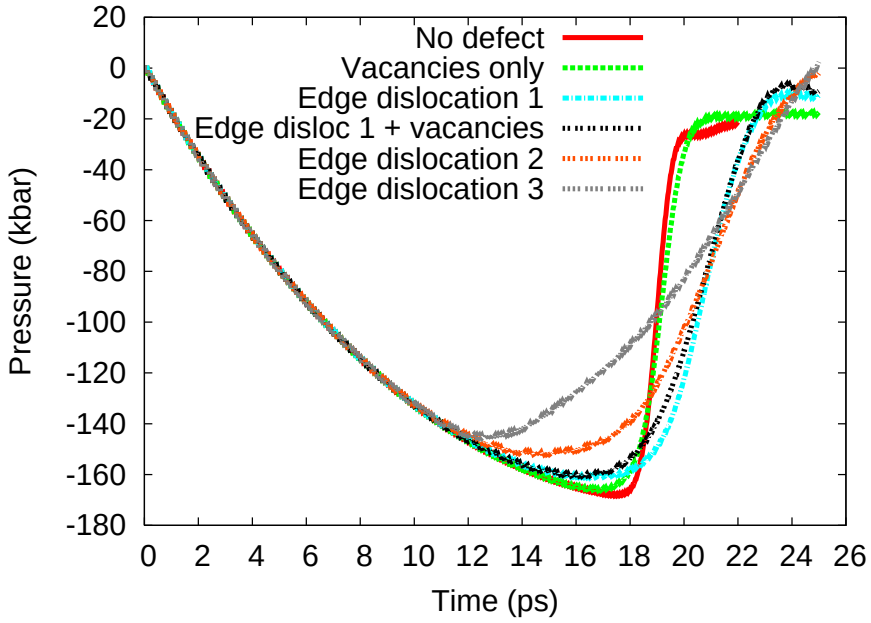

(a)

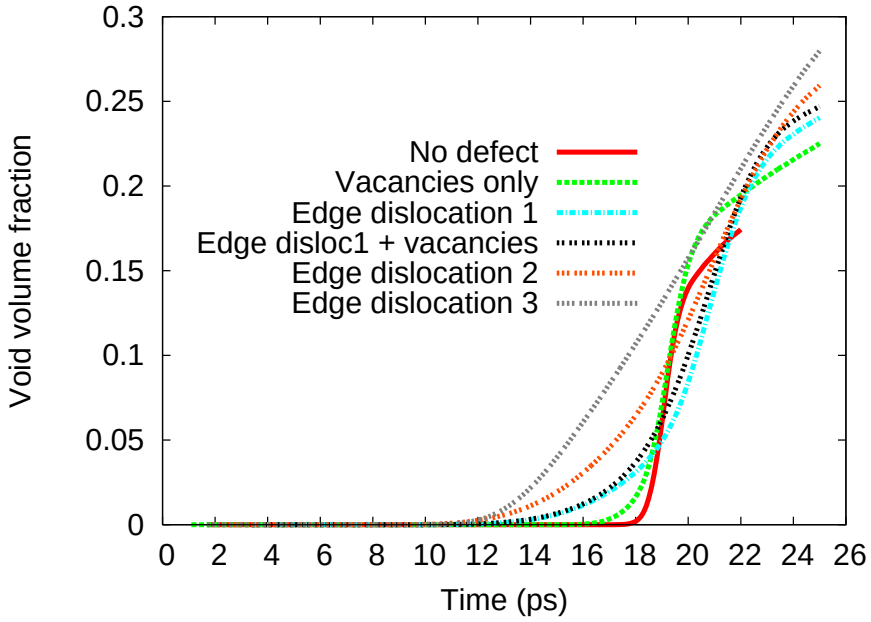

(b)

Figure 6.3: (*a*) Pressure-time profile for single crystal copper deformed triaxially at 5×10^9/s strain rate with pre-existing defects (*b*) Void volume fraction as a function of time for different defects in single crystal copper.

It is seen in Figure 6.3 (a) that as the system is triaxially expanded, the tensile pressure in the system is continuously increasing and becomes maximum at some

time point. After that it turns around and rapidly flattens off around some small value of tensile pressure. This turn around of pressure is due to stress relaxation resulting from the nucleation and growth of voids. Note that the turn around peak is not sharp – it is rounded due to inertial effects [96]. The nucleation and growth of voids result in a stress relaxation wave which takes time to reach the simulation box boundary to account for the stress relaxation in the domain. Due to this reason, the turn-around peak is rounded in all cases in Figure 6.3 (a). In perfect single crystal copper, there are no pre-existing nucleation sites. The nucleation sites in perfect crystal copper are created during the deformation itself and thus facilitate nucleation of voids. Once nucleation occurs, the growth of the voids takes place very rapidly. In Figure 6.3 (b) for a perfect single crystal, it is seen that there is a exponential growth of the voids. In this case, the growth rate of the voids is very high compared to expansion rate of the simulation domain. This is also true for the case of only vacancies in the domain. In these cases, coalescence of voids takes place at later times. When dislocations of different sizes are present in the domain as pre-existing defects, the exponential part of the void volume fraction in Figure 6.3 (b) approaches a linear shape as the size of the dislocation increases. The reason is that as the size of the dislocation increases, the number of nucleation sites also increases. Once the nucleation threshold is crossed, the growth and coalescence of voids take place rapidly, unlike coalescence of voids in perfect crystal copper at later times. For edge dislocation-3, the void volume fraction vs time graph (Figure 6.3 (b)) is linear. This indicates that the growth rate of the big voids resulting due to coalescence becomes equal to the expansion rate of the simulation domain.

For single crystal copper with pre-existing vacancies, the turn around of the pressure takes place at lower values of tensile pressure (166 kbar) compared to perfect crystal copper (168 kbar). This is due to the presence of vacancies in crystal copper which serve as void nucleation sites .

Snapshots (created using [4]) for single crystal copper at t=20 ps in Figure 6.3 (a) with pre-existing vacancies and dislocations are shown in Figure 6.4.

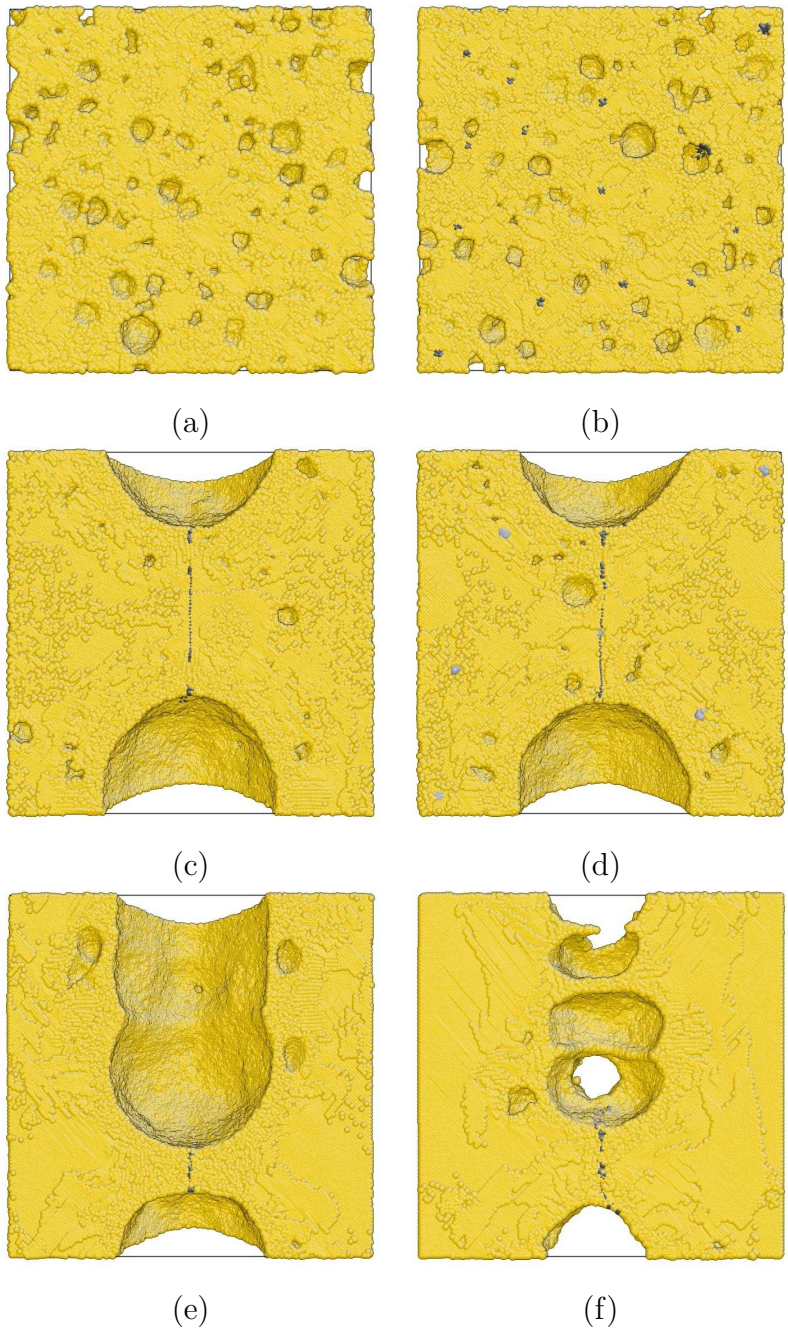

Figure 6.4: Snapshots showing nucleation, growth and coalescence in single crystal copper at 20 ps in Figure 6.3 (a) with defects: (*a*) Perfect crystal (*b*) Vacancies only – the black spots in the Figure show the locations of the vacancies in the domain (*c*) edge dislocation-1 (*d*) edge dislocation-1 and a few vacancies, shown by blue spots (*e*) edge dislocation-2, and (*f*) edge dislocation-3. The black line in the Figure shows the extra half plane.

6.1.2 Nucleation and Growth (NAG) parameters

The procedure for determination of best-fit NAG parameters is described in Chapter 3.6.3. The NAG parameters for single crystal copper deformed triaxially with pre-existing defects are shown in Table 6.1. It is seen in Table 6.1 that the void

Single crystal copper	NAG parameters					Relative error (%)
	P_{n0} (kbar)	P_{g0} (kbar)	P_1 (kbar)	$\dot{N}_0$ (m^{-3}- s^{-1})	η (bar-s)	
Perfect	160.0	21.2	0.167	7.1×10^{18}	3.4×10^{-8}	19.0
Vacancies only	160.0	20.6	1.09	1.3×10^{29}	6.7×10^{-8}	9.4
Edge dislocation-1	127.0	21.0	7.76	4.6×10^{29}	2.3×10^{-7}	10.7
Edge dislocation-1 and few vacancies	123.0	21.0	8.48	3.5×10^{29}	2.0×10^{-7}	9.0
Edge dislocation-2	80.7	19.0	7.37	4.9×10^{29}	3.4×10^{-7}	10.5
Edge dislocation-3	42.7	47.0	3.85	2.7×10^{20}	2.0×10^{-7}	13.5

Table 6.1: Best-fit NAG parameters for single crystal copper deformed triaxially at 5×10^9/s strain rate with pre-existing defects. N = 4×10^6

.

nucleation threshold decreases with increase in size of the dislocation. The comparison of void volume fraction obtained by NAG model and that by post-processor (Section 2.2.1) is shown in Figure 6.5 and the corresponding relative error at each data point for all the cases is shown in Figure 6.5 (f).

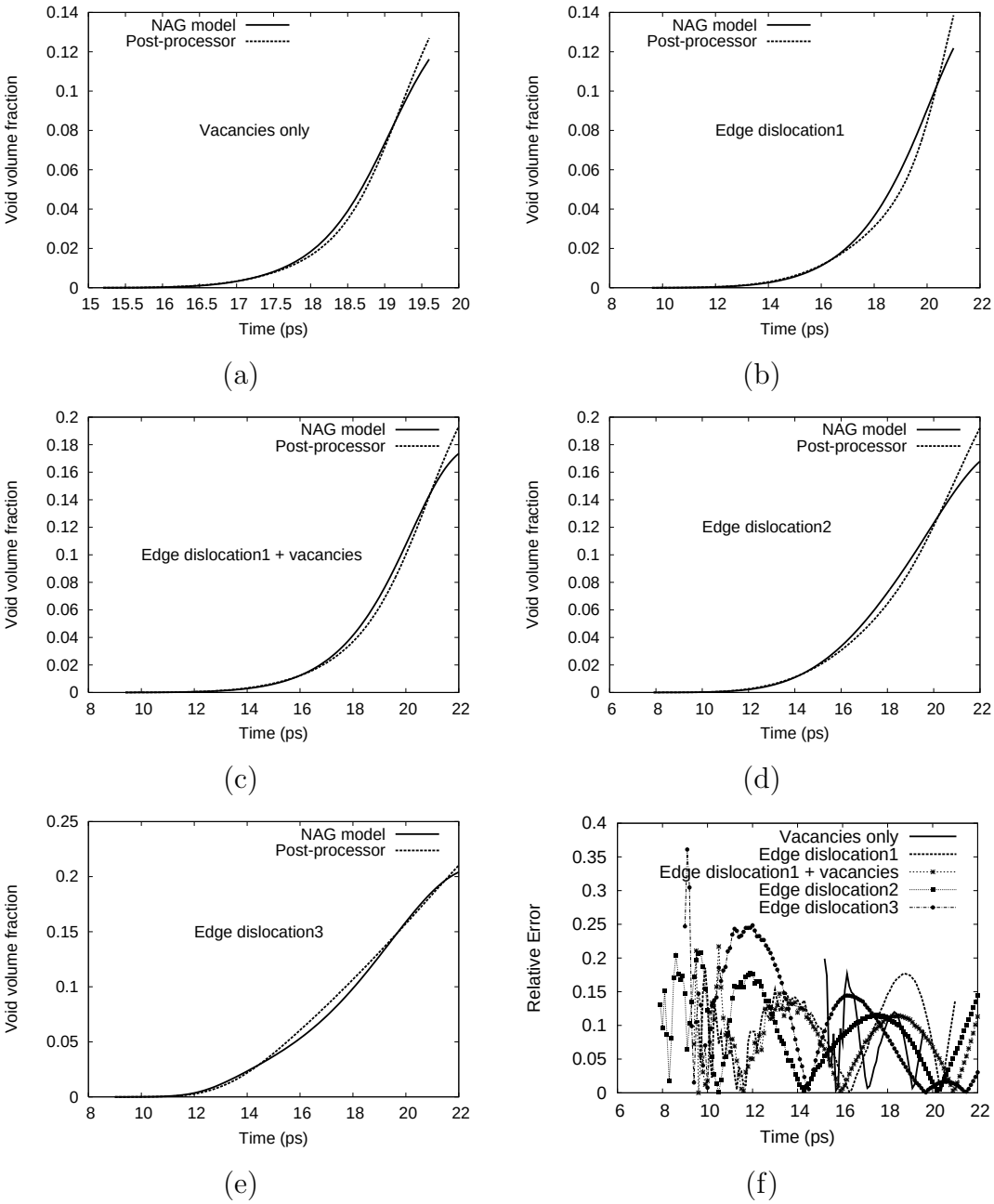

Figure 6.5: Comparison of void volume fraction obtained by NAG model and that by post-processor (Chapter 2.2.1) for single crystal copper deformed triaxially at 5×10^9/s strain rate with (a) vacancies only (b) edge dislocation-1 (c) edge dislocation-1 and few vacancies (d) edge dislocation-2, and (e) edge dislocation-3. (f) Relative error at each data point.

6.2 Hydrodynamic simulation

In the above section (Section 6.1.2), we have obtained NAG parameters for single crystal copper with different kinds of defects, such as dislocations and vacancies. We have used these parameters in a macro-scale hydrodynamic simulation, using a one dimensional Lagrangian hydrocode, to generate spall data. An impact-loaded spallation experiment involving single crystal copper [6] has been simulated using the code. To compute pressure in the computational cells, a six parameter equation of state [17] for copper has been used. We have used the Steinberg-Guinan strain-rate independent dynamic strength model [17] to compute the variation of yield strength and shear modulus with pressure, temperature and plastic strain in the material. The DFRACT model (NAG model), with model parameters obtained from atomistic simulations (Section 6.1.2), has been used to compute damage or porosity. The free surface velocity-time history obtained from simulation is used to derive spall threshold and scab thickness [17].

6.2.1 Perfect crystal copper: No spall

A slab of single crystal copper is impacted by an aluminum flyer with an impact velocity of 660 m/s. The free surface velocity of perfect crystal copper (target) obtained using our simulations and published experiments [6] is shown in Figure 6.6.

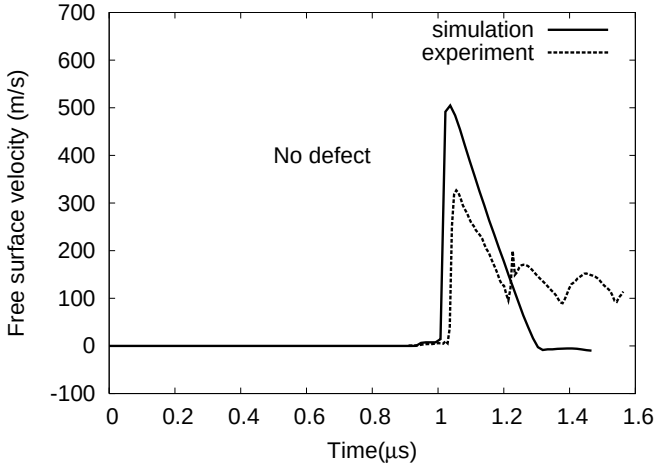

Figure 6.6: Comparison of free surface velocities of target (single crystal copper) obtained from hydrodynamic simulation and experiment. Aluminum flyer impacts single crystal copper with an impact velocity of 660 m/s.

It can be seen that in the simulation, there is no pull back in the free surface velocity of perfect single crystal copper. Now, pull back in free surface velocity is the signature of the spall [12]. This means that no spallation is observed in simulations for perfect crystal copper. Spall in real single crystals, therefore, must be due to the presence of various kinds of defects.

6.2.2 Single crystal copper wth pre-existing edge dislocation-1 and edge dislocation-2: Incipient spall

A comparison of free surface velocities for single crystal copper with pre-existing edge dislocation-1 (Figure 6.1 (b)) and edge dislocation-2 (Figure 6.1 (d)) is shown in Figure 6.7 (a) and Figure 6.7 (b), respectively.

In this case, simulations show pull back in the free surface velocities (Figure 6.7) of the target material, but no complete spall occurs. The pull back in the free surface velocity is due to the growth of the pre-existing voids. Note that in reality, voids nucleate near dislocations, stacking faults etc. Since the dislocation mechanism is missing in the hydrocode, the pre-existing voids are introduced to account for it. For the case of NAG parameters for edge dislocations 1 and 2, the tensile pressure in the material stays below the void nucleation threshold and therefore, no void nucleates. However, the tensile pressure exceeds the void growth threshold, leading to incipient spall of the material.

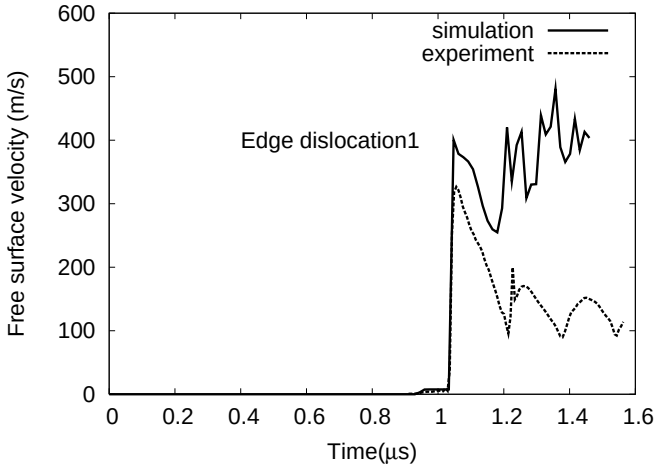

(a)

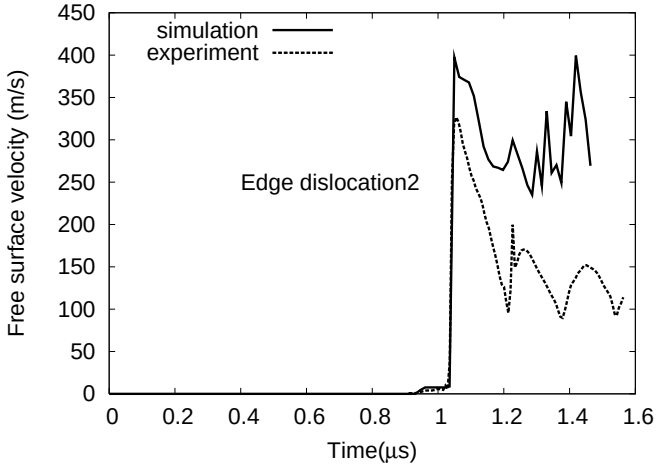

(b)

Figure 6.7: Comparison of free surface velocities obtained from hydrodynamic simulation and experiment for single crystal copper with pre-existing (a) edge dislocation-1 and (b) edge dislocation-2.

6.2.3 Single crystal copper with pre-existing edge dislocation-3: Complete spall

A comparison of free surface velocities obtained from simulation and experiment for single crystal copper with pre-existing edge dislocation-3 is shown in Figure 6.8 (a) and void volume fraction as a function of target thickness is shown in Figure 6.8 (b).

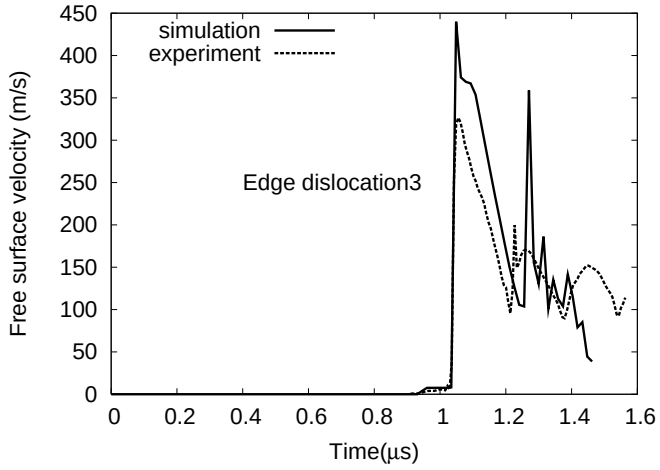

(a)

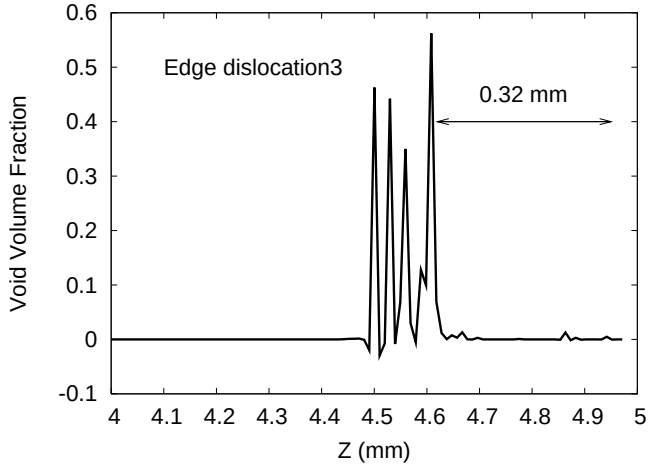

(b)

Figure 6.8: (*a*) Comparison of free surface velocities obtained from hydrodynamic simulation and experiment for single crystal copper with pre-existing edge dislocation-3 (*b*) Void volume fraction as a function of target thickness.

In Figure 6.8 (a), a clear pull back is seen in the free surface velocity of the target and complete spall of the material is observed. A comparison of spall strength and spall thickness obtained from simulation for single crystal copper with experiment [6] is shown in Table 6.2. It is seen in Table 6.2 that results agree reasonably well with published experimental results [6] within an error of 20%.

Method	Parameters	
	Spall strength (kbar)	Spall thickness (mm)
Simulation	48.0	0.32
Experiment	39.5± 0.1	0.3 (10%)

Table 6.2: Comparison of spall strength and spall thickness obtained from hydrodynamic simulation with the experiment [6].

6.3 Conclusion

We have performed MD simulations to simulate isotropic tension in single crystal copper with pre-existing defects, such as dislocations and vacancies. Best-fit NAG parameters are obtained. These parameters are then used in a macro-scale hydrodynamic simulation to generate spall data. The results are compared with published experimental data for single crystal copper. We find that our results come closest to published experimental results, within an error of 20%, for the case of a pre-existing edge dislocation (edge dislocation-3) defect. Other kinds of defects lead to larger variations in the free surface velocity.

The conclusions of the present work are as follows:

- A multi-scale model has been developed where NAG parameters obtained using MD simulations for single crystal copper with pre-existing defects is used in a macroscopic hydrodynamic code to simulate shock in single crystal.
- For a particular kinds of defect, multi-scale results match with experimental results within 20% error.

Chapter 7

High strain deformation of single crystal copper: Experiments and MD simulations

As mentioned in Chapter 1, hydrodynamic simulations require three main inputs to simulate impact and shock wave problems:

- Fracture parameters.
- Material strength during high strain-rate deformation.
- Equation of state.

All previous chapters have dealt with fracture. In this chapter, material strength parameters for single-crystal copper have been obtained by performing experiments at 10^3/s strain rate, using the Split Hopkinson Pressure Bar (SHPB) method [97].

Several workers [98–100] have performed experiments on single crystal copper to study the various aspects, such as activation of slip systems, under quasi-static loading. Here single crystal copper is uniaxially deformed at 10^3/s strain rate to get material strength parameters.

7.1 Split Hopkinson Pressure Bar

7.1.1 Theory

An SHPB consists of a compressed gas-gun, a striker bar, pressure bars (incident and transmission bars), specimen and data acquisition system, as shown in Figure 7.1. To record the incident, reflected and transmitted waves, strain gauges are mounted on the incident and transmission bars. The striker bar, accelerated by gas, hits the

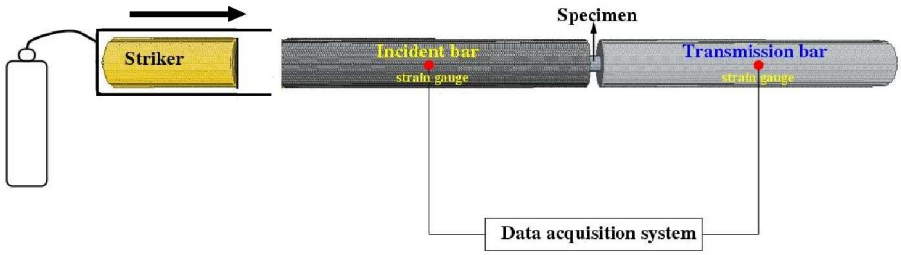

Figure 7.1: Schematic of split-Hopkinson pressure bar

incident bar, producing compressive stress waves at the point of impact. These waves move toward the free surfaces of the striker bar and the other end of the incident bar attached to the specimen. When the compressive wave reaches the free surface of the striker bar, it reflects as a tension wave. When this tension wave reaches the striker bar-incident bar interface, the striker bar gets separated out since tension can not pass through the interface. This leads to the creation of a compressive wave in the incident bar having a wave length (spatial duration) equal to twice the length of the striker bar. When the compressive wave reaches the incident bar-specimen interface, impedance mismatch occurs at the interface, leading to partial reflection of the wave as a tension wave in the incident bar and partial transmission of the compressive wave into the specimen. When the compressive wave reaches the specimen-transmission bar interface, again due to impedance mismatch, the wave is partially reflected as a compressive wave and partially transmitted as a compressive wave to the transmission bar. During this process, a compressive wave is trapped in the specimen which, by multiple reverberations, leads to plastic deformation of the specimen.

Using one-dimensional elastic wave propagation theory [101], assuming homogeneous deformation of the specimen under uniaxial stress conditions, the average

or engineering strain, stress and strain-rate in the specimen are given by

$$e_s(t) = -2\frac{c_0}{l}\int_0^t \epsilon_R(t)dt \tag{7.1}$$

$$s_s(t) = E\frac{A}{A_s}\epsilon_T(t) \tag{7.2}$$

$$\dot{e_s}(t) = -2\frac{c_0}{l}\epsilon_R(t) \tag{7.3}$$

where l is the initial length of the specimen, c_0 is the elastic wave velocity in the pressure bars ($c_0 = \sqrt{E/\rho}$), A is the cross-sectional area of the bar and A_s is the cross-sectional area of the specimen, E is the Young's modulus of the bar, t is the time duration, ϵ_R and ϵ_T are the axial strains obtained from the reflected and transmitted pulses, respectively.

The true stress, true strain and true strain-rate in the specimen [102] are given by

$$\sigma_s = s_s(t)[1 - e_s(t)] \tag{7.4}$$

$$\epsilon_s(t) = -\ln[1 - e_s(t)] \tag{7.5}$$

$$\dot{\epsilon_s} = \frac{\dot{e}_s(t)}{1 - e_s(t)} \tag{7.6}$$

7.1.2 Strain gauge output

The raw output obtained from strain gauges mounted on the incident and transmission bars for single crystal copper deformed at $\sim 10^3$/s strain rate is shown in Figure 7.2(a). The strain and stress produced in the specimen due to the impact of striker bar on the incident bar are obtained by using the following relations [103]

$$\epsilon = \frac{2\Delta V}{V_0 k G} \tag{7.7}$$

$$\sigma = \frac{2\Delta V E}{V_0 k G} \tag{7.8}$$

where ΔV is the signal from the strain gauges mounted on the bars, E is the elastic modulus of the bar, V_0 is the excitation voltage, k is the gage factor and G is the gain. The incident, reflected and transmitted stress waves are shown in Figure 7.2(b).

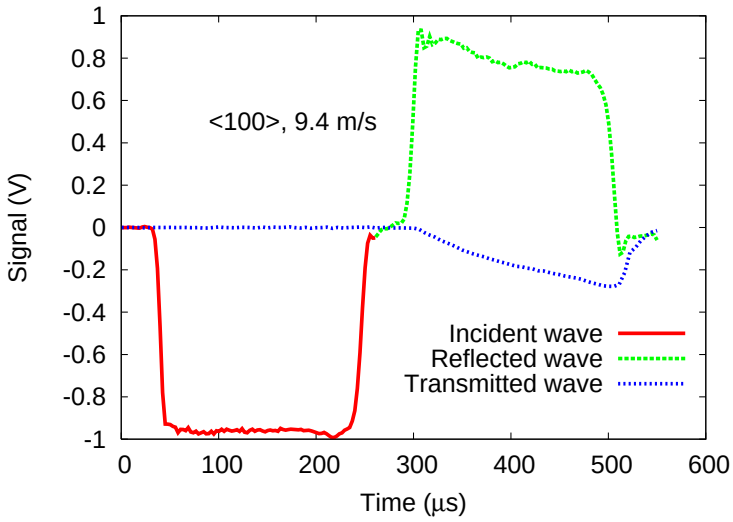

(a)

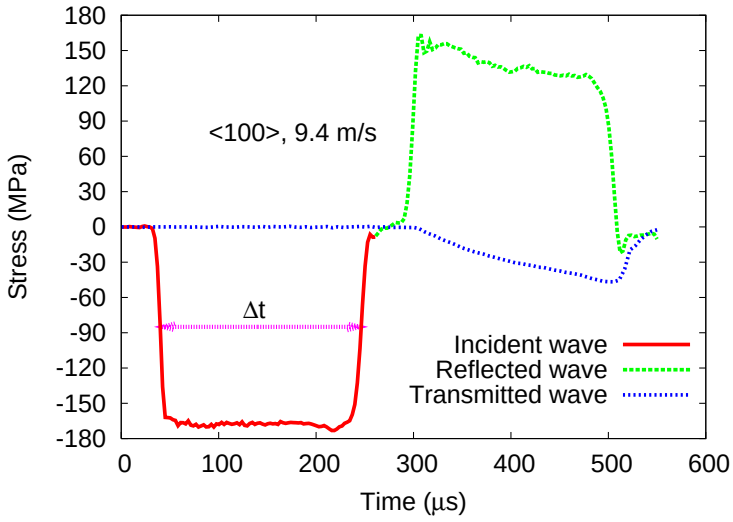

((b)

Figure 7.2: (*a*) Strain gauge raw output obtained from incident and transmission bars for high strain rate test on single crystal copper at room temperature for an impact velocity of 9.4 m/s in SHPB (*b*) Strain gauge raw output converted to stress for the impact velocity of 9.4 m/s.

7.1.3 Maximum stress generated in the incident bar and pulse duration

The maximum stress generated due to the impact of the striker bar on the incident bar is given by [104]

$$\sigma_{\max} = \frac{\rho c_0 v}{2} \tag{7.9}$$

where v is the velocity of the striker bar, ρ (7746 kg/m^3) is the density of the pressure bars and c_0 (4793 m/s) is the elastic wave velocity in the pressure bars.

For an impact velocity of 9.4 m/s, the maximum stress generated is given by

$$\sigma_{\max} = \frac{7746 \times 4793 \times 9.4}{2} = 174\text{MPa} \tag{7.10}$$

This is in agreement with the maximum stress obtained from the experiment on single crystal copper, as shown in Figure 7.2 (b).

The duration of the pulse generated is given by

$$\Delta t = \frac{2L}{c_0} = \frac{2 \times 0.5}{4793} = 208\mu s \tag{7.11}$$

where L is the length of the striker bar. The pulse duration calculated is also in agreement with that obtained from the experiment, as shown in Figure 7.2 (b).

7.2 Experimental Procedure

7.2.1 Preparation of single crystal specimens for SHPB

A single crystal copper of dimension 25.0 mm (diameter)× 20.0 mm (height) was grown by Bridgman method[1] (Figure 7.3). The neutron diffraction method has been used to determine the crystalline perfection and orientation of the copper sample. The instruments used were a Triple Axis Neutron Spectrometer (TAS) [105], and a Filter Detector Neutron Spectrometer (FDS) at Dhruva reactor, BARC. In these spectrometers, the (111) reflection of large copper single crystals are used to obtain a monochromatic neutron beam. The collimator in the monochromatic beam allows a beam cross section of 5.0 cm × 5.0 cm onto the sample and the horizontal divergence would be 1° [106].

[1]Single crystal copper is provided by Prof. Thamizhavel from Tata Institute of Fundamental Research (TIFR), Mumbai, India. This contribution is gratefully acknowledged.

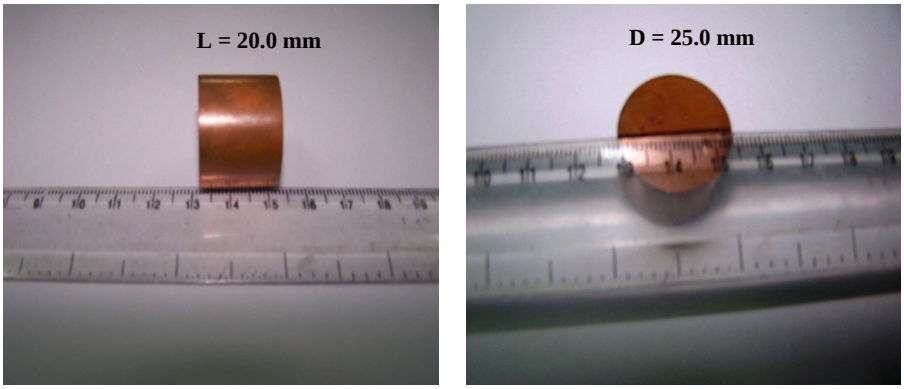

Figure 7.3: Cylindrical single crystal copper of dimension 25.0 mm (diameter)×20.0 mm (height).

The methodology employed is the measurement of a neutron diffraction rocking curve. This is the measurement of the intensity of an "hkl" reflection as the crystal is turned around its vertical axis, in order to characterize the quality of the crystal regarding its mosaicity $\Delta\theta$ – the planes that theoretically should be parallel to each other differ in reality by an angle $\Delta\theta$. In general, this rocking curve shows overlapping peaks if crystalline domains (closely aligned in the direction of measurement) are present in the crystal.

During the measurement, the neutron detector remains in a fixed position at the scattering angle $2\theta_{hkl}$ relative to the incident beam. The wavelength of the neutrons used was 2.3 Å. The crystal to be investigated was attached firmly to the head of a two-axis goniometer, with the cylinder axis vertical. The goniometer was then placed on the sample table of the spectrometer. Careful orientation of the crystal in the neutron beam was carried out in order to obtain the maximum intensity of the (111) and (200) reflections. The rocking curve was obtained by rotating the crystal in steps of 0.1° with a count time of 10 s for each step. The determined orientation of the copper crystal has helped in marking the <100> direction as well as confirming the $<0\bar{1}1>/<01\bar{1}>$ to be along the axis of the cylinder. The direction marked crystal copper is shown in Figure 7.4.

The rocking curve of the (200) reflection measured on the FDS is shown in Figure 7.5. In Figure 7.5, it is seen that only two good peaks are observed during the whole rotation of the sample. These peaks indicate that the single crystal copper is not a polycrystalline copper. In the inset of Figure 7.5, an expanded scale of the counts (intensity) axis is also shown. In the inset, it is seen that there are small

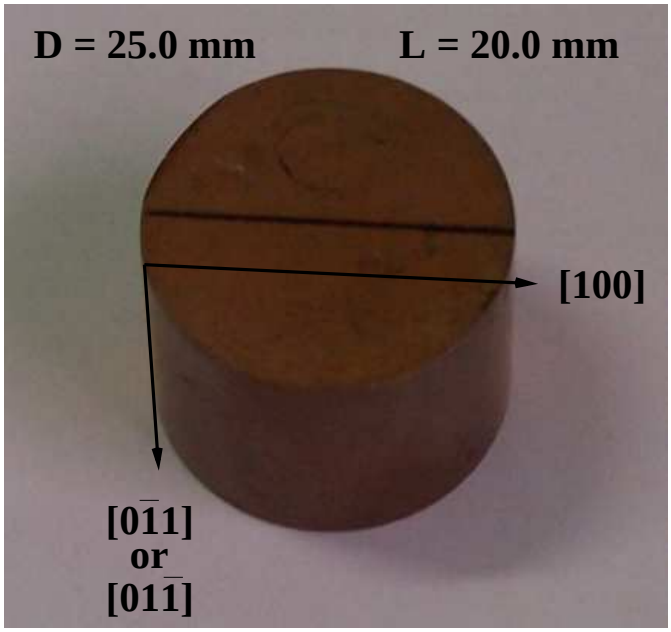

Figure 7.4: Direction marked single crystal copper (L×D = 20.0 mm ×25.0 mm).

peaks in between the two good (big) peaks. The presence of small peaks between the two big peaks signifies the presence of crystallites which are not aligned with the main ones. The rocking curve of (111) reflection (Figure 7.6) also shows the presence of small peaks in-between the big peaks. The rocking curve of the (200) reflection with an expanded scale of sample angle axis is shown in Figure 7.7. A Gaussian fit of the data (Figure 7.7) gives the width to be around 0.9°, which is a measure of the mosaicity of the crystal.

7.2.2 Energy Dispersive X-ray (EDX) Analysis

This technique is used to identify impurities in the specimen. In this technique, an electron beam is used to bombard the specimen. These electrons collide with atoms of different elements present in the specimen. Due to collisions with bombarded electrons, the inner shell electrons in the sample are ejected, leading to vacant positions in the inner shells. These vacant positions are occupied by the high energy electrons from the outer shells of the atoms. The transfer of outer shell electrons to inner shells leads to the release of energy by emitting X-rays. The amount of energy released depends on the energy difference between the energy levels (energy level from where the electron is ejected and that from which the electron is transferred to

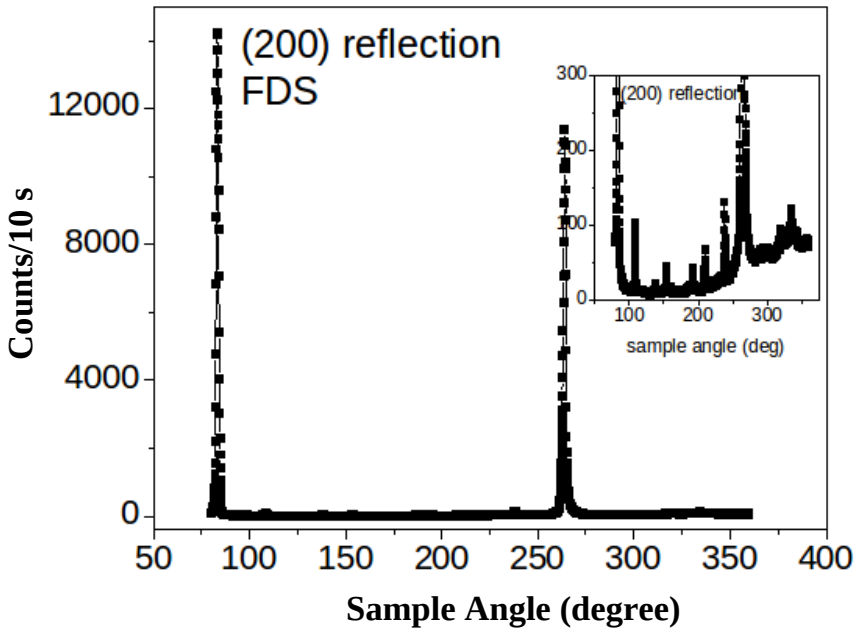

Figure 7.5: Rocking curve of (200) reflection for single crystal copper (Figure 7.3).

occupy the vacant position). The atoms of each element emit X-rays with a unique amount of energy. The measurement of amount of energy present in X-rays is used to identify the atoms present in the specimen.

The EDX spectrum for single crystal copper is shown in Figure 7.8. It is seen in Figure 7.8 that each of the peaks is unique to an atom and hence corresponds to a single element. As expected, the copper peak is the highest, which is a signature of high concentration of the element present in the specimen. Only a few impurities (C, O, Cl and Si) are present in the single crystal copper.

7.3 Johnson-Cook Material Model

The Johnson-Cook (JC) model [27] is a phenomenological model used to reproduce the response of the materials under impact and penetration conditions. The model connects the quasi-static and dynamic mechanical properties of the materials. The material responses which are described by this model are strain hardening, strain rate effect and thermal softening. In this model, the equivalent von Mises stress is

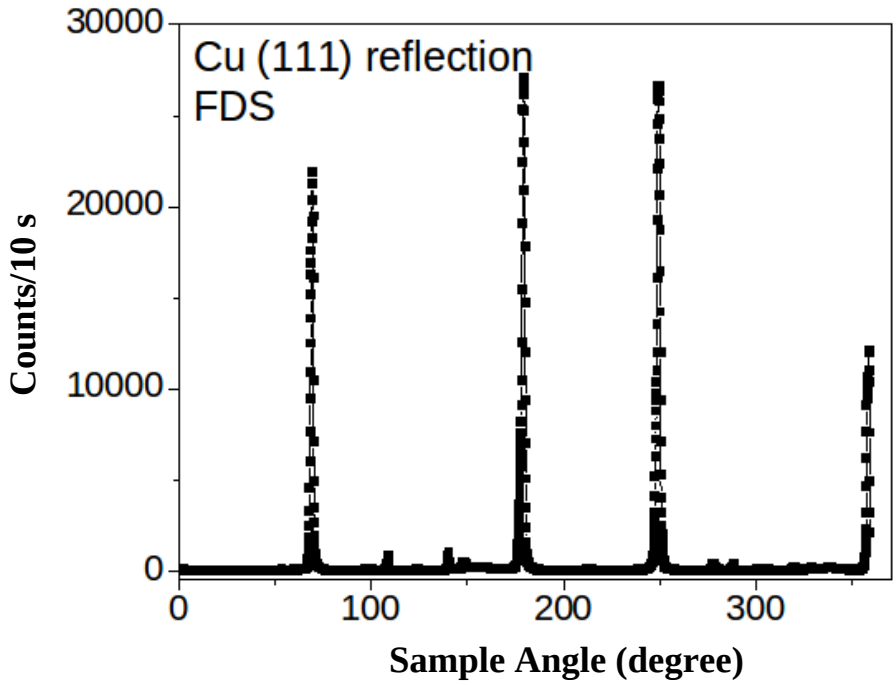

Figure 7.6: Rocking curve of (111) reflection for single crystal copper (Figure 7.3).

given by

$$\sigma_e \quad = \quad [A + B(\epsilon_e^p)^n][1 + C \ln \dot{\epsilon^*}][1 - T^{*m}] \tag{7.12}$$

where A is the quasi-static yield stress, B is the modulus of strain hardening, n is the strain hardening exponent, C is the strain rate hardening constant and m is the thermal softening constant, all of which are material constants. ϵ_e^p is the equivalent plastic strain, $\dot{\epsilon^*} = \frac{\dot{\epsilon_e^p}}{\dot{\epsilon_0}}$ is the plastic strain rate, $\dot{\epsilon_0}$ is the user-defined reference strain rate used to determine A, B, and n.

$$T^* = \frac{T - T_R}{T_M - T_R}$$

is the dimensionless temperature called the homologous temperature, T_M is the melting temperature and T_R is the reference temperature (room temperature) used to determine A, B and n.

There are three terms in parentheses on the right hand side of Eqn. 7.12:

- The first term [A + B $(\epsilon_e^p)^n$] represents the material properties under quasi-static loading.
- The second term [1 + C ln$\dot{\epsilon^*}$] describes the effect of strain-rate hardening.

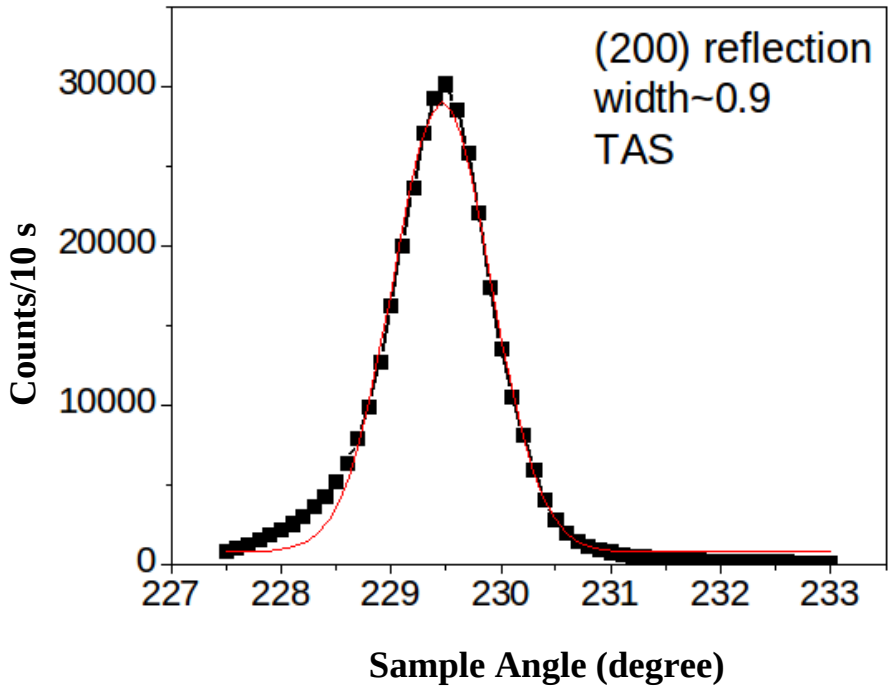

Figure 7.7: Rocking curve of (111) reflection for single crystal copper (Figure 7.3)

- The third term [1 - T^{*m}] describes the thermal softening effect due to imposed temperature.

If thermal softening effects are ignored, i.e. $T^* = 0$ for $T = T_R$, then Eqn. 7.12 becomes

$$\sigma_e = [A + B(\epsilon_e^p)^n][1 + C \ln \dot{\epsilon}^*] \tag{7.13}$$

If strain-rate effect and thermal softening effects are ignored, i.e. $\dot{\epsilon}^* = 1.0$ and $T^* = 0$, then Eqn. 7.12 becomes

$$\sigma_e = [A + B(\epsilon_e^p)^n] \tag{7.14}$$

This describes the relationship between stress and strain under quasi-static loading.

7.4 Results and Discussion

To determine the strength properties, quasi-static experiments using Universal Testing Machine (UTM) and dynamic experiments using SHPB have been performed on single crystal copper loaded along <100> and <110> directions. The details of

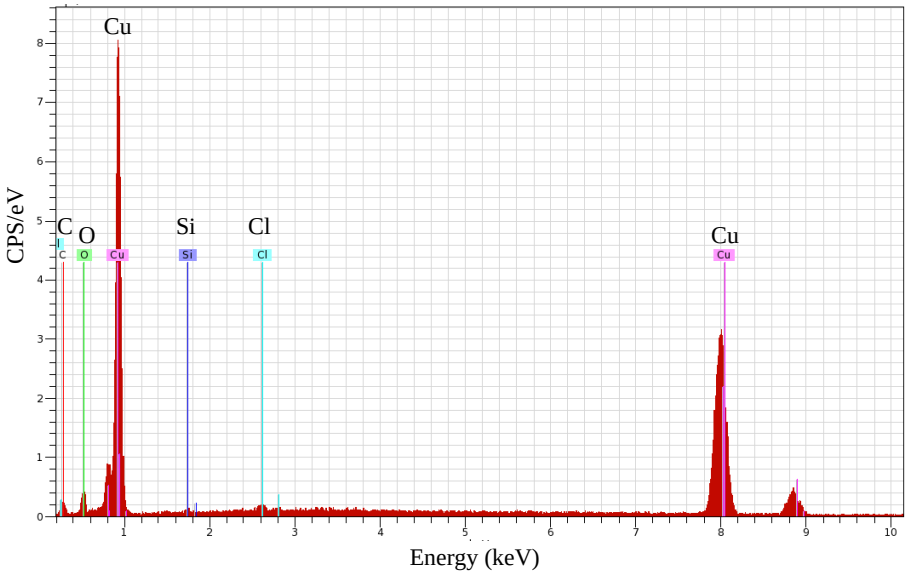

Figure 7.8: EDX spectrum for single crystal copper.

the quasi-static and dynamic compression experiments on single crystal copper are shown in Table 7.1 and Table 7.2, respectively.

Test No	Specimen size L×D (mm)	Orientation	Strain rate (/s)
1	3.94×4.04	100	0.0033
2	3.96×4.06	110	0.0033

Table 7.1: Experimental details for single crystal copper deformed under quasi-static loading at 300 K.

A comparison of true stress as a function of true strain for <100> and <110> loading directions under quasi-static loading is shown in Figure 7.9.

Test No.	Specimen size L×D (mm)	Orientation	Temperature (K)	Gas gun pressure (bar)	Striker bar velocity (m/s)	Average strain rate (/s)
1	3.88×4.04	100	300	1.5	9.38	2300
2	3.94×4.08	100	300	2.0	11.72	3000
3	3.94×4.06	100	300	2.5	13.33	3500
4	3.96×4.0	100	373	2.0	11.72	3000
5	3.96×4.0	100	473	2.0	11.72	3000
6	4.00×4.10	110	300	1.5	9.38	2200
7	3.94×4.10	110	300	2.5	13.33	3500
8	3.96×4.10	110	300	3.0	14.71	4200
9	4.0×4.02	110	373	2.0	11.72	3000
10	3.94×4.0	110	473	2.0	11.72	3000

Table 7.2: Experimental details for single crystal copper deformed under dynamic loading using SHPB.

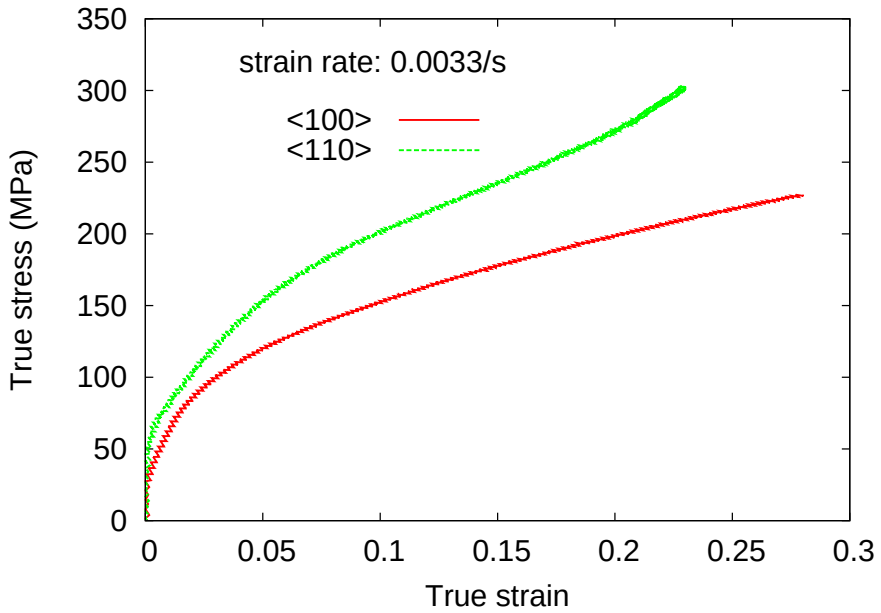

Figure 7.9: Comparison of true stress-true strain curves for single crystal copper deformed along <100> and <110> directions under quasi-static loading.

It is seen in Figure 7.9 that single crystal copper, deformed along the <110> direction, shows more hardening than that deformed along <100> direction.

True stress as a function of true strain at different strain rates is shown in Figure 7.10. Note that the strain rate under dynamic loading is not constant during the deformation.

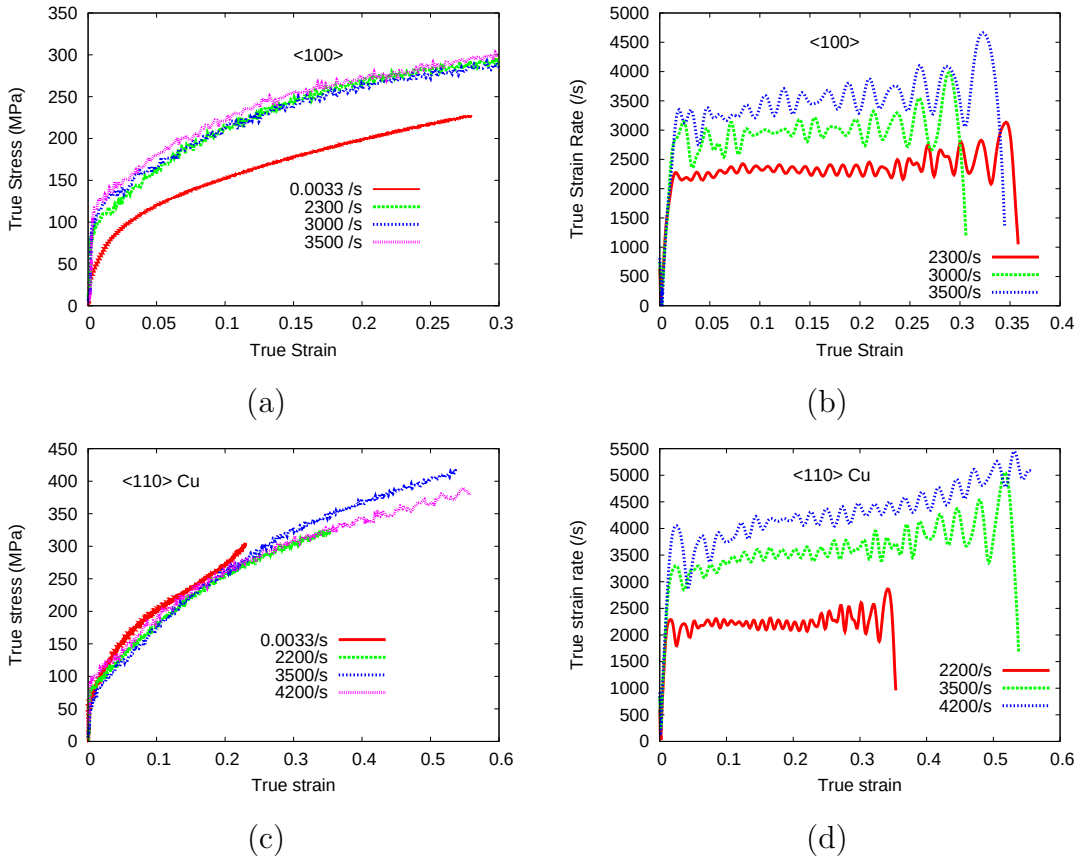

Figure 7.10: Deformation of single crystal copper at 300 K using UTM and SHPB. (*a*) True stress as a function of true strain for single crystal copper deformed along <100> direction (*b*) True strain rate-true strain curve for loading along <100> direction (*c*) True stress-true strain curve for loading along <110> direction (*d*) True strain rate-true strain curve for loading along <110> direction.

The quasi-static data for single crystal copper is used to get three parameters (A, B and n) for the JC model. The strain rate coefficient (C) is obtained by using stress-strain data at different strain rates, while the thermal softening coefficient (m) is obtained by using stress-strain data at different temperatures for a constant strain rate. JC model parameters for single crystal copper deformed along <100> and <110> directions are shown in Table 7.3. For experiments performed at room

JC model parameters	Orientation	
	<100>	<110>
A (MPa)	35.0	55.0
B (MPa)	355.3	537.8
n	0.46	0.62
C	0.022	0.0009
m	0.85	0.9

Table 7.3: JC model parameters for single crystal copper deformed at 10^3/s strain rate along <100> and <110> directions.

temperature (i.e., T = T_R), Eqn. 7.13 becomes

$$\sigma_e = \begin{cases} [35.0 + 355.3(\epsilon_e^p)^{0.46}][1 + 0.022 \ln \dot{\epsilon^*}] & for < 100 > \\ [55.0 + 537.8(\epsilon_e^p)^{0.62}][1 + 0.0009 \ln \dot{\epsilon^*}] & for < 110 > \end{cases} \tag{7.15}$$

For single crystal copper deformed along <100> and <110> directions, a comparison of true stress-true strain curves obtained from experiments and that using Eqn. 7.15 is shown in Figure 7.11.

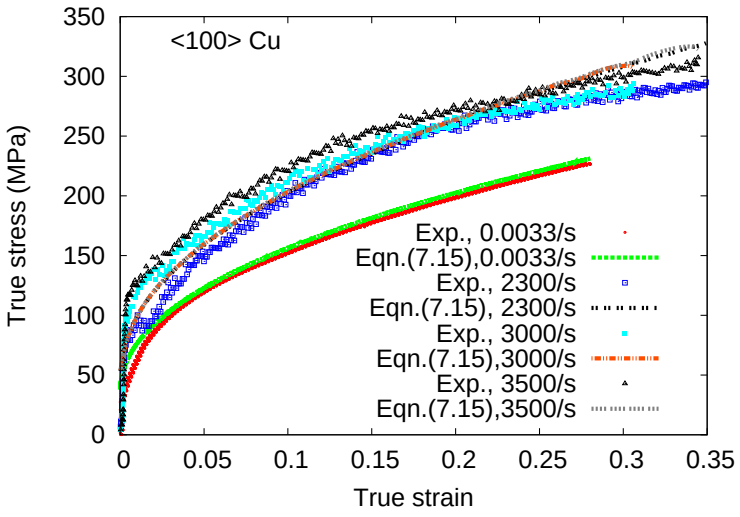

(a)

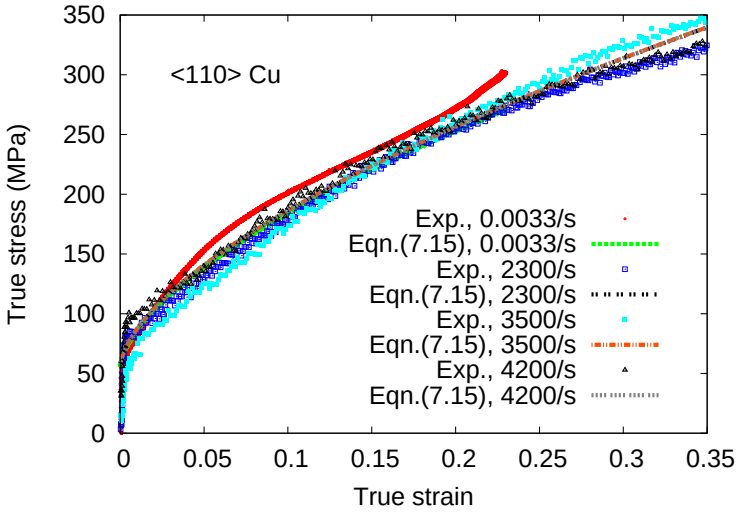

(b)

Figure 7.11: Comparison of true stress-true strain curves obtained from experiments and that using Eqn. 7.15 for single crystal copper deformed at 10^3/ strain rate along (a) <100> direction (b) <110> direction.

As mentioned above, by performing experiments at different temperatures at constant average strain rate, the thermal softening coefficient is determined. Therefore, Eqn. 7.13 becomes

$$\sigma_e = \begin{cases} [35.0 + 355.3(\epsilon_e^p)^{0.46}][1 + 0.022 \ln \dot{\epsilon^*}][1 - T^{*0.85}] & for < 100 > \\ [55.0 + 537.8(\epsilon_e^p)^{0.62}][1 + 0.0009 \ln \dot{\epsilon^*}][1 - T^{*0.9}] & for < 110 > \end{cases} \quad (7.16)$$

Comparison of true stress-true strain curves obtained from experiments and that using Eqn. 7.16 for single crystal copper deformed along <100> and <110> directions at different temperatures and different strain rates is shown in Figure 7.12.

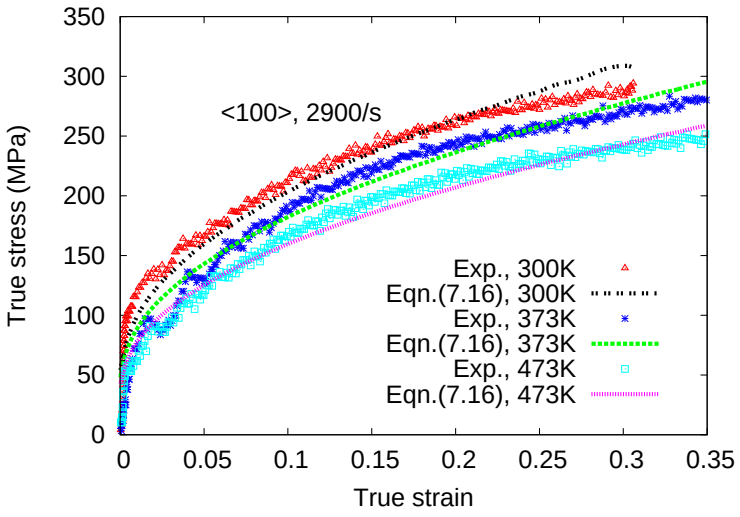

(a)

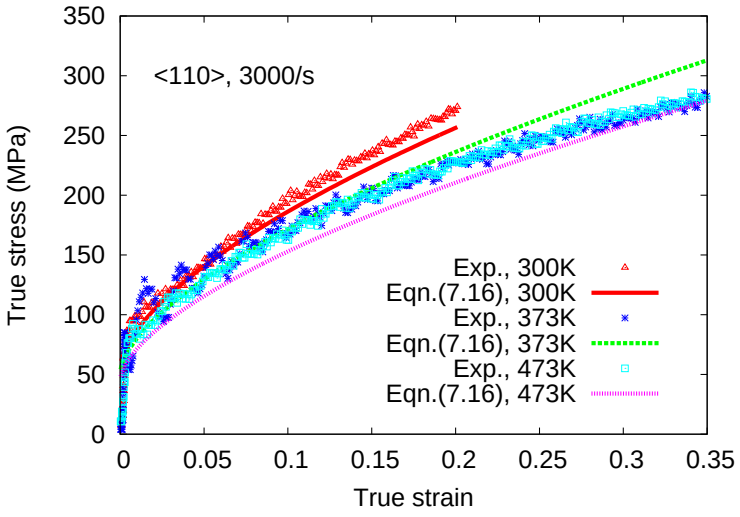

(b)

Figure 7.12: Comparison of true stress-true strain curves obtained from experiments and that using Eqn. 7.16 for single crystal copper deformed at 10^3/ strain rate along (a) <100> direction (b) <110> direction.

It can be seen from Figure 7.12 that there is good agreement between the stress-strain curves obtained by experiments and that obtained using Eqn. 7.16.

7.5 Estimation of dislocation density

To estimate the dislocation density in single crystal copper, neutron diffraction analysis has been carried out before and after the deformation of single crystal copper at 10^3/s strain rate. The analysis has been done for single crystal copper deformed along <100> direction. The neutron diffraction analysis method is described in Section 7.2.1.

The true stress-true strain curves and true strain rate-true strain curves for two specimens (specimen12 and specimen 13), deformed at two impact velocities of the striker bar, are shown in Figure 7.13.

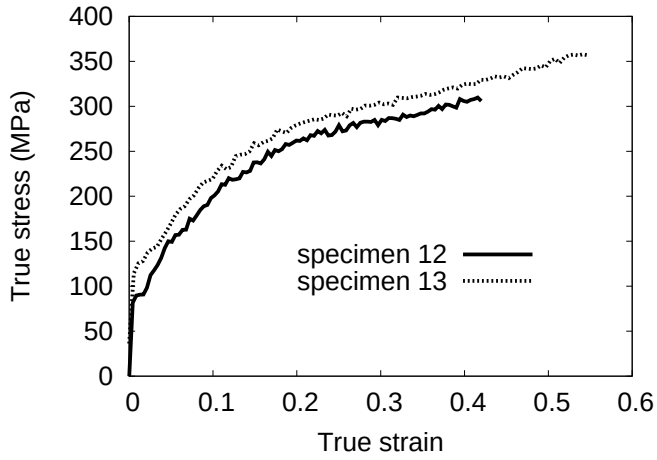

(a)

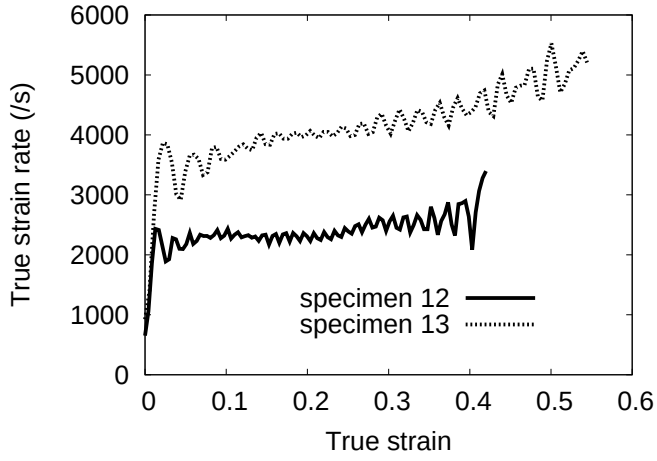

(b)

Figure 7.13: (a) True stress-true strain curves for specimen 12 and specimen 13 (b) True strain-rate as a function of true strain for specimen 12 and specimen 13.

The rocking curves of (200) and (220) reflections for specimen 12 and specimen 13, before and after the deformation, are shown in Figure 7.14.

The full width at half maximum (FWHM) for specimen 12 and specimen 13, before and after the deformation, is calculated using the rocking curves as shown in Figure 7.15 and Figure 7.16, respectively.

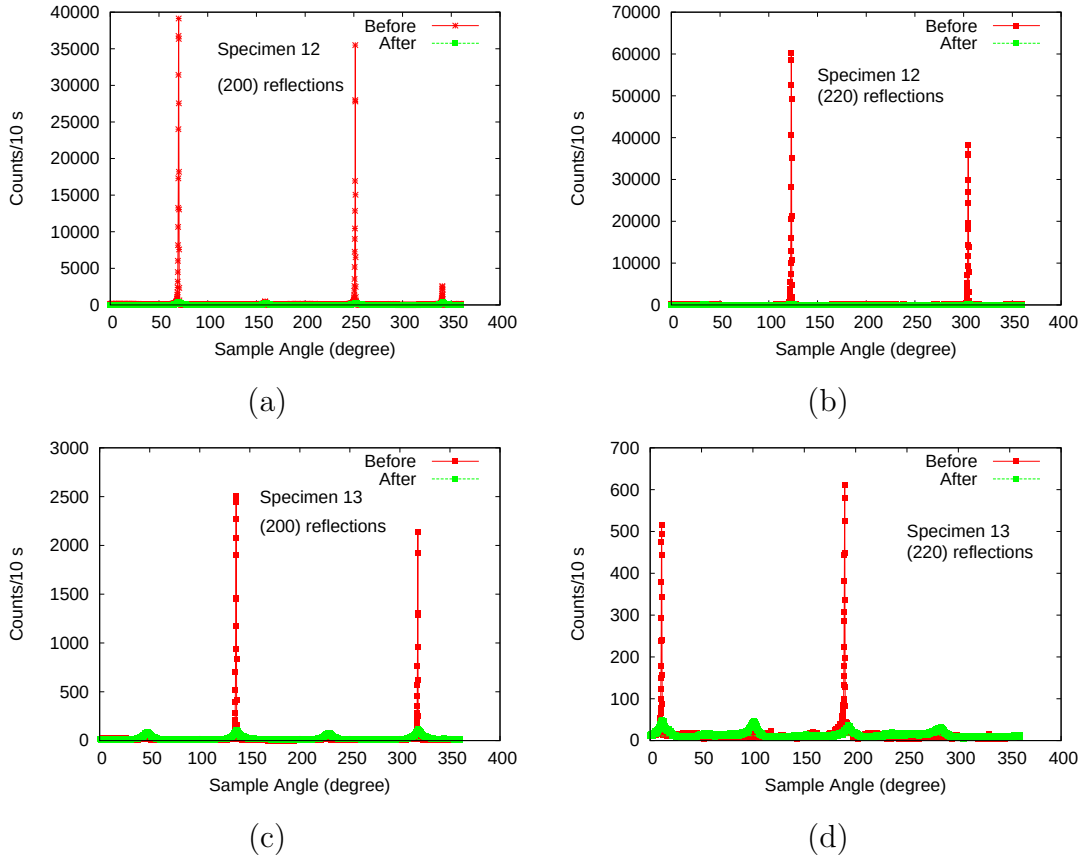

Figure 7.14: Rocking curve of (*a*) (200) reflections for specimen 12 (*b*) (220) reflections for specimen 12 (*c*) (200) reflections for specimen 13 (*d*) (220) reflections for specimen 13.

Assuming a random distribution of the dislocations on all possible slip systems, the average dislocation density (D) [107] is given by

$$D = \frac{\beta^2}{9b^2} \tag{7.17}$$

where β is the FWHM of the rocking curves measured by neutron diffraction, and b is the Burger vector (here b = $\frac{a}{2}$ <110> = 0.255 nm, a = 0.361 nm). Using Eqn. 7.17, the dislocation density for single crystal copper deformed along <100> and <110> directions is shown in Table 7.4.

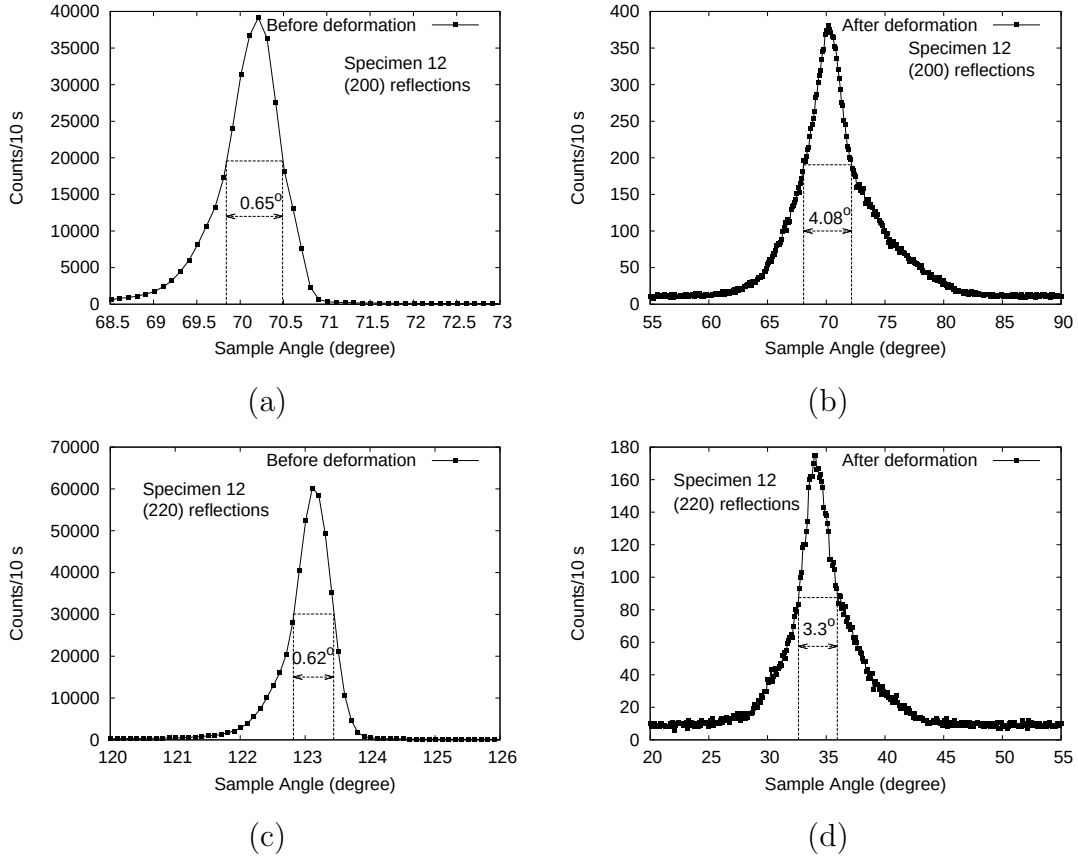

Figure 7.15: FWHM for specimen 12 (a) before deformation for (200) reflections (b) after deformation for (200) reflections (c) before deformation for (220) reflections and (d) after deformation for (220) reflections. Specimen 12 is deformed at 10^3/s (Figure 7.13) along <100> crystal direction.

7.6 Molecular dynamics simulation

To understand the shape changes observed in experiments on single crystal copper and to reproduce the number of active slip directions during deformation of single crystal copper loaded along <100> and <110> directions, MD simulations have been performed at high strain rate under uniaxial stress loading.

The simulation domain contains 100×100×100 unit cells along x-, y- and z-directions. Periodic boundary conditions are used along each direction. Equations of motion are integrated with a time step of 0.5 femto-second using velocity Verlet algorithm. After relaxing the system at 300 K temperature and 0 bar pressure for 100 pico-second, uniaxial compression at 5×10^9/s strain rate has been applied along the x-direction. The pressure along y- and z-directions has been controlled at 0

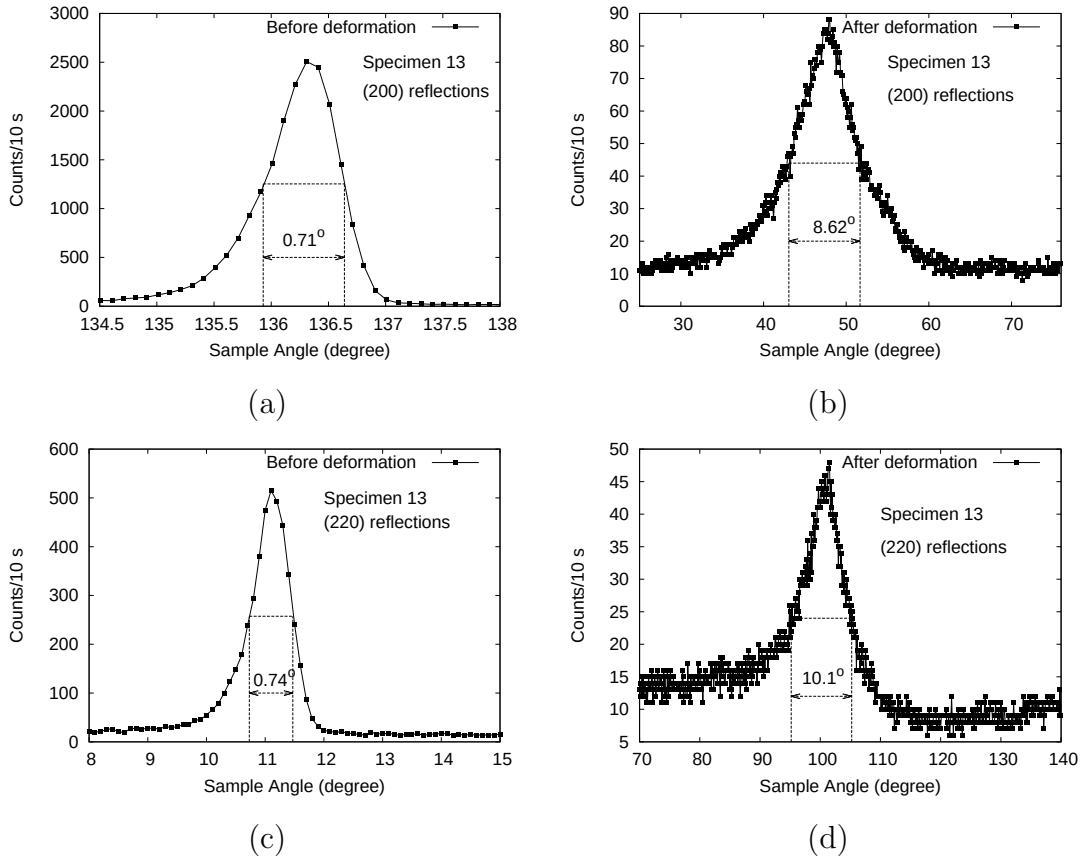

Figure 7.16: FWHM for specimen 13 (*a*) before deformation for (200) reflections (*b*) after deformation for (200) reflections (*c*) before deformation for (220) reflections and (*d*) after deformation for (220) reflections. Specimen 13 is deformed at 10^3/s (Figure 7.13) along <100> crystal direction.

pressure using an NPT ensemble, thereby letting the solid change shape and size along these directions.

7.6.1 Number of slip systems activated

Single crystal copper uniaxially compressed along <100> and <110> directions at 5×10^9/s strain rate first deforms elastically and then plastically once the threshold for dislocation nucleation is crossed. The deformation along the <100> direction leads to the activation of 8 slip systems and that along the <110> direction activates 4 slip systems [108] out of 12 active slip systems in FCC metals. In order to study the slip systems activated during dynamic deformation, Burger vectors have been calculated using the DXA code [109]. These Burger vectors are then used to get

Sample		(200) reflection		(220) reflection	
		FWHM (degree)	Average dislocation density ($/m^2$)	FWHM (degree)	Average dislocation density ($/m^2$)
12	Before deformation	0.65	2.2×10^{14}	0.62	2.0×10^{14}
	After deformation	4.08	86.6×10^{14}	3.3	56.6×10^{14}
13	Before deformation	0.71	2.6×10^{14}	0.74	2.8×10^{14}
	After deformation	8.62	386.7×10^{14}	10.1	530.9×10^{14}

Table 7.4: FWHM and average dislocation density for specimen 12 and specimen 13 before and after the deformation of single crystal copper obtained from rocking curves (Figure 7.15 and Figure 7.16).

the slip directions. The number of slip directions activated in single crystal copper deformed along <100> and <110> directions are shown in Figure 7.17.

It is seen in Figure 7.17 (a) that there are 8 sets of h, k and l values which indicate the activation of 8 slip directions. In Figure 7.17 (b), there are 4 sets of h, k and l values which indicate the activation of 4 slip directions in single crystal copper deformed along <110> direction. This reproduces the number of active slip directions observed by [108].

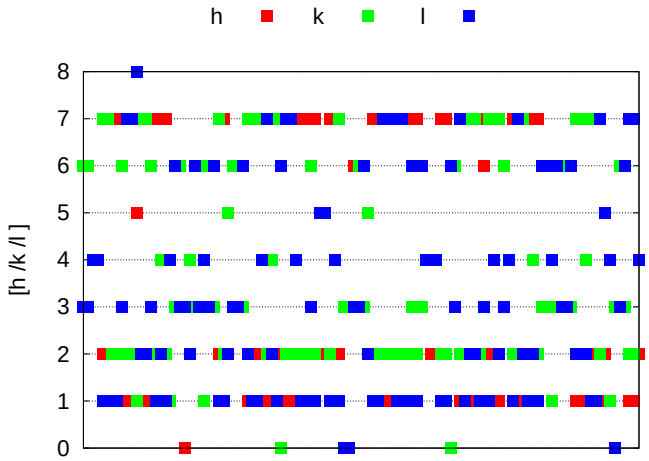

(a)

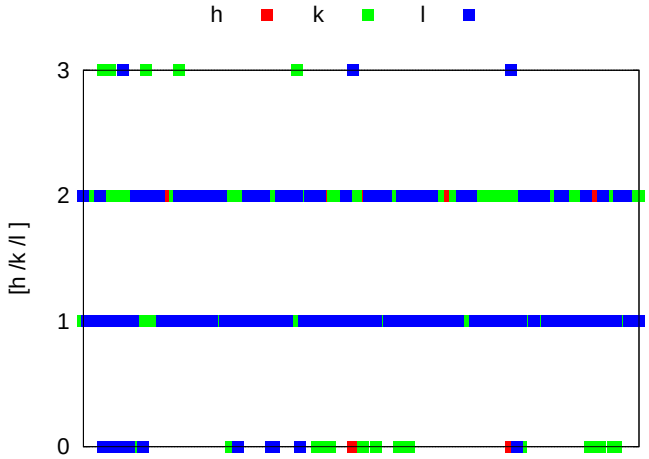

(b)

Figure 7.17: Number of slip directions activated during deformation of perfect single crystal copper at 5×10^9/s strain rate with 300K along (*a*) <100> direction (*b*) <110> direction.

7.6.2 Shape changes in the deformation of single crystal copper

The Poisson ratio as a function of strain for single crystal copper deformed at 5×10^9/s strain rate along <100> and <110> directions is shown in Figure 7.18.

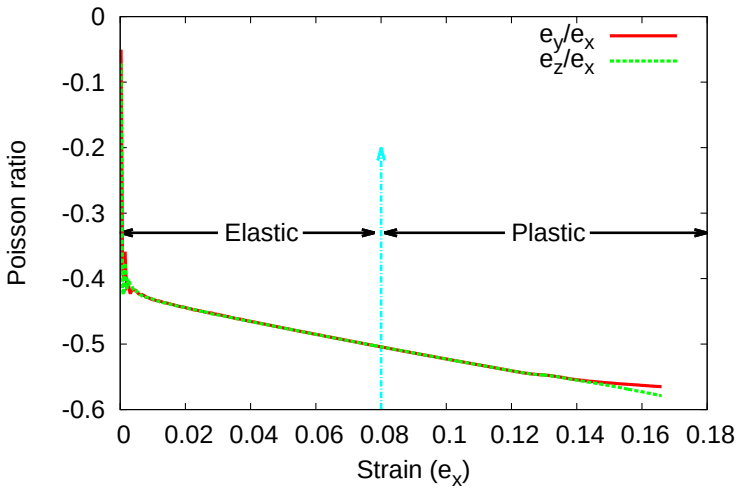

(a)

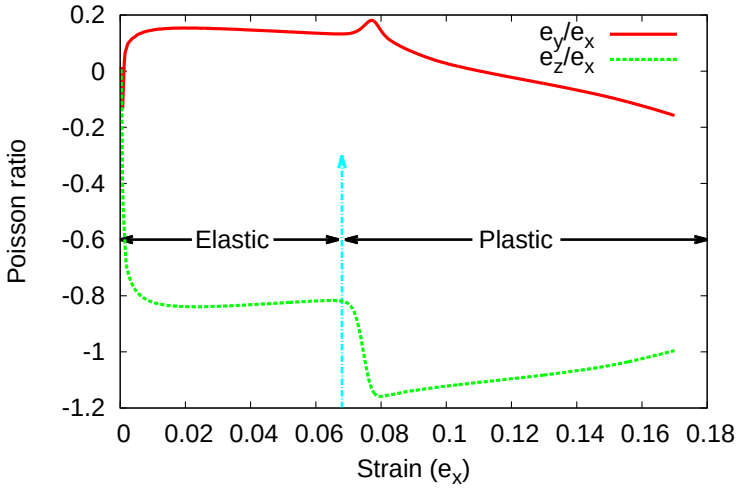

(b)

Figure 7.18: Poisson ratio as a function of strain in the direction of compression for single crystal copper deformed at 5×10^9 strain rate along (*a*) <100> direction (*b*) <110> direction.

The arrow in Figure 7.18 indicates the onset of plastic deformation due to homogeneous nucleation of dislocations. It is seen in Figure 7.18 (a) that for <100> loading direction, the Poisson ratio is negative for both y- and z-directions. This indicates the expansion of the crystal along y- and z-directions due to compression along x-direction. This supports the shape changes observed in experiments on cylindrical single crystal copper specimens loaded along <100> direction. The

image of single crystal copper specimen deformed along <100> direction at 10^3/s strain rate using SHPB is shown in Figure 7.19(a).

For loading along the <110> direction, the Poisson ratio is positive along the y-direction and negative along the z-direction, as shown in Figure 7.18(b). This indicates that during elastic deformation, the crystal contracts along the y-direction and expands along the z-direction due to compression in x-direction. Note that deformation of single crystal copper is large along the z-direction compared to y-direction. Note also that during plastic deformation, single crystal copper expands along both y- and z-directions, but with larger deformation along the z-direction. The image of the specimen deformed along <110> direction at 10^3/s strain-rate using SHPB is shown in Figure 7.19(b).

Thus, the shape changes observed in SHPB experiments on single crystal copper are validated by MD simulations.

(a) (b)

Figure 7.19: Single crystal copper deformed at 10^3/s strain rate using SHPB along (a) <100> direction (b) <110> direction.

To understand the shape changes of the above samples, Schmid factor calculations have been performed on the (111) slip plane to determine the activation of slip directions. It is known that shear stresses are produced when load is applied on the material [110]. The shear stress produced leads to slip in the material if it reaches a threshold value called critical resolved shear stress (CRSS). The critical resolved shear stress (τ) is given by

$$\tau_R = \sigma \cos\phi \cos\lambda \tag{7.18}$$

where σ is the axial stress, ϕ is the angle between normal to slip plane and the ten-

sion/compression axis, λ is the angle between slip direction and tension/compression direction. Here $\cos\phi\cos\lambda$ is called the Schmid factor (m). The value of Schmid factor determines activation of the slip systems. The slip systems which have highest Schmid factor will activate first.

Shape changes when deformed along <100> direction

For (111) slip plane and <100> compression axis, the angle between the two is given by

$$\cos\phi = \frac{(1)(1)+(1)(0)+(1)(0)}{\sqrt{1^2+1^2+1^2}\sqrt{1^2+0^2+0^2}} = \frac{1}{\sqrt{3}} \tag{7.19}$$

The slip plane (111) contains three slip directions: $<\bar{1}10>$, $<\bar{1}01>$ and $<0\bar{1}1>$. Therefore, the angle between slip directions and the compression axis (<100>) is given by

$$\cos\lambda = \frac{(\bar{1})(1)+(1)(0)+(0)(0)}{\sqrt{(\bar{1})^2+1^2+0^2}\sqrt{1^2+0^2+0^2}} = -\frac{1}{\sqrt{2}} \quad for <\bar{1}10> \tag{7.20}$$

$$\cos\lambda = \frac{(\bar{1})(1)+(0)(0)+(1)(0)}{\sqrt{(\bar{1})^2+0^2+1^2}\sqrt{1^2+0^2+0^2}} = -\frac{1}{\sqrt{2}} \quad for <\bar{1}01> \tag{7.21}$$

$$\cos\lambda = \frac{(0)(1)+(\bar{1})(0)+(1)(0)}{\sqrt{0^2+(\bar{1})^2+1^2}\sqrt{1^2+0^2+0^2}} = 0 \quad for <0\bar{1}1> \tag{7.22}$$

Therefore, the Schmid factor (m) for $<\bar{1}10>$ slip direction is given by

$$m_{<\bar{1}10>} = \cos\phi\cos\lambda = (\frac{1}{\sqrt{3}})(-\frac{1}{\sqrt{2}}) = -\frac{1}{\sqrt{6}} = -0.408 \tag{7.23}$$

Similarly, for $<\bar{1}01>$ and $<0\bar{1}1>$ slip directions, the Schmid factor is given by

$$m_{<\bar{1}01>} = \cos\phi\cos\lambda = (\frac{1}{\sqrt{3}})(-\frac{1}{\sqrt{2}}) = -\frac{1}{\sqrt{6}} = -0.408 \tag{7.24}$$

$$m_{<0\bar{1}1>} = \cos\phi\cos\lambda = (\frac{1}{\sqrt{3}})(0) = 0 \tag{7.25}$$

It is seen from Eqn. 7.23 and Eqn. 7.24 that the Schmid factor for $<\bar{1}10>$ and $<\bar{1}01>$ is equal and non-zero, which means that both these slip directions will activate simultaneously. For $<0\bar{1}1>$ slip direction, the Schmid factor is zero which means that no slip will occur along this direction since there is no shear stress along this direction (Eqn. 7.18). This is the reason why single crystal copper expands along y-

and z-directions when deformed along <100> direction (x-direction). The graphical representation of activation of slip directions on 4 active slip planes for single crystal copper deformed along <100> direction is shown in Figure 7.20 and the details of the slip systems are tabulated in Table 7.5.

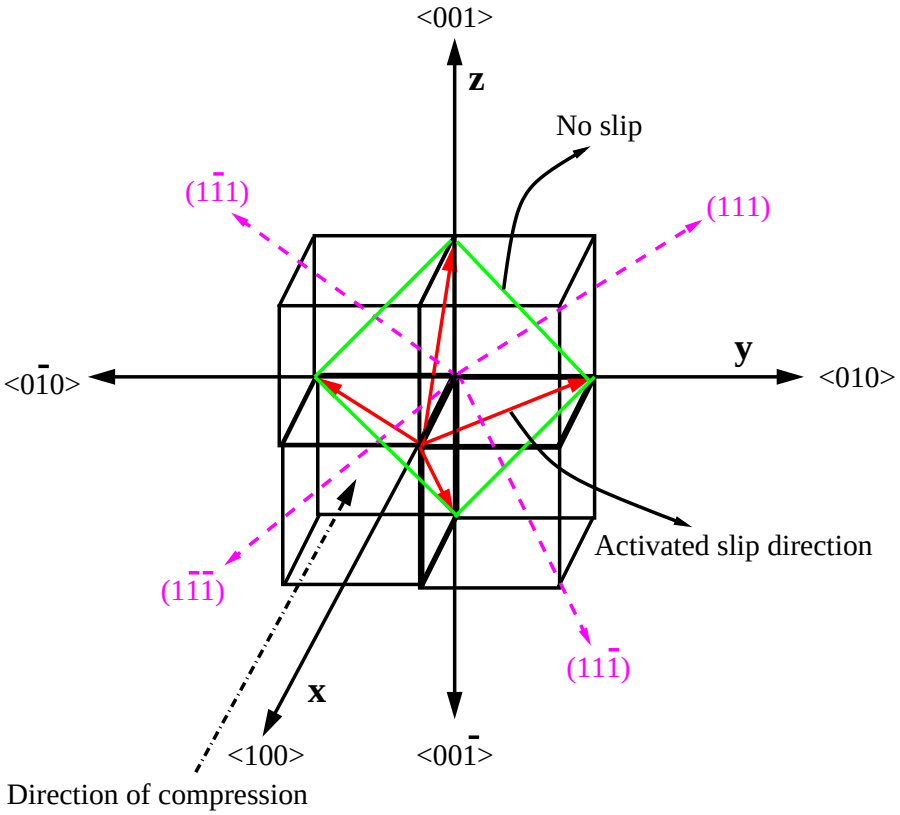

Figure 7.20: Graphical representation of activation of slip directions on 4 active slip planes for single crystal copper deformed along <100> direction.

Shape changes when deformed along <110> direction

The angle between (111) slip plane and <110> slip direction is given by

$$\cos\phi = \frac{(1)(1)+(1)(1)+(1)(0)}{\sqrt{1^2+1^2+1^2}\sqrt{1^2+1^2+0^2}} = \frac{2}{\sqrt{6}} \tag{7.26}$$

Slip system				Schmid factor
Slip plane normal (n)	$\cos\phi$ (n.c)	Slip direction (s)	$\cos\lambda$ (s.c)	(m)
(111)	0.577	$<\bar{1}10>$	-0.707	-0.408
		$<\bar{1}01>$	-0.707	-0.408
$(1\bar{1}1)$	0.577	$<\bar{1}01>$	-0.707	-0.408
		$<\bar{1}\bar{1}0>$	-0.707	-0.408
$(1\bar{1}\bar{1})$	0.577	$<\bar{1}0\bar{1}>$	-0.707	-0.408
		$<\bar{1}\bar{1}0>$	-0.707	-0.408
$(11\bar{1})$	0.577	$<\bar{1}0\bar{1}>$	-0.707	-0.408
		$<\bar{1}10>$	-0.707	-0.408

Table 7.5: All 8 slip systems which activate during the deformation of single crystal copper when deformed along <100> direction. Here c indicates the direction of compression (<100>).

The angle between slip directions ($<\bar{1}10>$, $<\bar{1}01>$ and $<0\bar{1}1>$) and compression axis (<110>) is given by

$$\cos\lambda = \frac{(\bar{1})(1)+(1)(1)+(0)(0)}{\sqrt{(\bar{1})^2+1^2+0^2}\sqrt{1^2+1^2+0^2}} = \frac{0}{\sqrt{6}} = 0 \quad for < \bar{1}10 > \tag{7.27}$$

$$\cos\lambda = \frac{(\bar{1})(1)+(0)(1)+(1)(0)}{\sqrt{(\bar{1})^2+0^2+1^2}\sqrt{1^2+1^2+0^2}} = \frac{-1}{\sqrt{4}} = \frac{-1}{2} \quad for < \bar{1}01 > \tag{7.28}$$

$$\cos\lambda = \frac{(0)(1)+(\bar{1})(1)+(1)(0)}{\sqrt{0^2+(\bar{1})^2+1^2}\sqrt{1^2+1^2+0^2}} = \frac{-1}{\sqrt{4}} = \frac{-1}{2} \quad for < 0\bar{1}1 > \tag{7.29}$$

Therefore, the Schmid factor for $<\bar{1}10>$, $<\bar{1}01>$ and $<0\bar{1}1>$ slip directions is given by

$$m_{<\bar{1}10>} = \cos\phi\cos\lambda = (\frac{2}{\sqrt{6}})(0) = 0 \tag{7.30}$$

$$m_{<\bar{1}01>} = \cos\phi\cos\lambda = (\frac{2}{\sqrt{6}})(-\frac{1}{2}) = -\frac{1}{\sqrt{6}} = -0.408 \tag{7.31}$$

$$m_{<0\bar{1}1>} = \cos\phi\cos\lambda = (\frac{2}{\sqrt{6}})(-\frac{1}{2}) = -\frac{1}{\sqrt{6}} = -0.408 \tag{7.32}$$

It is seen in Eqn. 7.30 that the Schmid factor is zero for $<\bar{1}10>$ slip direction, while it is non-zero for $<\bar{1}01>$ and $<0\bar{1}1>$ slip directions. Therefore, slip will occur along $<\bar{1}01>$ and $<0\bar{1}1>$ directions leading to expansion along z-direction. This is the reason why more deformation takes place along z-direction. The graphical representation of activation of slip directions on 2 active slip planes for single crystal copper deformed along <110> direction is shown in Figure 7.21 and details of the slip systems are tabulated in Table 7.6.

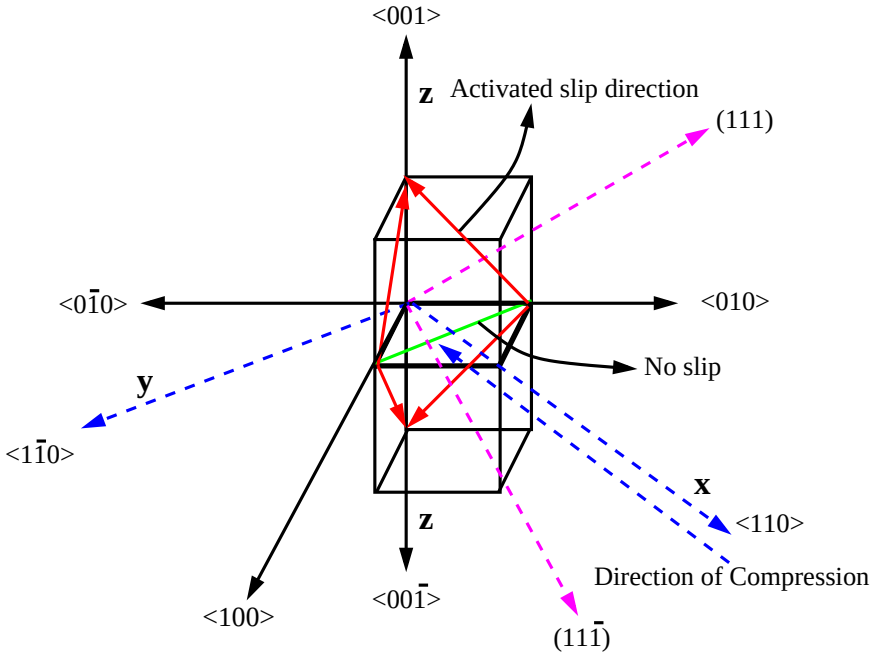

Figure 7.21: Graphical representation of activation of slip directions on 2 active slip planes for single crystal copper deformed along <110> direction.

Slip system				Schmid factor (m)
Slip plane normal (n)	$\cos\phi$ (n.c)	Slip direction (s)	$\cos\lambda$ (s.c)	
(111)	0.816	$<\bar{1}01>$	-0.50	-0.408
		$<0\bar{1}1>$	-0.50	-0.408
$(11\bar{1})$	0.816	$<\bar{1}0\bar{1}>$	-0.50	-0.408
		$<0\bar{1}\bar{1}>$	-0.50	-0.408

Table 7.6: All 4 slip systems which activate during the deformation of single crystal copper when deformed along <110> direction. Here c indicates the direction of compression (<110>).

7.7 Conclusions

The conclusions are as follows:

- The strength parameters for Johnson-Cook model have been obtained for single crystal copper deformed at 10^3/s strain rate along <100> and <110> directions. The value of yield strength and strain hardening parameter for single crystal copper deformed along the <110> direction is high compared to that deformed along the <100> direction.

- Neutron diffraction studies before and after the impact show the broadening of the diffraction peaks which is the signature of increased density of defects. The change in the diffraction peaks have been correlated with dislocations in the sample.

- Using MD simulations, the number of slip directions activated during the deformation of single crystal copper has been reproduced by computing the Burger vector for homogeneous nucleation of dislocations. Furthermore, shape changes observed in the experiments on single crystal copper have been validated by computing the Poisson ratio. The shape changes are understood in terms of the activation of preferred slip systems by performing the Schmid factor calculations.

Chapter 8

Conclusions and Future Scope

8.1 Conclusions

Solid fracture and dynamic strength under high strain rate deformation is of interest for high velocity impact and penetration problems. Existing fracture models at high strain rates, such as the void Nucleation and Growth model, involve several parameters. The best-fit values of those parameters are required for different materials of interest. These parameters are available in the open literature for few materials. The same applies to models for dynamic strength of solids. Therefore, for predictive hydrodynamic simulations, it is required to generate best-fit values of these parameters for different materials of interest.

This thesis studies the high strain rate deformation of single crystal copper, both by simulations and experiments, and covers two inputs to hydrodynamic simulations:

1. Void NAG model, which is one of the fracture models. The parameters for this model are determined by molecular dynamics simulations.

2. Johnson-Cook dynamic strength model. The parameters are obtained by performing quasi-static and dynamic compression experiments on single crystal copper using Universal Testing Machine and Split Hopkinson Pressure bar, respectively.

In this thesis, we obtain the void Nucleation and Growth (NAG) parameters for single crystal copper as well as their sensitivity to temperature. The effect of pre-existing defects on the NAG parameters is also studied and a multi-scale model is developed to generate spall data for single crystals. The void nucleation threshold

obtained is validated by high velocity impact of copper plates. We have performed these studies for single crystal copper, but the method of simulation is general enough to be extended to any other material, simply by changing the inter-atomic potential library. The important results of the present study are described below:

8.1.1 Application of a macroscopic void nucleation and growth model at the atomistic scales for perfect crystal copper

Molecular dynamics simulations are performed to study the nucleation and growth processes in single crystal copper under high strain rate deformation.

From the simulations, we conclude

- The Nucleation and Growth (NAG) model, originally developed for polycrystalline materials at (10^4-10^6)/s strain rates, is also applicable at high strain rates (5×10^9/s) at atomistic scales for perfect single crystals. The best-fit NAG parameters have been obtained for perfect single crystal copper at 300 K temperature.

- A comparison of NAG parameters for perfect single crystal copper with those obtained experimentally for polycrystalline copper, which are available in the literature, shows that

  - The threshold for void nucleation (160 kbar) is very high for single crystal copper as compared to that for polycrystalline copper (5 kbar). This is reasonable, since there are weak points in polycrystalline materials, e.g. grain junctions, which can lead to void nucleation at lower value of tensile pressure. This difference in void nucleation thresholds may also be the result of differences between the strain rates used in experiments and in MD simulations.

  - The low value of pressure sensitivity for void nucleation for single crystal copper, as compared to polycrystalline copper, indicates the rapid nucleation of voids for pressure above the void nucleation threshold.

  - The low value of material viscosity for single crystal copper indicates the rapid growth of voids once the void nucleation threshold is crossed.

- Perfect single crystals are not available for experiments. Real single crystals used in experiments contain defects. This could lead to a significant difference between experimental and MD values of nucleation threshold for single crystals. Hence, in order to validate the nucleation threshold obtained above, we have performed shock-wave simulations at the atomistic scales and determined the threshold tensile pressure at which nucleation starts. A good match has been found.

- The singular value decomposition analysis for single crystal copper triaxially deformed at 5×10^9/s shows that after the nucleation of first void

  - there is a shift in the frequencies of modes
  - new frequencies are created
  - strong modes correspond to the wavelength of λ, $3\lambda/2$ and $5\lambda/2$.
  - the hierarchy of modes changes after the void nucleation

8.1.2 Temperature sensitivity of void nucleation and growth parameters for single crystal copper- A molecular dynamics study

The effect of temperature on the nucleation and growth parameters have been studied for single crystal copper deformed at 5×10^9/s. The conclusions of this chapter are as follows:

- Best-fit NAG parameters have been obtained for single crystal copper deformed triaxially at 5×10^9/s strain rate with different temperatures. A systematic reduction in the magnitude of void nucleation and growth thresholds have been observed with rise in temperature.

- As the melting temperature of the single crystal copper is approached, a curious double-dip is observed in the pressure-time profile. A detailed of this anomaly has been performed, using statistical measures such as the structure factor, RDF, CSP and CNA. The study shows that the first minimum corresponds to the loss of the long-range order due to the creation of stacking

faults and an unknown structure and the system no longer has a FCC structure. There is no nucleation of voids at this juncture. The second minimum corresponds to the nucleation and incipient growth of voids.

In this chapter, we have shown (1) the effect of temperature on the nucleation and growth parameters of the DFRACT model for crystal copper and (2) analysis of the structural changes of the crystal subjected to high strain rate at different temperatures.

8.1.3 Effect of material damage on the spallation threshold of single crystal copper-A molecular dynamics study

High velocity impact of copper plates has been performed at impact velocities of 1100 m/s and 1000 m/s. The conclusions of this chapter are as follows:

- For impact at 1100 m/s impact velocity, the nucleation of voids takes place at two locations (x_1 and x_2) in the target. The CSP analysis for defects created shows that the stacking faults created rapidly converts to partial dislocations at location x_1 compared to that at location x_2. It is known that the dislocations soften the material surrounding the void and lead to growth of the voids. The rapid growth of voids at location x_1 is due to availability of many dislocations surrounding the voids leads to the spall of the material. Due to spall at location x_1, a compressive wave is generated which heals the voids at location x_2.

- For the non-contact impact of flyer-target system, spallation occurs at lower value of tensile pressure (112 kbar). This is due to the presence of defects which are created during initial passage of the shock. When the reflected release waves from the free surface interact subsequently causing tension, due to the defects, the nucleation threshold of voids decreases. For the in-contact impact of flyer-target system, defects are created only during the tension resulting from the interaction of release waves and not during initial passage of the shock. This means that there are no defects in advance to the tension in the contact case. These then lead to the nucleation of voids at higher value of tensile pressure (160 kbar) and hence spallation occurs at higher value of tensile pressure.

- Impact at 1000 m/s along the <100> direction shows that the nucleation and growth of voids take place at lower value of tensile pressure (124 kbar) corresponding to the tension resulting due to second traversal of the shock. For impact at 1100 m/s, nucleation and growth of voids take place at high tensile pressure (160 kbar) corresponding to the tension resulting from the first traversal of the shock. CSP analysis shows that partial dislocations and stacking faults are created during the tension created by first traversal of the shock and these defects become void nucleation sites for the tension resulting due to second traversal of the shock and thus lower the void nucleation threshold. This implies that high strain-rate history of the material affects the void nucleation threshold of the material.

- For impact at 1000 m/s along the <100> direction, a spall like signal which is a signature of spallation appears in the free surface velocity of the target. This is due to the stress relaxation resulting from the nucleation and growth of voids (which occur corresponding to second traversal of the shock) and not due to spallation of the material. When impact at 1000 m/s is performed along different crystal orientations (<110> and <111>), and with a simple grain boundary (bi-crystal), the nucleation and growth of voids occurs during the tension resulting from the first traversal of the shock and material undergoes spallation at late times.

- For impact at 1000 m/s along the <100> direction with a small change in the initial atomic positions along impact direction, the nucleation and growth of voids take place during the tension resulting due to second traversal of the shock and spallation occurs. This is different from the impact at 1000 m/s along <100> direction without perturbing initial atomic positions where nucleation and growth of voids take place during the tension due to second traversal of the shock and no spall occurs. This shows that for impact velocities close to spall threshold, spallation process is stochastic.

8.1.4 Multi-scale simulations of damage in single crystal copper with pre-existing defects

MD simulations have been performed to simulate isotropic tension in single crystal copper with pre-existing defects. The main conclusions are as follows:

- Best-fit NAG parameters have been obtained for single crystal copper triaxially deformed at 5×10^9/s strain rate with different defects (dislocations of different lengths and vacancies). The void nucleation threshold obtained decreases with increase in the length of the dislocation.

- The NAG parameters are then used in a macro-scale hydrodynamic simulation to generate spall data. Hydrodynamic simulation results for shock in single crystal copper show that

  - For NAG parameters obtained for perfect single crystal copper, no spallation occurs. Experimental single crystal spalls due to presence of defects.
  - For NAG parameters obtained for a pre-existing edge-dislocation having length equal to half of the side length of the simulation domain and containing only four atomic rows, pre-existing voids grow but no complete spall occurs. In this case, tensile pressure in the system exceeds the growth threshold of the material leading to incipient spall of the material [12].
  - For NAG parameters obtained for a pre-existing edge-dislocation having length equal to half the side length of the simulation domain and containing all atomic rows, nucleation and growth of the voids leads to the spall of the material. The results obtained match with the published experimental results [6] with 20% error.

- A multi-scale model has been developed where NAG parameters obtained using MD simulations for crystal copper with defects are used in a macroscopic hydrodynamic code to simulate shock in single crystal.

8.1.5 High strain rate deformation of single crystal copper-Experiments and MD simulations

Quasi-static and dynamic compression experiments have been performed on single crystal copper to obtain material strength parameters. Neutron diffraction analysis has been done to estimate the dislocation density in single crystal copper. MD simulations have been performed to reproduce active slip directions and to validate shape changes observed in experiments on single crystal copper. The conclusions are as follows:

- Johnson-Cook model parameters have been obtained for single crystal copper deformed at 10^3/s strain rate along <100> and <110> directions using SHPB. The value of yield strength and strain hardening parameter for single crystal copper deformed at 10^3/s strain rate along <110> direction is large compared to that deformed along <100> direction.

- Neutron diffraction studies before and after the impact show the broadening of the diffraction peaks which is the signature of increased density of defects. The change in the diffraction peaks has been correlated with the dislocations in the sample.

- Using MD simulations, the number of slip directions activated during the deformation of single crystal copper has been reproduced by computing the Burger vector for homogeneous nucleation of dislocations and shape changes observed in the experiments on single crystal copper have been validated by computing the Poisson ratio. The shape changes are understood in terms of activation of preferred slip systems by performing the Schmid factor calculations.

8.2 Future scope

The following studies can be performed to understand the failure of materials at high strain rates.

- We have used SRI-NAG model (also known as DFRACT model) to get the best-fit value of void nucleation and growth parameters for single crystal copper. Note that this model does not include the coalescence of voids. The study should be repeated after extending the model to include coalescence.

- Using SVD analysis, we have seen a shift in the frequency of the modes due to nucleation of first void. The linkage between the change in mode behaviour (before and after void nucleation) and the nucleation process itself needs to be quantified and to be understood in physical terms.

- Under triaxial deformation of single crystal copper at high strain rate (5×10^9/s), many voids nucleate. The detailed analysis of the void sizes, their morphology and their temperature dependence can be done in future.

- We have used edge dislocations in our study. The study needs to be repeated with with other defects such as stacking faults, twinning and screw dislocations. *In a real-life single crystal, there would be a statistical distribution of different kinds of defects. The study must be repeated with randomly-chosen distributions of defect type and size, and for a large enough number of combinations, to yield results with practical relevance.*

- The multi-scale model developed is applied here for single crystal copper only. The study can be performed with other single crystals of different materials to generalize the method.

- This study involves single crystal and bicrystal only. The study can be extended to polycrystalline materials with few grain boundaries.

- Experiments performed on single crystal copper do not include microscopic analysis of deformed samples. The microscopic analysis can be performed to study the changes in the microscopic properties due to deformation.

Bibliography

[1] T. Antoun, D. R. Curran, S. V. Razorenov, L. Seaman, G. I. Kanel, and A. V. Utkin, "Spall fracture," *Springer-Verlag, New York*, 2003.

[2] H. Tsuzuki, P. S. Branicio, and J. P. Rino, "Structural characterization of deformed crystals by analysis of common atomic neighborhood," *Computer Physics Communications*, vol. 177, pp. 518–523, 2007.

[3] W. Humphrey, A. Dalke, and K. Shulten, "VMD: Visual molecular dynamics," *Journal of Molecular Graphics*, vol. 14, no. 1, pp. 33–38, 1996.

[4] J. Li, "Atomeye: an efficient atomistic configuration viewer," *Modelling Simul. Mater. Sci. Eng.*, vol. 11, pp. 173–177, 2003.

[5] D. R. Curran, L. Seaman, and D. A. Shockey, "Dynamic failure of solids," *Physics Report*, vol. 147, no. 5,6, pp. 253–388, 1987.

[6] T. H. Antoun, L. Seaman, and D. R. Curran, "Dynamic failure of materials: volume 2-compilation of russian spall data," *Technical Report No. DSWA-TR-96-77-V2, Defense Special Weapons Agency Alexandria, VA*, 1998.

[7] R. E. Rudd and J. Belak, "Void nucleation and associated plasticity in dynamic fracture of polycrystalline copper: an atomistic simulation," *Computational Materials Science*, vol. 24, pp. 148–153, 2002.

[8] E. T. Seppala, J. Belak, and R. E. Rudd, "Effect of stress triaxiality on void growth in dynamic fracture of metals: A molecular dynamics study," *Physical Review B*, vol. 69, pp. 134101 (1–19), 2004.

[9] M. Zhou and R. J. Clifton, "Dynamic ductile rupture under conditions of plane strain," *International Journal of Impact Engineering*, vol. 19, no. 3, pp. 189–206, 1997.

[10] E. Moshe, S. Eliezer, E. Dekel, A. Ludmirsky, Z. Henis, M. Werdiger, I. B. Goldberg, N. Eliaz, and D. Eliezer, "An increase of the spall strength in aluminum, copper, and metglas at strain rates larger than 1e7/s," *Journal of Applied Physics*, vol. 83, no. 8, pp. 4004–4011, 1998.

[11] E. Dekel, S. Eliezer, Z. Henis, E. Moshe, A. Ludmirsky, and I. B. Goldberg, "Spallation model for the high strain rates range," *Journal of Applied Physics*, vol. 84, no. 9, pp. 4851–4858, 1998.

[12] R. W. Minich, J. U. Cazamias, M. Kumar, and A. J. Schwartz, "Effect of microstructural length scales on spall behavior of copper," *Metallurgical and Materials Transactions A*, vol. 35A, pp. 2663–2673, 2004.

[13] J. Belak, "On the nucleation and growth of voids at high strain-rates," *Journal of Computer-Aided Materials Design*, vol. 5, pp. 193–206, 1998.

[14] S. Traiviratana, E. M. Bringa, D. J. Benson, and M. A. Meyers, "Void growth in metals: Atomistic calculations," *Acta Materialia*, vol. 56, pp. 3874–3886, 2008.

[15] E. T. Seppala, J. Belak, and R. E. Rudd, "Onset of void coalescence during dynamic fracture of ductile metals," *Physical Review Letters*, vol. 93, pp. 245503 (1–4), 2004.

[16] M. A. Shehadeh, H. M. Zbib, and T. D. Rubia, "Multiscale dislocation dynamics simulations of shock compression in copper single crystal," *International Journal of Plasticity*, vol. 21, pp. 2369–2390, 2005.

[17] V. R. Ikkurthi and S. Chaturvedi, "Use of different damage models for simulating impact-driven spallation in metal plates," *International Journal of Impact Engineering*, vol. 30, pp. 275–301, 2004.

[18] W. J. Murphy et al, "The strength of single crystal copper under uniaxial shock compression at 100 gpa," *Journal of Physics: Condensed Matter*, vol. 22, pp. 065404 (5pp), 2010.

[19] L. P. Davila, P. Erhart, E. M. Bringa, M. A. Meyers, V. A. Lubarda, M. S. Schneider, R. Becker, and M. Kumar, "Atomistic modeling of shock-induced

void collapse in copper," *Applied Physics Letters*, vol. 86, pp. 161902 (1–3), 2005.

[20] G. P. Potirniche, M. F. Horstemeyer, G. J. Wagner, and P. M. Gullett, "A molecular dynamics study of void growth and coalescence in single crystal nickel," *International Journal of Plasticity*, vol. 22, pp. 257–278, 2006.

[21] J. Wang, S. Yip, S. R. Phillpot, and D. Wolf, "Crystal instabilities at finite strain," *Physical Review Letters*, vol. 71, no. 25, pp. 4182–4185, 1993.

[22] Z. Zhuang, Z. L. Liu, X. C. You, and Y. Guo, "Development of multi-scale computation framework to investigate the failure behavior of the materials," *Advanced Materials Research*, vol. 33-37, pp. 875–880, 2008.

[23] R. E. Rudd and J. Q. Broughton, "Coarse-grained molecular dynamics and the atomic limit of finite elements," *Physical Review B*, vol. 58, no. 10, pp. R5893–R5896, 1998.

[24] R. E. Rudd and J. Q. Broughton, "Coarse-grained molecular dynamics: Nonlinear finite elements and finite temperature," *Physical Review B*, vol. 72, pp. 144104 (1–32), 2005.

[25] J. E. Field, S. M. Walley, W. G. Proud, H. T. Goldrein, and C. R. Siviour, "Review of experimental techniques for high rate deformation and shock studies," *International Journal of Impact Engineering*, vol. 30, pp. 725–775, 2004.

[26] A. S. Milani, W. Dabboussi, J. A. Nemes, and R. C. Abeyaratne, "An improved multi-objective identification of johnson-cook material parameters," *International Journal of Impact Engineering*, vol. 36, pp. 294–302, 2009.

[27] G. R. Johnson and W. H. Cook, "Fracture characteristics of three metals subjected to various strains, strain rates, temperatures and pressures," *Engineering Fracture Mechanics*, vol. 21, no. 1, pp. 31–48, 1985.

[28] F. J. Zerilli and R. W. Armstrong, "Dislocation-mechanics-based constitutive relations for material dynamics calculations," *Journal of Applied Physics*, vol. 61, no. 5, pp. 1816–1825, 1987.

[29] D. J. Steinberg, S. G. Cochran, and M. W. Guinan, "A constitutive model for metals applicable at high-strain rate," *Journal of Applied Physics*, vol. 51, no. 3, pp. 1498–1504, 1980.

[30] D. J. Steinberg, "Constitutive model used in computer simulation of time-resolved, shock-wave data," *International Journal of Impact Engineering*, vol. 5, pp. 603–611, 1987.

[31] N. Bonora and P. P. Milella, "Constitutive modeling for ductile metals behavior incorporating strain rate, temperature and damage mechanics," *International Journal of Impact Engineering*, vol. 26, pp. 53–64, 2001.

[32] F. F. Abraham, D. Brodbeck, W. E. Rudge, J. Q. Broughton, D. Schneider, B. Land, D. Lifka, J. Gerner, M. Rosenkranz, J. Skivira, and H. Gao, "Ab initio dynamics of rapid fracture," *Modelling and Simulation in Material Science and Engineering*, vol. 6, pp. 639–670, 1998.

[33] M. Marder and J. Fineberg, "How things break: solids fail through the propagation of cracks, whose speed is controlled by instabilities at the smallest scales," *Physics Today*, vol. 49, pp. 24, 1996.

[34] M. J. Buehler and H. Gao, "Ultra-large scale simulations of dynamic materials failure," *Handbook of Theoretical and Computational Nanotechnology*, vol. X, pp. 1–41, 2005.

[35] M. Springborg, "Density-functional methods in chemistry and materials science," *Wiley Research Series in Theoretical Chemistry*, 1997.

[36] M. Warrier, "Multi-scale modeling of hydrogen isotope transport in porous graphite," *Ph.D Thesis*, 2004.

[37] K. Nordlund, "Introduction to atomistic simulations," *http://www.acclab.helsinki.fi/ knordlun/atomistiset*, 2003.

[38] D. Frenkel and B. Smit, "Understanding molecular simulaton: from algorithms to applications," *Academic Press,London*, 2002.

[39] M. S. Daw and M. I. Baskes, "Semi-empirical, quantum mechanical calculation of hydrogen embrittlement in metals," *Physical Review Letters*, vol. 50, no. 17, pp. 1285–1288, 1983.

[40] M. S. Daw and M. I. Baskes, "Embedded-atom method: Derivation and application to impurities, surfaces, and other defects in metals," *Physical Review B*, vol. 29, no. 12, pp. 6443–6453, 1984.

[41] M. P. Allen and D. J. Tildesley, "Computer simulation of liquids," *Oxford University Press, Oxford*, 1987.

[42] P. H. Hunenberger, "Thermostat algorithms for molecular dynamics simulations," *Advances in Polymer Science*, vol. 173, pp. 105–149, 2005.

[43] D. C. Rapaport, "The art of molecular dynamics simulation," *Cambridge University Press, New York*, 1995.

[44] W. G. Hoover, "Canonical dynamics: Equilibrium phase-space distributions," *Physical Review A*, vol. 31, no. 3, pp. 1695–1697, 1985.

[45] W. G. Hoover, "Constant-pressure equation of motion," *Physical Review A*, vol. 34, no. 3, pp. 2499–2500, 1986.

[46] G. A. Mansoori, "Principles of nanotechnology: Molecular-based study of condensed matter in small systems," *World Scientific Publishing Co. Pte. Ltd, Singapore*, 2005.

[47] http://matdl.org/matdlwiki/index.php/softmatter:Radial_Distribution_Function, ," .

[48] I. Khidirov, "Neutron diffraction," *InTech, Janeza Trdine 9, 51000 Rijeka, Croatia*, 2012.

[49] C. L. Kelchner, S. J. Plimpton, and J. C. Hamilton, "Dislocation nucleation and defect structure during surface indentation," *Physical Review B*, vol. 58, no. 17, pp. 11085–11088, 1998.

[50] K. J. Zhao, C. Q. Chen, Y. P. Shen, and T. J. Lu, "Molecular dynamics study on the nano-void growth in face-centered cubic single crystal copper," *Computational Materials Science*, vol. 46, pp. 749–754, 2009.

[51] J. D. Honeycutt and H. C. Andersen, "Molecular dynamics study of melting and freezing of small lennard-jones clusters," *Journal of Physical Chemistry*, vol. 91, no. 19, pp. 4950–4963, 1987.

[52] J. Schiotz, T. Vegge, F. D. Di Tolla, and K. W. Jacobsen, "Atomic-scale simulations of the mechanical deformation of nanocrystalline metals," *Physical Review B*, vol. 60, no. 7, pp. 971–983, 1999.

[53] H. Wang, "Nucleation in the ising model, lennard-jones liquid and the long-range fpu model," *Ph.D Thesis*, 2007.

[54] W. H. Press, S. A. Teukolsky, W. T. Vetterling, and B. P. Flannery, "Numerical recipes in c: The art of scientific computing," *Cambridge University Press*, 1988.

[55] A. Stukowski, "Visualization and analysis of atomistic simulation data with ovito-the open visualization tool," *Modelling Simul. Mater. Sci. Eng.*, vol. 18, pp. 015012, 2010.

[56] J. N. Johnson, "Dynamic fracture and spallation in ductile solids," *Journal of Applied Physics*, vol. 52, no. 4, pp. 2812–2825, 1981.

[57] H. Poritsky, "The collapse or growth of a spherical bubble or cavity in a viscous fluid," *Proceedings of the First U.S. National Congress of Applied Mechanics, ASME, New York*, p. 813, 1952.

[58] L. Davison, A. L. Stevens, and M. E. Kipp, "Theory of spall damage accumulation in ductile metals," *Journal of the Mechanics and the Physics of Solids*, vol. 25, pp. 11–28, 1977.

[59] S. Plimpton, "Fast parallel algorithm for short-range molecular dynamics," *Journal of Computational Physics*, vol. 117, pp. 1–19, 1995.

[60] S. M. Foiles, M. I. Baskes, and M. S. Daw, "Embedded-atom method functions for the fcc metals cu, ag, au, ni, pd, pt, and their alloys," *Physical Review B*, vol. 33, no. 12, pp. 7983–7991, 1986.

[61] D. J. Oh and R. A. Johnson, "Atomistic simulation of materials: Beyond pair potentials," *Plenum, New York, NY*, p. 233, 1989.

[62] J. B. Adams, W. G. Wolfer, and S. M. Foiles, "Elastic properties of grain boundaries in copper and their relationship to bulk elastic constants," *Physical Review B*, vol. 40, no. 14, pp. 9479–9484, 1989.

[63] X. W. Zhou, H. N. G. Wadley, R. A. Johnson, D. J. Larson, N. Tabat, A. Cerezo, A. K. Petford-Long, G. D. W. Smith, P. H. Clifton, R. L. Martens, and T. F. Kelly, "Atomic scale structure of sputtered metal multilayers," *Acta Materialia*, vol. 49, pp. 4005–4015, 2001.

[64] Y. Mishin, M. J. Mehl, D. A. Papaconstantopoulos, A. F. Voter, and J. D. Kress, "Structural stability and lattice defects in copper: Ab initio, tight-binding, and embedded-atom calculations," *Physical Review B*, vol. 63, pp. 224106 (1–16), 2001.

[65] E. Moshe, S. Eliezer, Z. Henis, M. Werdiger, E. Dekel, Y. Horovitz, S. Maman, I. B. Goldberg, and D. Eliezer, "Experimental measurements of the strength of metals approaching the theoretical limit predicted by the equation of state," *Applied Physics Letters*, vol. 76, no. 12, pp. 1555–1557, 2000.

[66] D. L. Tonks, D. J. Alexander, S. A. Sheffield, D. L. Robbins, A. K. Zurek, and W. R. Thissell, "Spallation strength of single crystal an polycrystalline copper," *J. Phys. IV France*, vol. 10, pp. Pr9–787–Pr9–792, 2000.

[67] G. I. Kanel, S. V. Razorenov, and V. E. Fortov, "Shock-wave and high-strain-rate phenomena in materials," *Marcel Dekker, New York, NY*, p. 775, 1991.

[68] S. V. Razorenov and G. I. Kanel, "The strength of copper single crystals and the factors governing metal fracture in uniaxial dynamic stretching," *Physics of Metals and Metallography*, vol. 74, no. 5, pp. 526–530, 1992.

[69] S. V. Razorenov, G. I. Kanel, K. Baumung, and H. J. Bluhm, "Hugoniot elastic limit and spall strength of aluminum and copper single crystals over a wide range of strain rates and temperatures," *AIP Conference Proceedings*, vol. 620, pp. 503–506, 2002.

[70] R. G. McQueen and S. P. Marsh, "Ultimate yield strength of copper," *Journal of Applied Physics*, vol. 33, no. 2, pp. 654–665, 1962.

[71] E. M. Bringa, J. U. Cazamias, P. Erhart, J. Stolken, N. Tanushev, B. D. Wirth, R. E. Rudd, and M. J. Caturla, "Atomistic shock hugoniot simulation of single-crystal copper," *Journal of Applied Physics*, vol. 96, no. 7, pp. 3793–3799, 2004.

[72] J. R. Asay and M. Shahinpoor, "High pressure shock compression of solids," *Springer-Verlag, New York*, 1993.

[73] S. N. Luo, Q. An, T. C. Germann, and L. B. Han, "Shock-induced spall in solid and liquid copper at extreme strain rates," *Journal of Applied Physics*, vol. 106, pp. 013502 (1–8), 2009.

[74] S. negi and S. Chaturvedi, "Normal mode analysis of a single-walled carbon nanotub based on molecular dynamic: A singular value decomposition study," *International Journal of Nanoscience*, vol. 9, no. 5, pp. 471–486, 2010.

[75] G. I. Kanel, S. V. Razorenov, A. Bogatch, A. V. Utkin, V. E. Fortov, and D. E. Grady, "Spall fracture properties of aluminum and magnesium at high temperatures," *Journal of Applied Physics*, vol. 79, no. 11, pp. 8310–8317, 1996.

[76] G. I. Kanel, K. Baumung, J. Singer, and S. V. Razorenov, "Dynamic strength of aluminum single crystals at melting," *Applied Physics Letters*, vol. 76, no. 22, pp. 3230–3232, 2000.

[77] E. B. Zaretsky, "Impact response of cobalt over the 300-1400 k temperature range," *Journal of Applied Physics*, vol. 108, pp. 083525 (1–7), 2010.

[78] M. Parrinello and A. Rahman, "Crystal structure and pair potentials: A molecular dynamics study," *Physical Review Letters*, vol. 45, no. 14, pp. 1196–1199, 1980.

[79] Z. Wang, U. Landman, R. L. B. Selinger, and W. M. Gelbart, "Molecular-dynamics study of elasticity and failure of ideal solids," *Physical Review B*, vol. 44, no. 1, pp. 378–381, 1991.

[80] R. M. Lynden-Bell, "The fracture of perfect crystals under uniaxial tension at high temperatures," *Journal of Physics: Condensed Matter*, vol. 4, pp. 2127–2138, 1992.

[81] S. Blonski and W. Brostow, "Molecular-dynamics simulations of stress relaxation in metals and polymers," *Physical Review B*, vol. 49, no. 10, pp. 6494–6500, 1994.

[82] R. M. Lynden-Bell, "A simulation study of induced disorder, failure and fracture of perfect metal crystals under uniaxial tension," *Journal of Physics: Condensed Matter*, vol. 7, pp. 4603–4624, 1995.

[83] C. Kittel, "Introduction to solid state physics," *John Wiley and Sons (Asia) Pte. Ltd., Singapore*, p. 58, 2004.

[84] A. K. Zurek, W. R. Thissell, J. N. Johnson, D. L. Tonks, and R. Hixson, "Micromechanics of spall and damage in tantalum," *Journal of Materials Processing Technology*, vol. 60, pp. 261–267, 1996.

[85] J. P. Fowler, M. J. Worswick, A. K. Pilkey, and H. Nahme, "Damage leading to ductile fracture under high strain-rate conditions," *Metallurgical and Materials Transactions A*, vol. 31A, pp. 831–844, 2000.

[86] J. M. Rivas, A. K. Zurek, W. R. Thissell, D. L. Tonks, and R. S. Hixson, "Quantitative description of damage evolution in ductile fracture of tantalum," *Metallurgical and Materials Transactions A*, vol. 31A, pp. 845–851, 2000.

[87] S. Eliezer, I. Gilath, and T. Bar-Noy, "Laser-induced spall in metals: Experiments and simulation," *Journal of Applied Physics*, vol. 67, no. 2, pp. 715–724, 1990.

[88] G. I. Kanel, S. V. Razorenov, A. V. Utkin, V. E. Fortov, K. Baumung, H. U. Karow, D. Rusch, and V. Licht, "Spall strength of molybdenum single crystals," *Journal of Applied Physics*, vol. 74, no. 12, pp. 7162, 1993.

[89] E. Moshe, S. Eliezer, E. Dekel, A. Ludmirsky, I. B. Goldberg, and D. Eliezer, "Measurements of laser driven spallation in tin and zinc using an optical recording velocity interferometer system," *Journal of Applied Physics*, vol. 86, no. 8, pp. 4242–4248, 1999.

[90] H. Tamura, T. Kohama, K. Kondo, and M. Yoshida, "Femtosecond-laser-induced spallation in aluminum," *Journal of Applied Physics*, vol. 89, no. 6, pp. 3520–3522, 2001.

[91] S. Cochran and D. Banner, "Spall studies in uranium," *Journal of Applied Physics*, vol. 48, no. 7, pp. 2729–2737, 1977.

[92] J. N. Johnson, G. T. Gray III, and N. K. Bourne, "Effect of pulse duration and strain rate on incipient spall fracture in copper," *Journal of Applied Physics*, vol. 86, no. 9, pp. 4892–4901, 1999.

[93] S. G. Srinivasan, M. I. Baskes, and G. J. Wagner, "Spallation of single crystal nickel by void nucleation at shock induced grain junctions," *Journal of Materials Science*, vol. 41, pp. 7838–7842, 2006.

[94] V. Dremov, A. Petrovtsev, P. Sapozhnikov, M. Smirnova, D. L. Preston, and M. A. Zocher, "Molecular dynamics simulations of the initial stages of spall in nanocrystalline copper," *Physical Review B*, vol. 74, pp. 144110 (1–5), 2006.

[95] S. Rawat, M. Warrier, S. Chaturvedi, and V. M. Chavan, "Temperature sensitivity of void nucleation and growth parameters for single crystal copper: a molecular dynamics study," *Modelling and Simulation in Materials Science and Engineering*, vol. 19, pp. 025007 (20pp), 2011.

[96] R. E. Rudd, "Void growth in bcc metals simulated with molecular dynamics using the finnis-sinclair potential," *Philosophical Magazine*, vol. 89, no. 34-36, 1-21, pp. 3133–3161, 2009.

[97] B. A. Gama, S. L. Lopatnikov, and J. W. Gillespie, "Hopkinson bar experimental technique: A critical review," *Appl. Mech. Rev*, vol. 57, no. 4, pp. 223–250, 2004.

[98] J. N. Florando, M. M. LeBlanc, and D. H. Lassila, "Multiple slip in copper single crystals deformed in compression under uniaxial stress," *Scripta Materialia*, vol. 57, pp. 537–540, 2007.

[99] S. R. Kalidindi and L. Anand, "Large deformation simple compression of a copper single crystal," *Metallurgical Transactions A*, vol. 24A, pp. 989–992, 1993.

[100] K. H. Kim and Y. M. Koo, "In-situ x-ray diffraction study of single-slip-conditioned copper single crystals during uniaxial deformations," *Philosophical Magazine A*, vol. 81, no. 2, pp. 479–488, 2001.

[101] U. S. Lindholm, "Some experiments with the split hopkinson pressure bar," *Journal of the Mechanics and Physics of Solids*, vol. 12, pp. 317–335, 1964.

[102] K. T. Ramesh and S. Narasimhan, "Finite deformations and the dynamic measurement of radial strains in compression kolsky bar experiments," *International Journal of Solids Structures*, vol. 33, no. 25, pp. 3723–3738, 1996.

[103] S. Sharma, V. M. Chavan, R. G. Agrawal, R. J. Patel, R. Kapoor, and J. K. Chakravartty, "Slip-hopkinson pressure bar: an experimental technique for high strain rate tests," *BARC Technical Report No - BARC/2011/E/013*, 2011.

[104] M. A. Meyers, "Dynamic behavior of materials," *John Wiley and Sons, Inc.*, 1994.

[105] S. L. Chaplot, R. Mukhopadhyay, P. R. Vijayaraghavan, A. S. Deshpande, and K. R. Rao, "Phonon density of states of tetracyanoethylene from coherent inelastic neutron scattering at dhruva reactor," *Pramana-Journal of Physics*, vol. 33, no. 5, pp. 595–602, 1989.

[106] M. N. Rao, S. Rawat, S. Sharma, V. M. Chavan, R. J. Patel, and S. L. Chaplot, "Neutron diffraction measurements of dislocation density in copper crystals deformed at high strain rate," *Submitted to DAE Solid State Physics Symposium*, 2012.

[107] X. H. Zheng, H. Chen, Z. B. Yan, Y. J. Han, H. B. Yu, D. S. Li, Q. Huang, and J. M. Zhou, "Determination of twist angle of in-plane mosaic spread of gan films by high-resolution x-ray diffraction," *Journal of Crystal Growth*, vol. 255, pp. 63–67, 2003.

[108] E. M. Bringa, S. Traiviratana, and M. A. Meyers, "Void initiation in fcc metals: Effect of loading orientation and nanocrystalline effects," *Acta Materialia*, vol. 58, pp. 4458–4477, 2010.

[109] A. Stukowski and K. Albe, "Extracting dislocations and non-dislocation crystal defects from atomistic simulation data," *Modelling and Simulation in Material Science and Engineering*, vol. 18, pp. 085001, 2010.

[110] G. E. Dieter, "Mechanical metallurgy," *McGraw-Hill Book Company (UK) Limited*, 1988.